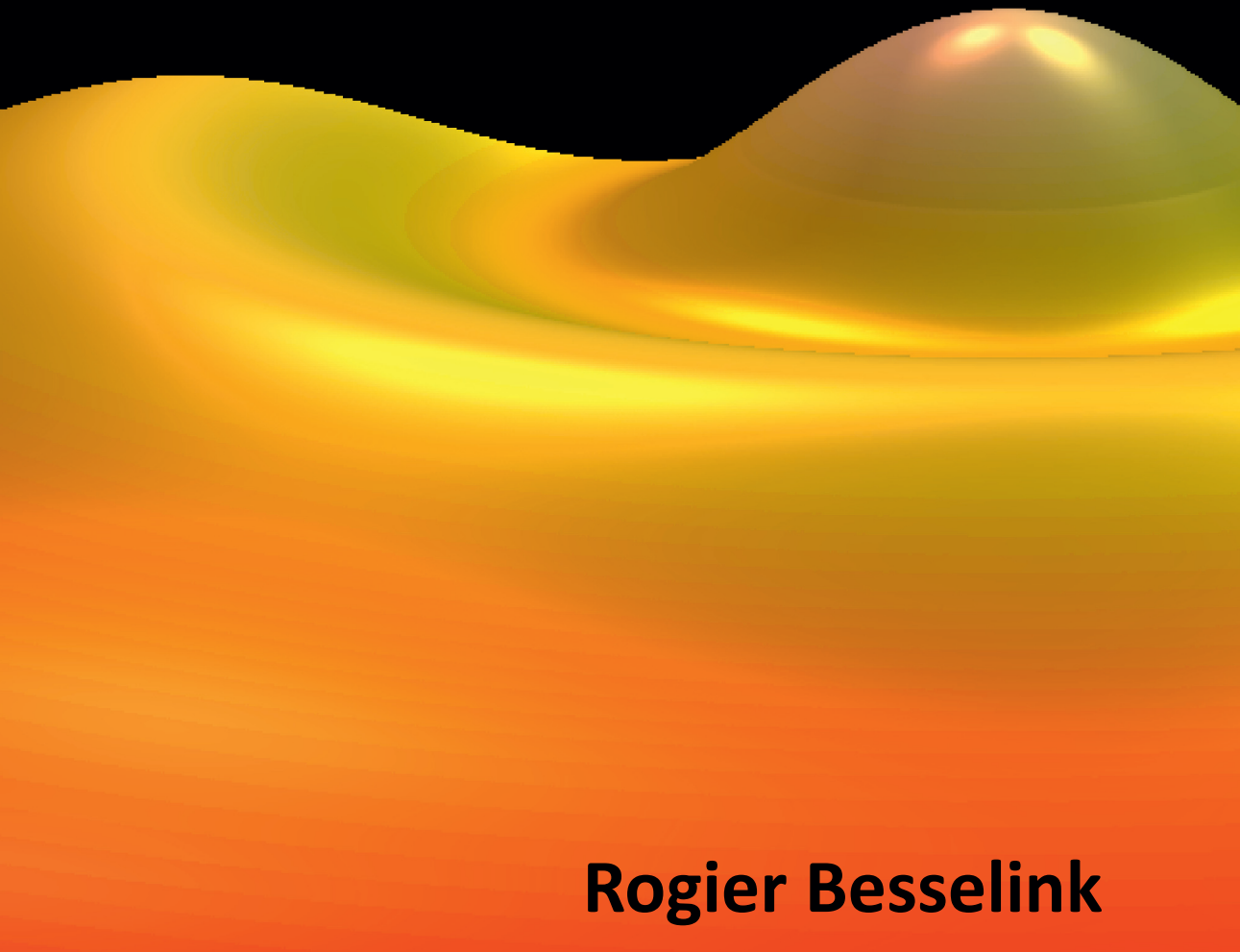


Understanding Microstructural Evolution in Mixed Metal-Oxide Silsesquioxane Glasses Through Wet-Chemical Synthesis



Rogier Besselink

**UNDERSTANDING MICROSTRUCTURAL EVOLUTION OF
MIXED METAL OXIDE SILSESQUIOXANE GLASSES THROUGH
WET-CHEMICAL SYNTHESIS**

Rogier Besselink

PhD committee

Chairman and secretary:

Prof. dr. ir. J.W.M. Hilgenkamp University of Twente

Supervisor:

Prof. dr. ir. J.E. ten Elshof University of Twente

Members:

Prof. dr. L. van Wüllen University of Augsburg
Prof. dr. A. Nijmeijer University of Twente
Prof. dr. ing. D.H.A. Blank University of Twente
Prof. dr. A.J.A. Winnubst University of Science and Technology
of China, Hefei / University of Twente

Referent:

Dr. A. Petukhov Utrecht University

Cover: Simulated 2D-small angle X-ray pattern of a mixture of correlated spherical agglomerates with branched polymeric agglomerates. The molecule on the backside represents: $\text{Nb}_8\text{O}_{10}(\text{OEt})_{20}$.

The work in this thesis was carried out at the Inorganic Materials Science Group at the faculty of Science and Technology and the MESA+ Institute for Nanotechnology, University of Twente, P.O. Box 217, 7500 AE, Enschede. This research was financially supported by (STW) the National Institute of Technical Sciences.

R. Besselink: *Understanding microstructural evolution of mixed metal oxide silsesquioxane glasses through wet-chemical synthesis.*

PhD Thesis, University of Twente, Enschede, The Netherlands

ISBN: 978-90-365-3637-0

DOI: 10.3990/1.9789036536370

Printed by: Gildeprint drukkerijen, Enschede, The Netherlands

Copyright ©2014 by: R. Besselink

**UNDERSTANDING MICROSTRUCTURAL EVOLUTION OF
MIXED METAL OXIDE SILSESQUIOXANE GLASSES THROUGH
WET-CHEMICAL SYNTHESIS**

PROEFSCHRIFT

ter verkrijging van
de graad van doctor aan de Universiteit Twente,
op gezag van de rector magnificus,
Prof. dr. H. Brinksma,
volgens besluit van het College voor Promoties
in het openbaar te verdedigen
op vrijdag 28 maart 2014 om 12:45 uur

door

Rogier Besselink

geboren op 28 februari 1983
te Doetinchem

Dit proefschrift is goedgekeurd door de promotor

Prof. dr. J.E. ten Elshof

Table of Contents

Chapter 1.	Introduction	9
1.1)	Sol-Gel Chemistry	10
1.2)	Sol-Gel Processing	22
1.3)	Porous Inorganic Membranes	26
1.4)	The Scope of the Thesis and Outline	30
1.5)	References	32
Chapter 2.	Theory of Small Angle Scattering	39
2.1)	Form Function	41
2.2)	Structure function	43
2.3)	Polydisperse Systems	51
2.4)	Non-particulate systems	52
2.5)	References	53
Chapter 3.	Rapid early stage Schultz-Zimm distributed mass-fractal growth studies on niobia/silsesquioxane mixtures	57
3.1)	Abstract	58
3.2)	Introduction	58
3.3)	Experimental section	60
3.4)	Theoretical Background	63
3.5)	Results and Discussion	72
3.6)	Conclusions	78
3.7)	References	78

Chapter 4.	Evolution of microstructure in mixed niobia-hybrid silica thin films from sol-gel precursors	83
4.1)	Abstract	84
4.2)	Introduction	84
4.3)	Experimental Section	86
4.4)	Derivation of $I(q)$	88
4.5)	Results and Discussion	96
4.6)	Conclusions	113
4.7)	References	114
S4.)	Supporting Information	121
S4.1)	SAXS- Porod regime	122
S4.2)	Nitrogen Sorption Measurements	123
S4.3)	References	124
Chapter 5.	Extent of niobia/silsesquioxane intermixing by solid state MAS-NMR	125
5.1)	Abstract	126
5.2)	Introduction	126
5.3)	Experimental Section	128
5.4)	Results and Discussion	130
5.5)	Conclusions	138
5.6)	References	139

Chapter 6.	Crystallized Nb ₈ O ₁₀ (OEt) ₂₀ from condensation of niobium ethoxide and acetone that exhibits remarkable anisotropy in thermal expansion	143
6.1)	Abstract	144
6.2)	Introduction	144
6.3)	Experimental Section	146
6.4)	Results and Discussion	147
6.5)	Conclusions	157
6.6)	References	157
S6.)	Supporting information	161
S6.1)	Extended lists of bond lengths and angles	162
S6.2)	References	165
Chapter 7.	A novel malonamide bridged silsesquioxane precursor for enhanced dispersion of transition and lanthanide metal ions in hybrid silica membranes	167
7.1)	Abstract	168
7.2)	Introduction	168
7.3)	Experimental Section	171
7.4)	Results and Discussion	177
7.5)	Conclusions	199
7.6)	References	200

Chapter 8.	Conclusions and Outlook	207
8.1)	General Conclusions	208
8.2)	Additional observations and remarks	209
8.3)	Future Perspective and outlook	210
8.4)	References	212
Summary		213
Samenvatting		217
Acknowledgement		221
Dankwoord		225

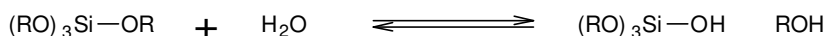
1.

Introduction

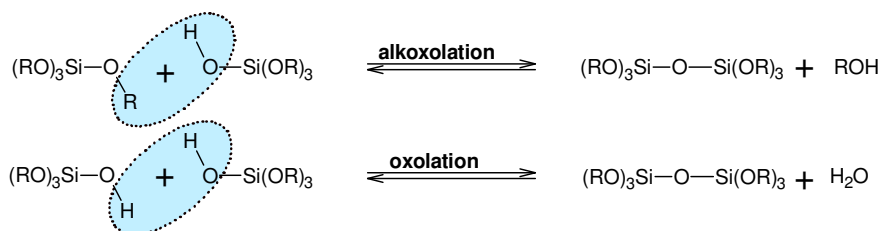
1.1. Sol-Gel chemistry

1.1.1. The chemistry of silicon alkoxides

Amorphous silicon oxides can be prepared via polymerisation reactions of silicon alkoxides with water. The silicon alkoxides initiate via a hydrolysis reaction (Scheme 1.1) and subsequently propagate via a number of different reaction processes (Scheme 1.2) [1-3]. Propagation mainly occurs via condensation reactions that either involves the elimination of water (oxolation) or the elimination of alcohol (alkoxolation).



Scheme 1.1. Hydrolysis of silicon alkoxides

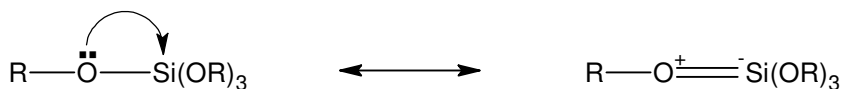


Scheme 1.2. Condensation of silicon alkoxides

In polar solvents, the polymerisation reactions pursue an equilibrium that strongly depends on the reaction conditions. Different structures and morphologies were obtained by tuning suitable reaction conditions, which makes these sol-gel techniques very attractive for a wide range of materials.

Propagation is in general terminated by limited mobility of reactive species that are entrapped into network and by reduction of reactive monomer species. The final product often contains a certain content of alkoxide groups can be removed by calcination. Silicon alkoxides are hydrophobic compounds with a low polarity. This is partly caused by the higher electronegativity of silicon (1,74) in comparison to early transition metal ions in metal alkoxides. A low polarity of silicon alkoxides corresponds with a very low solubility of silicon alkoxides in water [3]. In addition negative partial charge on oxygen of the alkoxide group is further stabilized by a

mesomeric interaction between occupied 2p-orbitals of oxygen and empty 3d-orbitals of silicon as illustrated in Scheme 1.3 [4]. In contrast to other metal alkoxides, silicon alkoxides are very weak Lewis acids/bases, which corresponds with a hydrolysis rate in water that is orders of magnitudes smaller in comparison to most metal alkoxides [1, 2].



Scheme 1.3. Overlap of between O 3p and empty Si 3d orbitals

The pH has a strong effect on the hydrolysis of silicon, while it determines the stability and the type of transition state and consequently it strongly affect the activation energy of hydrolysis. At a pH below the isoelectric point (IEP = 2.2) hydrolysis occurs via an acid catalysed mechanism and above IEP via a base catalysed mechanism [1].

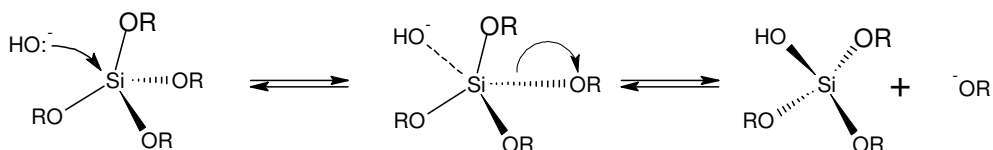
The polarity of the silicon oxide bond is partly determined by the type of alkoxide. This can be explained by an inductive effect. The longer the alkane chain of the alkoxide, the stronger is the electron propulsion of this chain which results in a stabilisation of the negative charge of oxygen. Therefore the rate of hydrolysis decreases in the sequence: $\text{Si}(\text{OC}_2\text{H}_5)_4 > \text{Si}(\text{OC}_4\text{H}_9)_4 > \text{Si}(\text{OC}_9\text{H}_{19})_4$ [2]. Steric hindrance can also play a role in the reactivity of alkoxide and the hindrance will increase with increase of the alkyl chain length. Thus, the observed reduction of hydrolysis rate as a function of alkyl chain length is also explained in terms of steric hindrance.

The alkoxide ligands of silicon alkoxide can exchange by a reaction with different alcohols. However, due to the low polarity of the silicon alkoxide bond, dissociation rarely occurs at room temperature and the exchange process takes a number of days. For example: It takes 5 days before 26% of $\text{Si}(\text{OMe})_4$ have exchanged a single methoxide ligand for an ethoxide ligand in ethanol ($\text{OMe}:\text{EtOH} = 1:1$) [5]. The dissociation of alkoxide ligands depends on the charge on the partial charge of the silicon atom. In the presence of either Bronsted or Lewis acids the oxygen atoms become more positively charged and therefore the strength of the silicon oxide bond decreases. For acid catalysed systems 90% of the silicon methoxide precursors are partly substituted within 2 hours [5]. A similar increase was

observed for Lewis catalysed hydrolysis of silicon methoxide, with either titanium(IV) isopropoxide or vanadium (V) oxy tri-isopropoxide.

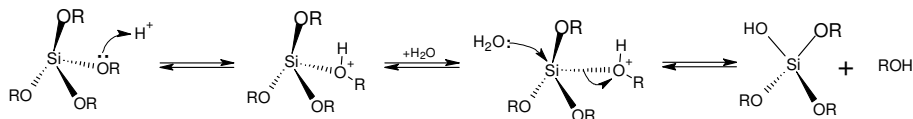
1.1.1.a. Hydrolysis of silicon alkoxides:

The basic catalysed mechanism occurs via a nucleophilic substitution according to an S_N2 -mechanism, which involves only one intermediate state (Scheme 1.4). The reaction involves the formation of a penta-coordinated negatively charged intermediate. The stability of this intermediate is dependent on the inductive effect of the substituents that surround the silicon atom. The stronger the acidity of this substituent, the weaker becomes the stability of the negatively charged intermediate. Therefore, the activation energy for hydrolysis decreases with the extent of hydroxyl-substitution in the sequence: $\text{Si(OR)}_4 < \text{Si(OR)}_3\text{OH} < \text{Si(OR)}_2(\text{OH})_2 < \text{Si(OR)(OH)}_3$. Hydrolysis is energetically favourable for already hydrolysed species that involves preferably the formation of Si(OR)(OH)_3 and Si(OH)_4 . Condensation of these high functionality hydrolysed species yield typically a highly branched dense structure.



Scheme 1.4. Base catalysed hydrolysis of silicon alkoxides.

In the past, the acid catalysed hydrolysis is often referred to occur via an S_N2 -mechanism, analogous to the basic catalysed mechanism. However, hydrolysis is facilitated when the coordination number is increased from 4 to 5, by substitution of alkoxide-ligands with glycols [6-8]. In this case a S_N2 mechanism is unlikely while the additional ligand will decrease the charge of the silicon atom causing the acidity of silicon to decrease. Meanwhile, the silicon oxygen bond length increases to some extent [6, 9] and the bond strength has become weaker. Hydrolysis is therefore not initiated by nucleophilic attack on silicon, however most likely via proton transfer towards a basic alkoxide-group. This is consistent a proton assisted S_N1 mechanism (Scheme 1.5) [3, 10].

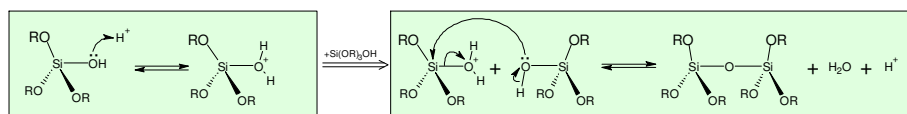


Scheme 1.5. Acid catalysed hydrolysis via a proton assisted S_N1 mechanism.

In the first step a positive charge intermediate is formed by an electrophilic attack of a proton on a basic alkoxide group (the rate limiting step). In the second step, an alcohol is substituted by a nucleophilic attack of aqueous oxygen. The stability of the positively charged intermediates decreases with the extent of hydroxyl-substitution in the sequence: Si(OR)₄ > Si(OR)₃OH > Si(OR)₂(OH)₂ > Si(OR)(OH)₃. In contrast to the basic catalysed mechanism the system preferably forms low hydroxyl substituted compounds. Condensation of these compounds yield a weakly branched polymers that still contains a number of alkoxide groups. Gelation of these weakly branched polymers results in an open network structure that can be used for microporous membranes.

1.1.1.b. Condensation of silicon alkoxides.

In analogy with the hydrolysis reactions, condensation of silicon alkoxides occurred either through acid or base catalysed mechanisms. The acid catalysed condensation is activated via a proton assisted nucleophilic substitution reaction. The reaction involves a fast protonation step a forms a positively charged intermediate. The second step is slow nucleophilic substitution of an hydroxyl group towards a protonated siloxan molecule (Scheme 1.6)



Scheme 1.6. Acid catalysed condensation of silicon alkoxides

The kinetics of acid catalysed hydrolysis and condensation of tetramethyl orthosiloxane (TMOS) and tetraethyl orthosiloxane (TEOS) at room temperature was investigated by proton and ²⁹Si-NMR [11-14]. The hydrolysis rates of TMOS were 30 times larger than the condensation rates, which indicates that condensation, is the rate limiting process. Condensation occurs via both alkoxation and oxolation simultaneously. For

small hydrolysis ratio's ($H_2O:TMOS < 0.5$) condensation occurs mainly by alkoxation, while oxolation dominates for large hydrolysis ratio's. The speed of protonation of alkoxide and hydroxide groups cannot be determined, while the proton exchange is much faster than the NMR-resonance decay. The measured chemical shift is simply the average of protonated and non-protonated species.

Increase of the hydrolysis ratio involves an increase of the hydrolysis rate. The increase silanol (SiOH) concentration causes an increase of condensation rate. ^{29}Si -NMR measurements reveal that sol with an hydrolysis ratio of 4 ($H_2O:TEOS$) contains oligomers with a average size of 3 TEOS units, while in the sol with an hydrolysis ratio of 10 has a average size of 20 TEOS units after 5 hours at room temperature. Nevertheless, the gelation time is 60 days in the case of an hydrolysis ratio of 10 and 35 days in the case with an hydrolysis ratio of 35. On the other hand, the gelation time of TEOS was increased from 35 days to 60 days for an increase of hydrolysis ratio from 4 to 10. This clearly suggests that particle growth and gelation is not only determined by the chemical reactions and other aspects including colloidal stability play a crucial role as well.

1.1.1.c. Silsesquioxanes

Silsesquioxanes are a particular class of silanes that is described by the formula: $RSiO_{3/2}$, where R is a carbon containing substituent [15, 16]. In analogy with conventional silicon alkoxides silsesquioxanes glasses can be synthesized through similar acid or based catalysed hydrolysis and condensation mechanisms. Nevertheless, the versatile chemistry of silsesquioxanes that is compatible organic, polymer and supramolecular chemistry allows a much larger variety of materials to be synthesized. Silsesquioxane precursors can be divided in two different classes: (1) (functionalized) polyhedral oligomeric silsesquioxanes (POSS) and (2) silsesquioxane alkoxides.

POSS molecules contained condensed Si-O-Si cages and the functional rest groups allows these silsesquioxanes to be incorporated in a variety of polymeric structures [17-19]. Recently, self-supportive polyPOSS-imide membrane films were synthesized that unlike conventional polymeric membranes do not suffer from chain-rearrangement-induced permeability loss at elevated temperatures [19] and unlike ceramic membranes these nanocomposites exhibit sufficient strength to remain self-supportive.

Alternatively, hybrid silsesquioxane glasses can be synthesized through hydrolysis and condensation either pendant or bridged silsesquioxane precursors [16]. A variety of different rest groups can be attached including alkyls, aryls, metallocenes, crown ethers and cyclames. This allows a tuneable extent of self-organization. For instance, bis-(alkyl-urea)-alkyl bridged silsesquioxanes arrange in a lamellar fashion due to cooperative attractive Van-der-Waals forces between alkyl chains and hydrogen bonds between the urea groups [20]. On the other hand, condensed tetrahedral silsesquioxanes showed only short-range order with very distinct nearest neighbour distances and hardly any long-range anisotropy [21].

Silsesquioxane alkoxides with relatively short bridging groups condense to amorphous glasses, in analogy with conventional silicon alkoxides [22]. Nevertheless, the introduction of hydrophobic alkyl chains within the glassy structure strongly reduced its susceptibility towards hydrolysis [23]. This made this material suitable for pervaporation of waste water under harsh conditions. Moreover, in comparison to conventional glasses the bridged silsesquioxane glasses exhibit substantially higher fracture energies [24, 25].

1.1.2. The chemistry of metal alkoxides

Hydrolytic polymerisation of metal alkoxides occurs via hydrolysis and condensation mechanisms that are similar to silicon alkoxides [3, 10]. However, the more ionic metal alkoxide bond is, the more sensitive it becomes towards hydrolysis and condensation. Transition metal alkoxides readily form metal oxide precipitates in contact with air that contains small fractions of moisture. FTIR-studies of Harris et al. [26] reveal the strong reactivity of titanium ethoxide and zirconium butoxide in water. Acid catalysed hydrolysis occurs readily: within 80 ms 36% and 60% of the alkoxide groups were hydrolysed of respectively the titanium ethoxide and zirconium butoxide. The measured water concentration maintained constant after 80 ms indicating that a steady state between hydrolysis and condensation was readily achieved after 80 ms.

The polarity of metal alkoxide bond is higher in comparison to silicon alkoxide bonds, which is partly due to the high partial charge of the metal atom. The partial charge on the metal atom is related with the average difference in Paulings electronegativity between the metal atoms and the

alkoxide groups [2]. This explains the enhanced reactivity of transition metal alkoxides. Nevertheless, it does not explain why a higher reactivity to hydrolysis/condensation when tin(VI)butoxide is added to silicon ethoxide [27], where the partial charge on tin is smaller ($\delta(M)=0.21$) in comparison to silicon ($\delta(M)=0.32$). However the partial charge model [11] does not encounter the resonance effect between empty d-orbitals of silicon and occupied p-orbitals of oxygen as discussed in paragraph 1.1.1. The actual charge of the silicon atom is reduced by p-electrons of oxygen located in π -orbitals formed by overlap of p and d-orbitals. This π -interaction is less pronounced for heavier elements of group 14 (germanium and tin) in comparison to silicon [7]. Consequently, the real charge of the silicon atom is probably much lower as derived from the partial charge model.

Furthermore, the chance of nucleophilic substitution is possibly enhanced by the chance to increase the coordination number of the metal or metalloid atom. In the case of transition metals, the coordination number is determined by the ionic radius and ligand field stabilisation energy. The situation is more complex in the case of p-block elements, while it involves more covalent metal/metalloid oxide bonds. The coordination number of silicon can be increased from four to five or six, which involves a hybridisation with empty d-orbitals. The existence of five and six coordinated silicon alkoxide complexes are reported in literature [6]. However, (sp³d)-hybridization is competitive to resonance effect between oxygen and a metal/metalloid centre. In the particular case of silicon the driving force to increase coordination number is strongly reduced by the extent of this resonance effect. Therefore, depending on the type of ligand, silicon complexes have typically fourfold coordinated, while most germanium or tin complexes have a six-fold coordination.

On the other hand, the nucleophilic substitution mechanism of metal alkoxides does not necessarily involve expansion of the coordination number. Metal alkoxides tend to increase their coordination number via oligomerization. The saturated coordination numbers have already been achieved for a large range of metal alkoxide precursors and coordination expansion is not necessarily the main driving force in hydrolysis. Transition metals of period 4 tend to have a coordination number of 6. For instance solid crystalline titanium (IV) ethoxide has a tetrameric structure (Figure 1.1), where titanium has a sixfold coordination of ethoxide ligands [28]. The tetramer contains two alkoxide ligands that are coordinated to three

titanium ions (μ_3 -bridged ligands) and four alkoxy ligand that are coordinated to two titanium ions (μ_2 -bridged ligands). The chance of nucleophilic addition has reduced for a tetramer in comparison to the monomer, while titanium has a higher coordination number in the tetramer. On the other hand, partial charge calculations [29] reveal that μ -bridged ligands have a higher partial charge in comparison to pendant ligands. For the titanium metoxide tetramer, the oxygen partial charges are respectively -0.74 for μ_3 -O, -0.66 for μ_2 -O and the partial charge for pendant ligands lies in range between -0.48 and -0.58. The bridged ligands are therefore stronger bases that are more susceptible towards protonation and will be hydrolysed at first. The formation of tetramers is not possible for titanium alkoxides that have large bulky alkyl chains, for instance crystalline titanium (IV) neopentoxide is dimeric [30] and crystalline titanium (IV) 2,6-isopropyl phenoxide is monomeric [31].

An alcoholic solution of alkoxide precursors does not always consist of one particular type molecule and often, it is a mixture of monomers and different types of oligomers that are in equilibrium with each other. The exact composition of a metal alkoxides dissolved in a alcohol is not always known and the chemistry of these alkoxides, even without the addition of modifiers, can be quite complex.

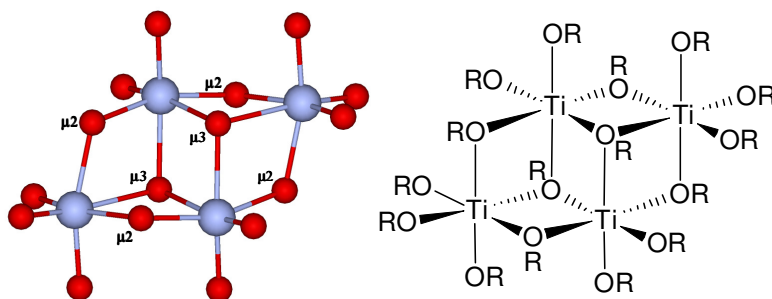


Figure 1.1. Oligomeric arrangement of a tetrameric titanium ethoxide.

Among all metal alkoxides, titanium and zirconium alkoxides have received most attention in the past decades. Nevertheless, the disadvantage of these elements in the preparation of membranes is their tendency towards the

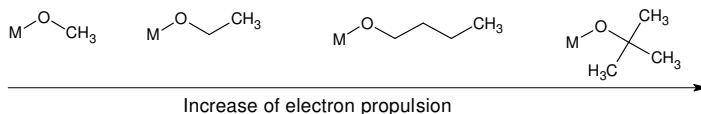
formation of dense crystalline particles. (examples titanium & zirconium crystallisation). Moreover, the heterometallic bonds in mixed titanium silsesquioxanes or zirconium silsesquioxanes derived products (ie.: Ti-O-Si and Zr-O-Si-bonds) rearrange in homonuclear bonds (ie. Ti-O-Ti, Zr-O-Zr and Si-O-Si) due to hydrolytic cleavage [32, 33]. Both the presence unreacted hydroxyl groups or the presence water enables this rearrangement towards thermodynamically more stable homonuclear bonds.

Amorphous oxides that were prepared from niobium penta-ethoxide gels were found to remain amorphous up to 400°C [34]. Based on DSC-measurements, the majority of niobium pentoxide crystallized at 578°C: A crystallisation temperature that is much higher than the crystallisation temperature of either zirconium or titanium oxide. Thus, in the case of niobium oxides the tendency to form separate crystalline clusters would be smaller. The Niobium penta-ethoxide molecule is a dimer that consist of two niobium atoms in a distorted octahedral of oxygen atoms [34]. Each niobium atom is surrounded by four pendant ethoxide groups and two ethoxide groups that are connected with the other niobium atom via μ -bridges. The polymerization niobium pentoxide precursors yields the formation of complex polymeric clusters of distorted corner-sharing and edge-sharing octahedral[34].

1.1.3. Modifiers for alkoxide polymerization.

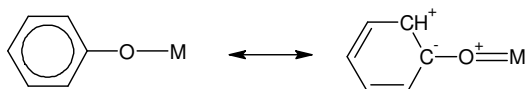
Doping of metal alkoxide in a silica-matrix is still difficult due to the high reactivity of the metal alkoxides. Homocondensation of metal alkoxides is preferred over heterocondensation with silicon alkoxides even when modifiers were added to reduce the reactivity of metal alkoxides. The calcined oxide will contain metal rich phases of metal oxide phases in a silica matrix that were observed by SAXS and TEM measurements for calcined mixed zirconium silicon xerogels [35]. Furthermore, the tendency of metal alkoxides to increase the coordination number results in the formation of dense crystalline domains and strongly reduce the microporosity of the amorphous silica matrix eg: Calcination of titanium doped silica xerogels yields the formation of anatase and rutile domains of titanium dioxide. The extent of phase separation and densification can be reduced with the addition of inhibitors or modifiers. These modifiers may affect the relativities of metal alkoxides in different ways as discussed below.

1. Inductive effect: The inductive effect can be explained in terms of partial charge model of Livage et al. [2]. The partial charge on the metal cation is stabilized by electron propulsion of the alkyl chain that increases with both the length and the extent of branching (Scheme 1.7).



Scheme 1.7. Inductive effect of ligands

2. Mesomeric effect: Titanium and tungsten phenoxides are less susceptible for hydrolysis in comparison to alkoxide equivalents [2, 36]. Phenoxides are known as a strong π -donor ligands that stabilizes the positive partial charge of the metal cation. Surprisingly silicon phenoxide was found to be more reactive towards hydrolysis. Probably, the mesomeric effect plays a minor role in the case of silicon and the increase of reactivity was possibly caused by the inductive effect of the phenoxide (Scheme 1.8).



Scheme 1.8. Mesomeric effect of phenoxides

3. Chelating effect: Substitution of a number of monodentate ligands for a multidentate ligand is entropically favourable while the number of reaction products is higher than the number of reactants [37]. Furthermore, bond formation with multidentate ligands is often cooperative in a positive sense and therefore also favourable from an enthalpic point of view. Calorimetric measurements of Blanchard et al. [37] reveal an increase of enthalpy when alkoxide ligands of zirconium or titanium were substituted by bidentate acetylacetonate ligands. Titanium(IV)-alkoxides were found to react with acetylacetonate up to a metal/chelating ligand-ratio of two ($r=2$). Further addition of acetylacetonate did not involve heat formation and the enthalpy remains constant. The existence of dimeric $[\text{Ti}(\text{OR})_3\text{acac}]_2$ with $r=1$ and monomeric $\text{Ti}(\text{OR})_2\text{acac}_2$ with $r=2$ where confirmed by X-ray crystallography [38]. In both cases the titanium ion is sixfold coordinated, which is the optimal coordination state of titanium. In the particular case of zirconium *n*-propoxide acac-substitution occurs up to a complexation ratio of $r=4$, which

involves the formation of a stable $Zr(acac)_4$ molecule [39]. Zirconium has a larger ionic radius in comparison with titanium and therefore it can increase their coordination number to 8 in the case of $Zr(acac)_4$. The $Zr(acac)_4$ molecule is very stable towards hydrolysis even at an excessive amount of water and therefore not suitable for microporous materials. Spijksma [39] has shown that for smaller complexation ratio's partly substituted zirconium propoxides were formed (for both iso and n-propoxide): sixfold coordinated $[Zr(OPr)_3acac]_2$ and sevenfold coordinated $[Zr(OPr)(acac)_3]$. However, during aging these compounds slowly rearrange in both $Zr(OPr)_4$ and $Zr(acac)_4$.

The number of functional groups reduces by substitution with acetylacetone and as a result the extent of branching reduces as well. This is in agreement with a reduction of a fractal dimension (for $r > 0.5$) that was reduced from 2.5 to 1.6 for a sol of yttrium doped zirconium propoxide [40]. Furthermore, the growth rate of the sols were reduced, which agrees with a reduction of the radius of gyration.

4. Bridging effect of ligands: Related to the geometry and flexibility, particular multidentate ligands form bridges between alkoxides. Bridge formation has two advantages: Firstly the intermixing of different type of alkoxides will be improved by bridge formation between different alkoxides. Furthermore, this opens a pathway for the synthesis of single source precursors that contains different types of metal or metalloid alkoxides. Secondly, molecular weight increases with the extent of bridge formation and therefore it reduces the diffusivity of the molecular building block in solution. At some point bridge formation result in diffusion limited growth that yields a limited and better controlled growth of sol particles. Furthermore, the extent on branching is reduced by diffusion limited growth, yielding a more porous open network structure.

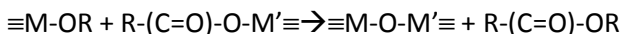
Mixed single source zirconium/titanium and hafnium/titanium precursors were successfully prepared with diethanol amine as a bridging ligand [41]. The isolated crystals contain zirconium (or hafnium) atom and two titanium atoms that were interconnected by three diethanol ligands. The reactivity of the single source precursor is solely determined by the titanium alkoxide groups and the more reactive zirconium centre was completely isolated. Membrane preparation of the precursor yields a homogeneous product that maintains homogeneous up to a calcinations temperature of 650°C [42]. The membrane showed a good selectivity for hydrogen/butane

mixtures, with a permselectivity of 54. The selectivity between hydrogen / methane mixtures was substantially smaller with respect to conventional silica membranes, which indicates that the mixed metal oxide precursor yields a larger pore structure.

Bridging ligands are useful in the preparation of mixed metal oxide precursors, although silicon alkoxide behave different. Firstly, ligand exchange is a much slower for silicon alkoxides and secondly silicon rarely increases their coordination number to 5 or 6. As a result the binding affinity of multidentate ligands is larger towards metal alkoxides. A different strategy was applied Puchberger et al [43, 44], were single source precursors were prepared via a covalent linkage between silicon and an organic diketonate ligand. The diketonate ligand is a chelating ligand that forms two ionic bridges with titanium isopropoxide.

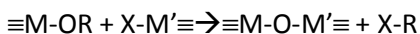
1.1.4. Heterogeneous bond formation through nonhydrolytic pathways

A complete different strategy towards homogeneous mixed metal oxide doped is a more selective condensation between two different functional groups. These reactions occur via a transesterification reaction without the presence of water and were therefore referred as nonhydrolytic condensation mechanism. Trans-esterification can occur through ester elimination or alkyl halide elimination mechanism [45]. The ester elimination mechanism is based on a reaction between a metal or metalloid alkoxide with a metal or metalloid carboxylate according to the following scheme:



Scheme 1.9 Condensation through ester elimination.

The alkylhalide elimination reaction occurs as follows:



Scheme 1.10 Condensation through alkyl halide elimination.

In the case of transition metals both ester and alkylhalide elimination reaction occurs around 100°C [45]. The reactivity of silicon alkoxides is

enhanced by metal complexes that act as Lewis acids. This strategy was successfully applied between silicon acetate or methylated silicon acetate and several metal alkoxides [27, 29-32, 45] (eg titanium, zirconium, tantalum and tin alkoxides).

The choice of a proper solvent plays an important role in the selectivity to either ester elimination or ligand exchange. When using pyridine in the reaction between silicon acetate and tin(IV) tert-butoxide the reaction was dominated by ligands exchange, while in the case using toluene as a solvent the reaction was dominated by ester elimination [32] Pyridine is a strong coordinating solvent due to the presence of the nitrogen lone pair. Hence, it forms strong electrostatic interactions with the tin moieties which effectively block the free coordination sites of tin and disable the ester elimination process. Toluene, on the other hand is a very apolar solvent and will not coordinate the tin atom.

1.2. Sol-Gel Processing.

1.2.2. Nucleation and Particle growth.

Sol-Gel processing of alkoxides starts with the formation of solids from a solution of monomeric or oligomeric precursor molecules. Molecules become attached to each other via hydrolysis and condensation reactions (paragraph 1.1) and form oxygen bridged polymeric structures. As the polymer size increases the solubility decreases and above a critical size particles are nucleated. Nucleation of particles involves the formation of solid liquid interfaces and the properties of the interfaces have a strong influence on growth and cluster formation of polymeric species. At this critical moment particles can either precipitate or form a heterogeneous colloidal dispersion of particles: A process that depends on the balance between repulsive and attractive forces between the solid interfaces of particles.

1.2.2. Colloidal stability

Stability of colloids are often described by the DLVO-theory that considers two distinct forces, namely Van-der-Waals (VdW) forces and Coulomb forces: VdW forces are attractive forces, arising from dipole/dipole or induced-dipole-induced-dipole interactions and coulomb forces are repulsive when sol-particles contain the same charge. The metal oxide clusters become charged due to either the adherence of negatively charged hydroxide or alkoxide ions on the metal atoms or the adherence of protons on the oxygen atoms. The extent in which either positively or negatively charged ions adhered to the sol particle surface depends on the nucleophilic / electrophilic character of the sol particle with respect to the pH. At a certain pH, the so-called isoelectric point (IEP) the particle is pH neutral. Stable sols are formed either below IEP, with the formation of positively charged sol-particles or above IEP with the formation of negatively charged sol-particles. Nevertheless, not all sol particles have the same isoelectric point, for instance due to size differences that causes differences in inductive effects. More importantly, large differences can be observed in the case of heterogeneous precursors with different metal/metalloid nuclei.

The DLVO theory is only applicable in the cases repulsion is mainly of an electric origin [46]. However, even at a high ionic strength [33] agglomeration of colloids did not always occur and rather uniform particles were stabilized. In such cases additional short range repulsive forces could play a predominant role. Short range repulsions were probably caused by a solvation barrier or steric hindrance. Particularly, in the case of metal and metalloid alkoxides that show a weak tendency to dissociate, the charge of nucleated particles could be limited. The strength of both the solvation barrier or steric barrier is effected by the type of ligands that surround the growing particle. For instance, nanosized titania particles (15 – 40 Angstrom) were stabilized in a sol which contains both acetylacetone and paratoluene sulfonic acid [36].

1.2.3. Gellation process

Acid catalyzed polymerization of silicon alkoxides results in the formation of weakly branched polymers. The polymer chain length increases in time, which involves an increase of viscosity of the alkoxide mixture. As the concentration of monomer the change of a formation of a linkage between polymer chains will increase. At the Gel-point polymer chains are linked together and formed a three-dimensional flexible network. This involved an change of a viscous polymer solution into a elastic gel-network. This transition is often measured by rheologic measurements as the point where the viscosity rapidly goes to infinity. However, in theory at the equilibrium point of gelation, the viscosity is infinite. The transition point should be determined by extrapolation that induces a large experimental error.

This problem can be avoided by oscillary shear experiments, while the applied strain is limited [40]. An oscillating strain is applied and the measured stress characterizes the visco-elastic behaviour. In the case of an elastic material the measured stress $\sigma(t)$ is proportional to the applied strain $\epsilon(t)$. The elastic behaviour is therefore characterized by the slope of the stress versus strain curve, the storage modulus G' . In the case of a viscous liquid the measured stress is delayed in comparison to the applied strain. This occurs because of two phenomena: Firstly, the liquid molecules slip over each other, while in the case of an elastic network the intramolecular connections contracts the material to his original position. Secondly, a floating liquid has a certain momentum and additional strain is required to stop the liquid flow. The maximum stress is measured at the point where the stress is reversed while the viscous sol is still floating. This viscous behaviour is related with the second derive of the stress as a function of stain, the loss modulus G'' .

Then, after the point of gelation, further development of the structure occurs during the aging process. The polymer chains are flexible and bend in order to form linkages between two chains and as a result, a certain amount of stress develops in the gel network. The gel-network contracts with the expulsion of an amount of solvent expulse through the pores. This stage of shrinkage is called: syneresis. Meanwhile, contraction occurs by a reduction of surface energy. Small pores will disappear, while two solid surfaces will approach each other. This involved a reduction of solid-liquid interface, thus a reduction of surface energy. Syneresis is a self limiting

process, which slows down by decreasing network permeability and increasing stiffness of the gel network.

1.2.4. Drying Processes

The drying process of silica-gels is well described by the Capillary mechanism. In the pores the overall pressure is increased by the capillary pressure and therefore the extent of evaporation at certain temperature was reduced. The capillary pressure P_c was determined by the curvature of the meniscus of the solvent-liquid interface. At the surface of gel that contains pores the curvature of the meniscus is determined by the pore radius. Furthermore, with the assumption of cylindrical shaped pores the capillary pressure is described by the Kelvin equation [47]:

$$P_c = \frac{2 \cdot \gamma_{LV} \cdot \cos(\theta)}{r_c} \quad (1.1)$$

The formation of porous gels requires good wetting of the solid material and the contact angle θ should be smaller than 90° and therefore the capillary pressure is always positive in these gels. During evaporation the solvent at the pore endings the curvature of the solvent meniscus increases, which correlates with a reduction of the curvature radius r_c and therefore causes an increase in capillary pressure. The curvature radius decreases to a critical point at which the curvature radius approaches the pore radius and the capillary pressure will reach its maximum (Figure 1.2). This is the moment at which dry shrinkage stops and at which the pore size is established [48, 49]. The volumetric strain (ϵ) at this point is related with the bulk modulus K_p and the volume fraction of solid material (ϕ_s) by the following equation:

$$\varepsilon = \frac{1 - \phi_s}{K_p} \cdot P_C \quad (1.2)$$

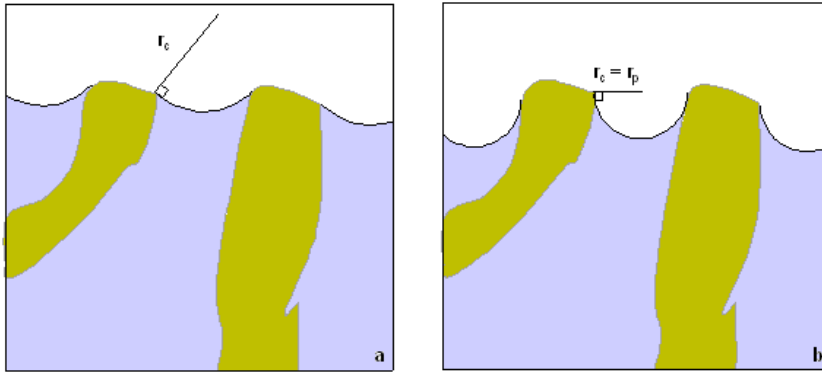


Figure 1.2 Illustration change in curvature of the solvent while drying a porous network structure going from (a) to (b).

1.3. Porous Inorganic Membranes

Inorganic membranes are being divided into two classes ion conducting membranes [50] and porous membranes [51-54]. Their transport mechanisms are completely different. Ion conducting membranes are dense and only allow transport of specific ions, whereas porous membranes can be compared with molecular sieves.

Porous membranes are existent in a variety of different pore sizes ranging from macroporous (>50nm), mesoporous (2-50nm) and microporous membranes (<2nm) [54]. Sol-gel derived macro- and mesoporous materials can be synthesized as a assemble of colloidal particles, or with the use of a template (a binder or surfactant) that is being burned off [49, 54]. On the other hand the formation of micropores that are close to the size of individual atoms always relies on the chemistry of atoms that are forming these pores. Therefore, the tuning size of micropores is more difficult and it required a proper understanding of the chemistry that is involved.

Microporous materials can be divided into two type of materials: (1) crystalline materials (such as metal organic frameworks and Zeolites [53, 55]), and (2) glassy networks [47, 56]. Crystalline membranes have a ideal pore size distribution and can yield high fluxes, however these materials cannot reach the small pore sizes of sol-gel derived silica glasses [57]. Consequently, their selectivity for small gas molecules including CO₂, N₂ O₂ CH₄ and H₂ is limited. Moreover, these materials are more susceptible for defects at the grain boundaries. On the order hand silica membranes are more selective, are less susceptible to defects and can be applied to different geometries, such as tubular shaped membranes [54, 56-58].

Despite their high selectivity the applicability of silica membranes was limited due to their limited hydrothermal and mechanical stability [23, 25, 52]. However, with the introduction of bridged silsesquioxanes (1,2-bis-(triethoxysilyl)-ethane (BTESE)) membranes were manufactured that remained stable for 2 years at $T=150^{\circ}\text{C}$ while separating water in water butanol mixtures [23]. The improvement of hydrothermal stability was dedicated to (1) the presence of Si-C-C-Si bonds that are not susceptible to hydrolysis and (2) the increased hydrophobicity that repels water from the Lewis acidic Si-nuclei. Consequently, these materials exhibit substantially higher fracture energies (BTESE: 6.95 J/m^2) as compared to conventional silica ($\text{SiO}_2 = 4 \text{ J/m}^2$) [24].

Neither conventional silica nor bridged silsequioxane membranes are sufficiently strong to be self-supportive. Therefore, a selective layer in a size range in between 50 - 200 nm is macro/mesoporous support. A macroporous support of α -alumina with a mesoporous support of γ -alumina is frequently being used for this purpose as illustrated in Figure 1.3

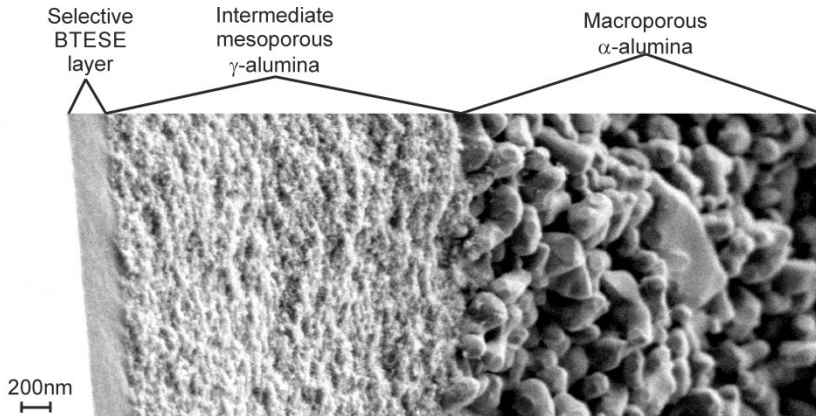


Figure 1.3. Secondary electron scanning microscopy image (SEI-SEM) of a dipcoated BTESE sol onto a meso/maco-porous $\gamma\text{-Al}_2\text{O}_3/\alpha\text{-Al}_2\text{O}_3$ support.

1.3.1. Transport mechanisms in porous membranes

The permselectivity of a porous membrane strongly depend on the type of transport mechanism that is involved. The transport mechanisms depend on the size difference pores and the molecules being transported different mechanisms can occur as illustrated in Figure 1.4 [54]. If the pores are substantially larger as compared to the molecules transport occurs trough viscous flow. Due to shear tension at the pore surface large velocity differences exhibit between similar sized molecules. Consequently, such systems are poorly selective and strongly pressure dependent.

In the case of Knudsen diffusion, molecules bounces ballistically between pore walls. The flux of such systems is determined by the frequency that molecules bounce against the pore wall. Large molecules experience a smaller free path length as compared to smaller molecules and will bounce more frequently against the pore walls. Consequently, large molecules will experience a large friction as compared to small molecules.

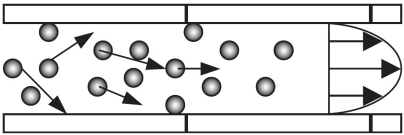
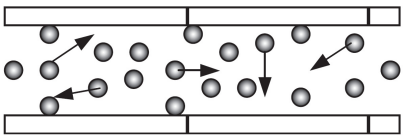
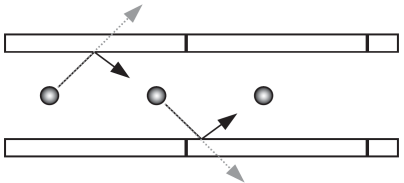
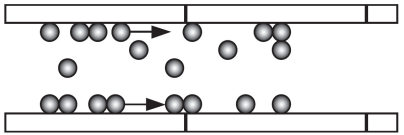
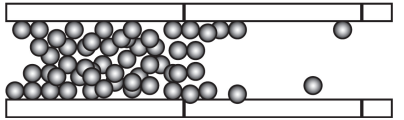

Type Membrane	Transport Mechanism	Selectivity
Macroporous >50	Viscous flow 	-
	Molecular diffusion 	-
Mesoporous 2nm - 50nm	Kundsen diffusion 	$\alpha_{A/B}^* = \sqrt{\frac{M_B}{M_A}}$
	Surface diffusion 	
	Capillary condensation / pore filling 	
Microporous >2nm	Micropore diffusion 	++

Figure 1.4. Transport mechanism through porous membranes. Reprinted from [54] with permission from Elsevier.

In the ideal case where pores are only slightly larger than one type of molecule, while other molecules are being expelled. In that case infinitively high selectivities can be reached through microporous diffusion of only one particular type of molecules. Diffusion is referred to as microporous diffusion if size of the pores is sufficiently small such that the molecules that go through the membrane continuously experience VdW forces of the surrounding membrane materials. In such case no distinction can be made between bulk and surface diffusion. Nevertheless, some molecules such as a mixture of N₂ and CO₂ have similar kinetic diameters of 3.30 Å and 3.64 Å, which are extremely difficult to separate solely by their difference in size [53].

1.4. Scope of this Thesis and Outline

The selective membrane layer of condensed silsesquioxanes may be altered by incorporating metal oxides within the matrix. Doping metal oxides was found useful either (1) to manipulate the membranes selectivity for instance by scavenging CO₂ with selective sites of Nb₂O₃ [59] and (2) to improve its hydrothermal stability [60-62]. Nevertheless, the realization of homogeneously distributed metal centres within a condensed silsesquioxane matrix is not straightforward from a synthesis point of view. Such systems tend to phase separate due to the mismatch in reactivity between the precursors being used. The synthesis is often optimized by trial and error and the evolution of the microstructure of such systems is poorly understood. This thesis is primarily focussed on monitoring and understanding different stages of the sol-gel chemistry of mixed metal alkoxide–silsesquioxane systems, and how these processes affect the final microstructure. It may allow us to find more systematic solutions to the mismatch in reactivity of metal alkoxides versus silicon alkoxides.

One technique that allows a relatively fast monitoring (up to 3s) of microstructural evolution is Synchrotron Radiation Small Angle X-ray Scattering (SAXS). Nevertheless, the interpretation of such data is not straightforward. The acquired data represent a probability distribution on a reciprocal space axis that is related to the probability of finding distance correlations between or within electron dense domains. Such data cannot be immediately translated into a true electron density map without making certain assumptions. **Chapter 2** describes the theory of SAXS in short. It

deals with the (1) the transformation between real and reciprocal space, and (2) the interpretation and applicability of particular models.

In-situ SAXS was used to monitor microstructural changes in mixed niobium pentaethoxide (NPE) / 1,2-bis-(triethoxysilyl)-ethane (BTESE) sol-gel systems as described in **Chapter 3** and **Chapter 4**. **Chapter 3** evaluates particle agglomeration processes in the very early stages of sol particle formation just after mixing alkoxide mixtures with acidified water diluted in ethanol. The agglomeration processes presumably occurs through irreversible Smoluchowski type agglomeration kernels that result in mass-fractal agglomerates. Experiments in the presence and absence of BTESE revealed a substantial influence of BTESE on the agglomeration process of NPE.

Chapter 4 is focused on the microstructural evolution of similar sols during the drying processes. These drying processes are characterized by three stages: (1) an induction stage in which growth of primary building blocks was observed, (2) a transition stage during which the solvent disappeared and a contrast between Nb-rich and Si-rich domains appeared and (3) a final densification stage. The microstructural evolution depends on the moment that niobium pentaethoxide was add to the system while preparing the mixed sols.

The network organization was characterized by solid state ^{13}C , ^{29}Si and ^{17}O solid state NMR as described in **Chapter 5**. Solid state NMR spectroscopy allows the assignment of specific atoms to be attached to the measured nuclei. These techniques provide insight into the extent of remnant organic residues, condensed groups and heteronuclear Si-O-Nb linkages as being assigned by ^{17}O -NMR. The influence of chelating ligands acetylacetonone and 2-methoxyethanol was examined. Acetylacetonone in particular was found to improve the distribution of niobium within the silsesquioxane mixtures.

The condensation reaction of niobium ethoxide is controlled more easily by replacing water for a less nucleophilic oxolation source such as acetone as described in **Chapter 6**. Niobium ethoxide condenses slowly through aldol addition and ether elimination mechanisms which consequently crystallized as $\text{Nb}_8\text{O}_{10}(\text{OEt})_{20}$. Single X-ray crystallography revealed a remarkable thermal anisotropy of the refined crystals that were measured at $T=150\text{K}$ and $T=296\text{K}$.

Alternatively, the dispersion of metals within the silsesquioxane matrix may be improved by a proper design of the silsesquioxane monomer. Fortunately, the chemistry of silsesquioxanes is compatible with organic chemistry. Therefore, it allows the attachment of specific groups being capable of coordinating metal centers. **Chapter 7** is specifically focused on the synthesis and applicability of a malonamide bridged silsesquioxane *N,N,N',N'*-tetrakis-(triethoxysilylpropyl)-malonamide (referred to as TTPMA). TTPMA enhances the dispersion of Ce^{4+} and Ni^{2+} by coordinating these metals before the addition of acidified water. This chapter contains an extensive evaluation of the synthesis and characterization of Ce-TTPMA and Ni-TTPMA coated composite membranes.

1.5. References.

1. Brinker, C.J.S., G. W. , *Sol Gel Science, The Physics and Chemistry of Sol-Gel Processing*. Vol. 1. 1990, San Diego: Academic Press. 1-881.
2. Livage, J., M. Henry, and C. Sanchez, *Sol-gel chemistry of transition metal oxides*. Prog. Solid State Ch., 1988. **18**(4): p. 259-341.
3. Kessler, V.G. and G.A. Seisenbaeva, *New Insight into Mechanisms of Sol-Gel Process and New Materials and Opportunities for Bioencapsulation and Biodelivery*, in *Sol-Gel Methods for Materials Processing*. 2008, Springer. p. 139-153
4. Sanchez, J. and A. McCormick, *Kinetic and thermodynamic study of the hydrolysis of silicon alkoxides in acidic alcohol solutions*. J. Phys. Chem., 1992. **96**(22): p. 8973-8979.
5. Yoshida, H., et al., *Control of the structure of niobium oxide species on silica by the equilibrium adsorption method*. Catal Today, 1996. **28**(1): p. 79-89.
6. Rankin, S.E. and A.V. McCormick, *Hydrolysis pseudoequilibrium: challenges and opportunities to sol-gel silicate kinetics*. Chem. Eng. Sci., 2000. **55**(11): p. 1955-1967.
7. Harris, M.T., et al., *FTIR spectroscopy, SAXS and electrical conductivity studies of the hydrolysis and condensation of zirconium and titanium alkoxides*. J. Sol-Gel Sci. Technol., 1997. **8**(1-3): p. 41-47.
8. Simonsen, M.E. and E.G. Sogaard, *Sol-gel reactions of titanium alkoxides and water: influence of pH and alkoxy group on cluster*

- formation and properties of the resulting products.* J. Sol-Gel Sci. Technol., 2010. **53**(3): p. 485-497.
9. Ranjit, K.T. and K.J. Klabunde, *Solvent effects in the hydrolysis of magnesium methoxide, and the production of nanocrystalline magnesium hydroxide. An aid in understanding the formation of porous inorganic materials.* Chem. Mater., 2005. **17**(1): p. 65-73.
 10. Kessler, V.G., et al., *New insight in the role of modifying ligands in the sol-gel processing of metal alkoxide precursors: A possibility to approach new classes of materials.* J. Sol-Gel Sci. Technol., 2006. **40**(2-3): p. 163-179.
 11. Broussous, L., et al., *SAXS Study of Formation and Growth of Tin Oxide Nanoparticles in the Presence of Complexing Ligands.* J. Phys. Chem. B, 2002. **106**(11): p. 2855-2860.
 12. Hu, M.-C., et al., *Probing the early-stage/rapid processes in hydrolysis and condensation of metal alkoxides.* J. Mater. Sci., 2000. **35**(8): p. 1957-1971.
 13. Wilkinson, A.P., et al., *In situ x-ray diffraction study of crystallization kinetics in $PbZr_{1-x}Ti_xO_3$ (PZT, $x = 0.0, 0.55, 1.0$).* Chem. Mater., 1994. **6**(6): p. 750-754.
 14. Fan, J., S.W. Boettcher, and G.D. Stucky, *Nanoparticle assembly of ordered multicomponent mesostructured metal oxides via a versatile sol-gel process.* Chem. Mater., 2006. **18**(26): p. 6391-6396.
 15. Baney, R.H., et al., *Silsesquioxanes.* Chem. Rev., 1995. **95**(5): p. 1409-1430.
 16. Lerouge, F., G. Cerveau, and R.J.P. Corriu, *Supramolecular self-organization in non-crystalline hybrid organic-inorganic nanomaterials induced by van der Waals interactions.* New J. Chem, 2006. **30**(10): p. 1364-1376.
 17. Gnanasekaran, D., K. Madhavan, and B. Reddy, *Developments of polyhedral oligomeric silsesquioxanes (POSS), POSS nanocomposites and their applications: a review.* J Sci Ind Res, 2009. **68**(6): p. 437-464.
 18. Dalwani, M., et al., *Ultra-thin hybrid polyhedral silsesquioxane-polyamide films with potentially unlimited 2D dimensions.* J. Mater. Chem., 2012. **22**(30): p. 14835-14838.
 19. Raaijmakers, M.J.T., et al., *Sieving of Hot Gases by Hyper-Cross-Linked Nanoscale-Hybrid Membranes.* Journal of the American Chemical Society, 2013. **136**(1): p. 330-335.

20. Moreau, J.J., et al., *Self-organized hybrid silica with long-range ordered lamellar structure*. J. Am. Chem. Soc., 2001. **123**(32): p. 7957-7958.
21. Lerouge, F., G. Cerveau, and R.J.P. Corriu, *Hydrophobic induced supramolecular self-organization of tetrahedral units based on van der Waals interactions*. J Mater Chem, 2006. **16**(1): p. 90-95.
22. Agirre, I., et al., *Hybrid organosilica membranes and processes: Status and outlook*. Sep. Purif. Technol., 2014. **121**: p. 2-12.
23. Castricum, H.L., et al., *Hybrid ceramic nanosieves: Stabilizing nanopores with organic links*. Chem. Commun., 2008(9): p. 1103-1105.
24. Dubois, G., et al., *Molecular Network Reinforcement of Sol-Gel Glasses*. Advanced Materials, 2007. **19**(22): p. 3989-3994.
25. Dubois, G., et al., *Superior mechanical properties of dense and porous organic/inorganic hybrid thin films*. J. Sol-Gel Sci. Technol., 2008. **48**(1-2): p. 187-193.
26. Francisco, M.S.P., R. Landers, and Y. Gushikem, *Local order structure and surface acidity properties of a Nb₂O₅/SiO₂ mixed oxide prepared by the sol-gel processing method*. J. Solid State Chem., 2004. **177**(7): p. 2432-2439.
27. Bradley, D. and I. Thomas, 687. *Organosilyloxy-derivatives of metals. Part I. Alkylsilyloxy-derivatives of titanium, zirconium, niobium, and tantalum*. J. Chem. Soc. (Resumed), 1959: p. 3404-3411.
28. Ibers, J.A., *Crystal and Molecular Structure of Titanium (IV) Ethoxide*. Nature, 1963. **197**(4868): p. 686-687.
29. Caruso, J., et al., *Solvent-dependent ester elimination and ligand exchange reactions between trimethylsilyl acetate and tin (IV) tetra-tert-butoxide*. Inorg. Chem., 1995. **34**(2): p. 449-453.
30. Iwasaki, M., et al., *Preparation of high homogeneity BaO-TiO₂-SiO₂ gel*. J. Sol-Gel Sci. Technol., 1994. **2**(1-3): p. 387-391.
31. Jansen, M. and E. Guenther, *Oxide gels and ceramics prepared by a nonhydrolytic sol-gel process*. Chem. Mater., 1995. **7**(11): p. 2110-2114.
32. Caruso, J., et al., *Ester elimination versus ligand exchange: the role of the solvent in tin-oxo cluster-building reactions*. J. Chem. Soc., Chem. Commun., 1995(2): p. 157-158.

33. Look, J.L. and C. Zukoski, *Colloidal Stability and Titania Precipitate Morphology: Influence of Short-Range Repulsions*. J. Am. Ceram. Soc., 1995. **78**(1): p. 21-32.
34. Bansal, N.P., *Low-temperature synthesis, pyrolysis and crystallization of tantalum oxide gels*. J. Mater. Sci., 1994. **29**(19): p. 5065-5070.
35. Gaudon, A., et al., *Phase separation in sol-gel derived ZrO₂-SiO₂ nanostructured materials*. J. Eur. Ceram. Soc., 2005. **25**(2-3 SPEC. ISS.): p. 283-286.
36. Scolan, E. and C. Sanchez, *Synthesis and characterization of surface-protected nanocrystalline titania particles*. Chemistry of Materials, 1998. **10**(10): p. 3217-3223.
37. Blanchard, J., et al., *Hydrolysis and Condensation Reactions of Transition Metal Alkoxides: Calorimetric Study and Evaluation of the Extent of Reaction*. Eur. J. Inorg. Chem., 1998. **1998**(8): p. 1115-1127.
38. Errington, R.J., et al., *β -diketonate derivatives of titanium alkoxides: X-ray crystal structures and solution dynamics of the binuclear complexes $[\{Ti(OR)_3(dik)\}_2]$* . Polyhedron, 1998. **17**(5): p. 659-674.
39. Spijksma, G.I., et al., *Stabilization and destabilization of zirconium propoxide precursors by acetylacetone*. Chem. Commun., 2004. **10**(16): p. 1874-1875.
40. In, M. and R. Prud'homme, *Fourier transform mechanical spectroscopy of the sol-gel transition in zirconium alkoxide ceramic gels*. Rheologica acta, 1993. **32**(6): p. 556-565.
41. Spijksma, G.I., et al., *Nona-coordinated MO₆N₃ centers M = Zr, Hf as a stable building block for the construction of heterometallic alkoxide precursors*. Inorg. Chim. Acta, 2007. **360**(6): p. 2045-2055.
42. Spijksma, G.I., et al., *Microporous Zirconia-Titania composite membranes derived from diethanolamine-modified precursors*. Adv. Mater., 2006. **18**(16): p. 2165-2168.
43. Puchberger, M., et al., *Reaction of metal alkoxides with 3-alkyl-substituted acetylacetone derivatives—coordination vs. hydrodeacylation*. New J. Chem., 2004. **28**(11): p. 1289-1294.
44. Rupp, W., N. Hüsing, and U. Schubert, *Preparation of silica-titania xerogels and aerogels by sol-gel processing of new single-source precursors*. J. Mater. Chem., 2002. **12**(9): p. 2594-2596.
45. Vioux, A., *Nonhydrolytic sol-gel routes to oxides*. Chem. Mater., 1997. **9**(11): p. 2292-2299.

46. Barnes, G.T. and I.R. Gentle, *Interfacial Science*. 2005, New York: Oxford University Press.
47. Brinker, C., et al., *Sol-gel strategies for controlled porosity inorganic materials*. *J. Membr. Sci.*, 1994. **94**(1): p. 85-102.
48. Raman, N., et al., *Sol-gel strategies for amorphous inorganic membranes exhibiting molecular sieving characteristics*. 1994, Sandia National Labs., Albuquerque, NM (United States).
49. Raman, N.K., M.T. Anderson, and C.J. Brinker, *Template-based approaches to the preparation of amorphous, nanoporous silicas*. *Chem. Mater.*, 1996. **8**(8): p. 1682-1701.
50. Bouwmeester, H.J.M. and A.J. Burggraaf, *Chapter 10 Dense ceramic membranes for oxygen separation*, in *Membrane Science and Technology*, A.J. Burggraaf and L. Cot, Editors. 1996, Elsevier. p. 435-528.
51. Lu, G.Q., et al., *Inorganic membranes for hydrogen production and purification: A critical review and perspective*. *J. Colloid Interf. Sci.*, 2007. **314**(2): p. 589-603.
52. Agirre, I., et al., *Hybrid organosilica membranes and processes: Status and outlook*. *Sep. Purif. Technol.*, 2014. **121**: p. 2-12.
53. Li, J.-R., et al., *Carbon dioxide capture-related gas adsorption and separation in metal-organic frameworks*. *Coordin. Chem. Rev.*, 2011. **255**(15–16): p. 1791-1823.
54. Ayrál, A., et al., *Microporous silica membrane: basic principles and recent advances*. *Membr. Sci. Technol.*, 2008. **13**: p. 33-79.
55. Wee, S.-L., C.-T. Tye, and S. Bhatia, *Membrane separation process—Pervaporation through zeolite membrane*. *Sep. Purif. Technol.*, 2008. **63**(3): p. 500-516.
56. de Vos, R.M. and H. Verweij, *Improved performance of silica membranes for gas separation*. *J. Membr. Sci.*, 1998. **143**(1–2): p. 37-51.
57. Shekhawat, D., D.R. Luebke, and H.W. Pennline, *A review of carbon dioxide selective membranes*. US Department of Energy, 2003.
58. Xomeritakis, G., et al., *Tubular ceramic-supported sol-gel silica-based membranes for flue gas carbon dioxide capture and sequestration*. *J. Membr. Sci.*, 2009. **341**(1): p. 30-36.
59. Boffa, V., et al., *Microporous niobia-silica membrane with very low CO₂ permeability*. *ChemSusChem*, 2008. **1**(5): p. 437-443.
60. Qi, H., et al., *Hybrid Organic-Inorganic Microporous Membranes with High Hydrothermal Stability for the Separation of Carbon Dioxide*. *ChemSusChem*, 2010. **3**(12): p. 1375-1378.

61. Qi, H., et al., *Effect of Nb content on hydrothermal stability of a novel ethylene-bridged silsesquioxane molecular sieving membrane for H₂/CO₂ separation*. J. Membr. Sci., 2012. **421–422**(0): p. 190-200.
62. Kanezashi, M. and M. Asaeda, *Hydrogen permeation characteristics and stability of Ni-doped silica membranes in steam at high temperature*. J. Membr. Sci., 2006. **271**(1-2): p. 86-93.

2.

Theory of small Angle X-ray Scattering

By convention, the scattered intensity is described as a function of the scattering vector \mathbf{q} . The \mathbf{q} -vector describes the displacement of the scattered wave with respect to its original trajectory. When particles are isotropically dispersed the intensity averages out over all possible orientations. Consequently, the intensity becomes only dependent on the length of the \mathbf{q} -vector, the q -value. The q -value is independent of the azimuthal angle in the plane of the detector and only depends on the scattering angle θ , as described by the equation:

$$q = 4\pi \cdot \sin(\theta) / \lambda \quad (2.1)$$

Unlike θ the q -value is characteristic for a particular feature size and does not depend on the wavelength λ . When interpreting SAXS data, a system can be characterized either as a particulate system or a non-particulate system [1, 2]. A particulate system is characterized as an assembly of particles with a certain shape in a particular arrangement. Its scattering intensity function $I(q)$ is described as the product of two separate functions: (1) the form function $P(q)$ that describes the characteristic scattering intensity arising from intraparticle correlations is only dependent on the size and shape of particles, and (2) the structure function $S(q)$ that arises from inter-particle correlations is solely dependent on how particles are arranged or agglomerated with respect to each other. The intensity function for particulate systems is described by [1-3]:

$$I(q) = N \cdot (\Delta\rho)^2 \cdot S(q) \cdot P(q) \quad (2.2)$$

Herein, N represents the number of particles in the beam and $\Delta\rho$ represents the average difference in electron density between particles and their surroundings. Some systems, such as bicontinuous systems cannot be interpreted as an assembly of particles. The intensity function of such non-particulate systems cannot be described by separate form and structure functions. These systems are further discussed in section 2.4.

2.1. Form function

The form function $P(q)$ describes the characteristic scattering intensity of isolated particles. In the case of well dispersed particles at relatively low concentrations, mutual particle interference is negligible and the intensity function $I(q)$ is solely described by a form function i.e. $S(q) = 1$. SAXS from isolated particles arises from the fact that the electron density inside particles is larger than the electron density of the surrounding medium. Consequently, X-rays have an enlarged probability to scatter inside a particle rather than outside. The scattered intensity correlates with the probability that two waves scatter simultaneously at a particular vector \mathbf{r} separated from each other. Therefore, when the probability of finding two locations within a particle for all possible separation vectors \mathbf{r} (i.e. the so-called correlation function $\gamma(\mathbf{r})$) is known, its corresponding intensity function can be derived by a conversion of $\gamma(\mathbf{r})$ to reciprocal space through the Fourier transform [1-3]:

$$\mathbf{I}(\mathbf{q}) = \int_V \gamma(\mathbf{r}) \cdot \exp(i \cdot \mathbf{q} \cdot \mathbf{r}) dV \quad (2. 3)$$

For instance, for an isolated sphere with a radius $R = 1$ and a homogeneous electron distribution, a normalized electron density profile can be defined as 1 inside the sphere and 0 outside the sphere. When placing the origin in the center of the sphere, the electron density profile is described by Figure 2.1a. Its corresponding $\gamma(\mathbf{r})$ (Figure 2.1b) is defined as the convolution product of the electron density profile with itself averaged over its volume. At a length of 0, $\gamma(\mathbf{r})$ is 1 by definition [4] and with increasing length of \mathbf{r} , the number of possibilities of placing vector \mathbf{r} inside a sphere decreases. $\gamma(\mathbf{r})$ becomes zero when the length of \mathbf{r} becomes larger than the diameter of the sphere ($2R$). The determination of $\gamma(\mathbf{r})$ through the convolution integral is usually omitted by calculation of the amplitude function $\mathbf{A}(\mathbf{q})$ (Figure 2.1d) by the Fourier transform [1, 2]:

$$\mathbf{A}(\mathbf{q}) = \int_V \Delta\rho(\mathbf{r}) \cdot \exp(i \cdot \mathbf{q} \cdot \mathbf{r}) dV \quad (2. 4)$$

The intensity function is easily derived from $\mathbf{A}(\mathbf{q})$ as the square of its modulus (Figure 1e). Note that for asymmetric particles such as droplet shaped particles the amplitude function is complex while the intensity function is always real and positive. For isotropic particles such as spheres the Fourier transform can be simplified to an integral of scalar elements:

$$A(q) = 4\pi \cdot \int_0^{\infty} \Delta\rho(r) \cdot r^2 \cdot \frac{\sin(q \cdot r)}{(q \cdot r)} dr \quad (2.5)$$

In the case of an isolated anisotropic particle, such as a cylinder or a plate its scattering intensity is essentially anisotropic as well. Yet, when particles are randomly dispersed inside a particular medium, the scattering intensity averages out over all possible orientations and the measured $I(q)$ becomes isotropic. Combined with the loss of the imaginary component of the amplitude functions, the intensity function has substantially less information when the particles become randomly oriented. Therefore, when $I(q)$ is measured its corresponding electron density distribution function cannot be derived unambiguously. Instead, assumptions should be made concerning possible particles and $I(q)$ can be fitted through iterative processes. By convention, the part of the amplitude $A(q)$ and intensity $I(q)$ functions that only describe intra-particle correlations are represented by $F(q)$ and $P(q)$, respectively, and weighted over V_p and V_p^2 , where V_p is the particle volume. Consequently, both $F(q)$ and $P(q) \rightarrow 1$ for $q \rightarrow 0$. A variety of different form functions have been derived and a clear overview was given by Pedersen [5].

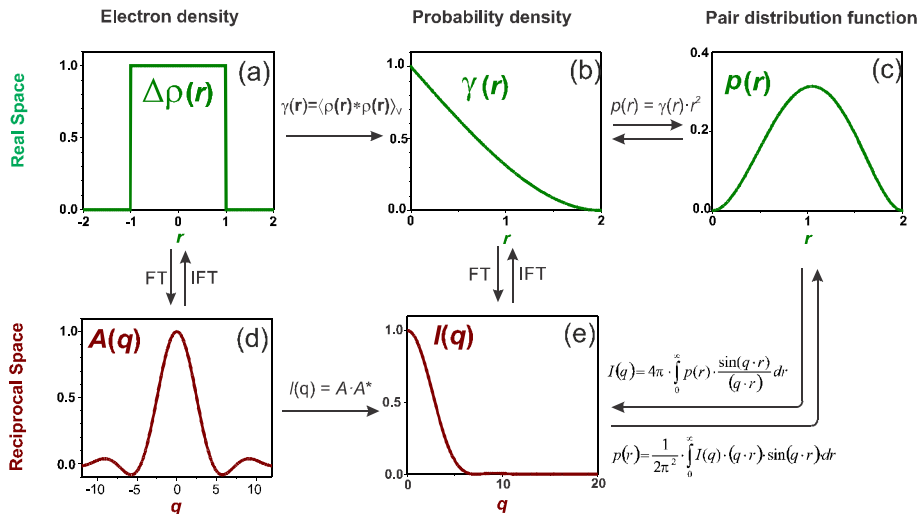


Figure 2.1 A scheme that illustrates the relationships between the relevant functions in the analysis of SAXS data, using an isolated sphere with $r_0 = 1$ as example. (a) the electron density distribution function, (b) the (auto)correlation function, (c) the pair distance distribution function, (d) the amplitude function, (e) the scattering intensity function. Note that both $A(q)$, $\gamma(r)$ and $I(q)$ are normalized over the volume of a sphere.

Instead of fitting the experimental data, the data can be converted to a pair (distance) distribution function $p(r)$ (Figure 2.1c). This function is closely related to $\gamma(r)$, however in the case of $\gamma(r)$ any vector \mathbf{r} in all possible spherical angles ϕ and θ are weighted evenly regardless of the length of \mathbf{r} . On the other hand, $p(r)$ also encounters for the fact that the probability of finding correlation within the imaginary sphere described by r scales with the surface of this imaginary sphere $4\pi r^2$. Therefore, $p(r)$ is scaled by r^2 (Figure 2.1b-c). The advantage of determining $p(r)$ is that particular features give better distinguishable features as compared to $I(q)$. For instance hollow particles result in truncated curves of $p(r)$ and for increasing elongation of a particle $p(r)$ becomes more tailed [1, 2].

2.2 Structure function

The structure function is a part of the intensity function that arises from constructive scattered waves that are originating from different particles. This function is a representation of the probability that a particular particle is surrounded by another particle. For isotropic systems structure factors

can be divided in two type of systems: (1) correlated systems that can describe packing of colloidal particles and (2) polymeric systems that can be described by either fractallic or wormlike models. By convention, the structure function is weighted over the square of the particle volume of the repetitive unit (known as the primary particle), such that $S(q \rightarrow \infty) = 1$.

2.2.1 Correlated systems

When increasing the concentration of a colloid, particles will start to interfere with each other and the scattered intensity cannot be described solely by the form function. The simplest case is the interference between hard non-sticky spheres. Their interference pattern is solely determined by the impossibility that two hard spheres of radius R_{HS} interpenetrate. In other words, the repulsive potential between two spheres is infinite when the radial distance $r < 2 \cdot R_{HS}$ and becomes zero when $r > 2 \cdot R_{HS}$. For very dilute systems the probability that two particles collide is negligible. Thus, the location of particles is random and no interparticle interference is observed. With increasing concentration, the probability that spheres collide increases and the probability of finding two particles at a separation distance $\sigma = 2 \cdot R_{HS}$ becomes larger. Hence, a correlation peak appears in the intensity spectrum at $q \sim 2\pi/\sigma$.

The solution of the structure factor of hard non-sticky spheres relies on the equation of state of non-ideal gases with a limited compressibility [6]. One of the most straightforward solutions was given by Fournet, who used a Born-Green Approximation (Equation 2.6, Table 2.1). The model works reasonably well and has been applied several times, but at high concentrations it underestimates the extent of higher order correlations, i.e. correlations that arise from the third and a fourth sphere interacting with two other spheres [6-9]. At higher packing densities an extended formula is needed, based on a Percus-Yevick approximation (Equation 2.7, Table 2.1) [10-12]. This approach have been applied for colloidal packing of a variety of different nanocomposites [10-16].

Table 2.1 Structure functions of correlated spheres

Definition / Energy potential	Structure function	Nr / ref
Born Green Approximation: $U_{\text{HS}}(r, R_s) = \begin{cases} \infty & \text{for } r \leq \sigma \\ 0 & \text{for } r > \sigma \end{cases}$	$S(q, \sigma) = \frac{1}{1 + 8 \cdot \phi \cdot \frac{\sin(q \cdot \sigma) - q \cdot \sigma \cdot \cos(q \cdot \sigma)}{(q \cdot \sigma)^3}}$	(2.6) [6-9]
Hard non-sticky sphere Percus-Yevic Approximation $U_{\text{HS}}(r, R_s) = \begin{cases} \infty & \text{for } r \leq \sigma \\ 0 & \text{for } r > \sigma \end{cases}$	$S(q, \sigma) = \frac{1}{1 + 24 \cdot \left(\frac{\phi}{K}\right) \cdot (\alpha \cdot Y_1(K) + \beta \cdot Y_2(K) + \gamma \cdot Y_4(K))}$ $K = q \cdot \sigma, \quad \alpha = \frac{(1+2\phi)^2}{(1-\phi)^4}, \quad \beta = -6 \cdot \phi \cdot \frac{\left(1 + \frac{\phi}{2}\right)^2}{(1-\phi)^4}, \quad \gamma = \frac{\phi \cdot \alpha}{2}$	(2.7) [10-12]
Hard sticky sphere with square well potential based on PY approximation $U_{\text{sw}}(r, R_s) = \begin{cases} \infty & \text{for } r \leq \sigma \\ -\varepsilon & \text{for } \sigma < r \leq \lambda \cdot \sigma \\ 0 & \text{for } r > \lambda \cdot \sigma \end{cases}$	$S(K) = \frac{1}{1 + 24 \cdot \left(\frac{\phi}{K}\right) \cdot C(K)}$ <p>where:</p> $C(K) = \alpha \cdot Y_1(K) + \beta \cdot Y_2(K) + \left(\frac{\phi \cdot \alpha}{2}\right) \cdot Y_4(K) - \left(\frac{\varepsilon}{k_B \cdot T}\right) \cdot F_c(K)$ $F_c(K) = \left(\frac{\sin(\lambda \cdot K) - \lambda \cdot K \cdot \cos(\lambda \cdot K)}{K^2} - Y_1(K)\right), \quad K = q \cdot \sigma$ $\alpha = \frac{(1+2\phi)^2 + \phi^3 \cdot (\phi - 4)}{(1-\phi)^4}, \quad \beta = -\left(\frac{\phi}{3}\right) \cdot \frac{(18 + 20 \cdot \phi - 12 \cdot \phi^2 + \phi^4)}{(1-\phi)^4}$	(2.8) [17]
Hard sticky sphere with Baxter potential based on PY approximation $\frac{U_{\text{sw}}(r, R_s)}{k_B \cdot T} = \begin{cases} \infty & \text{for } r \leq \sigma \\ \ln\left(\frac{12r \cdot \Delta}{\sigma + \Delta}\right) & \text{for } \sigma < r \leq \sigma + \Delta \\ 0 & \text{for } r > \sigma + \Delta \end{cases}$	$S(K) = \frac{1}{1 - C(K)}$ <p>where:</p> $C(K) = \frac{2 \cdot \phi \cdot \lambda}{K} \cdot \sin(K) - 2 \left(\frac{\phi \cdot \lambda}{K}\right)^2 \cdot (1 - \cos(K)) - \left(\frac{24 \cdot \phi}{K}\right) \cdot F_c(K)$ $F_c(K) = \left(\alpha \cdot Y_1(K) + \beta \cdot Y_2(K) + \left(\frac{\alpha \cdot \phi}{2}\right) \cdot Y_4(K)\right), \quad K = q \cdot \sigma$ $\alpha = \frac{(1+2\phi - \mu^2)}{(1-\phi)^4}, \quad \beta = -\left(\frac{3\phi \cdot (2+\phi)^2 - 2\mu \cdot (1+7\phi + \phi^2) + \mu^2 \cdot (2+\phi)}{2 \cdot (1-\phi)^4}\right)$ $\gamma = \frac{\phi \cdot (2+\phi)}{6 \cdot (1-\phi)^2}, \quad \varepsilon = \tau + \frac{\phi}{1-\phi}, \quad \lambda = \frac{6}{\phi} \cdot (\varepsilon - \sqrt{\varepsilon^2 - \gamma}), \quad \mu = \lambda \cdot \phi \cdot (1-\phi)$	(2.9) [18-19]
^(#) With standard integrals $Y_n(K)$: $Y_n(K) = \int_0^1 x^n \cdot \sin(K \cdot x) dx$		
that correspond to:		
$Y_1(K) = \frac{\sin(K) - K \cdot \cos(K)}{(K)^2}, \quad Y_2(K) = \frac{2 \cdot K \cdot \sin(K) + (2 - K^2) \cdot \cos(K) - 2}{(K)^3}$ $Y_4(K) = \frac{(-K^4 + 12K^2 - 24) \cdot \cos(K) + 4(K^3 - 6K) \cdot \sin(K) + 24}{(K)^5}$		

In real systems, such as nanocomposites [12, 14, 20-23], ionomers [10] and microemulsions [24, 25], electron dense particles are often separated by electron lean regions. The electron lean regions often stabilize the electron dense particles. Such systems can be modeled as core-shell particles, as illustrated in Figure 2.2a. When such particles are dispersed in a solvent it is essentially a ternary system. However, if the difference in electron density between solvent and electron lean regions is sufficiently small, the scattering by the electron lean regions may be neglected and such systems are reduced to binary systems, with a form factor with core radius R_C and structure function with a separation distance $\sigma = 2 \cdot R_{HS} = 2 \cdot (R_{Core} + R_{Shell})$.

An example of such a system with $S(q) = (2.7$ and $P(q) =$ Guinier approximation is shown Figure 2.2b for varying volume fractions ϕ . With increasing volume fraction the following phenomena are observed: (1) The height of the correlation peak increases as the number of correlations between spheres increases, (2) the correlation peak becomes narrower as the free volume in which the sphere can move reduces and the packing of spheres becomes more rigid, and (3) the intensity at low- q value decreases due to a decrease in contrast in electron density between particles and their surroundings, since the surroundings contain increasing numbers of particles. Note that the latter statement is only valid for systems that contain non-sticky spheres, where long-range order is absent. However, if for instance the Van der Waals forces are sufficiently strong, particles assemble either temporarily or permanently into larger agglomerates and next-nearest-neighbor correlations (second, third, etc.) are observed. These systems are well described by structure functions that include a small attractive well, such as spheres with a square well potential [17] and Baxter Sticky spheres [18, 19], as described by Equation (2.8) and (2.9) respectively (Table 2.1).

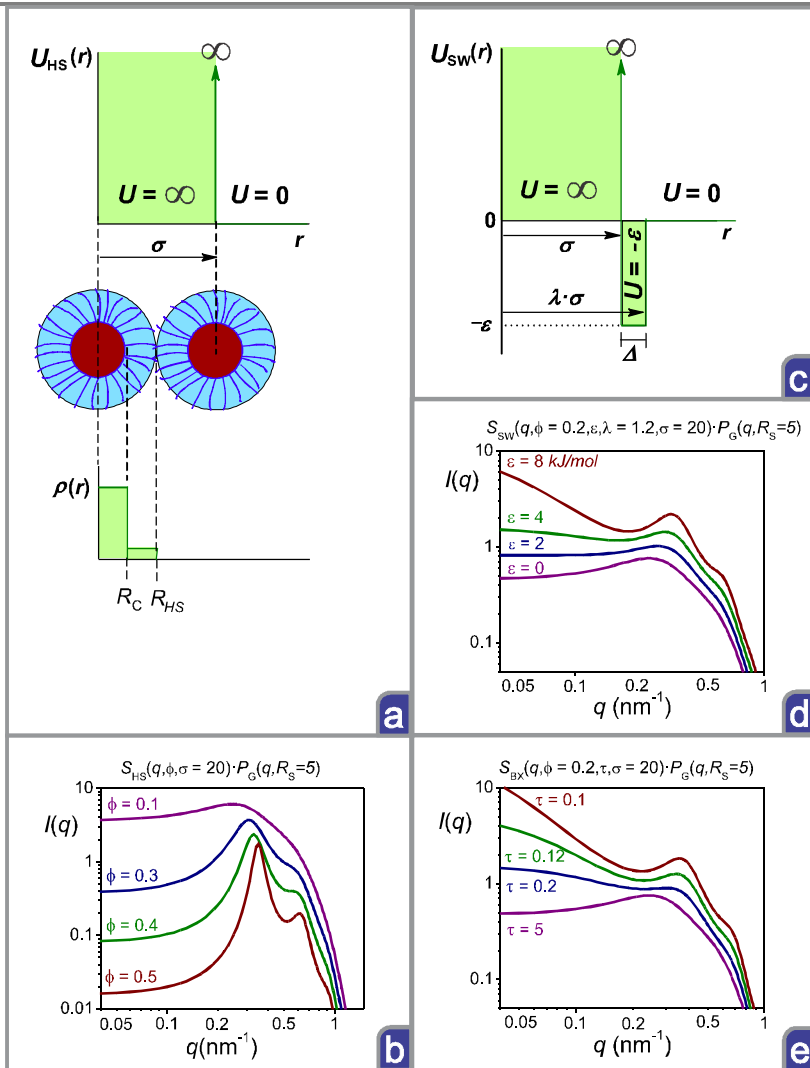


Figure 2.2. (a) Illustration of spherical agglomerates with a core-shell electron density distribution, separated at a distance $\sigma = 2R_{HS}$ (b) Simulated $I(q)$ following a hard sphere packing potential, with varying volume fractions ϕ and a constant $\sigma = 20\text{nm}$. (c) Illustration of hard sphere packing with a square well potential of depth ε in between σ and $\lambda \cdot \sigma$. (d) Simulated $I(q)$ of packed spheres with a square well potential and varying depths ε , for $\phi = 0.2, \sigma = 20\text{ nm}$ and $\lambda = 1.2$. (e) Simulated $I(q)$ of packed spheres following an attractive Baxter potential with varying reduced temperatures (τ) of an infinity small attractive layer, with $\phi = 0.2$ and $\sigma = 20\text{ nm}$. For all simulations (b, d, e) the form function of the core was described by a Guinier approximation of spheres with a cross-sectional radius $R_C = 5\text{ nm}$ ($R_G = 3\text{nm}$).

In the case of a square well potential, between a minimum radial separation distance σ and a distance $\lambda \cdot \sigma$, particles experience a mutual attractive force ε while they do not interact beyond that point ($U = 0$) as illustrated in Figure 2.2c [17]. The extent of correlations between particles increases with increasing depth ε and increasing length $\Delta = \sigma \cdot (\lambda - 1)$ of the well. Contrary to the case of non-sticky spheres, not only the direct particle-particle correlations increase with ε , as observed by the increasing intensity of the correlation peak (Figure 2.2d), but next-nearest neighbor (second, third, etc.) correlations increase as well, as evidenced by an increasing intensity in the low- q regime. Note that next-nearest neighbor correlations are most pronounced at relatively low volume fractions of particles ϕ , since small agglomerates are easily distinguishable from their surroundings. At higher ϕ the agglomerates approach each other and next-nearest neighbor correlations are diminished by longer distance correlations, and the intensity in the low- q -regime drops. Meanwhile, due to an increasing number of next-nearest neighbor correlations the correlation peak becomes more intense, similar to non-sticky spheres. The square well model has been applied for a variety of systems including colloidal nanoparticles [26-29], micro-emulsions [25] and micelles [30].

In analogy with the square well model of Baxter, sticky spheres also introduce an adhesive force beyond a separation distance σ . However, unlike the square well potential the length of the well is defined as infinitely small, i.e. $\Delta \rightarrow 0$ so that adhesion only depends on the reduced temperature τ , which is essentially a ratio between the actual temperature and a certain critical temperature of a system. Therefore, τ is a measure of the mobility of particles in the system and decreases with increasing adhesive force between particles. As τ decreases, an increasing amount of particles will agglomerate and consequently the scattering intensity of the low- q regime and the correlation peak increases (Figure 2.2e). The use of a single parameter that characterized the particle adhesion is more straightforward from an analysis point of view, since Δ is often unknown and a particular value should be assumed. On the other hand, the square well potential was found to give more realistic scattering curves [29, 31].

2.2.2. Mass-fractal structure functions

Small particles may agglomerate in a random fashion forming small branched assemblies. Depending on the reaction kinetics, for instance whether a reaction is rate limited or diffusion limited, particles assemble in varying morphologies and packing densities [32, 33]. Such randomly packed systems may be described as mass fractals. When a number of small building blocks with radius r_0 is assembled as a massfractal, the expected number of building blocks inside an imaginary sphere with radius r is given by [34, 35]:

$$N(r) = \left(\frac{r}{r_0} \right)^D \quad (2.10)$$

Here, the dimensionality D is related to the packing density of the agglomerate. A particle can only be regarded as a mass fractal when the building blocks are packed so that the system is self-similar over at least one order of magnitude. A system is referred to as self-similar when a particular way that particles are packed together on a small length scale is similar to the way that particles are packed on a larger scale. As illustrated in Figure 3, the red circles were packed inside a blue dotted circle similar to the way that the blue dotted circles were packed inside the green dotted circle. For fractalic systems the packing of blue dotted circles inside the green dotted circle does not necessarily need to be an exact replica of the red balls inside the blue dotted circle. As long as the average packing dimensionality remains constant over different radii r within a certain size range, it obeys Equation (2.10) and the system can be referred as a fractal. Note that the blue dotted circle, which is one order of magnitude larger as the red circle contains 29 red circles and the green dotted circle, which is one order of magnitude large as the blue dotted circles contains 29 blue dotted circles. Therefore, the packing dimensionality remain constant at $D = {}^{10}\log(29) = 1.46$ for two orders of magnitude.

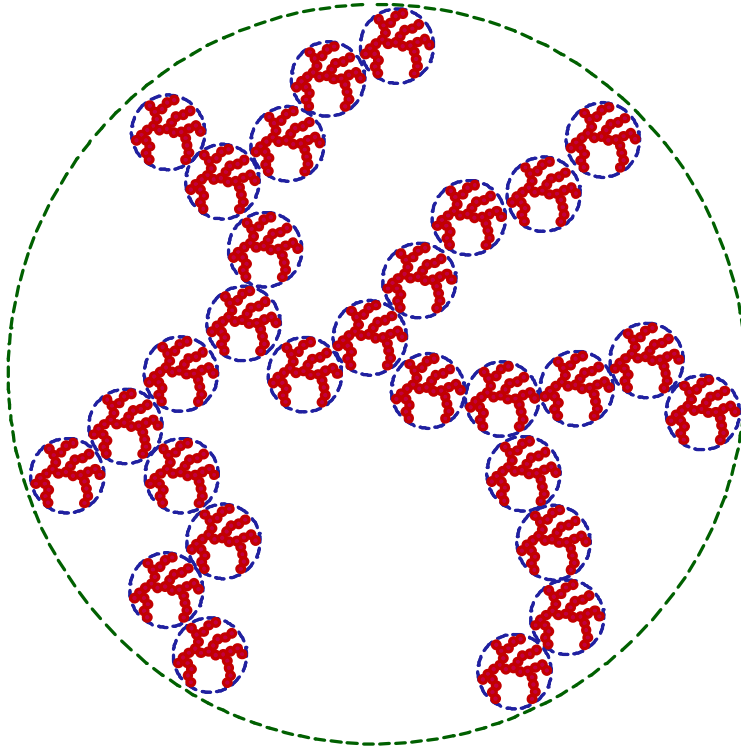


Figure 3. A conceptual illustration of a self-similar agglomerate. The blue dotted circles inside the green dotted circle is self-similar compared to the red circles inside the blue dotted circle. Both are consistent with $D = {}^{10}\log(29) = 1.46$.

Its pair distance distribution function $g_0(r)$ describes the probability of finding a correlation at given r , while the cumulative distribution $N(r)$ Equation (2.10) describes the probability of a correlation within a sphere of radius r . Consequently, the pair correlation function $g_0(r)$ is described by a derivative of $N(r)$:

$$g_0(r) = \frac{1}{4\pi \cdot r^2} \cdot \frac{dN}{dr} = \frac{D}{4\pi \cdot N_p} \cdot \frac{r^{D-3}}{r_0} \quad (2.11)$$

Here, N_p is the total number of particles and $g_0(r)$ is closely related to $\chi(r)$. However, it only considers pairwise interactions between two different particles. The function $g_0(r)$ ((2.12) represents an fractal agglomerate with

an infinite size and a cut-off function was introduced to define the finite agglomerate size. When introducing an exponential cut-off function $\exp(-r/\xi)$, the relation for pairwise interactions given by Zernike and Prins [36] was solved analytically [34, 35]:

$$S_{MF}(q, D, \xi, r_0) = 1 + \frac{D \cdot \Gamma(D-1) \cdot \sin[(D-1) \cdot \arctan(q \cdot \xi)]}{(q \cdot r_0)^D \cdot \left(1 + \frac{1}{(q \cdot \xi)^2}\right)^{\left(\frac{D-1}{2}\right)}} \quad (2.12)$$

This structure function is useful to describe a variety of systems including some sol-gels. However, in particular cases, for instance when growth is controlled by diffusion limited cluster aggregation, these aggregates were found to be less polydisperse as an exponential cutoff function implies. In these cases sharper cutoff functions are more realistic, as explained in more detail by Sorensen and Wang [33]. Moreover, we derived a new fractal model with a variable Schultz-Zimm distributed cutoff as it is described in more detail in the next chapter (Chapter 3).

2.3. Polydisperse systems

If the form function of a monodisperse system is known, then the form function of a polydisperse system is [1]:

$$P_D(q, x) = \frac{\int_0^\infty D(x, \mu) \cdot P(q, x) \cdot m(x)^p dx}{\int_0^\infty D(x) \cdot m(x)^p dx} = \frac{\int_0^\infty D(x) \cdot P(q, x) \cdot x^{p-d} dx}{\int_0^\infty D(x) \cdot x^{p-d} dx} \quad (2.13)$$

where x is a particular size parameter, $P_D(q, x)$ and $P(q, x)$ are the form functions of a polydisperse and a monodisperse system, respectively. $D(x, \mu)$ is a probability distribution function that also depends on the average size μ ; m is a mass term and p is an exponent that depends on the type of distribution. Since the scattering intensity scales with the square of the mass or volume of electrons that are involved, a number, volume and intensity weighted average are weighted by $p = 2, 1$ and 0 , respectively. The mass term, which in the case of SAXS is proportional to the number of

electrons, scales with x^d , where d represents the number of dimensions in which the size parameter x is applied. For instance, in the case that x represents the length of a cylinder $d=1$, when x represents the radius of a cylinder $d = 2$, and when x represents the radius of a sphere $d=3$.

When interparticle correlations are involved, the calculation of the intensity function becomes more complex since it involves essentially all interactions between particle one with size x_1 and particle 2 with size x_2 , particle 3 with size x_3 , etc. Fortunately, these systems can be approximated by the local monodisperse approximation (LMA), which assumes that particles are only surrounded by other particles of the same size [37]. Following this approximation the corresponding scattering intensity can be described as:

$$I_D(q, x) = N \cdot (\Delta\rho)^2 \cdot \frac{\int_0^\infty D(x, \mu) \cdot P(q, x) \cdot S(q, x) \cdot m(x)^p dx}{\int_0^\infty D(x, \mu) \cdot m(x)^p dx} \quad (2. 14)$$

$$I_D(q, x) = N \cdot (\Delta\rho)^2 \cdot \frac{\int_0^\infty D(x, \mu) \cdot P(q, x) \cdot S(q, x) \cdot x^{p \cdot d} dx}{\int_0^\infty D(x, \mu) \cdot x^{p \cdot d} dx} \quad (2. 15)$$

2.4. Non-particulate systems

Some systems, such as bicontinuous systems cannot be interpreted as an assembly of particles. Instead, these systems can be analyzed by statistical models that describe characteristic fluctuations in the electron density. A useful model for bicontinuous systems was proposed by Teubner and Strey. It characterizes electron density fluctuations by two characteristic length scales, namely a correlation length ξ and a domain scale length d [38]:

$$I(q) = \frac{8\pi \cdot V \cdot c_2 \cdot \Delta\rho^2}{\xi \cdot (a_2 + c_1 \cdot q^2 + c_2 \cdot q^4)} \quad (2.16)$$

where:

$$\xi = \frac{1}{\sqrt{\left(\frac{1}{2} \cdot \sqrt{\left(\frac{a_2}{c_2}\right)} + \frac{1}{4} \cdot \left(\frac{c_1}{c_2}\right)\right)}} \text{ and:}$$
$$\frac{d}{2\pi} = \frac{2\pi}{\sqrt{\left(\frac{1}{2} \cdot \sqrt{\left(\frac{a_2}{c_2}\right)} - \frac{1}{4} \cdot \left(\frac{c_1}{c_2}\right)\right)}}$$

This expression combines an expression of randomly sized spheres with a characteristic ξ with an expression that has a quasi-periodic repeat distance d . In analogy with Debye's equation of randomly distributed overlapping spheres [39], the specific surface area of one phase in another phase is inversely proportional to the specific surface area: $S/V = 4 \phi (1-\phi) / \xi$, where S/V is a surface to volume ratio and ϕ is the volume fraction of either one of both phases in a two-phase system. This equation allows the description of various microemulsions ranging from ordered lamellas ($\xi \gg d$), until randomly sized spheres ($\xi \ll d$) [24, 38]. An increasing ξ/d ratio corresponds to an increasing extent of order, which corresponds to a more pronounced and narrower correlation peak in the intensity profile. This approach has been extended for more complex systems as extensively discussed by Antony Roberts [40].

2.5. References

1. Feigin, L.A. and D.I. Svergun, *Structure analysis by small-angle x-ray and neutron scattering* 1987, New York: Plenum Press.
2. Glatter, O. and O. Kratky, *Small-angle x-ray scattering* 1982, London: Academic Press.
3. Craievich, A., *Small Angle X-ray Scattering by Nanostructured Materials*, in *Handbook of Sol-Gel Science and Technology; Processing Characterisation and Applications*, S. Sakka and R.M.

-
- Almeida, Editors. 2005, Kluwer Academic Publishers: New York, Boston, Dordrecht, London, Moscow. p. 161-189.
4. Debye, P. and A. Bueche, *Scattering by an inhomogeneous solid*. J. Appl. Phys., 1949. **20**(6): p. 518-525.
 5. Pedersen, J.S., *Analysis of small-angle scattering data from colloids and polymer solutions: modeling and least-squares fitting*. Adv. Colloid Interfac., 1997. **70**(0): p. 171-210.
 6. Guinier, A. and G. Fournet, *General Theory*, in *Small-Angle Scattering of X-rays* 1955, John Wiley & Sons: New York. p. 5-82.
 7. Yarusso, D.J. and S.L. Cooper, *Microstructure of ionomers: interpretation of small-angle x-ray scattering data*. Macromol., 1983. **16**(12): p. 1871-1880.
 8. Dahmouche, K., et al., *Nanostructure and luminescent properties of sol-gel derived europium-doped amine functionalised hybrids*. J. Sol-gel Sci. Technol., 2006. **37**(2): p. 99-104.
 9. Beaucage, G. and D.W. Schaefer, *Structural studies of complex systems using small-angle scattering: a unified Guinier/power-law approach*. J. Non-Cryst. Solids, 1994. **172-174, Part 2**(0): p. 797-805.
 10. Kinning, D.J. and E.L. Thomas, *Hard-sphere interactions between spherical domains in diblock copolymers*. Macromol., 1984. **17**(9): p. 1712-1718.
 11. Ashcroft, N.W. and J. Lekner, *Structure and Resistivity of Liquid Metals*. Phys. Rev., 1966. **145**(1): p. 83-90.
 12. Terrill, N.J., et al., *Small-angle X-ray scattering studies on colloidal dispersions of polyaniline-silica nanocomposites*. Langmuir, 1993. **9**(8): p. 2093-2096.
 13. Manet, S., et al., *Structure of micelles of a nonionic block copolymer determined by SANS and SAXS*. J. Phys. Chem. B, 2011. **115**(39): p. 11318-11329.
 14. Besselink, R., et al., *Evolution of microstructure in mixed niobia-hybrid silica thin films from sol-gel precursors*. J. Colloid Interf. Sci., 2013. **404**(0): p. 24-35.
 15. Stawski, T.M., et al., *Development of nanoscale inhomogeneities during drying of sol-gel derived amorphous lead zirconate titanate precursor thin films*. Langmuir, 2011. **27**(17): p. 11081-11089.
 16. Stawski, T.M., et al., *Nanostructure development in alkoxide-carboxylate-derived precursor films of barium titanate*. J. Phys. Chem. C, 2012. **116**(1): p. 425-434.
-

17. Sharma, R.V. and K.C. Sharma, *The structure factor and the transport properties of dense fluids having molecules with square well potential, a possible generalization*. Physica A, 1977. **89**(1): p. 213-218.
18. Menon, S.V.G., V.K. Kelkar, and C. Manohar, *Application of Baxter's model to the theory of cloud points of nonionic surfactant solutions*. Phys. Rev. A, 1991. **43**(2): p. 1130-1133.
19. Baxter, R., *Percus–Yevick equation for hard spheres with surface adhesion*. J. Chem. Phys., 1968. **49**: p. 2770.
20. Gaudon, A., et al., *Phase separation in sol-gel derived ZrO₂-SiO₂ nanostructured materials*. J. Eur. Ceram. Soc., 2005. **25**(2-3 SPEC. ISS.): p. 283-286.
21. Gaudon, A., et al., *From amorphous phase separations to nanostructured materials in sol-gel derived ZrO₂:Eu³⁺/SiO₂ and ZnO/SiO₂ composites*. J. Non-Cryst. Solids, 2006. **352**(21-22): p. 2152-2158.
22. Rodrigues, D.E., et al., *Structural Features of Sol-Gel derived hybrid Inorganic Organic Network Ceramer Materials by Small-Angle X-ray Scattering*. Chem. Mater., 1992. **4**(6): p. 1437-1446.
23. Santilli, C., et al., *Controlled Drug Release from Ureasil– Polyether Hybrid Materials*. Chem. Mater., 2009. **21**(3): p. 463-467.
24. Schubert, K.-V., et al., *Small angle neutron scattering near Lifshitz lines: Transition from weakly structured mixtures to microemulsions*. J. Chem. Phys., 1994. **101**(6): p. 5343-5355.
25. Fisher, S., et al., *Solubilization of simvastatin and phytosterols in a dilutable microemulsion system*. Colloid Surface B, 2013. **107**, p. 35-42.
26. Orts-Gil, G., et al., *Characterisation of silica nanoparticles prior to in vitro studies: from primary particles to agglomerates*. J Nanopart. Res., 2011. **13**(4): p. 1593-1604.
27. Graf, P., et al., *Peptide-Coated Silver Nanoparticles: Synthesis, Surface Chemistry, and pH-Triggered, Reversible Assembly into Particle Assemblies*. Chem. Eur. J., 2009. **15**(23): p. 5831-5844.
28. Pontoni, D., et al., *Interactions and kinetic arrest in an adhesive hard-sphere colloidal system*. J. Chem. Phys., 2003. **119**: p. 6157.
29. Sztucki, M., et al., *Kinetic arrest and glass-glass transition in short-ranged attractive colloids*. Phys. Rev. E, 2006. **74**(5): p. 051504.
30. Simmons, B., et al., *Small Angle Neutron Scattering Study of Mixed AOT + Lecithin Reverse Micelles*. Langmuir, 2002. **18**(22): p. 8345-8349.

31. Dawson, K., et al., *Higher-order glass-transition singularities in colloidal systems with attractive interactions*. Phys. Rev. E, 2000. **63**(1): p. 011401.
32. Brinker, C.J.S., G. W. , *Sol Gel Science, Phys. Chem. Sol-Gel Processing*. Vol. 1. 1990, San Diego: Acedemic Press. 1-881.
33. Sorensen, C.M. and G.M. Wang, *Size distribution effect on the power law regime of the structure factor of fractal aggregates*. Phys. Rev. E, 1999. **60**(6): p. 7143-7148.
34. Chen, S.H. and J. Teixeira, *Structure and fractal dimension of protein-detergent complexes*. Phys. Rev. Lett., 1986. **57**(20): p. 2583-2586.
35. Teixeira, J., *Small-angle scattering by fractal systems*. J. Appl. Crystallogr., 1988. **21**(6): p. 781-785.
36. Zernike, F.t. and J. Prins, *Die beugung von roentgenstrahlen in fluessigkeiten als effekt der molekuelanordnung*. Zeitschrift für Physik, 1927. **41**(6-7): p. 184-194.
37. Pedersen, J., *Determination of size distribution from small-angle scattering data for systems with effective hard-sphere interactions*. J. Appl. Crystallogr., 1994. **27**(4): p. 595-608.
38. Teubner, M. and R. Strey, *Origin of the scattering peak in microemulsions*. J. Chem. Phys., 1987. **87**(5): p. 3195-3200.
39. Debye, P., H. Anderson, and H. Brumberger, *Scattering by an inhomogeneous solid. II. The correlation function and its application*. J. Appl. Phys., 1957. **28**(6): p. 679-683.
40. Roberts, A.P., *Statistical reconstruction of three-dimensional porous media from two-dimensional images*. Phys. Rev. E, 1997. **56**(3): p. 3203-3212.

3.

**Rapid early stage Schultz-Zimm
distributed mass-fractal growth studies
on niobia/ silsesquioxane mixtures**

3.1. Abstract

Rapid in-situ SAXS measurements were performed to measure early-stage agglomeration processes under a continuous flow of niobium ethoxide mixtures. The growth characteristics of niobium ethoxide were characterized in the presence and absence of a silsesquioxane 1,2-bis-(triethoxysilyl)-ethane (BTESE) at $T=25$ and $T=40^{\circ}\text{C}$. Data was analysed with a newly derived mass-fractlic model. Unlike the conventional exponential cutoff model, a variable cutoff function in the correlation function was being introduced without introducing laborious numerical calculations. An increasing sharpness of the cutoff function was associated with an decreasing polydispersity

The analysed data both in the presence and absence of BTESE revealed rather monodisperse selpreserving polydispersities that were associated with diffusion limited cluster agglomeration (DLCA). In the absence of BTESE growth could be characterized by Smolucowski type agglomeration kernels with a homogeneity parameter $\lambda\sim 0$. Nevertheless, in the presence of BTESE the growth exponents became substantially smaller ($p<0.2$, with $R_G\sim t^p$). The reduced growth exponent could not be described by irreversible Smoluchowski type kernels and was more consistent with reversible Lifshitz-Slyozov type agglomeration kernels. The growth of the niobia clusters was clearly suppressed by the presence of BTESE.

3.2. Introduction

Organically bridged silsesquioxanes exhibit very high hydrothermal, acid and mechanical stability, which is substantially larger than SiO_2 [1-5]. Therefore, it can withstand very harsh conditions, which make it potentially suitable as a carrier for catalytic materials. It can also exhibit micropores, when processed properly, suitable for filtration and pervaporation or for membrane reactors [2-7]. To widen its applicability to other molecular separation processes and catalysis, bridged silsesquioxanes may be altered by doping them with transition metal oxides. Hence, selective transition

metal centres are created that may be useful either for catalytic purposes or to alter the molecular diffusivity and/or adsorption in these materials. For instance, the introduction of nickel, cobalt, zirconium and niobium oxides in silica and hybrid silica membranes was found to enhance the H_2/N_2 and H_2/CO_2 permselectivity [8-14]. Nevertheless, homogeneous distribution of metal oxides within a matrix of bridged silsesquioxanes is not straightforward from a synthetic point of view. The metal oxide tends to be introduced either as metal salt, or as a metal alkoxides that tends to phase separate while the networks forms. Metal salts do not contribute to the gel network of the silsesquioxane, and are therefore poorly compatible with these networks and simply phase separate as metal salts. Metal alkoxides do form gels, however their reactivity is known to be orders of magnitude higher than that of silicon alkoxides [15-17]. Optimization of such mixed systems is often a matter of trial and error. Nevertheless, we may find more systematic solutions by gaining more insight into the kinetics of such evolving systems.

Much is known concerning the kinetics of silicon alkoxides, which because of their relatively low reactivities allow monitoring by a large number of characterization techniques. These include ^{29}Si -NMR, which not only monitors the number of specific chemical groups, but also the number of specific groups that are coordinating the silicon atom [18-21]. It allows the identification of different reaction rate constants depending on the chemical nature of the Si atom. In the case of metal alkoxides NMR cannot be used due to the very fast kinetics of these materials [15-17], combined with the complex nature of their quadrupolar nuclei [22]. Consequently, only a limited number of kinetic studies on metal alkoxides were found in literature which rely on other techniques including Small Angle X-ray Scattering (SAXS), Fourier Transform Infrared Spectroscopy (FTIR), electron conductivity and dynamic light scattering (DLS) [23-28]. Alternatively, macroscopic effects including turbidity and geltime have often been used to predict effects on the molecular level [29-31]. However, on a macroscopic additional effects play a role, such as micellar stabilization. Hence, the kinetics on microscopic level are not always directly correlated with the kinetics on molecular level [16].

The extremely fast early stage reaction kinetics of titanium and zirconium alkoxides were already well described by the work of Harris et al. [21, 23]. In the work presented here we focused on the nucleation and growth of niobium penta-ethoxide, and the extent to which growth is influenced by the presence of a bridged silsesquioxane, i.e. 1,2-bis-(triethoxysilyl)-ethane (BTESE). Niobia was proven to be a useful dopant either for scavenging CO₂ or as Lewis acid catalyst [12, 32-34]. The early stages of these growth kinetics were monitored by time-resolved Synchrotron Small Angle X-ray Scattering (SAXS) experiments. This approach not only allows us to determine the agglomerate sizes, but also their shape and polydispersity in 5 s timeframes.

3.3. Experimental Section

3.3.1. Recipe mixing experiments

All precursor solutions were prepared inside a glovebox under nitrogen atmosphere. The synthesis was performed under atmospheric conditions. Firstly, a mixed metal alkoxide precursor solution was made in dry ethanol which contained 0.635 mol/L 1,2-bis-triethoxysilyl-ethane (BTESE) sol and 0.318 mol/L niobium pentaethoxide (NPE, ABCR chemicals, 99.99%). This corresponds to a [Si]:[Nb] ratio of 4:1 and an overall ethoxide concentration [-OEt] = 5.4 mol/L, i.e. including the ethoxide groups of both BTESE and NPE. Secondly, diluted nitric acid solutions were prepared which contained [H₂O] = 3.857 mol/L and [HNO₃] = 0.129 mol/L in dry ethanol. By mixing an equal volume of the combined alkoxide precursor solution and the diluted nitric acid solution a hydrolysis ratio [H₂O]/[(Si)-OEt] = 1, an acid ratio [HNO₃]/[(Si)-OEt] = 1/30 and [-OEt] = 2.7 mol/L was reached. Particle growth in these solutions was monitored at $T=25^{\circ}\text{C}$ and $T=40^{\circ}\text{C}$, and these samples are further referred to as SiNbT25 and SiNbT40, respectively.

Experiments were also performed in the absence of BTESE. NPE precursor solutions with a concentration of 0.318 mol/L Nb were prepared. Similarly to the mixtures with BTESE exactly the same diluted nitric acid solutions were used and also mixed in a equal volume ratio with the NPE precursor solution. Particle growth in these mixtures was also monitored at $T=25^{\circ}\text{C}$

and $T=40^{\circ}\text{C}$, and these samples are further referred to as NbT25 and NbT40, respectively.

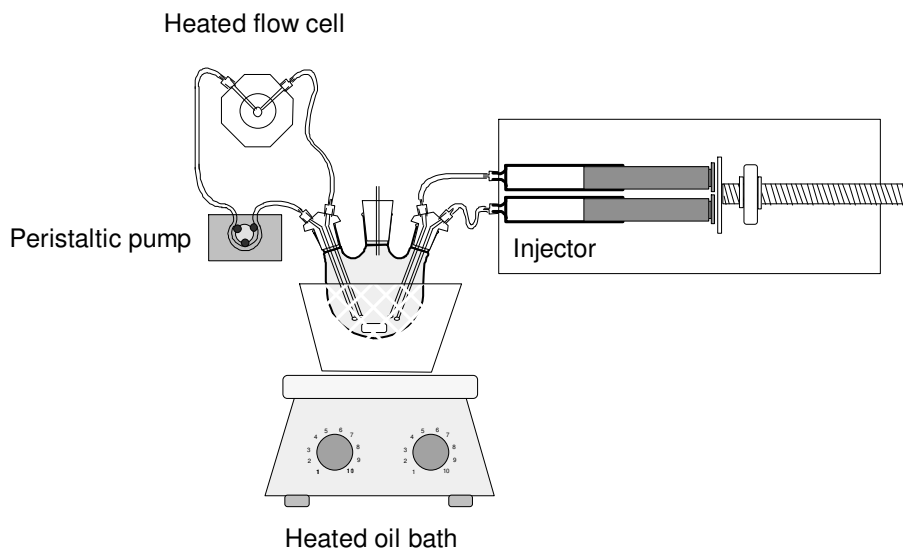


Figure 3.1. Schematic diagram of mixing setup used in SAXS experiments.

3.3.2. Mixing Setup

SAXS mixing experiments were executed with a setup as illustrated in Figure 3.1. A homemade flowcell was used that consisted of an aluminium housing with luerlock connectors for connecting tubes. The cell consisted of two Kapton foils that were compressed against an aluminium interior by two aluminium rings with sealing rubbers outside the cell. The cell itself was cylindrical with a depth of 1mm and a cross-sectional diameter of 5mm. Continuous flow between the flow cell and the reactor that consisted of a 25mL three-neck round-bottom flask was arranged by a Masterflex peristaltic pump. The dead time between the round-bottom flask and the flow cell was 10s. Before mixing the solutions rapid SAXS-measurements were already started to ensure that measurement was immediately done when mixing the solutions. Then, the measurement was initiated by a timer

that started the injector. In 8s the injector injected both 12 mL of diluted nitric acid solution and 12mL of metal alkoxide solution simultaneously into the three-neck round-bottom flask. The round-bottom flask contained a small vent to release overpressure that was formed during injection.

3.3.3. Time-resolved SAXS experiments

Small-angle X-ray scattering was carried out using synchrotron radiation on the Dutch-Belgian beamline, DUBBLE BM-26B of the ESRF in Grenoble [35]. The X-ray beam with an energy of 12keV was focused on a corner of the 2D Pilatus 1M CCD-detector to maximize the covered range of scattering angles. A beam stop was applied to shield the detector from the direct beam and avoid saturation of the outgoing signal. The detector was placed at a distance of 1.36 m from the sample, which resulted in a measurable q -range: $0.17 < q < 6.00 \text{ nm}^{-1}$. All scattering data were found to be independent of the scattering angle in the plane of the detector, which indicated that particles were isotropic or isotropically dispersed throughout the sample. Therefore, all channels with the same q value were averaged with each other. Silver behenate was used as calibration standard for the determination of the absolute scale of the scattering vector q in our experiments [36].

All curves were normalized by dividing the scattering intensity by the time of data acquisition and the signal of the ionization chamber in front of the sample. A background subtraction procedure was carried out. For sols, the scattering signal of a capillary filled with ethanol was subtracted.

3.4. Theoretical background

3.4.1. Characterization of SAXS data

3.4.1a. Mass-fractal agglomerates with an exponential cut-off length ξ

After a short hydrolysis period, small clusters of BTESE and NPE nucleated and subsequently agglomerated into amorphous assemblies of these primary clusters. In analogy with previous reported SAXS-experiments on mixed BTESE/NPE sols [37], these agglomerates could be well described in terms of mass fractals. Due to shadow effect of the vacuum tubing that was used to reduce scattering from air between the sample and the detector, the measurements were only reliable up to $q = 6 \text{ nm}^{-1}$. Consequently, the transition from the fractal regime to the Porod regime could not be observed and the radii of the primary nuclei could not be determined. This obstacle was circumvented by using an alternative scattering intensity function for mass fractals as described by Sorensen [38]:

$$S_{\text{EC}}(q, D_f, \xi) = \frac{\sin((D_f - 1) \cdot \text{atan}(q \cdot \xi))}{(D_f - 1) \cdot q \cdot \xi \cdot (1 + (q \cdot \xi)^2)^{\left(\frac{D_f - 1}{2}\right)}} \quad (3.1)$$

Herein, D_f describes the dimensionality of mass fractals, and ξ the typical cut-off distance that determines the finite size of an agglomerate. This intensity function is closely related to the structure function of mass fractals as described by Teixeira [39, 40]. However, the radius of the primary scatters or nuclei (r_0) is assumed to be infinitely small (i.e. $\lim r_0 \rightarrow 0$), in contrast to the mass fractal description of Teixeira, where r_0 has a finite value. Therefore, Equation (3.1) cannot be normalized over the volume of the primary scatterer. Instead, it is normalized over the volume of the whole agglomerate as determined by ξ . Note that the ξ -parameter is

introduced as an exponentially decaying function ($h(r, \xi) = \exp(-r/\xi)$) in the pair correlation function for 3-dimensional agglomerates:

$$\gamma(r, D_f, \xi) = r^{D_f-3} \cdot h(r, \xi) \quad (3.2)$$

The typical volume (Porod volume) of such an agglomerate is described by [41, 42]:

$$V_A = \int_0^{\infty} 4 \cdot \pi \cdot r^2 \cdot \gamma(r) dr = 4\pi \cdot \Gamma(D_f) \cdot \xi^{D_f} \quad (3.3)$$

where Γ represented the gamma function. Since Equation (3.1) was normalized over its entire agglomerate volume, it is being normalized as a form function and it obeys $S(q \rightarrow 0) = 1$. Throughout, the q -region $P(q)$ was set to 1 and the overall scattering intensity was described by:

$$I(q) = I_0 \cdot S(q) \quad (3.4)$$

where $I_0 = N \cdot (V_A)^2$, which corresponds to the scattering intensity at $q \rightarrow 0$ (since $S(q \rightarrow 0) = 1$), N is the particle number density and V_A the particle volume of the fractal agglomerate (Equation (3.3)). Note that the ratio $I_0 / V_A = N \cdot V_A \cdot (\Delta\rho^2)$ is proportional to the mass concentration of agglomerates in the solution, while the contrast in electron density ($\Delta\rho$) is presumably constant during agglomeration. The radius of gyration of these agglomerates can be extracted when D_f and ξ are known through the equation:

$$R_G = \xi \cdot \sqrt{\frac{D_f \cdot (D_f + 1)}{2}} \quad (3.5)$$

3.4.1b. Mass-fractal agglomerates with a Schultz-Zimm distributed cut-off length.

As discussed by Sorensen [38] the diffusion limited cluster aggregation (DLCA) mechanism typically leads to less polydisperse agglomerates as implied by the exponentially decaying cut-off function. Sharper cut-off functions such as a Gaussian cutoff ($h(r, \xi) = \exp(-(r/\xi)^2)$) were found to be more realistic for a variety of different aggregation mechanisms. On the other hand, it would be convenient to define a function where the sharpness of the cutoff function could be related to the degree of polydispersity. Therefore, firstly we introduce an infinitely sharp cut-off function; i.e. a unit step or Heaviside step function $h(r, \xi) = H(\xi - r)$. The intensity function of a mass-fractal with a hard cutoff function was described by an rotationally averaged Fourier transform:

$$S_{HC}(q, \xi) = \frac{4\pi}{q \cdot V_A} \int_0^{\infty} H(\xi - r) \cdot r^{D_f-2} \cdot \sin(q \cdot r) dr = \frac{4\pi}{q \cdot V_A} \int_0^{\xi} r^{D_f-2} \cdot \sin(q \cdot r) dr \tag{3.6}$$

Herein, $H(\xi - r)$ represents the unit step function. $H(\xi - r) = 1$ for $r < \xi$ and $H(\xi - r) = 0$ for $r > \xi$. V_p represents the volume of the agglomerate. Instead of using the unit step function we can also move the upper boundary of the sine transform from ∞ to ξ , as shown in the right hand side part of Equation (3.6). Secondly, polydispersity is introduced by the integral:

$$S_{SC}(q, \xi) = \int_0^{\infty} w(\xi) \cdot I_{hf}(q, \xi) d\xi \tag{3.7}$$

Herein, $w(\xi)$ is an intensity weighted probability density function of the cutoff parameter ξ . We applied a Schultz-Zimm distribution [43] which was found to give realistic results in earlier studies on similar systems [37, 44-46]:

$$w(\xi, \mu, z) = \frac{a^{Z+1}}{\Gamma(Z+1)} \cdot \xi^Z \cdot \exp(-a \cdot \xi) \quad (3.8)$$

where

$$a = \frac{Z+1}{\mu}$$

and μ is the intensity weighted average of ξ and the Z-parameter is related to the distribution of the cutoff distance, i.e.: the variance of ξ corresponds to $(\sigma_\xi)^2 = \mu^2/(Z+1)$. By combining Equation (3.6), Equation (3.7) and Equation (3.8) we obtain:

$$S_{SC}(q, a, D_f, Z) = \frac{4\pi \cdot a^{Z+1}}{q \cdot V_p \cdot \Gamma(Z+1)} \cdot \int_0^\infty \left[\xi^Z \left(\int_0^\xi r^{D_f-2} \cdot \sin(q \cdot r) dr \right) \cdot \exp(-a \cdot \xi) \right] d\xi \quad (3.9)$$

This integral can be evaluated as a Laplace transform and for integer values of Z an analytical solution is given by:

$$S_{SCI}(q, a, D_f, \zeta) = \frac{4\pi \cdot a^{Z+1}}{2i \cdot q \cdot V_p \cdot \Gamma(Z+1)} \cdot (-1)^Z \cdot \frac{d^Z}{da^Z} \left(\frac{1}{a} \cdot \left(\frac{1}{(a-i \cdot q)^{D-1}} - \frac{1}{(a+i \cdot q)^{D-1}} \right) \right) \quad (3.10)$$

where i is the imaginary number. The derivatives of a that are expanding with increasing Z-value can be generalized by the following Riemann's sum:

$$S_{SC}(q, a, D_f, \zeta) = \frac{4\pi}{2i \cdot q \cdot V_p} \cdot \sum_{\eta=0}^Z \left(\frac{\Gamma(D_f + \eta - 1)}{\Gamma(\eta + 1)} \cdot a^\eta \cdot \left(\frac{1}{(a - i \cdot q)^{D_f + \eta - 1}} - \frac{1}{(a + i \cdot q)^{D_f + \eta - 1}} \right) \right) \quad (3.11)$$

Herein, η is an integer variable that varies from 0 to Z. In analogy with the mass-fractal structure function with an exponential cutoff ((3.1), the function was normalized over its agglomerate volume V_A such that $S(q \rightarrow 0) = 1$. The Porod volume of such agglomerate is described by:

$$V_A = 4\pi \cdot \left(\frac{a^{Z+1}}{\Gamma(Z+1)} \right) \cdot \int_0^\infty \xi^Z \left(\int_0^\xi r^{D_f-3} \cdot r^2 dr \right) \cdot \exp(-a \cdot \xi) d\xi \quad (3.12)$$

which corresponded to:

$$V_A = \frac{4\pi \cdot \Gamma(D_f + Z + 1)}{D_f \cdot \Gamma(Z + 1)} \cdot \left(\frac{\mu}{Z + 1} \right)^{D_f} \quad (3.13)$$

Then, after normalization of Equation (3.11) with Equation (3.13), and replacing complex elements with goniometric equations we obtain:

$$S_{SC}(q, a, D_f, Z) = \left(\frac{a}{q} \right) \cdot \frac{D_f \cdot \Gamma(Z + 1)}{\Gamma(D_f + Z + 1)} \cdot \sum_{\eta=0}^Z \frac{\Gamma(D_f + \eta - 1)}{\Gamma(\eta + 1)} \cdot \frac{\sin \left((D_f + \eta - 1) \cdot \operatorname{atan} \left(\frac{q}{a} \right) \right)}{\left(1 + \left(\frac{q}{a} \right)^2 \right)^{\left(\frac{D_f + \eta - 1}{2} \right)}} \quad (3.14)$$

Now, let us define ζ as the integer part of Z and ϕ as the fractional part of Z . Then, the contribution of the ϕ to $S_{sc}(q)$ may be approximated as a ϕ fraction of the $\eta = \zeta + 1$ element of the Riemann's Sum. Consequently the structure function for all values of $Z = \zeta + \phi$ can be approximated by:

$$S_{sc}(q, \mu, D_f, Z) = \frac{D_f \cdot \Gamma(Z + 2)}{(q \cdot \mu) \cdot \Gamma(D_f + Z + 1)} \cdot (S_I + \phi \cdot S_F) \quad (3.15)$$

where:

$$S_I = \sum_{\eta=0}^{\zeta} \left(\frac{\Gamma(D_f + \eta - 1)}{\Gamma(\eta + 1)} \cdot \frac{\sin\left((D_f + \eta - 1) \cdot \operatorname{atan}\left(\frac{q \cdot \mu}{Z + 1}\right)\right)}{\left(1 + \left(\frac{q \cdot \mu}{Z + 1}\right)^2\right)^{\left(\frac{D_f + \eta - 1}{2}\right)}} \right)$$

and:

$$S_F = \frac{\Gamma(D_f + \zeta)}{\Gamma(\zeta + 2)} \cdot \frac{\sin\left((D_f + \zeta) \cdot \operatorname{atan}\left(\frac{q \cdot \mu}{Z + 1}\right)\right)}{\left(1 + \left(\frac{q \cdot \mu}{Z + 1}\right)^2\right)^{\left(\frac{D_f + \zeta}{2}\right)}}$$

where S_I and S_F represent the contributions of the integer and fractional values of Z to $S_{sc}(q)$. For comparison of the Schultz cut-off model with the exponential cutoff model it is more convenient to express the size of a cluster by the radius of gyration that is derived from [41, 42]:

$$(R_G)^2 = \frac{1}{2} \cdot \frac{\int_0^{\infty} r^4 \cdot \gamma(r) dr}{\int_0^{\infty} r^2 \cdot \gamma(r) dr} \quad (3.16)$$

that corresponds to:

$$(R_G)^2 = \frac{1}{2} \cdot \frac{\int_0^{\infty} \xi^z \left(\int_0^{\xi} r^4 \cdot r^{D_f-3} dr \right) \cdot \exp(-a \cdot \xi) d\xi}{\int_0^{\infty} \xi^z \left(\int_0^{\xi} r^2 \cdot r^{D_f-3} dr \right) \cdot \exp(-a \cdot \xi) d\xi} \quad (3.17)$$

which solution is given by:

$$R_G = \left(\frac{\mu}{Z+1} \right) \cdot \sqrt{\frac{1}{2} \cdot \frac{D_f \cdot (D_f + Z + 1) \cdot (D_f + Z + 2)}{(D_f + 2)}} \quad (3.18)$$

Since $\gamma(r)$ is essentially an auto-convolution product of $\Delta\rho(r)$ a hard cutoff function is not realistic. Therefore, the relative variance of ξ that can be derived from the Z parameter is always larger, because relative variance of R_G and the relationship between them depends on the geometry of the fractal. Alternatively, we may extract a polydispersity factor C_p following the procedure described by Sorensen and Wang [38]. Provided that $S(q)$ is normalized over the entire agglomerate volume Equation (3.13), such that $S(q \rightarrow 0) = 1$, the effective structure function in the fractal regime ($q \cdot R_G \gg 1$) is described by:

$$S_{\text{eff}}(q, R_G) = C \cdot C_p \cdot (q \cdot R_G)^{-D_f} \quad \text{for: } q \cdot R_G \gg 1 \quad (3.19)$$

where the constant C is related to the geometry of the fractalic agglomerate and experimental results revealed that $C = 1.0 \pm 0.05$ for mass fractals with D_f in a range between 1.7 and 2.1 [38]. C_p is a measure of the polydispersity and is defined by:

$$C_p = \frac{M_1}{M_2} \cdot \left(\frac{M_{(2+2/D_f)}}{M_2} \right)^{\left(\frac{D_f}{2} \right)} \quad (3.20)$$

where M_j represents the j^{th} moment of the particle size distribution, and is defined as:

$$M_j = \int_0^{\infty} (N_{pa})^j \cdot n_{pa}(N_{pa}) \cdot dN_{pa} \quad (3.21)$$

Here N_{pa} represents the number of primary particles per agglomerate and $n_{pa}(N_{pa})$ represents the particle number distribution function of primary particles per agglomerate. The C_p value increases with increasing polydispersity and it can be associated with a particular growth mode, i.e. $C_p \sim 1.5$ for diffusion limited cluster aggregation (DLCA) and $C_p > 2$ for reaction limited cluster aggregation (RLCA) [38]. C_p is a size independent measure of polydispersity and solely depends on Z and D_f , and it can be derived from Equation (3.14) by taking the limit $(q \cdot R_G) \rightarrow \infty$ of $S_{sc}(q \cdot R_G) \cdot (q \cdot R_G)^{D_f}$, which corresponds to:

$$C \cdot C_p = \sin \left[(D_f - 1) \cdot \frac{\pi}{2} \right] \cdot \left(\frac{D_f \cdot \Gamma(D_f - 1) \cdot \Gamma(Z + 1)}{\Gamma(D_f + Z + 1)} \right) \cdot \left(\frac{1}{2} \cdot \frac{D_f \cdot (D_f + Z + 1) \cdot (D_f + Z + 2)}{(D_f + 2)} \right)^{\left(\frac{D_f}{2} \right)} \quad (3.22)$$

Note that the Riemann's sum diminished since the limit was dominated by the $\eta=0$ element of the Riemann's sum. As illustrated in Figure 2 by simulations of $S_{Sc}(q, \mu, D_f, Z)$ with $R_G=10$ nm and $D_f=2$, the height of the fractal regime as characterized by $C \cdot C_p$ decreases with increasing Z values.

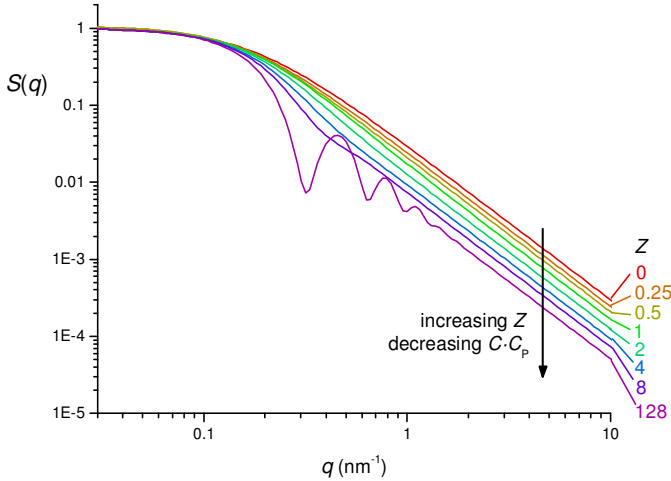


Figure 3.2. Simulated curves of $S_{Sc}(q, \xi, D_f, Z)$, with $R_G=10$ nm and $D_f=2$ being held constant and $z = 0, 0.25, 0.5, 1, 2, 4, 8, 128$, which corresponds to $C \cdot C_p = 3.00, 2.45, 2.10, 1.67, 1.25, 0.93, 0.73$ and 0.52 , respectively.

3.3.2. Growth kinetics

After a very short nucleation period growth is presumably accomplished by irreversible coagulation of primary nuclei which can be described by the Smoluchowski type agglomeration kernels [47-52]:

$$R_G(t) = \left(\sqrt[p]{R_{G,t=0}} + k \cdot t \right)^p \quad (3.23)$$

where:

$$p = \frac{1}{D_f(1-\lambda)}$$

Herein, p is a growth exponent that determines the order of the reaction, k is a reaction rate constant and λ the homogeneity parameter. This equation includes a crossover regime between diffusion limited cluster aggregation (DLCA: $\lambda \sim 0$) and reaction limited cluster aggregation (RLCA: $\lambda \sim 1$) and is only valid for non-gelling agglomeration kernels ($\lambda < 1$). Moreover, these agglomeration kernels imply a self-preserving polydispersity. This means that depending on the growth limiting process (i.e. to what extent this is described by either DLCA or RLCA) a particular extent of polydispersity is preserved. The relation between D_f , λ and the polydispersity parameter C_p depends on the aggregation regime as determined by the Knudsen number (Kn) [49]. Due to the interaction with solvent molecules in liquid media the mean free path of a particle is extremely small and $\text{Kn} \sim 0$. Particles move by diffusion following the Stokes-Einstein relationship with a diffusion coefficient $D \sim R_h^{-1}$, where R_h is the hydrodynamic radius of a particle. In such a case C_p is described by [38]:

$$C_p(D_f, \lambda) = \frac{1}{(2-\lambda)} \cdot \left[\frac{\Gamma\left(3-\lambda + \frac{2}{D_f}\right)}{\Gamma(3-\lambda)} \right]^{\left(\frac{D_f}{2}\right)} \quad (3.24)$$

3.5. Results and discussion

As Figure 3.3 illustrates, the time resolved experiments of sample NbT25 could be described well by the Schultz cutoff function Equation (3.15) (colored lines). On the other hand, the exponential cutoff function (Equation (3.1), black lines) cannot follow the sharp curvature of the experimental data in the Guinier region. Consequently, the D and R_G values obtained from the fits were systematically larger than obtained from the

Schultz cutoff function. For instance, for $t = 1$ min with the Schultz cutoff: $Z = 6.3 \pm 0.7$, $D_f = 1.39 \pm 0.01$ and $R_G = 2.51 \pm 0.07$ nm, while for the exponential cutoff $D_f = 1.93 \pm 0.04$ and $R_G = 2.92 \pm 0.07$ nm. In view of the goodness of the fit to the experimental data, the Schultz cutoff model was therefore considered more suitable for these datasets.

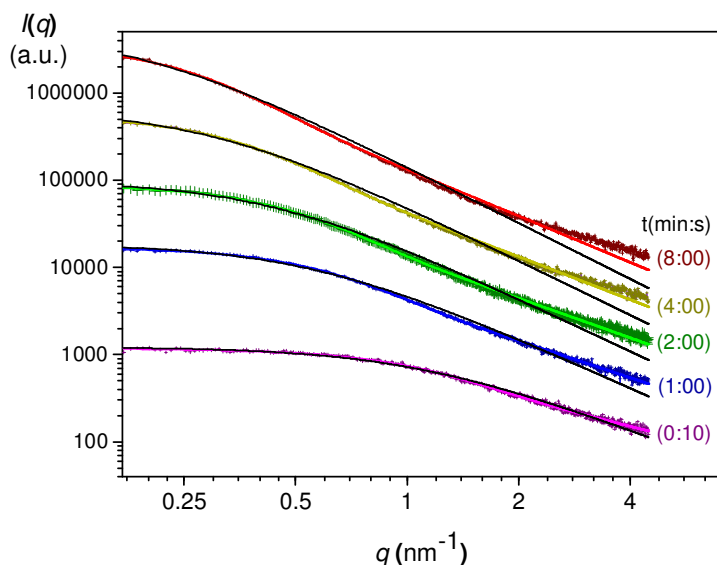


Figure 3.3. Fitted experimental data of sample NbT25 at different time intervals by using either the exponential cutoff model (black lines) or the Schultz cutoff model (colored lines).

Immediately after mixing the niobium pentaethoxide solutions and diluted nitric acid solutions in the absence of BTESE (sample NbT25 and NbT40), small agglomerates with $R_G > 1$ nm were formed instantaneously (Figure 3.4a). Then, the agglomerates grew further, roughly following $R_G \sim t^{0.5}$. Since the initial stage of the growth process was described with a growth exponent < 1 , this stage cannot be described by a gelling agglomeration kernel, despite the fact that these systems will gel eventually. Instead, it could be described well by Equation (3.23). The optimized fit parameters are given in Table 3.1.

The ratio I_0/V_A (Figure 3.4b), which is proportional to the mass of agglomerates in the sol, was used as a measure of the extent of particle

nucleation. At both temperatures roughly 50% already nucleated before the first SAXS data points were recorded. After $t = 2$ min, I_0/V_A leveled off. Thus, the mass concentration of agglomerates became nearly constant after $t = 2$ min. Therefore, all growth after $t = 2$ min occurred predominantly by cluster-cluster aggregation.

A similar trend was observed for the mass-fractal dimension D_f . In the initial stage of the reaction a substantial number of primary particles nucleated. However, the extent of agglomeration of these primary particles was limited. Therefore, the number of primary particles that built up the agglomerate was too small for the agglomerate to be regarded as a mass fractal. While the agglomerates grew in time, an increasing number of primary particles contributed to the agglomerate until eventually well-defined mass-fractals were formed. In the case of sample NbT25, at $t = 8$ min the fractal region ranged over approximately one order of magnitude in a range between $0.4 \text{ nm}^{-1} < q < 4 \text{ nm}^{-1}$ (Figure 3.3) and a mass-fractal dimension could be roughly established. Beyond this point the value of D_f levelled off towards $D_f = 1.88$ (Table 3.1), as illustrated in Figure 3.4c. At $T = 40^\circ\text{C}$ the particles grew substantially faster, the rate constant k (Table 3.1) was roughly 8 times larger than at $T = 25^\circ\text{C}$, while the growth exponent ρ was roughly 1.2 times smaller. Effectively, the agglomerates grew 4 times faster at $T = 40^\circ\text{C}$. R_G reached ~ 6 nm after $t = 2$ min, as compared to $T = 25^\circ\text{C}$ where a similar gyration radius was reached after $t = 8$ min. Consequently, at $T = 40^\circ\text{C}$ D_f levelled off to $D_f = 1.91$ already after 2 min of reaction time.

At $T = 25^\circ\text{C}$ a decreasing value of Z and an increasing value of $C \cdot C_p$ within the first 8 min imply an increasing polydispersity within this time frame. After $t = 8$ min both values levelled off. This trend can be explained by the extent of nucleation as characterized by the ratio I_0/V_A . As long as new primary particles nucleate while other agglomerates grow the polydispersity will continue to increase. However, as the ratio I_0/V_p levelled off, Z and $C \cdot C_p$ levelled off as well. This is consistent with agglomeration kernels that imply a self-preserving particle distribution during growth of fractal agglomerates [38, 47, 49, 51-53]. For sake of clarity the trends of Z and $C \cdot C_p$ at $T = 40^\circ\text{C}$ are omitted since these trends strongly overlap with the data at $T = 25^\circ\text{C}$. Nevertheless, throughout the reaction process their values remained roughly constant within the error margins of the fit. Optimized values are listed in Table 3.1.

At both temperatures the agglomeration process was DLCA as indicated by final $D_f \sim 1.9$ and $C \cdot C_p \sim 1.0$ values. The growth exponent ρ was consistent with λ close to zero, which confirms the proposed DLCA mechanism. Yet, the C_p value calculated from the λ was ~ 1.5 , larger than the static C_p values of ~ 1.0 as derived from Z. Possibly, since C is related to the geometry of a single agglomerate, it is lower in the present case ($C \sim 2/3$) than the previously reported experimental results implied [38]. Our findings suggest a lower variation in branch sizes per agglomerate, i.e. less elongated and more spherically shaped agglomerates.

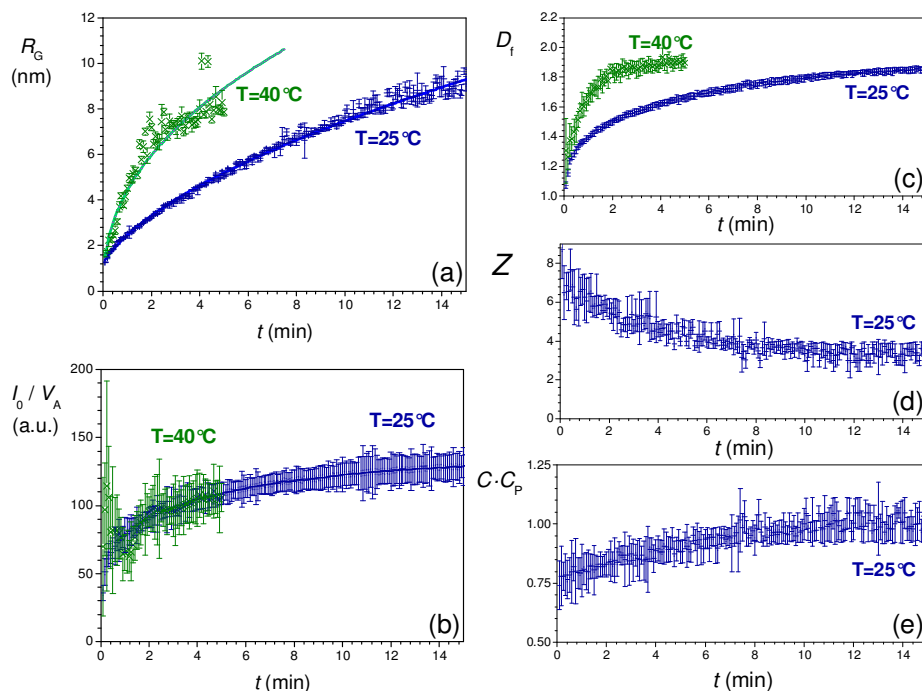


Figure 3.4. Optimized parameters derived from fitting the Schultz cutoff function for mixing experiments without BTESE. a) R_G , b) I_0/V_A , and c) D_f of NbT25 and NbT40 ;d) Z and e) $C \cdot C_p$ of sample NbT25.

Table 3.1 Characteristic parameters of the self preserving Smoluchovski-type reaction kernels of fractal particles with a Schultz cutoff function.

Sample	NbT25	NbT40	SiNbT25	SiNbT40
$R_{Gt=0}$	1.22 ± 0.02	0	1.66 ± 0.04	1.92 ± 0.01
k (min ⁻¹)	3.61 ± 0.11	30 ± 6	3.6 ± 0.60	2.7 ± 0.5
p	0.56 ± 0.01	0.44 ± 0.02	0.14 ± 0.02	0.18 ± 0.02
D_{ffinal}	1.88 ± 0.01	1.91 ± 0.04	1.68 ± 0.01	1.66 ± 0.02
Z_{final}	3.2 ± 0.6	4.8 ± 1.6	2.58 ± 0.13	2.84 ± 0.03
$C \cdot C_{Pfin}(Z, D_f)$	1.0 ± 0.1	0.9 ± 0.2	1.1 ± 0.1	1.0 ± 0.1
λ	0.04 ± 0.01	-0.20 ± 0.05	-3.2 ± 0.1	-2.4 ± 0.1
$C_p(\lambda, D_f)$	1.5 ± 0.1	1.5 ± 0.1		

The agglomeration of sol-gel mixtures that contained both BTESE and NPE (samples SiNbT25 and SiNb40) were characterized by the parameters Z , R_G and the ratio I_0/V_A (Figure 3.5). After a very short induction period, the Z -parameter remained constant at $Z \sim 2.5$ at both temperatures (25 °C and 40°C), see Figure 3.5a,b (colored symbols) except for several frames where $Z \sim 2$ (grey symbols in Figure 3.5a,b). Especially in the early stages of the reaction, when the size of the fractal regime is very limited, deviations of the Z -parameter were observed. Moreover, due to the relatively short measurements it may be sensitive to thermal noise as well. Despite some deviations, the Z -values were clearly larger than zero. Thus, these systems were more monodisperse as implied by the exponential cutoff model.

The deviation in Z led to systematically overestimated values of R_G and I_0/V_A , see grey data points in Figure 3.5c-e. However, despite this deviation, these data points reveal the same trend in R_G and I_0/V_A . R_G increased most rapidly in the first 10s after mixing, before the first SAXS profiles were recorded. After the first 10s R_G grew slowly further by roughly 25% at both temperatures. By comparing data from the experiments with and without BTESE, it can be concluded that the presence of BTESE had a negligible effect on the initial size of nucleated particles. However, subsequent growth of niobia clusters was clearly suppressed by the presence of BTESE. The growth exponent p was substantially smaller, which led to unrealistic values of λ (Table 3.1) when it is assumed that agglomeration can be described by irreversible Smoluchowski type rate equations. Instead, the

reduced growth exponents p were more consistent with reversible Lifshitz-Slyozov type agglomeration kernels [48, 54-56]. Most likely, the nucleated niobia particles/clusters were surrounded by BTESE derived moieties, which affected their agglomeration behaviour.

In analogy with the experiments without BTESE, nucleation occurred predominantly within the first 2 min as indicated by the ratio I_0/V_A (Figure 3.5d,e). However, the values of I_0/V_A were substantially larger, which therefore included the nucleation from both NPE and BTESE precursors. Within a short nucleation period Z levelled off (Figure 3.5a,b) even more quickly than I_0/V_A . The subsequent growth process did not affect polydispersity. Compared to the experiments without BTESE both Z and D_f levelled off at lower values, which effectively resulted in a similar value for $C \cdot C_p$.

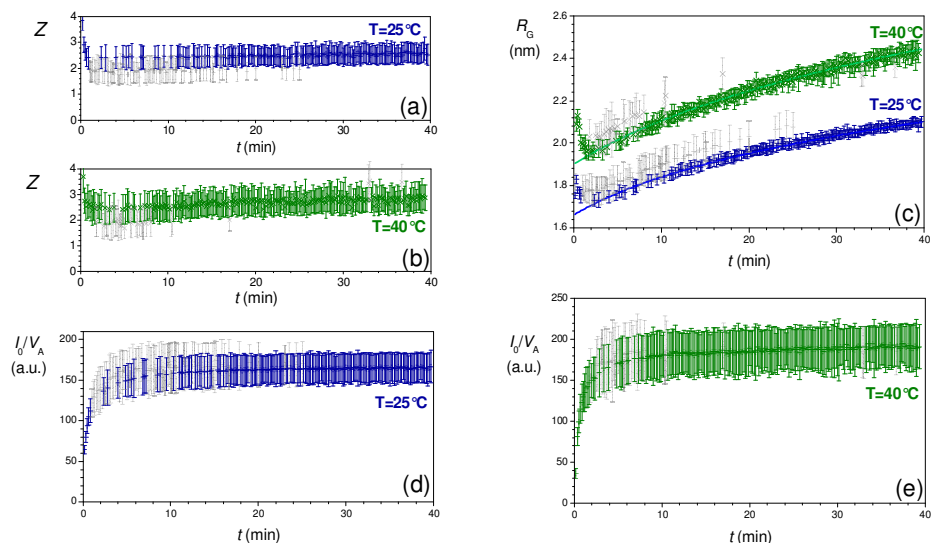


Figure 3.5. Optimized parameters derived from fitting the Schultz cutoff function for mixing experiments with BTESE. a) Z of SiNbT25, b) Z of SiNbT40, c) R_G of SiNbT25 and SiNbT40, d) I_0/V_A of SiNbT25 and e) I_0/V_A of SiNbT40.

3.6. Conclusions

After a short nucleation period of ~ 2 min, growth of NPE-derived clusters occurred through diffusion limited cluster aggregation following irreversible Smoluchowski type agglomeration kernels. The DLCA type mechanism led to relatively sharp cutoff functions that were much better described by the Schultz cutoff model than by the exponential cutoff model. The derived $C \cdot C_p$ values levelled off at 1.0 ± 0.1 , being consistent with DLCA type self-preserving agglomeration kernels.

In the sols with BTESE, the speed of nucleation was scarcely affected by the presence of BTESE. Nevertheless, further growth of the sols was clearly affected, as expressed by a reduced value of both the fractal dimension D_f and growth exponent p after a certain time of reaction. The reduced growth exponent could not be described by irreversible Smoluchowski type kernels and was more consistent with reversible Lifshitz-Slyozov type agglomeration kernels. The growth of the niobia clusters was clearly suppressed by the presence of BTESE.

3.7. References

1. Oliver, M.S., et al., *Molecular Origins of the Mechanical Behavior of Hybrid Glasses*. Adv. Funct. Mater., 2010. **20**(17): p. 2884-2892.
2. Castricum, H.L., et al., *Hydrothermally stable molecular separation membranes from organically linked silica*. J. Mater. Chem., 2008. **18**(18): p. 2150-2158.
3. Castricum, H.L., et al., *High-performance hybrid pervaporation membranes with superior hydrothermal and acid stability*. J. Membr. Sci., 2008. **324**(1-2): p. 111-118.
4. Kanezashi, M., et al., *Organic-inorganic hybrid silica membranes with controlled silica network size: Preparation and gas permeation characteristics*. J. Membr. Sci., 2010. **348**(1-2): p. 310-318.
5. Agirre, I., et al., *Hybrid organosilica membranes and processes: Status and outlook*. Sep. Purif. Technol., 2014. **121**: p. 2-12.
6. Agirre, I., et al., *Acetalization reaction of ethanol with butyraldehyde coupled with pervaporation. Semi-batch*

- pervaporation studies and resistance of HybSi[®] membranes to catalyst impacts.* J. Membr. Sci., 2011. **371**(1): p. 179-188.
7. Kreiter, R., et al., *Evaluation of hybrid silica sols for stable microporous membranes using high-throughput screening.* J. Sol-Gel Sci. Technol., 2010: p. 1-8.
 8. Igi, R., et al., *Characterization of co-doped silica for improved hydrothermal stability and application to hydrogen separation membranes at high temperatures.* J. Am. Ceram. Soc., 2008. **91**(9): p. 2975-2981.
 9. Kanezashi, M. and M. Asaeda, *Hydrogen permeation characteristics and stability of Ni-doped silica membranes in steam at high temperature.* J. Membr. Sci., 2006. **271**(1-2): p. 86-93.
 10. Qi, H., et al., *Effect of Nb content on hydrothermal stability of a novel ethylene-bridged silsesquioxane molecular sieving membrane for H₂/CO₂ separation.* J. Membr. Sci., 2012. **421–422**(0): p. 190-200.
 11. Qi, H., et al., *Hybrid Organic–Inorganic Microporous Membranes with High Hydrothermal Stability for the Separation of Carbon Dioxide.* ChemSusChem, 2010. **3**(12): p. 1375-1378.
 12. Boffa, V., et al., *Microporous niobia-silica membrane with very low CO₂ permeability.* ChemSusChem, 2008. **1**(5): p. 437-443.
 13. Boffa, V., et al., *Microporous niobia-silica membranes: Influence of sol composition and structure on gas transport properties.* Micropor. Mesopor. Mat., 2009. **118**(1-3): p. 202-209.
 14. Yoshida, K., et al., *Hydrothermal stability and performance of silica-zirconia membranes for hydrogen separation in hydrothermal conditions.* J. Chem. Eng. Jpn, 2001. **34**(4): p. 523-530.
 15. Livage, J., M. Henry, and C. Sanchez, *Sol-gel chemistry of transition metal oxides.* Prog. Solid State Ch., 1988. **18**(4): p. 259-341.
 16. Kessler, V.G., et al., *New insight in the role of modifying ligands in the sol-gel processing of metal alkoxide precursors: A possibility to approach new classes of materials.* J. Sol-Gel Sci. Technol., 2006. **40**(2-3): p. 163-179.
 17. Brinker, C.J.S., G. W. , *Sol Gel Science, The Physics and Chemistry of Sol-Gel Processing.* Vol. 1. 1990, San Diego: Acedemic Press. 1-881.
 18. Sanchez, J. and A. McCormick, *Kinetic and thermodynamic study of the hydrolysis of silicon alkoxides in acidic alcohol solutions.* The J. Phys. Chem., 1992. **96**(22): p. 8973-8979.

19. Rankin, S.E. and A.V. McCormick, *Hydrolysis pseudoequilibrium: challenges and opportunities to sol–gel silicate kinetics*. Chem. Eng. Sci., 2000. **55**(11): p. 1955-1967.
20. Assink, R.A. and B.D. Kay, *The chemical kinetics of silicate sol–gels: Functional group kinetics of tetraethoxysilane*. Colloids and Surfaces A: Physicochemical and Engineering Aspects, 1993. **74**(1): p. 1-5.
21. Pouxviel, J., et al., *NMR study of the sol/gel polymerization*. J. Non-Cryst. Solids, 1987. **89**(3): p. 345-360.
22. Bonhomme, C., et al., *Advanced Solid State NMR Techniques for the Characterization of Sol–Gel-Derived Materials*. Acc. Chem. Res., 2007. **40**(9): p. 738-746.
23. Harris, M.T., et al., *FTIR spectroscopy, SAXS and electrical conductivity studies of the hydrolysis and condensation of zirconium and titanium alkoxides*. J. Sol-Gel Sci. Technol., 1997. **8**(1-3): p. 41-47.
24. Simonsen, M.E. and E.G. Søgaaard, *Sol–gel reactions of titanium alkoxides and water: influence of pH and alkoxy group on cluster formation and properties of the resulting products*. J. Sol-Gel Sci. Technol., 2010. **53**(3): p. 485-497.
25. Broussous, L., et al., *SAXS Study of Formation and Growth of Tin Oxide Nanoparticles in the Presence of Complexing Ligands*. J Phys. Chem. B, 2002. **106**(11): p. 2855-2860.
26. Hu, M.-C., et al., *Probing the early-stage/rapid processes in hydrolysis and condensation of metal alkoxides*. Journal of materials science, 2000. **35**(8): p. 1957-1971.
27. Wilkinson, A.P., et al., *In situ x-ray diffraction study of crystallization kinetics in $PbZr_{1-x}Ti_xO_3$ (PZT, $x= 0.0, 0.55, 1.0$)*. Chem. Mater., 1994. **6**(6): p. 750-754.
28. Fan, J., S.W. Boettcher, and G.D. Stucky, *Nanoparticle assembly of ordered multicomponent mesostructured metal oxides via a versatile sol-gel process*. Chem. Mater., 2006. **18**(26): p. 6391-6396.
29. Percy, M., et al., *The influence of β -diketones on the induction times for hydrolysis of zirconium (IV) alkoxides*. J. Mater. Chem. 1999. **9**(2): p. 499-505.
30. Sedlar, M. and M. Sayer, *Reactivity of titanium isopropoxide, zirconium propoxide and niobium ethoxide in the system of 2-methoxyethanol, 2,4-pentanedione and water*. J. Sol-Gel Sci. Technol., 1995. **5**(1): p. 27-40.
31. Ranjit, K.T. and K.J. Klabunde, *Solvent effects in the hydrolysis of magnesium methoxide, and the production of nanocrystalline*

- magnesium hydroxide. An aid in understanding the formation of porous inorganic materials.* Chem. Mater., 2005. **17**(1): p. 65-73.
32. Tanabe, K., *Application of niobium oxides as catalysts.* Catal. Today, 1990. **8**(1): p. 1-11.
33. Francisco, M.S.P., R. Landers, and Y. Gushikem, *Local order structure and surface acidity properties of a Nb₂O₅/SiO₂ mixed oxide prepared by the sol-gel processing method.* J. Solid State Ch., 2004. **177**(7): p. 2432-2439.
34. Yoshida, H., et al., *Control of the structure of niobium oxide species on silica by the equilibrium adsorption method.* Catal. Today, 1996. **28**(1): p. 79-89.
35. Bras, W., et al., *Recent experiments on a combined small-angle/wide-angle X-ray scattering beam line at the ESRF.* J. Appl. Crystallogr., 2003. **36**(3 I): p. 791-794.
36. Bras, W., et al., *Field-induced alignment of a smectic-a phase: A time-resolved x-ray investigation.* J. Chem. Phys., 2004. **121**(9): p. 4397-4413.
37. Besselink, R., et al., *Evolution of microstructure in mixed niobia-hybrid silica thin films from sol-gel precursors.* J. Colloid Interf. Sci., 2013. **404**(0): p. 24-35.
38. Sorensen, C.M. and G.M. Wang, *Size distribution effect on the power law regime of the structure factor of fractal aggregates.* Phys. Rev. E, 1999. **60**(6 B): p. 7143-7148.
39. Teixeira, J., *Small-angle scattering by fractal systems.* J. Appl. Crystallogr., 1988. **21**(6): p. 781-785.
40. Chen, S.H. and J. Teixeira, *Structure and fractal dimension of protein-detergent complexes.* Phys. Rev. Lett., 1986. **57**(20): p. 2583-2586.
41. Feigin, L.A. and D.U. Svergun, *Structure analysis by small angle X-ray and neutron scattering* 1987, New York: Plenum Press. 334.
42. Porod, G., *Small Angle X-ray Scattering.* Vol. 15. 1982, New York: Acedamic Press. 515.
43. Kotlarchyk, M. and S.H. Chen, *Analysis of small angle neutron scattering spectra from polydisperse interacting colloids.* J. Chem. Phys., 1983. **79**: p. 2461.
44. Stawski, T.M., et al., *Erratum: Nanoscale structure evolution in alkoxide-carboxylate sol-gel precursor solutions of barium titanate (J. Phys. Chem. C (2010) 115 (20449-20459) DOI: 10.1021/jp206572q).* J. Phys. Chem. C, 2011. **115**(48): p. 24028.

45. Stawski, T.M., et al., *Nanoscale structure evolution in alkoxide-carboxylate sol-gel precursor solutions of barium titanate*. J. Phys. Chem. C, 2011. **115**(42): p. 20449-20459.
46. Pontoni, D., T. Narayanan, and A.R. Rennie, *Nucleation and growth kinetics of colloidal silica*, 2004. p. 227-230.
47. Oh, C. and C.M. Sorensen, *Light scattering study of fractal cluster aggregation near the free molecular regime*. J. Aerosol Sci., 1997. **28**(6): p. 937-957.
48. Pontoni, D., T. Narayanan, and A. Rennie, *Time-resolved SAXS study of nucleation and growth of silica colloids*. Langmuir, 2002. **18**(1): p. 56-59.
49. Pierce, F., C. Sorensen, and A. Chakrabarti, *Computer simulation of diffusion-limited cluster-cluster aggregation with an Epstein drag force*. Physical Review E, 2006. **74**(2): p. 021411.
50. Ball, R., et al., *Universal kinetics in reaction-limited aggregation*. Phys. Rev. Lett., 1987. **58**(3): p. 274.
51. Wu, M.K. and S.K. Friedlander, *Enhanced power law agglomerate growth in the free molecule regime*. J. Aerosol Sci., 1993. **24**(3): p. 273-282.
52. Van Dongen, P. and M. Ernst, *Dynamic scaling in the kinetics of clustering*. Phys. Rev. Lett., 1985. **54**(13): p. 1396.
53. Dekkers, P.J. and S.K. Friedlander, *The self-preserving size distribution theory: I. Effects of the Knudsen number on aerosol agglomerate growth*. J. Colloid Interf. Sci., 2002. **248**(2): p. 295-305.
54. Lifshitz, I.M. and V.V. Slyozov, *The kinetics of precipitation from supersaturated solid solutions*. J. Phys. Chem. Solids, 1961. **19**(1): p. 35-50.
55. Conti, M., A. Lipshtat, and B. Meerson, *Scaling anomalies in the coarsening dynamics of fractal viscous fingering patterns*. Phys. Rev. E, 2004. **69**(3): p. 031406.
56. Sharon, E., et al., *Coarsening of Fractal Viscous Fingering Patterns*. Phys. Rev. Lett., 2003. **91**(20): p. 205504.

4.

Evolution of microstructure in mixed niobia-hybrid silica thin films from sol-gel precursors

4.1. Abstract

The evolution of structure in sol-gel derived mixed bridged silsesquioxane-niobium alkoxide sols and drying thin films was monitored in-situ by small angle X-ray scattering. Since sol-gel condensation of metal alkoxides proceeds much faster than that of silicon alkoxides, the incorporation of *d*-block metal dopants into silica typically leads to formation of densely packed nano-sized metal oxide clusters that we refer as metal oxide building blocks in a silica-based matrix. SAXS was used to study the process of niobia building block formation while drying the sol as a thin film at 40-80°C. The SAXS curves of mixed niobia-hybrid silica sols were dominated by the electron density contrast between sol particles and surrounding solvent. As the solvent evaporated and the sol particles approached each other, a correlation peak emerged. Since TEM microscopy revealed the absence of mesopores, the correlation peak was caused by a heterogeneous system of electron-rich regions and electron poor regions. The regions were assigned to the presence of small clusters that are rich in niobium which are dispersed in a matrix that mainly consisted of hybrid silica. The correlation peak corresponded with correlation distances in the range between 1 and 3 nm that was associated with the typical distances between the electron dense clusters. A relationship between the pre-hydrolysis time of the silica precursor and the size of the niobia building blocks was observed. When 1,2-bis(triethoxysilyl)ethane was first hydrolyzed for 30 min before adding niobium pentaethoxide, the niobia building blocks reached a radius of 0.4 nm. Simultaneous hydrolysis of the two precursors resulted in somewhat larger average building block radii of 0.5 to 0.6 nm. This study shows that acid catalyzed sol-gel polymerization of mixed hybrid silica niobium alkoxides can be rationalized and optimized by monitoring the structural evolution using time-resolved SAXS.

4.2. Introduction

Molecular separation with membranes is an attractive alternative for distillation since it can lead to substantial energy savings in the dehydration of biomass fuels [1] and organic solvents [2-3]. Hybrid organosilica membranes are very suitable for such tasks, since these materials combine

the advantages of both organic and inorganic membranes, i.e.: the high fracture resistance and hydrothermal stability of organic membranes and the high flux and thermal stability of inorganic membranes [4-5]. Exposure of silica to moisture at 70°C already leads to hydrolysis of Si-O-Si bonds. The presence of organic bridges in the network made the network less susceptible for hydrolysis. However, further improvement is desirable for industrial application.

A possible approach to improve the hydrothermal and chemical stability of siloxanes and silsesquioxanes is by doping transition metals into the silicon oxide network, such as titanium [6], zirconium [7-8] niobium [9], nickel [10] or cobalt [11]. However, sol-gel synthesis of transition metal-doped siloxanes usually leads to the formation of dense nanosized transition metal oxide building blocks embedded inside an amorphous silica matrix [12], as it was observed by transmission electron microscopy (TEM) or small angle X-ray scattering (SAXS) [13-14]. Transition metal centers easily form cationic complexes that are surrounded by a large number of ligands (coordination number 6-8), in contrast to silicon which commonly forms neutral tetragonal complexes [15]. Moreover, the metal alkoxide bonds are more labile and susceptible towards hydrolysis and condensation compared to the more covalently bonded tetragonal silicon alkoxide bonds [16]. Several strategies have been applied to improve the homogeneity of mixed transition metal/silicon oxide materials, but the intermixing on atomic scale, which is crucial for sufficient membrane permeability, is still a challenge.

Our interest is particularly focused on the atomic mixing of niobium in a hybrid silica matrix. ^{17}O MAS NMR experiments revealed that acid-catalyzed sol-gel synthesis leads to a high degree of atomic mixing at low niobium concentrations, i.e. Nb/Si = 14/86 and 6/94 [17]. Even if amorphous niobia building blocks were formed, their crystallization would only occur at temperatures above 400°C [18], which is higher than the annealing temperature of 300°C of hybrid organosilica membranes [19]. No limitations are thus expected with regard to matrix integrity. Hydrated Nb_2O_5 forms strong Lewis and Bronsted acid sites upon annealing at 100°C at pH < 5.6 (indicator method) [20]. Substitution in a silica matrix was found to enhance the Lewis acidity of the Nb centers as compared to that in Nb_2O_5 [21]. Contrary to vanadium (V) oxides, which are frequently used as acid catalysts, niobium oxides are more difficult to reduce and chemically more stable [22]. It is therefore a promising catalyst for application at

moderate temperatures, in e.g.: preferential CO oxidation in hydrogen-rich environments [23], esterification [24-25], dehydrogenation [26], aldol condensation [27] and conversion of the biomass derivative γ -valerolacetone into pentanoic acid [28]. The presence of acid sites was found to enhance chemisorption of CO₂ on mixed SiO₂-Nb₂O₅ and hybrid silica Nb₂O₅ microporous membranes and therefore strongly reduced the CO₂ permeability in comparison with nonpolar gases like H₂, CH₄ and SF₆ [29-30].

The final microstructure is established after a sol has been coated and dried on a support. The details of the drying processes of sol-gel films are often not well understood. In situ small X-ray scattering has been found to be a valuable method for monitoring the reorganization of meso/microstructure in drying systems, for instance in the self-assembly of mesostructured sol-gel films [31] and the formation of different electron-dense/lean phases in barium titanate films from alkoxide-carboxylate systems [32]. We used time-resolved SAXS to investigate the reorganization of the microstructure and the formation of different electron dense/lean phases during the drying process of thin sol-gel films of niobium pentaethoxide and 1,2-bis(triethoxysilyl)ethane.

4.3. Experimental Section

4.3.1. Synthesis of mixed niobia/BTESE sols

All precursor solutions were prepared inside a glovebox under nitrogen atmosphere. The reflux synthesis was performed under atmospheric conditions. A 0.45 mol/L 1,2-bis-triethoxysilyl-ethane (BTESE) sol was prepared by adding dropwise an acidic ethanol solution [33] to a 0.9 mol/L solution of BTESE (ABCR chemicals, 97%) in dry ethanol with a hydrolysis ratio $[H_2O]/[(Si)-OEt] = 1$ and an acid ratio $[HNO_3]/[(Si)-OEt] = 1/30$. In a separate bottle niobium pentaethoxide (NPE, ABCR chemicals, 99.99%) was diluted in ethanol yielding a molar concentration $[NPE] = 0.54$ mol/L. The BTESE sols were all refluxed at $T=60^\circ C$ for 60 min. The NPE solution was added after either 0, 30 or 60 minutes of refluxing, and these samples are designated as p00, p30 and p60, respectively. Hence, the NPE solution was refluxed at $T=60^\circ C$ for 60, 30 or 0 min, respectively. The molar ratio

[Nb]/[Si] was kept constant at 1/4 in this series and the overall initial ethoxide concentration was kept constant at [OEt] = 2.7 mol/L. The samples were dried as thin films using a drying setup with a rotating aluminum rotor-heat that was covered with Kapton foil as described in more detail elsewhere [32]. All samples were heated using a 150 W infrared lamp. Samples p00 and p60 were dried at $T = 60^\circ\text{C}$ and samples p30 were dried at $T = 40, 60$ or 80°C , respectively.

4.3.2. SAXS Experiments

The colloidal samples were placed in capillary glass tubes (Hilgenberg, Germany) of 80 mm length, 1.5 mm diameter and $\sim 10\ \mu\text{m}$ wall thickness. Small-angle X-ray scattering was carried out using synchrotron radiation on the Dutch-Belgian beamline, DUBBLE BM-26B of the ESRF in Grenoble [34]. The X-ray beam with an energy of 16 keV was focused on a corner of the 2D Pilatus 1M CCD-detector to maximize the covered range of scattering angles. A beam stop was applied to shield the detector from the direct beam and avoid saturation of the outgoing signal. The detector was placed at a distance of 1.5 m from the sample, which allowed us to obtain data in the range $0.20 < q < 9.00\ \text{nm}^{-1}$. All scattering data were found to be independent of the scattering angle in the plane of the detector. As this indicates that the samples were isotropically dispersed, the measured intensities from all channels with the same q value were averaged. Silver behenate was used as calibration standard for the determination of the absolute scale of the scattering vector q in our experiments [35].

The scattering intensity of the capillary containing a given colloidal sample was collected as a function of the scattering vector q . All curves were normalized by dividing the scattering intensity by both the time of data acquisition and the total intensity of the scattered signal. A background subtraction procedure was carried out. For sols, the scattering signal of a capillary filled with ethanol was subtracted, while for the drying sols only the scattering signal of the clean kapton foil was subtracted. The static SAXS data of sols were obtained in 5 min data collection periods and the in situ-measurements in 1 min periods.

4.3.3. TEM measurements

From sample p60, 30 μ L sol was spin-cast (Laurell WS- 400B-6NPP-Lite spincoater) onto holey carbon TEM copper grids (CF200-Cu, Electron Microscopy Sciences) at 4000 rpm for 40 s. Then the as-prepared films were dried at 60°C for 24 hours in a furnace and used for transmission electron microscopy characterization (Philips CM300STFEG at 300 kV). Samples were investigated at low magnification to find typical areas and features of interest were examined at high magnification (GATAN 2048 2048 Ultrascan1000 CCD camera). The microscope software packages GATAN Microscopy Suite 1.8.

4.4. Derivation of the Scattering intensity function.

Positive interference of scattered waves originates either from electrons within the same particle (intraparticle interference) or from electrons located in different particles (interparticle correlations). The scattering intensity can therefore be divided into a form factor, $P(q)$ and a structure factor $S(q)$, scaled with the number density of particles, N , and the contrast in electron density between particles and their surrounding medium, $\Delta\rho$ (Equation (4.1)):

$$I(q) = N \cdot (\Delta\rho)^2 \cdot S(q) \cdot P(q) \quad (4.1)$$

In the model that is described below to model the scattering of X-rays by drying sol-gel films, the sol particles are described in terms of self-assembled small primary building blocks. A building block contains a small number of niobium and/or hybrid silicon monomers and is considered as the smallest cluster of atoms that can be discriminated from the surrounding solvent in a SAXS-pattern by a difference in electron density. For the sake of simplicity, we assume that these building blocks (primary scatterers) are spherical with radius r_0 . This assumption was in agreement with the majority of scattering curves that indicated a $I \sim q^{-4}$ dependence in the high q -region. Only the initial stages of the drying process revealed a deviating behavior. These building blocks can be described by a spherical form factor $P(q)$, (4.2 [36-38]).

$$P(q, r_0) = \left[3 \cdot \frac{\sin(q \cdot r_0) - q \cdot r_0 \cdot \cos(q \cdot r_0)}{q^3 \cdot r_0^3} \right]^2 \quad (4.2)$$

These building blocks may assemble into two different spatial arrangements. Firstly, they can assemble into a branched polymer-like arrangement with scattering behavior as described in section 3.1. Secondly, a condensed phase can form that gives rise to a correlation peak in the X-ray scattering curve. In the latter case the scattering intensity can be interpreted as a liquid-like packing of building blocks as described in section 3.2. During the sol condensation and film drying process both phases may coexist. For simplicity, we assume that the two types of structures are constructed of the same type of primary scatterer, such that the total scattering intensity can be described as a linear combination of the contributions of both phases to the total scattering intensity (section 3.3).

4.4.1. Mass-fractal-like sol particles

Small spherical building blocks may arrange themselves randomly forming larger sol particles with a branched polymeric structure. Such assemblies of building blocks are well understood in terms of mass-fractal models [15, 39-40]. Various acid-catalyzed silica sols, including Nb-doped silica, have been modelled successfully in terms of mass fractals [41]. When monodisperse spherical building blocks of radius r_0 are packed together with a packing density that can be characterized by the so-called fractal dimension D , then the number of building blocks n within an imaginary sphere of effective radius r is described by [39-40]:

$$n = \left(\frac{r}{r_0} \right)^D \quad (4.3)$$

The structure function S_{MF} (Equation (4.4)) of mass-fractal agglomerates was derived by Teixeira [39]. The agglomerates were giving a finite size by

introducing an exponentially decaying element in the autocorrelation function ($\exp(-r/\xi)/r$), where the agglomerate size was characterized by the cut-off length ξ . This approach was based on the assumption the sol particle radius was distributed exponentially. Although DLCA-based systems generally have narrower size distributions [42-43], Equation (4.4) was in a good agreement with our experimental data. In addition, the expression is convenient from a practical point of view, since the Fourier transform was solved analytically.

$$S_{MF}(q, D, \xi, r_0) = 1 + \frac{D \cdot \Gamma(D-1) \cdot \sin[(D-1) \cdot \arctan(q \cdot \xi)]}{(q \cdot r_0)^D \cdot \left(1 + \frac{1}{(q \cdot \xi)^2}\right)^{\left(\frac{D-1}{2}\right)}} \quad (4.4)$$

Here Γ represents the gamma function. The radii of primary building blocks, r_0 are considered to be monodisperse. The radius of gyration of the agglomerates can be calculated from D and ξ via (4.5) [43]:

$$R_g = \xi \cdot \sqrt{\frac{D \cdot (D+1)}{2}} \quad (4.5)$$

4.4.2. Packing of hard spheres

While drying a sol, dispersed small sol particles eventually become supersaturated and assemble into larger randomly closed packed agglomerates that subsequently condense. In all mixed oxide sols these segregated assemblies gave a broad correlation peak in the corresponding scattering curves. The correlation peak indicates the presence of a modulated pattern of alternating electron rich and electron lean regions. The maximum of the correlation peak was associated with the a typical

quasi-periodic distances between alternating electron dense regions that are separated by electron lean regions as this had been reported for phase separated systems such as ionomers [44], nanocomposites [12-13,45] and microemulsions [46]. The absence of higher order correlation peaks is due to the absence of long range order in the alternating regions. When the building blocks are considered as hard monodisperse spheres in randomly oriented liquid-like packing, the corresponding interference function is as described by Fournet [36]. They applied the equation of state from Born and Green for hard spheres ((4.6), in which ϵ is a constant close to unity [36], $C(q, \phi, R_s)$ the direct correlation function between spherical particles, and R_s is the separation radius of particles. The typical distance between particles equals $L_s = 2R_s$. See Figure 4.1.

$$S_c(q, \phi, R_s) = \frac{1}{1 + 8 \cdot \phi \cdot \epsilon \cdot C(q, \phi, R_s)} \quad (4.6)$$

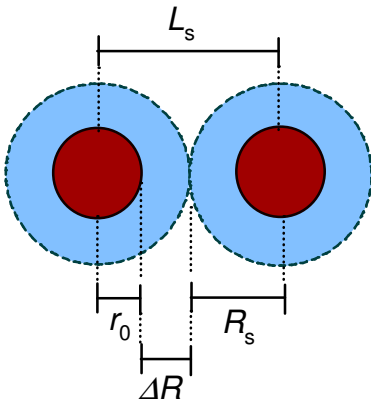


Figure 4.1. Definitions of length scales in the hard sphere model.

The parameter ϕ represents the local volume fraction of particles in the surroundings of a specific particle. It is defined as the ratio between the overall particle volume divided by the total available volume. It has a maximum value of 0.74 for close-packed hexagonal and cubic lattices. For

multiple particle interactions the direct correlation function can be described by a Percus-Yevick approximation giving [44-45]:

$$\begin{aligned}
 C(q, \phi, L_S) = & 3 \cdot \lambda_1 \cdot \frac{\sin(A) - A \cdot \cos(A)}{A^3} \\
 & + 3 \cdot \lambda_2 \cdot \frac{2 \cdot A \cdot \sin(A) + (2 - A^2) \cdot \cos(A) - 2}{A^4} \\
 & + \frac{3}{2} \cdot \phi \cdot \lambda_1 \cdot \frac{-A^4 \cdot \cos(A) + 4(3A^2 - 6)\cos(A) + 4(A^3 - 6A) \cdot \sin(A) + 24}{A^6}
 \end{aligned}$$

where

(4.7)

$$A = q \cdot L_S \quad L_S = 2 \cdot R_S \quad \lambda_1 = \frac{(1 + 2 \cdot \phi)^2}{(1 - \phi)^4} \quad \lambda_2 = \frac{-6\phi \cdot \left(1 + \frac{\phi}{2}\right)^2}{(1 - \phi)^4}$$

This model was used successfully by us to model the evolution of certain species upon gelation and upon drying of sol-gel precursors of BaTiO₃ [25,47]. Nevertheless, in the experiments discussed below, the correlation peaks were broader, indicating that we need to consider a substantial variation in separation distances. Polydispersity can be introduced into this model by applying the local monodisperse approximation [48] which assumes that particles correlate only with particles of similar size. This approach reduces amount of calculation strongly, yet it still provides a reliable relationship between peak broadening and polydispersity [48]. The scattering intensity of a polydisperse correlated system, $I(q, \phi, \mu_{r_0}, \sigma_{r_0})$ can thus be described by the following integral:

$$I_{PC}(q, \phi, \mu_{r_0}, \sigma_{r_0}) = N \cdot \Delta\rho^2 \int P(q, r_0) \cdot S_C(q, \phi, R_S(r_0)) \cdot D_P(r_0) dr_0 \quad (4.8)$$

Herein $P(q, r_0)$ is the form factor (Equation (4.2)), $S(q, \phi, R_S(r_0))$ the structure function (Equation (4.6)) where the outer radius $R_S(r_0)$ is described as a

function of radius r_0 of the inner electron dense region. $N(r_0)$ is described as the number weighted particle size distribution. However, the probability of finding correlations scales with the square of the number of electrons within the correlation sphere. Thus, when introducing either a number weighted distribution function or a volume weighted distribution, $m^2(r_0)$ or $m(r_0)$, respectively, needs to be introduced in the integral equation, where m represents the mass of electrons within the particle radius r_0 [37]. With a uniform particle density and the particles being spherical, $m \sim r^3$ holds. When introducing the weighting parameter and normalizing the intensity function for introducing the weighting factor [37] the scattering intensity of polydisperse randomly packed spheres can be described by:

$$I_{\text{PC}}(q, \phi, \mu_{r_0}, \sigma_{r_0}) = \frac{N \cdot \Delta \rho^2 \int P(q, r_0) \cdot S_C(q, \phi, R_S(r_0)) \cdot D_p(r_0) \cdot r_0^p dr_0}{\int D_p(r_0) \cdot r_0^p dr_0} \quad (4.9)$$

The parameter p is equal to 6 or 3 for number and volume weighted distributions, respectively. In the case that $p = 0$, (4.9 is reduced to (4.8 and the distribution can be considered as an intensity weighted distribution. Pedersen considered the outer radius that is separating the particles described by either $R_S = C \cdot r_0$ or $R_S = \Delta R + r_0$, where C and r_0 are considered as non-distributed constants [48]. It was assumed that the variation in R_S was typically much larger than the variation in r_0 . When we assume that r_0 is monodisperse, while R_S is polydisperse, the form factor can be removed from the integral. Then, the structure factor of correlated spheres with an intensity weighted polydisperse outer shell separation distance, ($L_S = 2R_S$) can be described by:

$$S_{\text{PC}}(q, \phi, \mu_{L_S}, \sigma_{L_S}) = \int w(L_S, \mu_{L_S}, \sigma_{L_S}) \cdot S_C(q, \phi, L_S) \cdot dL_S \quad (4.10)$$

Here $w(L_S, \mu_{L_S}, \sigma_{L_S})$ is a particle size distribution of average μ_{L_S} , with particle separation L_S and standard deviation σ_{L_S} . The parameter p determines the weighting of distribution. We applied a Zimm-Schultz-Flory distribution [49]

which gave reliable distributions to describe sol-gel derived silica particles in an earlier study [50].

$$w(L_S, \mu_{L_S}, z) = \frac{L_S^z}{\Gamma(z+1)} \cdot \left(\frac{z+1}{\mu_{L_S}} \right)^{z+1} \cdot \exp\left(-\left(\frac{z+1}{\mu_{L_S}}\right) \cdot L_S\right) \quad (4.11)$$

The z -parameter determines the broadness of the distribution and the corresponding standard deviation is given by:

$$\sigma_{L_S} = \frac{\mu_{L_S}}{\sqrt{z+1}} \quad (4.12)$$

4.4.3. Heterogeneous mixture of mass-fractal-like sol particles and solid phase with internal correlations

When the system consists of a heterogeneous mixture of polymeric agglomerates with mass-fractal-like scattering behavior, and solid randomly packed agglomerates that are constructed from the same primary scatterers, the intensity function can be written as a linear combination of the mass-fractal function (Equation (4.4)) and the structure function for packing of polydisperse spheres (Equation (4.6) and (4.10)). This approach was introduced to model the nanoscale structure evolution in drying barium titanium alkoxide carboxylate sol-gel films [32, 47]. Cross interference between both phases was neglected since it is probably a heterogeneous process consisting of a condensed phase and a dispersed phase that do not interact with each other. Together with the form function (Equation (4.2)), the scattering intensity of such mixtures can be described by:

$$I_{\text{mix}}(q) = I_0 \cdot (\eta \cdot S_{\text{PC}}(q, \phi, \mu_{L_S}, \sigma_{L_S}) + (1-\eta) \cdot S_{\text{MF}}(q, D, \xi, r_0)) \cdot P(q, r_0) \quad (4.13)$$

Here I_0 is a scaling constant related to the scattering intensity at $q \rightarrow 0$, and η is a dimensionless parameter with a value between 0 and 1 that describes to what extent the SAXS curve can be described in terms of correlated agglomerates. This parameter is hereafter referred to as the conversion coefficient. It is the ratio of the number of segregated secondary phase particles to the total number of scattering particles.

Since the model is relatively complex we have also determined model independent parameters that will support the observed trends in the previously described model, namely the invariant Q_{inv} (Equation (4.14)) [15,37-38], the integral correlation length L_C (Equation (4.15)), [37-38,51] and the correlation or Porod volume V_C (Equation (4.16)) [37-38]. The invariant is a measure of the overall extent of electron density fluctuations in the sample, and L_C and V_C are average integral length and integral volume of the electron lean and electron dense domains within the measured region, respectively.

$$Q_{inv} \equiv (\Delta n_e)^2 = \int_0^{\infty} I(q) \cdot q^2 dq \quad (4.14)$$

$$L_C \equiv \frac{\langle L_i^2 \rangle}{\langle L_i \rangle} = \frac{\pi \cdot \int_0^{\infty} I(q) \cdot q \cdot dq}{Q_{inv}} \quad (4.15)$$

$$V_C \equiv \frac{\langle V_i^2 \rangle}{\langle V_i \rangle} = \frac{2\pi^2 \cdot \lim_{q \rightarrow 0} (I(q))}{Q_{inv}} \quad (4.16)$$

4.5. Results and Discussion

4.5.1. Hydrolysis and condensation of mixed sol particles

The small hybrid silica sol particles from curve a in Figure 1 could be well described by a Guinier approximation [38, 52]. Niobium penta-ethoxide (NPE) is very prone towards hydrolysis and a solution with $[NPE] = 0.54$ mol/L, $[-OR]:[H_2O]:[HNO_3] = 1:1:(1/30)$ formed a gel within a few minutes. The corresponding scattering curve is curve b in Figure 4.2. The scattering curve of the larger mixed niobia-hybrid silica particles in curve c could be described better as branched polymeric particles using the mass-fractal equation (4.4). Here a solution of NPE in ethanol ($[NPE] = 0.54$ mol/L) was added to a solution of prehydrolysed BTESE sol with a scattering curve as shown by curve a, while keeping the overall alkoxide group concentration constant at $[-OR] = 2.7$ mol/L. It is noted that these sol particles should not be considered as "true" fractals, since self-similarity over length scales in these particles was limited. Nevertheless, it is the best theory available to describe the interparticle correlations in statistically branched polymeric assemblies, and has been applied successfully to describe other systems as well [29, 53]. The equation could be fitted very well to the experimental SAXS curves and is based on only four free parameters (I_0 , D , r_0 and ξ), where I_0 is a scaling constant that depends on the number of electron density fluctuations and the contrast in electron density. Since the self-similarity across length scales was limited, the mass-fractal region was small and not very distinctive and the accuracy of the D -parameter was limited. However, the fit enabled us to determine a reliable value for R_g (Equation (4.5)).

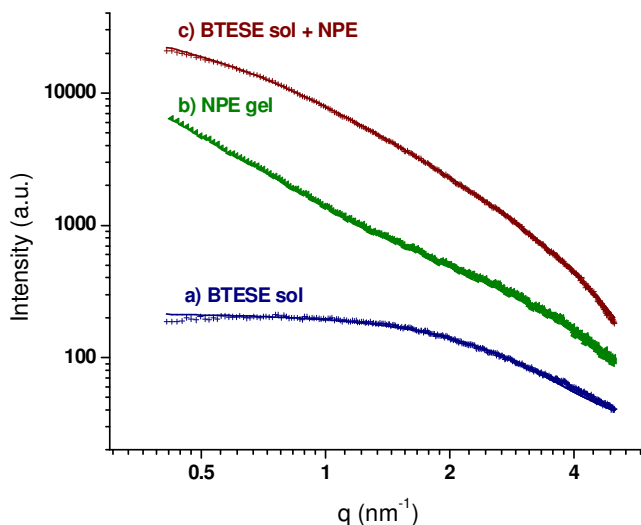


Figure 4.2. SAXS curves of sols. (a) BTESE sol after 1 h reflux at 60°C; (b) Niobium penta-ethoxide (NPE) gel; (c) The BTESE sol after 1 h reflux at 60°C with NPE-solution added after the 1 hour and then measured after 2 minutes. For the sake of clarity, graphs b and c were shifted upwards by multiplication and their original shape remained intact.

After 1 h at 60°C, the BTESE sol of curve “a” contained particles with an average radius of gyration $R_g = 0.49$ nm. In contrast to the NPE sol (curve b) instant gelation did not occur when a solution of NPE was added to the BTESE sol. The straight line at low q -values in the case of curve “b” indicated that R_g is too large to measure within this q -range and should be larger than 10 nm. When NPE was added to prehydrolyzed BTESE the resulting SAXS curve (curve “c”) revealed the presence of larger particles in the sol with a cut-off distance $\xi = 1.3$ nm and fractal dimension $D = 1.9$. The fitted values of r_0 became of the order of ~ 0.05 nm, which is physically impossible. This indicates that in this stage, the primary building blocks cannot be well described as spheres. Probably, these building blocks have a more polymeric and/or elongated shape. The ξ value corresponds to a radius of gyration $R_g = 2.1$ nm. The presence of BTESE in the sol seems to inhibit the growth of niobium oxide building blocks and prevent their aggregation. The sols with shorter prehydrolysis times were almost identical to sample p60.

4.5.2. The film drying process

The scattering intensity of a drying film of prehydrolyzed sol sample p60 as a function of drying time in air shown in Figure 4.3 represents a typical drying process. The SAXS curves are colored as a guide to the eye to distinguish the three basic stages of drying. In the initial stage of drying (blue curves) the shape of the SAXS patterns remained almost unchanged, except for the observed decrease of scattering intensity at high q . This decrease indicates that the smallest building blocks were disappearing. Since the region with constant slope in the $\log I$ - $\log q$ plot was small at $q > 1.5 \text{ nm}^{-1}$, the scattering curves are characteristic for small branched nano-sized sol particles that contain a small number of building blocks. At $q < 1.5 \text{ nm}^{-1}$ the curve flattened. This regime was well described by a Guinier approximation for spherical particles [42-43], which indicates that these dispersed sol particles had a limited size.

In the second stage of the drying process (green curves), ethanol that initially surrounded the sol particles had been replaced by other sol particles with similar electron densities due to solvent evaporation, resulting in diminishing $\Delta\rho$ between sol particles and their surrounding environment. The decrease of $\Delta\rho$ caused a strong decrease of scattering intensity, especially at low q -values. We visually observed the appearance of a separate solid phase in the drying sol within this same time frame. Since the liquid film was spread evenly over the continuously rotating rotor-head of the drying set-up, the scattering profile was an average of scattering contributions from the spatially separated sol phase and the newly forming condensed solid phase. At $t > 20 \text{ min}$ (red curves), most of the ethanol had evaporated and a clear correlation peak became visible in the SAXS pattern at $q \sim 4.0 \text{ nm}^{-1}$. This type of correlation peak suggests a repetitive separation distance of $2\pi/q = 1.5 \text{ nm}$ between certain electron contrasted domains that correlate with each other within the agglomerated powder [12-13].

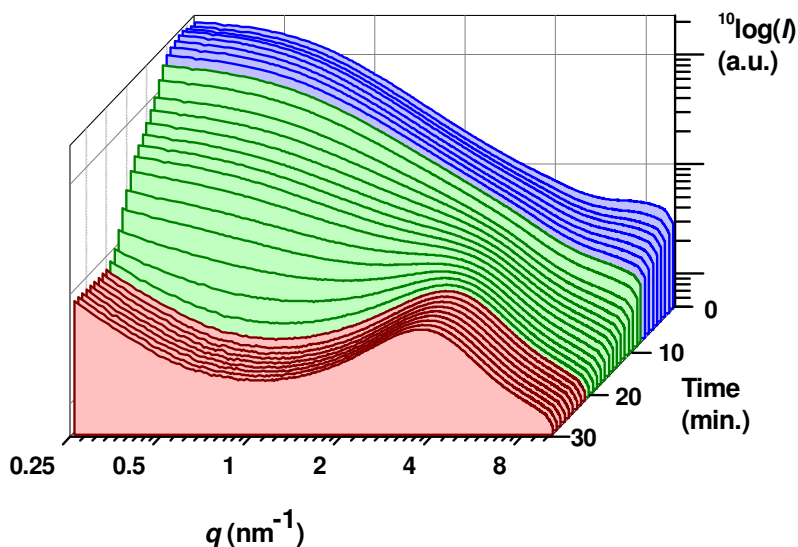


Figure 4.3. Evolution of SAXS curves during drying of thin film of sample p60 at 60°C. Colors are a guide to the eye and indicate the three stages of drying as discussed in the text.

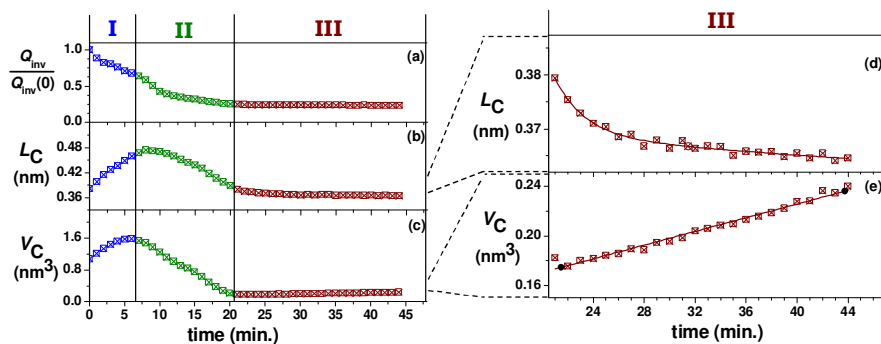


Figure 4.4. (a) The ratio of invariant Q_{inv} and initial invariant $Q_{inv,t=0}$; (b) integral correlation length L_C ; (c) correlation or Porod volume V_C of sample p60 as a function of drying time at $T = 60^\circ\text{C}$ and in a set with more detail: (d) integral correlation length; (e) correlation volume in the final stage of the drying process. Colors are a guide to the eye and indicate the three stages of drying as discussed in the text.

The model independent parameters, i.e. the invariant Q_{inv} (Equation (4.14)), the correlation length L_C (Equation (4.15)), and the correlation or Porod volume V_C (Equation (4.16)) were calculated (See Figure 4.4).

The regimes outside the measured q -range were approximated with a Guinier approximation $I \sim \exp(q^2 R_g^2 / 3)$ and Porod law $I \sim q^{-4}$ [36-38,54]. We had performed two measurements in a regime at $(3 < q < 32 \text{ nm}^{-1})$ [see Supplementary Information]. These measurements revealed correlation peaks that were associated with Nb-Nb distances [55]. Since, this regime was dominated by atomic correlations we cannot verify the validity of Porod's law in this regime, however we cannot expect that this regime contains substantial information of the size of these building blocks either at these length scales. Thus, in order to gain some insight concerning the evolution of heterogeneous matrix as a simplified assembly of electron dense and electron poor regions we could use Porod's law. Moreover, in the following discussion we used the invariant Q_{inv} , the correlation length L_C and Porod volume V_C as a measure of electron dense and electron lean regions. The interpretation of these parameters became more straightforward when we ignore the fact that these regions were actually build from atoms and when we assume that these regions themselves have a homogeneous electron density distribution. Therefore, we neglect the correlation peaks at $q > 9 \text{ nm}^{-1}$, since these correlations were associated with atomic correlations that overlap with the Porod regime of building blocks.

Q_{inv} decreased gradually and leveled off after 20 min, after which a dry film remained (Figure 4.4a). The trend reveals the reduction of $\Delta\rho$ as a result of physical loss of solvent as discussed above. The evolution of the integral correlation length L_C reveals three stages: An initial (induction) stage in which L_C increased slightly; a second (transition) stage during which L_C decreased with time, and a final stage in which it remained constant. The increase of L_C in the first stage coincides with a decrease in scattering intensity at high q as discussed above, while the bending point at low q remained unchanged. Thus, the primary building blocks from which the sol particles were assembled increased in size, while the sol particle size itself remained constant. The phenomenon can be understood in terms of Ostwald ripening, where the smallest entities with the highest curvatures

dissolve. However, it may also involve rearrangements of entities, such that the building blocks became more spherical. In either case the system will reduce its overall surface energy and the sharpest curvatures will disappear. As the smallest features in a system disappear, the value of L_c increases. The decrease in L_c during the second stage coincided with the strong decrease in scattering intensity at low q . Since the sol particles approach each other, the contrast between particles and solvent diminished. Hence the distance correlation that was associated with the outer radius of these particles diminished as well. What remained is a correlation length that is associated only with the size of the building blocks that form the network. In the final stage, in which the network was consolidated, L_c leveled off and remained constant. The correlation volume V_c followed a similar but more pronounced trend as L_c .

The dried film consisted of alternating electron-rich and electron-lean regions. It is most probable that L_c is a measure of the average size of these regions. The contrast in electron density can either be caused by a contrast between pores and matrix, or between niobium-rich and silicon-rich regions. The absence of mesopores was verified by both TEM and N_2 adsorption. The N_2 adsorption isotherm revealed only marginal N_2 adsorption. Thus, if the material contained any pores, these were smaller than the kinetic diameter of nitrogen [see supporting information]. The TEM measurements were performed on a spincoated layer on a holey carbon grid, see Figure 4.5. The dried film was optically uniform (Figure 4.5a), except for a few exceptionally large spots (> 5 nm), see Figure 4.5b. Besides the large spots, we observed many much smaller spots (≤ 1 nm), which can be associated with the presence of small electron-rich niobium centers. The sizes of these spots were close to the resolution of our TEM equipment. The amorphous region in Figure 4.5a contained both niobium and silicon, as shown by the EDX measurement in Figure 4.6a. The dark spots in Figure 4.5b with the highest electron densities contained a higher concentration of niobium (Figure 4.6c) than the surrounding lighter regions (Figure 4.6b). We may therefore assign the correlation peak in the SAXS curve to the presence of alternating regions that are enriched in either niobia or hybrid silica.

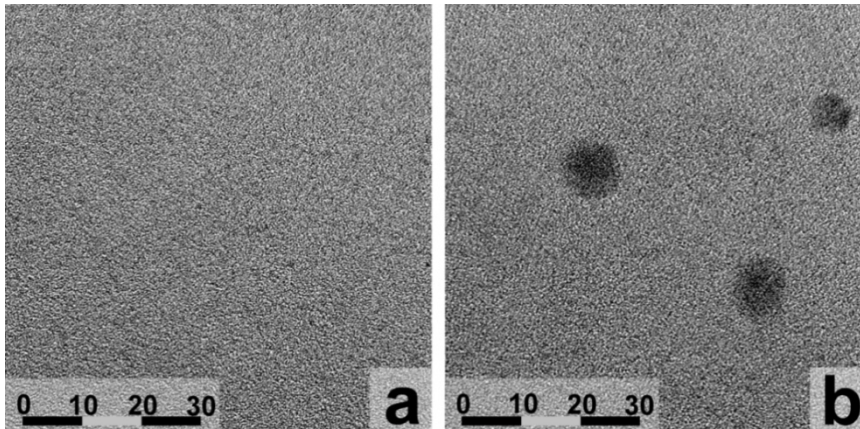


Figure 4.5. TEM image of dried film sample p60. (a) General overview; (b) Examples of anomalously large dark spots. The scale bar represents the scale in nm.

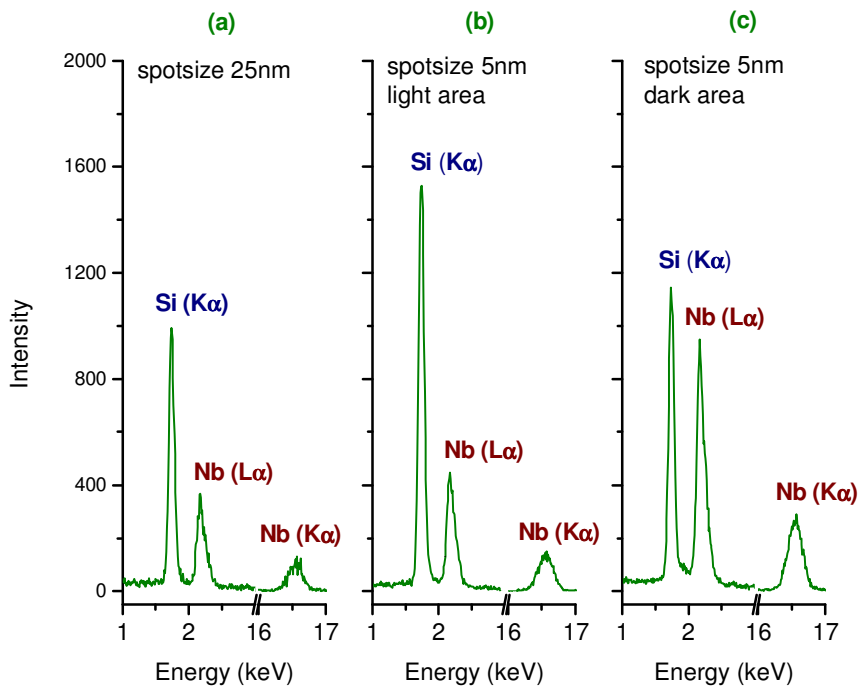


Figure 4.6. EDX analysis of as-dried film p60. (a) Measurement with 25 nm spotsize in Figure 4.5a; (b) Measurement of 5 nm spot in light area of Figure 4.5b; (c) Measurement of 5 nm spot in dark area of Figure 4.5b.

To account for the observed phenomena and SAXS profiles, we propose in Figure 4.7a schematic representation of the structure evolution process on nanometer-scale during reaction and film drying that is consistent with the experimental data. First the BTESE sol hydrolyzed and condensed, forming small sol particles (Figure 4.7a) with $R_g = 0.49$ nm. Then NPE was added, which formed small particles and reacted with the pre-hydrolyzed BTESE (Figure 4.7b). Then the sol was dried as a thin film. During the first stage of drying, the slope of the SAXS curve at high q in Figure 4.3 became steeper. This indicates that the Porod region (where $I \sim q^{-4}$) shifted effectively to lower q , showing that the size of the primary building blocks increased (Figure 4.7b and Figure 4.6c). Probably, in this stage the smallest entities dissolved via Ostwald ripening. This explained the reduction of the overall number of electron density fluctuations, which is represented by Q_{inv} (Figure 4.4a) as well as it explained increasing average sizes of electron rich and electron lean domains as represented by V_C and L_C (Figure 4.4b,c).

In the second stage of drying (green curves in Figure 4.3) the average distance between sol particles decreased, thereby decreasing the electron density contrast between sol particles and their surroundings. A solid phase with a correlation peak in its SAXS curve developed (Figure 4.7c and 6d). This process typically occurs on length scales > 1 nm, and was confirmed by the decreasing scattering intensity at low q in Figure 4.3. The number of correlations at these length scales reduced and therefore the average length scale as indicated by both V_C and L_C (Figure 4.4b,c) reduced as well. However, the still ongoing autonomous growth of the primary building blocks counteracted this effect to some extent. The maximum value of both V_C and L_C was reached when both effects counterbalanced. After that moment, the reduction of $\Delta\rho$ between sol particles and surroundings became dominant, so that both V_C and L_C decreased. Since V_C is a volume-weighted term and L_C is a length-weighted term, V_C is less sensitive to the increase of primary segment radius. The precise moment when the above mentioned effects counterbalance occurred earlier in time for V_C than for L_C .

Finally, the trends in Q_{inv} , L_C and V_C leveled off in the third stage. After $t = 24$ min L_C still decreased slowly (Figure 4.4b,d). Most likely, the capillary forces that were developed during drying caused further densification of the solid phase and reduction of the building block-to-building block distances. On

the other hand, V_C is sensitive to large distance fluctuations. These were slightly increasing, as shown by the increasing slope at low q -values in Figure 4.3 (red curves). This suggests an increasing degree of disorder in the building block-to-building block packing distance upon drying.

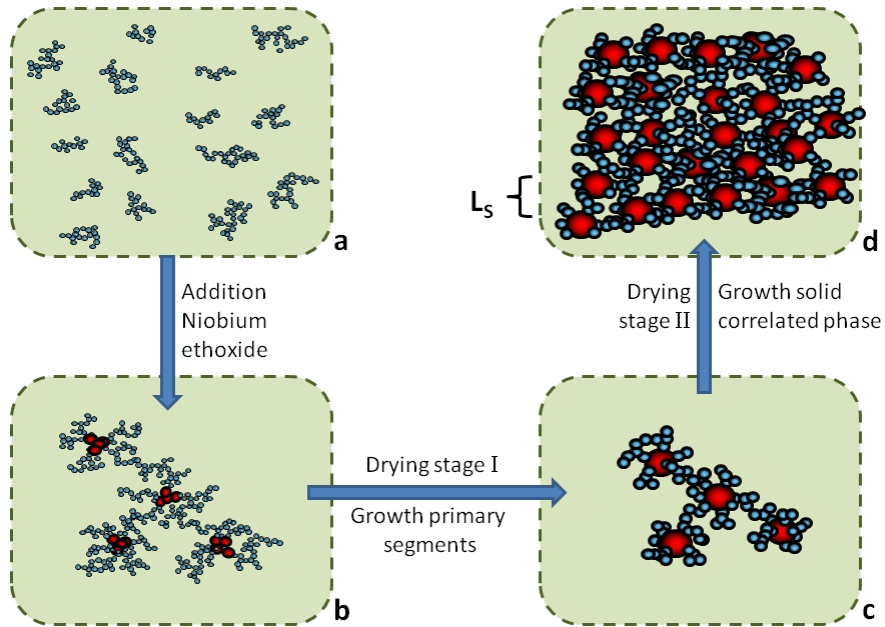


Figure 4.7. Schematic representation of proposed mechanism of condensation and aggregation of mixed niobia/hybrid silica during drying of thin film sols.

In the second stage of the drying process, we visually observed the formation of a secondary solid phase. Thus, in this stage a heterogeneous system was present in the film, in which a solid phase developed from a nanosized sol. The phase formation and separation process was accompanied by the formation of a characteristic SAXS correlation peak that represented particular distances between electron-rich domains. Both the dispersed sol phase and the newly formed solid phase had a characteristic integral correlation length L_C . After a short induction period during which nucleation sites for the solid phase formed, the solid phase

continued growing from the solid-liquid interface. Therefore, the scattering profile was dominated by both the dispersed and the solid phases. We can define a conversion parameter, α_{L_c} that quantifies the degree of transition from the initial polymeric sol with correlation length L_C^P into a solid phase consisting of a correlated stack of similarly-sized building blocks with a typical correlation length L_C^C (Equation (4.17)). Here L_C^P is defined as the correlation length before the transition stage (at the beginning of stage II) and L_C^C as the correlation length after the transition (at the end of stage III). Analogously, we can define a similar conversion parameter α_{V_c} for the correlation volume ((4.18). The two resulting conversion parameters α_{L_c} and α_{V_c} read:

$$\alpha_{L_c}(t) = \frac{L_C^P - L_C(t)}{L_C^P - L_C^C} \quad (4.17)$$

$$\alpha_{V_c}(t) = \frac{V_C^P - V_C(t)}{V_C^P - V_C^C} \quad (4.18)$$

The corresponding curves in Figure 4.8 follow a typical sigmoidal trend. After an induction period in which ethanol evaporated (Figure 6b), the particle solution became supersaturated in concentration, which facilitated the agglomeration process (Figure 6c). A solid phase with characteristic correlation peak in its SAXS curve grew until $t \sim 20$ min. There α_{L_c} and α_{V_c} were close to 1, showing that the conversion was nearly complete. The phase transformation rate can be fitted to the Johnson-Mehl-Avrami-Kolmogorov (JMAK) equation [56], which was developed to characterize crystallization processes, but has also been applied to describe the growth of silica [57] and the solidification of glasses [58-60]

$$\alpha = A \cdot \left[1 - \exp\left(-k \cdot (t - t_i)^d\right) \right] \quad (4.19)$$

Here A is a normalization constant, k a reaction rate constant, d a parameter that is characteristic for a particular growth mechanism, and t_i is an induction time that expresses the moment that conversion starts. We found similar JMAK-parameters for both conversion coefficients except for

t_i , which was 4.3 ± 0.4 min and 1.3 ± 0.5 min for α_{L_c} and α_{V_c} , respectively. These times are somewhat before the moment t_{\max} at which we find the maxima in V_c and L_c . While t_i indicates the onset of the transition process towards a condensed phase, t_{\max} is also related to growth effects of the primary particles, as discussed above. For both conversion coefficients, $d = 3 \pm 0.4$ which indicated that the packing of sol particles was associated with a polyhedral growth mechanism [56]. This means that the sol particles became randomly packed in all three dimensions. The other parameters were $k = (4.4 \pm 0.1) \cdot 10^{-4}$ and $(4.6 \pm 0.1) \cdot 10^{-4} \text{ min}^{-d}$, and $A = 0.99 \pm 0.01$ and 0.98 ± 0.01 for α_{L_c} and α_{V_c} , respectively.

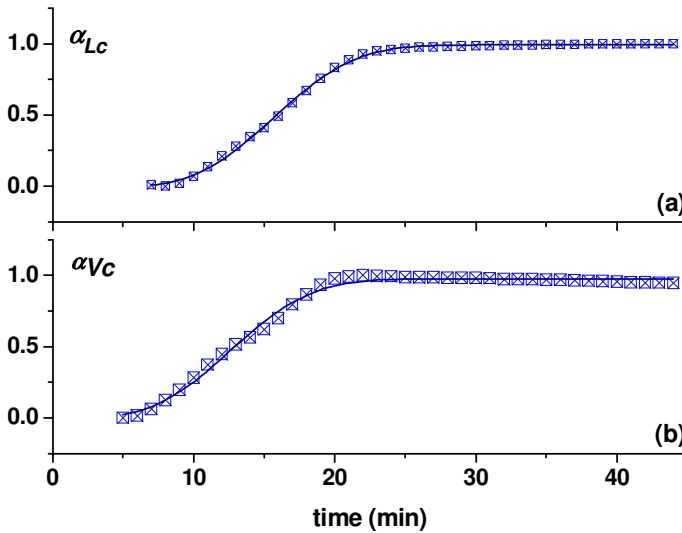


Figure 4.8. The conversion of a sol towards a dried gel of sample p60 during film drying at $T = 60^\circ\text{C}$, characterized by evolution of (a) correlation length L_c , and (b) correlation volume V_c . The drawn lines indicate the best fits to the JMAK equation.

4.5.3. Modeling the film drying process

As analyzed above, the initial sol consisted of branched small particles and the corresponding SAXS curve could be described well in terms of a mass-fractal ((4.4)). Upon drying, a solid phase developed, and a correlation peak showed up in the SAXS curve, which could be assigned to niobium-rich

regions inside a hybrid silica matrix. Since we have no indications that niobia building blocks have a preferential growth direction we assumed that the building blocks were approximately spherical. Since long range order was absent, liquid-like random packing of building blocks is the most plausible interpretation of the correlation peak [40]. The niobia building blocks were dispersed in a hybrid silica matrix that kept them separated from each other. The nanostructure of the solid phase can thus be characterized in terms of length scales, namely the core radius (r_0) of the niobium-rich building blocks (i.e. primary scatterers), and the mean building block-to-building block distance (μ_{L_s}) from the correlation peak. The scattering intensity of the solid phase can therefore be described by Equation (4.7). However, since the correlation peak was rather broad, we included the effect of polydispersity by the local monodisperse approximation (Equation ((4.10)). During the film drying process we assume the presence of a spatially separated mixture of a solid phase with internal structural correlations, and a polymeric sol in an ethanol matrix.

We optimized the model parameters ($l_0, \eta, \xi, D, \phi, \mu_{L_s}, \sigma_{L_s}, r_0$, (4.13) by applying simplex [61] iterations until the correlation coefficient, R_{corr} , was 0.998 or higher. However, at $t < 16$ min we did not find a clear evolution of the conversion parameter, η . This was due to the absence of a correlation peak at $t < 16$ min, so that the distinction that could be made between correlated aggregates (solid phase) and polymeric sol particles was poor. In order to be able to fit the data properly, we needed a proper approximation of the extent of conversion as characterized by η . As was demonstrated above, the conversion from sol into a solid was accompanied by a clear change in V_C (Figure 4.4c). Therefore, the change of in V_C expressed in terms of α_{V_c} provides a proper estimate of η . When taking into account that α_{V_c} is a volume-weighted coefficient and η is a number-weighted conversion coefficient, then we can approximate η by:

$$\eta(t) \approx \frac{\alpha_{V_c}(t) / V_C^C}{\alpha_{V_c}(t) / V_C^C + (1 - \alpha_{V_c}(t)) / V_C^P} = \frac{1}{1 + \left(\frac{1 - \alpha_{V_c}(t)}{\alpha_{V_c}(t)} \right) \cdot \frac{V_C^C}{V_C^P}} \quad (4.20)$$

The remaining seven parameters (I_0 , ξ , D , ϕ , μ_{Ls} , σ_{Ls} , r_0 , (4.13) were optimized by fitting to the experimental curves. The best fits matched well with the experimental SAXS curves, with correlation coefficients R_{corr} of at least 0.999. See Figure 4.9. The modeled data only deviated from the experimental data in the initial stage of the drying process, at $t = 0 - 5$ min, where the scattering intensity leveled off above $q \sim 4 \text{ nm}^{-1}$. The data in that small time frame could not be described well using a spherical form factor. The quality of fit might be improved by an ellipsoid or cylindrical form factor, but since it would increase the complexity of our model, and was not expected to provide further insight, we did not attempt to improve these fits in the time frame between 0 and 5 min.

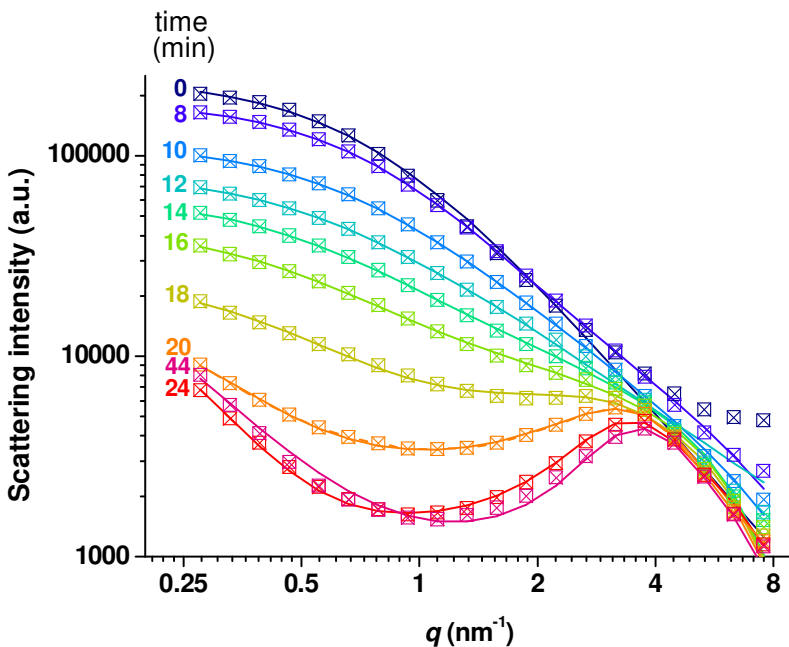


Figure 4.9. The modeled SAXS curves at several timescales while drying sample p60 at $T=60^\circ\text{C}$ using (4.13). The conversion parameter α_V was calculated from (4.20). Colors are a guide to the eye.

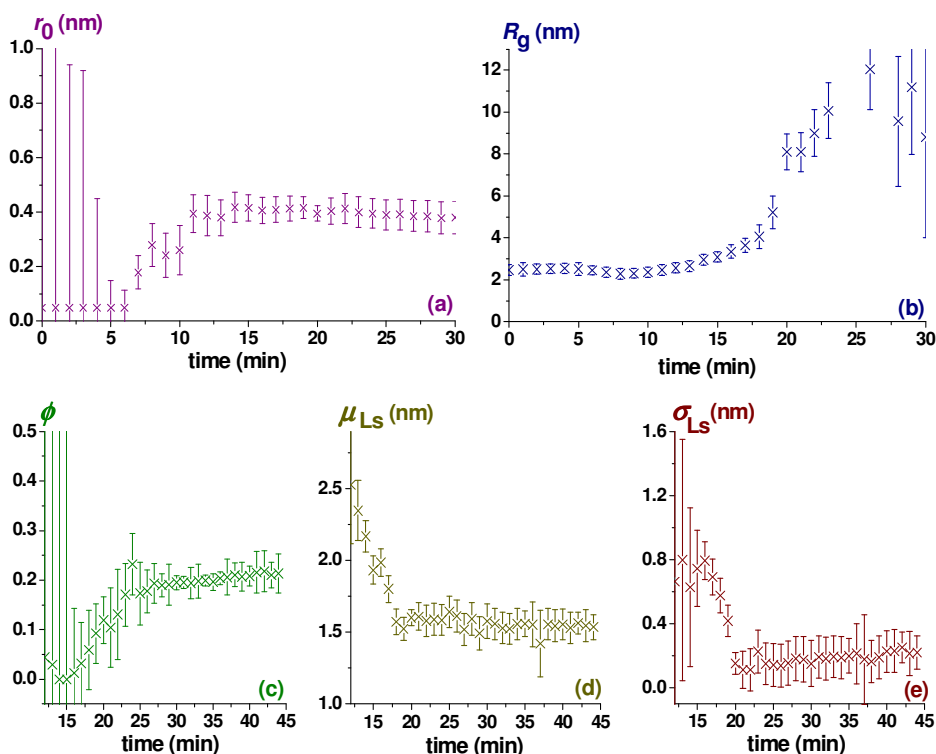


Figure 4.10. Parameters from fitting drying sample p60 at $T = 60^\circ\text{C}$ using Equation (4.13). (a) Primary particle radius r_0 ; (b) radius of gyration of sol particles R_g ; (c) building block volume fraction in the local surroundings of a building block ϕ ; (d) intensity-averaged building block-to-building block distance μ_{L_s} ; (e) mean square deviation in distribution of building block-to-building block distance σ_{L_s} .

At $t > 8$ min the curves could be fitted using a spherical form function and r_0 increased to ~ 0.4 nm (Figure 4.10a). The increase coincided with an increase of V_C , and may be related to Ostwald ripening as discussed above. At $t > 12$ min, r_0 leveled off. The size of the building blocks is similar to the size of the niobia core of a $\text{Nb}_8\text{O}_{10}(\text{OEt})_{20}$ complex [62]. The Nb_8O_{16} core has an radius of gyration R_g of 0.33 nm, which corresponds to a spherical cross-sectional radius of $r_0 = R_g (5/3)^{1/2} = 0.42$ nm [37]. In the calculation of latter value we discarded the surrounding carbon atoms and pendant oxygen atoms since these have a similar electron density as ethanol, and can

therefore not be distinguished from the solvent matrix. Within the first 15 min, the radius of gyration of the polymeric units remained approximately constant at $R_g=1.5\text{nm}$ (Figure 4.10b). Then R_g increased rapidly to $R_g\sim 8.5\text{nm}$. At $t> 20$ min the bending point in the SAXS curve moved outside the q -range covered by our equipment, and R_g became too large to determine. Its value can be considered close to infinite as soon as all ethanol has evaporated. At $t >15$ min a correlation peak appeared in the SAXS curves. From this moment onwards, the local volume fraction ϕ , mean building block-to-building block distance μ_{L_s} , and its standard deviation σ_{L_s} of L_s were determined by fitting to (4.13, see Figure 4.10 c-e. At $t = 17 - 22$ min the extent of correlation between the electron-rich niobium building blocks clearly increased, as indicated by the increase of ϕ . The majority of building blocks formed a separate solid phase. At $t = 12-19$ min the building block-to-building block distance μ_{L_s} clearly decreased, while the typical size r_0 , which was mainly determined by the size of the electron-rich Nb-based building blocks remained constant from $t = 12$ min. onwards. Because the solvent between the building blocks evaporated, the available volume in which building blocks could move freely became smaller as well. Therefore, the standard variation of building block-to-building block distance σ_{L_s} decreased simultaneously with μ_{L_s} .

In the third and final stage of the drying process, both r_0 and μ_{L_s} decreased slightly. Since the solvent had already evaporated, this suggests a densification process of the as-formed solid phase. Moreover, ϕ increased, indicating increased interference between different niobia building blocks. In other words, since the building blocks are approaching each other the probability that a correlation between building blocks is found increased in the course of time. On the other hand, σ_{L_s} slowly increased, indicating an increased degree of disorder in μ_{L_s} .

4.4. Effect of prehydrolysis of silica

The time during which we hydrolyzed BTESE before adding the NPE-precursor (i.e. pre-hydrolysis time) was 60, 30 min and 0 min in samples p60, p30 and p00, respectively. The radius of gyration after 1 h of reaction time decreased to 2.2, 2.0, and 1.5 nm, respectively, as determined from fitting data to the mass-fractal equations (4.4) and (4.5). The initial integral correlation length L_c of the simultaneously hydrolyzed sample p00 was substantially larger compared to the pre-hydrolyzed samples p30 and p60, see Figure 4.11a. All samples showed the same general trend: first, an

increase of L_C due to the increasing size of primary building blocks, followed by a decrease since the contrast between the polymeric agglomerates and their surroundings disappeared. The difference in L_C between samples p30 and p60 was marginal although the radius of gyration of p30 was substantially larger than p60. The correlation volume V_C , which is dominated by the largest features in the system, revealed that the second stage, at which V_C decreases, starts straightaway for sample p00. See Figure 4.11b. The final correlation volume was mainly determined by remaining polymeric aggregates and was found to be independent of the actual synthesis procedure.

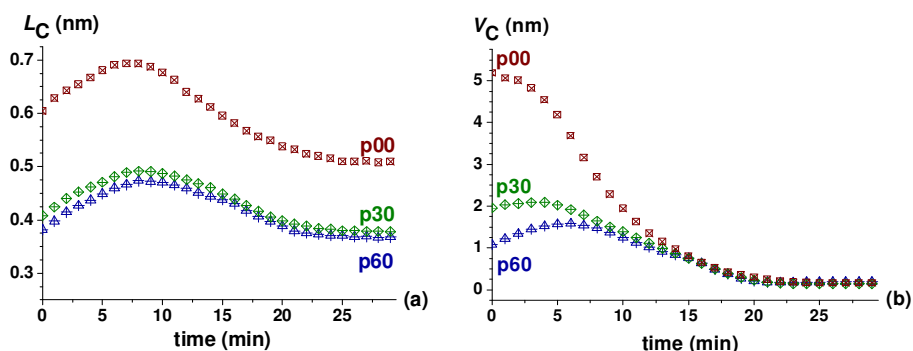


Figure 4.11.(a) Integral correlation length; (b) correlation or Porod volume with varying prehydrolysis time of BTESE of samples p00, p30, p60 as a function of drying time at $T = 60^\circ\text{C}$.

In samples p00 and p30 a sharp transition in r_0 is observed in Figure 4.12a. However, it was difficult to find a unique solution from the experimental data and the sharp transition was in disagreement with the smooth transition that we observed for L_C and V_C in the same period of time (Figure 4.11). After the second stage of drying process the values of r_0 and L_C of samples p30 and p60 were almost identical. This means that although the initial radius of gyration of p30 was clearly larger compared to p60, the size of and distances between niobia-rich building blocks were similar after 20 min. In sample p00 both r_0 and μ_{L_s} were substantially larger than in samples p30 and p60.

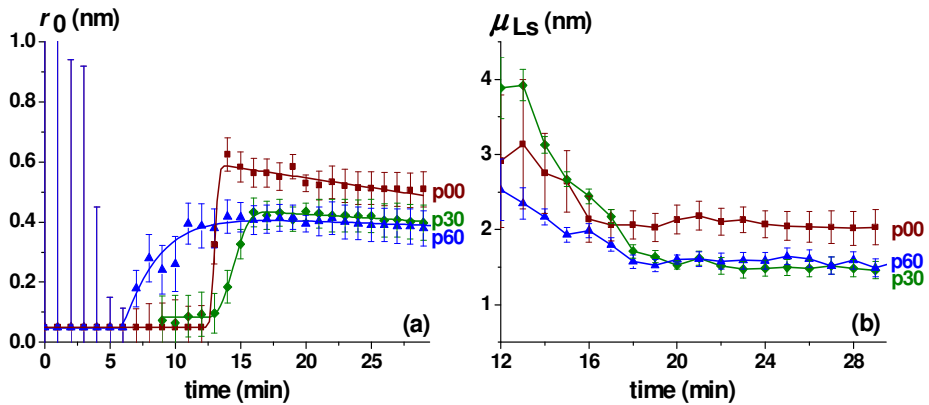


Figure 4.12. (a) Primary particle radius r_0 of samples p00, p30 and p60 with different prehydrolysis times of BTESE; (b) Intensity averaged building block-to-building block distance μ_{L_s} of the same samples.

4.4. The effect of drying temperature

When the drying temperature was decreased from 80 °C to lower temperatures, the change of both r_0 and μ_{L_s} became more gradual and the induction period increased. See Figure 4.13. However, the trends are similar. After an induction period, r_0 increased rapidly, followed by slow densification during which r_0 decreased slowly. For the sake of clarity, the initial r_0 values were removed from the graph, since the error margins were rather large. Within the parameter uncertainties the sizes of these building blocks were not substantially different after solvent evaporation, i.e. $r_0 \sim 0.4$ nm. Probably, the drying temperature only has a minor influence on the size of the niobium-rich regions. Their size was probably established at the moment when the NPE precursor was added to the pre-hydrolyzed BTESE sol. The scattering intensity in that stage was dominated by the electron density contrast between both types of oxide building blocks and the solvent phase around these building blocks. The value of r_0 was determined by the sizes of the niobia and hybrid silica building blocks. After evaporation of ethanol, the contrast between the electron-rich niobia and electron-poor hybrid silica became the major contribution to the overall contrast in

electron density. This means that these niobia building blocks were not necessarily absent before the drying process started and their presence became more prominently visible when the solvent evaporated.

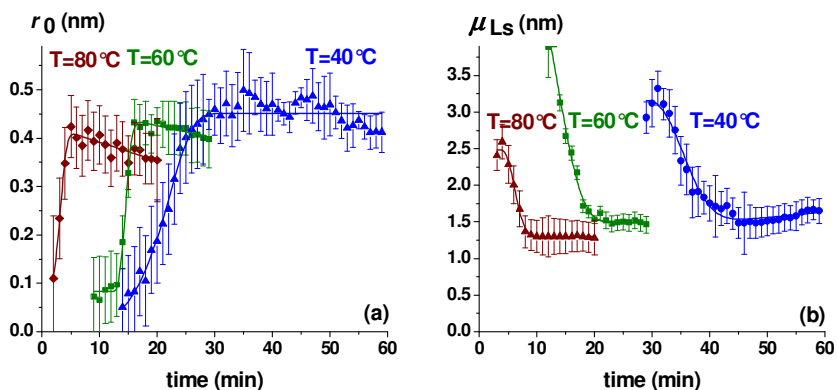


Figure 4.13. Evolution of (a) r_0 and (b) μ_{Ls} at 3 drying temperatures, $T=40$, 60 and 80°C.

4.6. Conclusions

The drying process of sol-gel derived niobia-hybrid silica mixed oxide thin films can be divided into three different stages. The first is an induction stage during which the primary building blocks were growing while the overall sol particle remained constant in size. The shape of the sol particles could be described in terms of a mass-fractal model. During this stage the solvent concentration in the system was high. The second represents a transition during which sol particles approach each other as a result of ethanol evaporation. In the third stage, a densification process takes place in the as-dried film after solvent evaporation, which is accompanied by some small structural reconstructions.

Before the transition process started, the SAXS curve was mainly determined by the electron density contrast between sol particles and surrounding ethanol matrix. During the transition process this contribution was reduced to zero due to solvent evaporation. However, electron density contrast between small molecular niobium-rich building blocks and the

surrounding hybrid silica matrix remained. This finally led to a correlation peak in the SAXS curves. The position of this peak was determined by the building block-to-building block distances between the small niobia building blocks. Building block sizes were extracted using hard sphere form functions and structural interference functions that were based on a Percus-Yevick approximation of hard spheres. When hybrid silica was hydrolyzed before adding NPE (samples p30 at three different drying temperatures and sample p60), all contained niobium-rich building blocks with a radius of ~ 0.4 nm, which is of the order of the size of an Nb_8O_{16} core. The sample p00 for which NPE was added at the beginning of the sol preparation process gave rise to niobium-rich building blocks with a larger average radius of 0.5 – 0.6 nm. This shows that hydrolysis of the hybrid silica sol before NPE addition gives rise to smaller niobium-rich building blocks in the mixed oxide film after drying.

The drying temperature influenced the rate at which the sol was dried. However, it had a negligible effect on the size of the niobium-rich building blocks. The size of these building blocks is thus likely established during the sol preparation process and not during drying.

4.7. References

1. Vane, L. M., *A review of pervaporation for product recovery from biomass fermentation processes*. J. Chem. Technol. Biotechnol. 2005, **80**(6), p.603-629.
2. van Gemert, R. W.; Petrus Cuperus, F., *Newly developed ceramic membranes for dehydration and separation of organic mixtures by pervaporation*. J. Membr. Sci. 1995, **105**(3), p. 287-291
3. Urtiaga, A. M.; Gorri, E. D.; Gómez, P.; Casado, C.; Ibáñez, R.; Ortiz, I., *Pervaporation Technology for the Dehydration of Solvents and Raw Materials in the Process Industry*. Drying Technol. 2007, **25** (11), p. 1819-1828.
4. Castricum, H. L.; Sah, A.; Kreiter, R.; Blank, D. H. A.; Vente, J. F.; Ten Elshof, J. E., *Hydrothermally stable molecular separation membranes from organically linked silica*. J. Mater. Chem. 2008, **18**(18), p. 2150-2158.

5. Kreiter, R.; Rietkerk, M. D. A.; Castricum, H. L.; Van Veen, H. M.; Ten Elshof, J. E.; Vente, J. F., *Evaluation of hybrid silica sols for stable microporous membranes using high-throughput screening*. J. Sol-Gel Sci. Technol. 2011, **57** (3), p. 245-252.
6. Fotou, G. P.; Lin, Y. S.; Pratsinis, S. E., *Hydrothermal stability of pure and modified microporous silica membranes*. J. Mater. Sci. 1995, **30** (11), p. 2803-2808.
7. Yoshida, K.; Hirano, Y.; Fujii, H.; Tsuru, T.; Asaeda, M., *Hydrothermal stability and performance of silica-zirconia membranes for hydrogen separation in hydrothermal conditions*. J. Chem. Eng. Jpn. 2001, **34** (4), p. 523-530.
8. Asaeda, M.; Sakou, Y.; Yang, J.; Shimasaki, K., *Stability and performance of porous silica-zirconia composite membranes for pervaporation of aqueous organic solutions*. J. Membr. Sci. 2002, **209**(1), p. 163-175.
9. Boffa, V.; Blank, D. H. A.; ten Elshof, J. E., *Hydrothermal stability of microporous silica and niobia-silica membranes*. J. Membr. Sci. 2008, **319**(1-2), p. 256-263.
10. Kanezashi, M.; Asaeda, M., *Hydrogen permeation characteristics and stability of Ni-doped silica membranes in steam at high temperature*. J. Membr. Sci. **2006**, 271 (1-2), 86-93.
11. Igi, R.; Yoshioka, T.; Ikuhara, Y. H.; Iwamoto, Y.; Tsuru, T., *Characterization of co-doped silica for improved hydrothermal stability and application to hydrogen separation membranes at high temperatures*. J. Am. Ceram. Soc. 2008, **91**(9), p. 2975-2981.
12. Gaudon, A.; Dauger, A.; Lecomte, A.; Soulestin, B.; Guinebretière, R., *Phase separation in sol-gel derived ZrO₂-SiO₂ nanostructured materials*. J. Eur. Ceram. Soc. 2005, **25**(2-3 SPEC. ISS.), p. 283-286.
13. Rodrigues, D. E.; Brennan, A. B.; Betrabet, C.; Wang, B.; Wilkes, G. L., *Structural features of sol-gel-derived hybrid inorganic-organic network ceramer materials by small-angle x-ray scattering*. Chem. Mater. 1992, **4**(6), p. 1437-1446;
14. Dahmouche, K.; Santilli, C. V.; Pulcinelli, S. H.; Craievich, A. F., *Small-Angle X-ray Scattering Study of Sol-Gel-Derived Siloxane-PEG and Siloxane-PPG Hybrid Materials*. J. Phys. Chem. B 1999, **103**(24), p. 4937-4942.
15. Brinker, C. J. S., G. W. , *Sol Gel Science, The Physics and Chemistry of Sol-Gel Processing*. Academic Press: San Diego, 1990; Vol. 1, p. 1-881.

16. Kessler, V. G.; Spijksma, G. I.; Seisenbaeva, G. A.; Håkansson, S.; Blank, D. H. A.; Bouwmeester, H. J. M., *New insight in the role of modifying ligands in the sol-gel processing of metal alkoxide precursors: A possibility to approach new classes of materials*. J. Sol-Gel Sci. Technol. 2006, **40**(2-3), p. 163-179.
17. Drake, K. O.; Carta, D.; Skipper, L. J.; Sowrey, F. E.; Newport, R. J.; Smith, M. E., *A multinuclear solid state NMR study of the sol-gel formation of amorphous Nb₂O₅-SiO₂ materials*. Solid State Nucl. Magn. Reson. 2005, **27**(1-2), p. 28-36.
18. Bansal, N. P., *Synthesis and thermal evolution of structure in alkoxide-derived niobium pentoxide gels*. J. Mater. Sci. 1994, **29**(17), p. 4481-4486.
19. Kreiter, R.; Rietkerk, M. D. A.; Castricum, H. L.; Van Veen, H. M.; Ten Elshof, J. E.; Vente, J. F., *Stable hybrid silica nanosieve membranes for the dehydration of lower alcohols*. ChemSusChem 2009, **2**(2), p. 158-160.
20. Iizuka, T.; Ogasawara, K.; Tanabe, K., *Acidic and catalytic properties of niobium pentaoxide*. Bull. Chem. Soc. Jpn. 1983, **56**(10), p. 2927-2931.
21. Prakash, A. M.; Kevan, L., *Synthesis of niobium silicate molecular sieves of the MFI structure: Evidence for framework incorporation of the niobium ion*. J. Am. Chem. Soc. 1998, **120**(50), p. 13148-13155.
22. Nowak, I.; Ziolek, M., *Niobium Compounds: Preparation, Characterization, and Application in Heterogeneous Catalysis*. Chem. Rev. 1999, **99**(12), p. 3603-3624.
23. Guerrero, S.; Miller, J. T.; Wolf, E. E., *Activity and selectivity control by niobium for the preferential oxidation of Co on Pt supported catalysts*. Appl. Catal. A 2007, **328**(1), p. 27-34.
24. Tanabe, K., *Application of niobium oxides as catalysts*. Catal. Today 1990, **8**(1), 1-11.
25. (a) Srilatha, K.; Lingaiah, N.; Sai Prasad, P. S.; Prabhavathi Devi, B. L. A.; Prasad, R. B. N.; Venkateswar, S., *Influence of Carbon Chain Length and Unsaturation on the Esterification Activity of Fatty Acids on Nb₂O₅ Catalyst*. Ind. Eng. Chem. Res. 2009, **48**(24), p. 10816-10819; (b) Srilatha, K.; Lingaiah, N.; Devi, B. L. A. P.; Prasad, R. B. N.; Venkateswar, S.; Prasad, P. S. S., *Esterification of free fatty acids for biodiesel production over heteropoly tungstate supported on niobia catalysts*. Appl. Catal. A, 2009, **365**(1), p. 28-33.

26. West, R. M.; Braden, D. J.; Dumesic, J. A., *Dehydration of butanol to butene over solid acid catalysts in high water environments*. J. Catal. 2009, **262**(1), p. 134-143.
27. Higashio, Y.; Nakayama, T., *One-step synthesis of methyl isobutyl ketone catalyzed by palladium supported on niobic acid*. Catal. Today 1996, **28**(1–2), p. 127-131.
28. (a) Pagán-Torres, Y. J.; Gallo, J. M. R.; Wang, D.; Pham, H. N.; Libera, J. A.; Marshall, C. L.; Elam, J. W.; Datye, A. K.; Dumesic, J. A., *Synthesis of Highly Ordered Hydrothermally Stable Mesoporous Niobia Catalysts by Atomic Layer Deposition*. ACS Catal. 2011, **1**(10), p. 1234-1245; (b) Pham, H. N.; Pagan-Torres, Y. J.; Serrano-Ruiz, J. C.; Wang, D.; Dumesic, J. A.; Datye, A. K., *Improved hydrothermal stability of niobia-supported Pd catalysts*. Appl. Catal. A, 2011, **397**(1–2), p. 153-162.
29. (a) Boffa, V.; ten Elshof, J. E.; Petukhov, A. V.; Blank, D. H., *Microporous niobia-silica membrane with very low CO₂ permeability*. ChemSusChem 2008, **1**(5), p. 437-443. (b) Boffa, V.; ten Elshof, J. E.; Garcia, R.; Blank, D. H. A., *Microporous niobia-silica membranes: Influence of sol composition and structure on gas transport properties*. Micropor. Mesopor. Mat. 2009, **118**(1-3), p. 202-209;
30. Qi, H.; Han, J.; Xu, N.; Bouwmeester, H. J. M., *Hybrid Organic–Inorganic Microporous Membranes with High Hydrothermal Stability for the Separation of Carbon Dioxide*. ChemSusChem 2010, **3**(12), p. 1375-1378.
31. (a) Innocenzi, P.; Malfatti, L.; Kidchob, T.; Costacurta, S.; Falcaro, P.; Piccinini, M.; Marcelli, A.; Morini, P.; Sali, D.; Amenitsch, H., *Time-Resolved Simultaneous Detection of Structural and Chemical Changes during Self-Assembly of Mesostructured Films*. J. Phys. Chem. C, 2007, **111**(14), p. 5345-5350; (b) Malfatti, L.; Kidchob, T.; Falcaro, P.; Costacurta, S.; Piccinini, M.; Guidi, M. C.; Marcelli, A.; Corrias, A.; Casula, M. F.; Amenitsch, H.; Innocenzi, P., *Highly ordered self-assembled mesostructured membranes: Porous structure and pore surface coverage*. Micropor. Mesopor. Mat. 2007, **103**(1–3), p. 113-122.
32. Stawski, T. M.; Veldhuis, S. A.; Besselink, R.; Castricum, H. L.; Portale, G.; Blank, D. H. A.; Ten Elshof, J. E., *Nanostructure development in alkoxide-carboxylate-derived precursor films of barium titanate*. J. Phys. Chem. C, 2012, **116**(1), p. 425-434.

-
33. Castricum, H. L.; Kreiter, R.; Van Veen, H. M.; Blank, D. H. A.; Vente, J. F.; Ten Elshof, J. E., *High-performance hybrid pervaporation membranes with superior hydrothermal and acid stability*. J. Membr. Sci. 2008, **324**(1-2), p. 111-118.
 34. Bras, W.; Dolbnya, I. P.; Detollenaere, D.; Van Tol, R.; Malfois, M.; Greaves, G. N.; Ryan, A. J.; Heeley, E., *Recent experiments on a combined small-angle/wide-angle X-ray scattering beam line at the ESRF*. J. Appl. Crystallogr. 2003, **36**(3 I), p. 791-794.
 35. Bras, W.; Emsley, J. W.; Levine, Y. K.; Luckhurst, G. R.; Seddon, J. M.; Timimi, B. A., *Field-induced alignment of a smectic-a phase: A time-resolved x-ray investigation*. J. Chem. Phys. 2004, **121**(9), p. 4397-4413.
 36. Guinier, A.; Fournet, G., *Small-Angle Scattering of X-rays*. John Wiley & Sons: New York, 1955; Vol. 1, p 19-28, 40-52.
 37. Feigin, L. A.; Svergun, D. U., *Structure analysis by small angle X-ray and neutron scattering*. Plenum Press: New York, 1987; p 34-49, 59-64, 68-73, 76-81, 84-94, 195-197, 230-239.
 38. Porod, G., *Small Angle X-ray Scattering*. Academic Press: New York, 1982; Vol. 15, p 21-35, 41-48.
 39. Teixeira, J., *Small-angle scattering by fractal systems*. J. Appl. Crystallogr. 1988, **21**(6), p. 781-785;
 40. Chen, S. H.; Teixeira, J., *Structure and fractal dimension of protein-detergent complexes*. Phys. Rev. Lett. 1986, **57**(20), p. 2583-2586.
 41. Boffa, V.; Castricum, H. L.; Garcia, R.; Schmuhl, R.; Petukhov, A. V.; Blank, D. H. A.; Ten Elshof, J. E., *Structure and growth of polymeric niobia-silica mixed-oxide sols for microporous molecular sieving membranes: A saxs study*. Chem. Mater. 2009, **21**(9), p. 1822-1828.
 42. Lin, M. Y.; Klein, R.; Lindsay, H. M.; Weitz, D. A.; Ball, R. C.; Meakin, P., *The structure of fractal colloidal aggregates of finite extent*. J. Colloid Interface Sci. 1990, **137**(1), p. 263-280;
 43. Sorensen, C. M.; Wang, G. M., *Size distribution effect on the power law regime of the structure factor of fractal aggregates*. Phys. Rev. E, 1999, **60**(6 B), p. 7143-7148.
 44. Kinning, D. J.; Thomas, E. L., *Hard-sphere interactions between spherical domains in diblock copolymers*. Macromol. 1984, **17**(9), p. 1712-1718.
 45. Terrill, N. J.; Crowley, T.; Gill, M.; Armes, S. P., *Small-Angle X-ray Scattering Studies on Colloidal Dispersions of Polyaniline-Silica Nanocomposites*. Langmuir. 1993, **9**, p. 2093-2096.
-

46. (a) Schubert, K. V.; Strey, R. Kline, S. R.; Kaler, E. W., *Small angle neutron scattering near Lifshitz lines: Transition from weakly structured mixtures to microemulsions* J. Chem. Phys. 1994, **101**(6), p. 5343-5355. (b) Teubner, M., Strey, R. *Origin of scattering peaks in microemulsions*. J. Chem. Phys. 1987, **87**(5), p. 3195-3200.
47. (a) Stawski, T. M.; Veldhuis, S. A.; Besselink, R.; Castricum, H. L.; Portale, G.; Blank, D. H. A.; Ten Elshof, J. E., *Nanoscale structure evolution in alkoxide-carboxylate sol-gel precursor solutions of barium titanate*. J. Phys. Chem. C, 2011, **115**(42), p. 20449-20459; (b) Stawski, T. M.; Veldhuis, S. A.; Besselink, R.; Castricum, H. L.; Portale, G.; Blank, D. H. A.; Ten Elshof, J. E., *Erratum: Nanoscale structure evolution in alkoxide-carboxylate sol-gel precursor solutions of barium titanate* (J. Phys. Chem. C (2010) **115** (20449-20459) DOI: 10.1021/jp206572q). J. Phys. Chem. C 2011, **115**(48), p. 24028.
48. Pedersen, J., *Determination of size distribution from small-angle scattering data for systems with effective hard-sphere interactions*. J. Appl. Crystallogr. 1994, **27**(4), p. 595-608.
49. Flory, P. J., *Molecular Size Distribution in Three Dimensional Polymers. III. Tetrafunctional Branching Units*. J. Am. Chem. Soc. 1941, **63**(11), p. 3096-3100.
50. Wagner, J., *Small-angle scattering from spherical core-shell particles: an analytical scattering function for particles with Schulz-Flory size distribution*. J. Appl. Crystallogr. 2004, **37**(5), p. 750-756.
51. Quintanilla, J.; Reidy, R. F.; Gorman, B. P.; Mueller, D. W., *Gaussian random field models of aerogels*. J. Appl. Phys. 2003, **93**(8), p. 4584-4589.
52. Hjelm, R. P.; Schteingart, C.; Hofmann, A. F.; Sivia, D. S., *Form and structure of self-assembling particles in monoolein-bile salt mixtures*. J. Phys. Chem. 1995, **99**(44), p. 16395-16406.
53. (a) Torma, V.; Peterlik, H.; Bauer, U.; Rupp, W.; Hüsing, N.; Bernstorff, S.; Steinhart, M.; Goerigk, G.; Schubert, U., *Mixed silica titania materials prepared from a single-source sol-gel precursor: A time-resolved SAXS study of the gelation, aging, supercritical drying, and calcination processes*. Chem. Mater. 2005, **17**(12), p. 3146-3153; (b) Sinkó, K.; Torma, V.; Kovács, A., *SAXS investigation of porous nanostructures*. J. Non-Cryst. Solids, 2008, **354**(52-54), p. 5466-5474; (c) Freltoft, T.; Kjems, J. K.; Sinha, S. K., *Power-law correlations and finite-size effects in silica particle aggregates*

- studied by small-angle neutron scattering.* Phys. Rev. B, 1986, **33**(1), p. 269-275.
54. Svergun, D. I.; Koch, M. H. J., *Small-angle scattering studies of biological macromolecules in solution.* Rep. Prog. Phys. 2003, **66**(10), p. 1735-1782.
55. Francisco, M. S. P.; Landers, R.; Gushikema, Y., *Local order structure and surface acidity properties of a Nb₂O₅/SiO₂ mixed oxide prepared by the sol-gel processing method* J. Solid State Chem. 2004, **177**, p. 2432-2439
56. (a) Avrami, M., *Kinetics of phase change. I: General theory.* J. Chem. Phys. 1939, **7**(12), 1103-1112; (b) Avrami, M., *Kinetics of phase change. II Transformation-time relations for random distribution of nuclei.* J. Chem. Phys. 1940, **8**(2), p. 212-224; (c) Avrami, M., *Granulation, phase change, and microstructure kinetics of phase change.* III. J. Chem. Phys. 1941, **9**(2), p. 177-184.
57. Tobler, D. J.; Shaw, S.; Benning, L. G., *Quantification of initial steps of nucleation and growth of silica nanoparticles: An in-situ SAXS and DLS study.* Geochim. Cosmochim. Acta 2009, **73**(18), p. 5377-5393.
58. Wondraczek, L.; Deubener, J.; Mixture, S. T.; Knitter, R., *Crystallization Kinetics of Lithium Orthosilicate Glasses.* J. Am. Ceram. Soc. 2006, **89**(4), p. 1342-1346;
59. Ferreira, E. B.; Lopez-Richard, V.; Zanotto, E. D.; Marques, G. E., *Analytical Model for Heterogeneous Crystallization Kinetics of Spherical Glass Particles.* J. Am. Ceram. Soc. **2009**, **92**(11), p. 2616-2618;
60. Pas, S. J.; Dargusch, M. S.; MacFarlane, D. R., *Crystallisation kinetics of some archetypal ionic liquids: isothermal and non-isothermal determination of the Avrami exponent.* Phys. Chem. Chem. Phys. 2011, **13** (25), p. 12033-12040.
61. Spendley, W.; Hext, G. R.; Himsforth, F. R., *Sequential Application of Simplex Designs in Optimisation and Evolutionary Operation.* Technometrics 1962, **4**(4), p. 441-461.
62. Kessler, V. G.; Turova, N. Y.; Yanovskii, A. I.; Belokon, A. I.; Struchkov, Y. T., *The structure of Nb₈O₁₀(OEt)₂₀ and the nature of crystalline metal alkoxides.* Russ. J. Inorg. Chem. 1991, **36**(7), p. 1-7.

S4.) Supporting Information

**Evolution of microstructure in mixed
niobia-hybrid silica thin films from sol-
gel precursors**

S4.1. SAXS-measurements including the Porod regime

For sample p60 two measurements were performed in the high q -regime ($3 < q < 32 \text{ nm}^{-1}$), one sol before drying and one powder that was dried for 44 min using an infra red lamp at a constant temperature $T=60^\circ\text{C}$. The curves do not show an ideal $I \sim q^{-4}$ regime, but instead we observed correlation peaks with maxima at 14.6 and 17.1 nm^{-1} for $t_{\text{dry}} = 0$ and 44 min , respectively, which corresponded to separation distances of 0.43 and 0.37 nm , respectively. The latter distance can be assigned to Nb-Nb distances in amorphous Nb_2O_5 in the dried powder, while Nb-Si distances were expected at lower distances of 0.34 nm [1]. However, since this correlation peak was rather broad we can neither confirm nor reject the presence of Nb-O-Si entities in this powder. The distances were larger in the sol before drying, indicating that it contained more loosely bound Nb-O-Nb, Nb-O-Si and Si-O-Si entities. In any case, we were convinced that these correlation peaks should be assigned to atomic correlations that overlap with the Porod regime of small building blocks in the system.

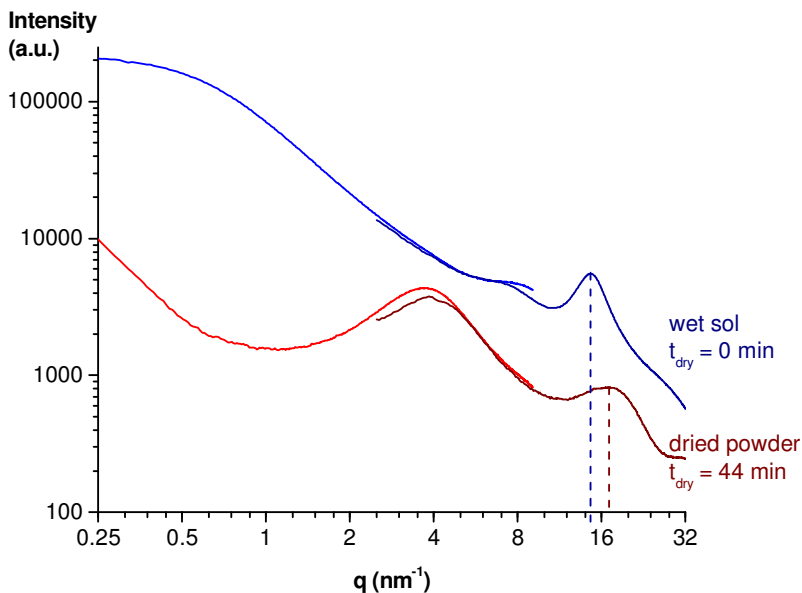


Figure S4.1. SAXS curves of sample p60 at $t = 0$ and $t = 44 \text{ min}$ during drying, measured in two different q -ranges: $0.25 < q < 9 \text{ nm}^{-1}$ and $3 < q < 32 \text{ nm}^{-1}$.

S4.2. Nitrogen sorption measurements.

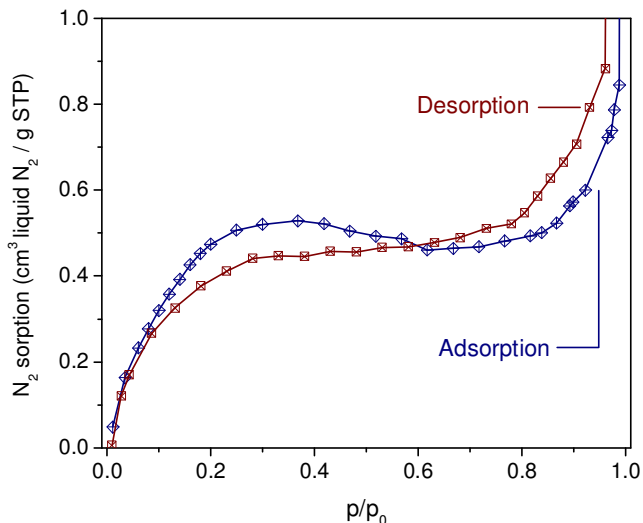


Figure S4.2. Nitrogen adsorption/desorption curve at T=77K of sample p60.

Nitrogen sorption measurements were performed at 77K in Micromeritics Tristar Instrument. The samples were firstly degassed at 300°C in a nitrogen atmosphere. From the adsorption isotherm, the surface area was determined by the Dubinin method, modified by Kaganer [2-3], represented by Equation (S4.1) with n the gas adsorbed at relative pressure p/p^0 , n_m the monolayer capacity of the surface, both expressed in mol/g adsorbent, and D an adsorbate-dependent constant.

$$\log(n) = \log(n_m) + D \cdot \left(\log\left(\frac{p^0}{p}\right) \right)^2 \quad (\text{S4.1})$$

Surface areas A were subsequently determined according to Equation (S4.2) in which N_A is Avogadro's number and a_m the area occupied by a molecule in the completed monolayer, taken as 0.162nm^2 for N_2 (ISO 9277).

$$A = n_m \cdot a_m \cdot N_A \quad (\text{S4.2})$$

The nitrogen sorption measurements revealed a very low N₂ sorption with a calculated surface area of 5,2 m²/g. As we had observed for undoped BTESE powders, nitrogen sorption is low in these types of hybrid silicas compared to conventional SiO₂ powders and membranes [4-5]. The microporosity can only be determined with gases that have a smaller kinetic diameter than nitrogen. Nevertheless, these results prove the absence of mesopores in the system.

S4.3. References

1. Francisco, M. S. P.; Landers, R.; Gushikema, Y., *Local order structure and surface acidity properties of a Nb₂O₅/SiO₂ mixed oxide prepared by the sol-gel processing method* J. Solid State Chem. 2004, **177**, p. 2432–2439
2. Dubinin, M. M. *On physical feasibility of Brunauer's micropore analysis method*, J. Colloid Interf. Sci. 1974, **46**, p. 351–356
3. Kaganer, M. G. *A new method for the determination of the specific adsorption surface of adsorbents and other finely dispersed substances*, Zh. Fiz. Khim. 1959, **33**, p. 2202–2210.
4. (a) Castricum, H. L.; Kreiter, R.; Van Veen, H. M.; Blank, D. H. A.; Vente, J. F.; Ten Elshof, J. E., *High-performance hybrid pervaporation membranes with superior hydrothermal and acid stability*. J. Membr. Sci. 2008, **324**(1-2), p. 111-118. (b) Castricum, H. L.; Sah, A. Kreiter, R.; Blank, D. H. A.; Vente, J. F.; Elshof, J. E. *Hydrothermally stable molecular separation membranes from organically linked silica*, J. Mater. Chem. 2008, **18** p. 2150–2158.
5. Vos, R. M. de; Verweij, H. *Improved performance of silica membranes for gas separation*, J. Membr. Sci. 1998, **143**, p. 37–51.

5.

**Extent of niobia/silsesquioxane
intermixing by solid state MAS-NMR**

5.1. Abstract

In this work different synthesis routes were evaluated with the aim of optimizing the incorporation of niobium within a hybrid silica matrix on an atomic scale. The fast kinetics of the hydrolysis/polycondensation of the organic Nb precursor $\text{Nb}(\text{OEt})_5$ entails a segregation of the resulting material into Nb_2O_5 and a silica based network. To overcome this effect we a) performed a prehydrolysis of 1,2 bis-triethoxy-ethane (BTESE) prior to adding niobium penta-ethoxide (NPE), or b) attempted to reduce the availability of Nb via a complexation of Nb by either acetyl acetone or 2-methoxy-ethanol. The network organization was evaluated from results of FTIR as well as ^{13}C , ^{29}Si and ^{17}O MAS NMR spectroscopy. The prehydrolysis of BTESE and the addition of 2-methoxy-ethanol induced a but only moderate mixing of Nb and Si, leading to a network in which islands of Nb_2O_5 are linked to the hosting silica based matrix via Nb-O-Si bonds. Contrary, the use of acetylacetonate lead to a mixing of Nb and Si on the atomic scale, producing a mixed Nb-O-Si network without any extended clusters of segregated Nb_2O_5 . The Si-C-C-Si bridge from the silsesquioxane is found to survive the condensation process and is even present in the resulting materials after annealing at 200 °C.

5.2. Introduction

Microporous hybrid silica membranes are known for both their chemical and thermal robustness [1-3]. Composite membranes with a selective hybrid silica layer have been successfully applied in pervaporation [1-5] of small molecules such as water and lower alcohols, and in gas separation [6-8]. The ability of microporous silica to separate such mixtures appears to be mainly based on size differences between molecules. We may extend the applicability of these membranes by incorporating transition metal oxides into the network to enhance the affinity for particular molecules. For instance, the introduction of nickel, cobalt, zirconium and niobium oxides in silica and hybrid silica membranes was found to enhance the H_2/N_2 and H_2/CO_2 permselectivity [9-15]. Yet, the homogeneous distribution of metal oxides into a bridged silsesquioxane matrix is not straightforward from a synthesis point of view: The metal oxide that is introduced, either as metal salt or as metal alkoxide, tends to phase separate while the silica matrix

forms. In the case of metal alkoxides, phase separation is induced by the high reactivity of the metal alkoxide precursors that hydrolyze and condense much faster compared to silicon alkoxides. On the other hand, niobium oxalate was successfully used to incorporate niobia into the tetragonal environment of mesoporous MCM-41 silicates [16, 17]. However, the use of oxalates requires calcination temperatures above 500°C, which makes them unsuitable for doping organically modified and hybrid silsesquioxanes.

The reactivity of metal alkoxides can be modified by introducing chelating ligands. Acetylacetone has often been applied to temper the reactivity of metal alkoxides. The enol tautomer of acetylacetone can dissociate one proton and subsequently form a bidentate complex with an enolic and ketonic oxygen atom [18]. The extent to which monodentate alcohol ligands are replaced by bidentate acetyl acetone ligands strongly depends on the type of metal ion. For instance, above an equimolar ratio of acetylacetone with respect to zirconium isopropoxide, zirconium readily forms an eightfold coordinated $Zr(acac)_4$ complex with a complexation ratio (Hacac/M) of 4 [19]. On the other hand, adding acetylacetone to niobium (V) and titanium (IV) ethoxides only changes the oligomeric nature of these alkoxides from a dimeric and tetrameric form for niobium and titanium ethoxide, respectively [20, 21], towards monomeric complexes upon addition of sufficient acetylacetone [18, 22, 23]. Here, the metal centers keep their six-fold coordination, even when adding an excessive amount of either acetylacetone or 2-methoxy-ethanol [18]. It raises the question whether these chelating ligands substantially reduce the sensitivity of $Nb(OEt)_5$ to such an extent that it enhances the homogeneous distribution of niobium centers within a hybrid silica matrix. ^{17}O -NMR studies clearly revealed an increase of hetero linkages in zirconium and titanium-containing glasses when acetylacetone was added before sol formation, which makes this ligand a promising candidate for niobia doped glasses as well [24-26].

An alternative approach to temper the condensation rate of metal alkoxide precursors is to first hydrolyze the silicon ethoxide groups before adding the metal alkoxide. As a consequence, the free water concentration is reduced, while the concentration of hydrolyzed silica is higher. The latter species can potentially condense with niobium ethoxide moieties and form heterogeneous Nb-O-Si linkages. A previous SAXS study revealed that the size of electron-dense niobia clusters decreased when the bridged

silsesquioxane precursor was firstly hydrolyzed for 1 h at $T=60^{\circ}\text{C}$ [27]. Since Nb^{5+} is generally too large to fit into an oxygen anion tetrahedron, it will unlike silicon remain in an octahedral environment [27].

The current study is focused on the dispersion of Nb^{5+} cations inside a hybrid silsesquioxane matrix. The degree of mixing between Nb and Si is inferred from ^{17}O MAS NMR data. ^{17}O NMR has been shown to be a very powerful technique to gain insight in the dispersion and oxygen coordination of transition metal cations in silica based glasses [24-26, 28-32], since the isotropic chemical shift values for the ^{17}O nucleus in the various possible linkages (Si-O-Si, Si-O-Nb, Nb-O-Nb) are distinctively different.

5.3. Experimental Section

5.3.1. Synthesis of mixed niobia/BTESE sols

All precursor solutions were prepared inside a glovebox under dry nitrogen atmosphere. The reflux synthesis was performed under atmospheric conditions. For sol A the 1,2-bis-triethoxysilyl-ethane (abbreviated as BTESE, ABCR chemicals, 97%) precursor was initially partly hydrolyzed and condensed before adding niobium pentaethoxide (abbreviated as NPE, ABCR chemicals, 99.99%) precursor. In a separate beaker NPE was diluted in ethanol yielding a molar concentration $[\text{NPE}] = 0.54 \text{ mol/L}$. The BTESE sol was rapidly cooled down to room temperature in a cold water bath ($T=10^{\circ}\text{C}$) for 1 min and then the NPE solution was added dropwise. In the case of samples B,C and D: NPE and BTESE were mixed in a molar ratio of $[\text{BTESE}]/[\text{NPE}] = 2/1$. Then acetylacetone (acac) was added to sample B ($[\text{acac}]/[\text{Nb}] = 2$), 2-methoxy-ethanol (2MOE) was added to sample C ($[2\text{MOE}]/[\text{Nb}] = 2$) and in the case of sample D no additives were added. Then samples B, C and D were diluted in ethanol to yield a final overall ethoxide concentration of $[-\text{OEt}] = 5.4 \text{ mol/L}$ (including silicon and niobium ethoxide groups). Then an acidic ethanol solution was added dropwise to samples B, C and D to yield the same hydrolysis and acid ratios as in sample A. Subsequently, sols B,C and D were refluxed for 1 h at $T=60^{\circ}\text{C}$. All sols finally had an overall ethoxide concentration of $[-\text{OEt}] = 2.7 \text{ mol/L}$, a hydrolysis ratio $[\text{H}_2\text{O}]/[-\text{OEt}] = 1.0$, an acid ratio $[\text{HNO}_3]/[-\text{OEt}] = 1/30$ and a niobium to silica ratio of $\text{Nb/Si}=1/4$. For the ^{17}O -NMR experiments we hydrolyzed the sols with 35% ^{17}O -enriched distilled water (Sigma-Aldrich)

and for the FTIR experiments we hydrolyzed the sols with conventional doubly distilled water. The sols (5mL) were dried for 30 min in a petridish (diameter 9cm) at $T=60^{\circ}\text{C}$ using a temperature controller coupled to a 150W infrared lamp located 12cm away from the sample. The dried film was ground and dried in a furnace at $T=60^{\circ}\text{C}$ for 24 h.

5.3.2. FTIR-measurements

The Fourier Transform Infrared (FTIR) measurements were performed using a Bruker Tensor 27 equipped with a KBr beamsplitter, a Pike Gladi ATR diamond attenuated total reflectance (ATR) unit and a liquid nitrogen cooled MCT broadband detector. The FTIR spectra were recorded in 5 min, with a resolution of 1 cm^{-1} . The Fourier transform (FT) was performed with 9480 phase interferogram points and a Blackman-Harris 3-term apodization function.

5.3.3. Solid State NMR

The ^{13}C CPMAS NMR experiments were performed employing a BRUKER Avance III spectrometer operating at resonance frequencies of 75.5 MHz and 300.27 MHz for ^{13}C and ^1H , respectively. MAS was performed at 7000 Hz with a relaxation delay time of 10 s. Typically, 1024 to 4096 scans were accumulated. The ^{17}O and ^{29}Si MAS NMR spectra were recorded on a Varian VNMRs 500 spectrometer operating at 67.76 MHz and 99.29 MHz for ^{17}O and ^{29}Si , respectively. The ^{17}O MAS NMR spectra were recorded at spinning speeds of 38 kHz employing a Varian 1.6 mm triple resonance T^3 -MAS probe, using a recycle time of 1 s. $\pi/8$ pulses and single pulse excitation were used to acquire the data. The ^{29}Si MAS NMR spectra were recorded employing a Varian 5 mm triple resonance T^3 MAS probe, a MAS frequency of 7 kHz and a recycle delay of 150 s. Spectra are referenced to TMS for ^{29}Si , Adamantane (downfield signal at 38.5 ppm) for ^{13}C , and H_2^{17}O for ^{17}O .

5.4. Results and discussion

The FTIR spectra for the as prepared samples are collected in Figure 5.1 together with the spectrum of anhydrous, pristine ethanol for comparison. The signals are dominated by peaks that are associated with ethanol and hydrolysed and condensed silicon moieties. Only in sample B, which contains acetylacetone, we observed a small shoulder at 940 cm^{-1} . This value is close to 960 cm^{-1} which is often associated with Si-O-Nb moieties [33, 34]. However, since this vibration is detected after addition of acetylacetone to NPE, we assign this signal to vibrations of conjugated C=O and C=C bonds of the acetylacetone ligand coordinated to niobium [35].

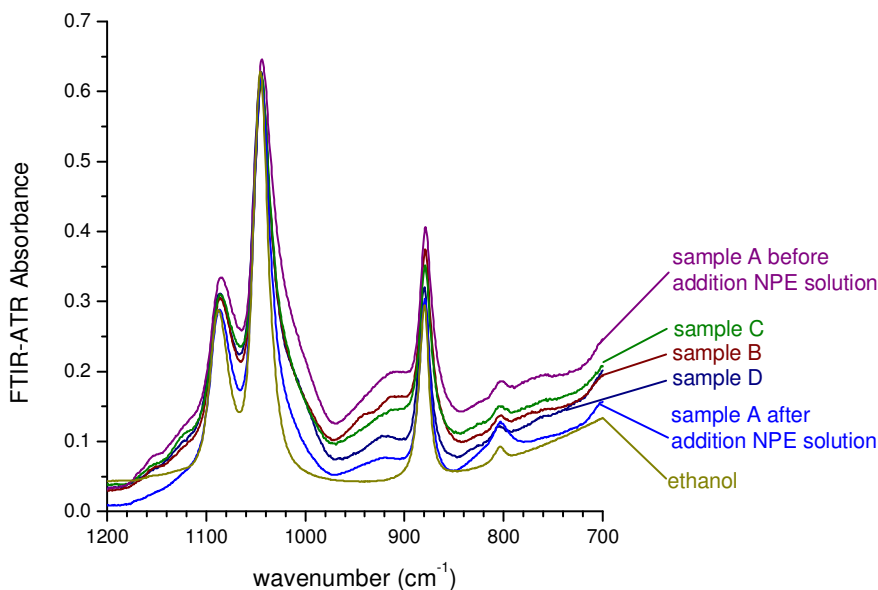


Figure 5.1. FTIR spectra of sols A-D (before drying).

Vibrations at 1150 cm^{-1} and 760 cm^{-1} indicate the presence of remnant Si-OEt groups of the BTESE precursor [36]. These vibrations are substantially broader than in pure BTESE, most likely due to the polar character of the surrounding medium. This made it difficult to quantify the amount and

compare the different samples. The Si-OEt vibration at 760 cm^{-1} was the weakest for sample B, which indicates that for the acac sample almost all ethoxide groups were released from silicon.

The addition of NPE to the prehydrolyzed BTESE (sample A) exhibits a clear effect on the FTIR spectrum. The intensity of the vibrations at 920 cm^{-1} and 1020 cm^{-1} that are assigned to Si-OH and Si-O-Si vibrations, respectively [36], is considerably smaller after addition of NPE. Such a reduction cannot be explained solely by the effect of dilution (1.4 times on volume). Possibly, the addition of NPE reduced the free water concentration and since the free water concentration is coupled with the concentration of hydrolyzed and condensed silicon species, their concentrations reduced as well. Thus, the addition of NPE may have reversed the prehydrolysis proces of BTESE, i.e. an esterification proces with the formation of SiOEt. However, the vibration at 1150 cm^{-1} and 760 cm^{-1} associated with SiOEt did not increase upon NPE addition and a vibration around 800 cm^{-1} increased instead. The exact cause of the increased intensity around 800 cm^{-1} remained unclear.

It is noted that NPE also has vibrations located around 920 cm^{-1} [37]. Nevertheless, in a separate experiment in the absence of BTESE we observed that this vibration peak rapidly reduced when an equivalent amount of water was added. Therefore, the peak at 920 cm^{-1} is probably dominated by Si-OH vibrations instead of Nb-O-Et vibrations.

Therefore, it is questionable whether prehydrolysis of silica had a substantial effect on the distribution of niobia in the sol. Upon comparison of samples B and C, which contained acetylacetone and 2-methoxyethanol as chelating ligands, respectively, with sample D that had no chelating additives, an enlarged Si-OH vibration was observed at 920 cm^{-1} in the latter sample. For both samples B and C, the presence of chelating ligands may have reduced the amount of water that reacted with the NPE precursor, so that more water was available for hydrolysis of BTESE.

The ^{13}C CPMAS and ^{29}Si MAS NMR spectra of the ^{17}O -enriched sols, dried at $T=60^\circ\text{C}$, are shown in Figure. 5.2. In the ^{13}C CPMAS NMR spectra (Figure 5.2a), the signal at approx. 4 ppm may be assigned to the ethylene bridge carbon of BTESE. Its presence confirms that the Si-C-C-Si bridge stays intact during the hydrolysis and polycondensation steps. The weak signals around 18 ppm and 58 ppm may be assigned to the methyl and methylene group of ethanol/ethoxy groups. This indicates either the presence of ethanol, presumably trapped within the pores of the membrane, or an incomplete

hydrolysis/polycondensation of the mixed network. In the spectrum of sample C, we find additional signals at approx. 61.8 ppm and 74.0 ppm, which can be assigned to the C_α and C_β carbon nuclei of the 2-methoxyethanol (as represented by $\text{HO}-C_\alpha\text{H}_2-C_\beta\text{H}_2-\text{O}-C_\gamma\text{H}_3$) added as complexing agent. Likewise, in the spectrum of D, the additional signals at 27 ppm (C_α of acetylacetonate), 106 ppm (C_β of acetylacetonate) and 193 ppm (C_γ of acetylacetonate), indicate the presence of immobilized acetylacetonate ligands ($[\text{H}_3\text{C}_\alpha-(\text{C}_\beta\text{O})-\text{C}_\gamma\text{H}-(\text{C}_\beta\text{O})-\text{C}_\alpha\text{H}_3]^-$). Since the signal for C_β was found at 106 ppm and no extended intensity was observed in the range of 58 – 60 ppm, the overwhelming majority of the acetylacetonate ligand is present in its enolic form.

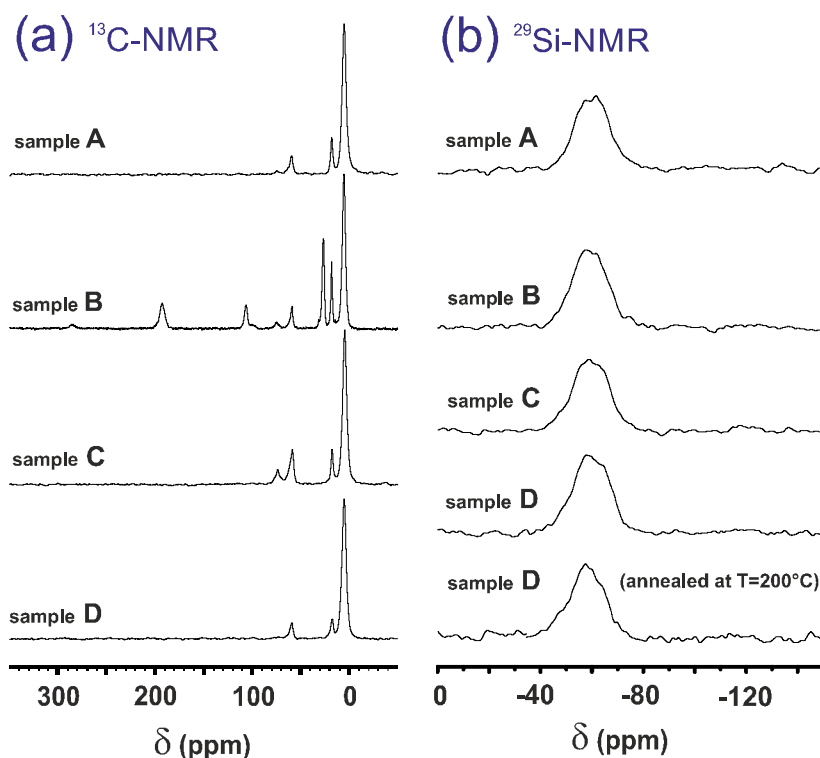


Figure 5.2. ^{13}C CPMAS NMR spectra (a) and ^{29}Si MAS NMR spectra (b) for the sol-gel derived niobia-hybris silica powders studied in this work. Spinning speed of 6 kHz were used to record the spectra. For the ^{13}C CPMAS spectra, ^{13}C and ^1H rf fields of 50 kHz, a contact time of 2 ms and a repetition delay of 5 s were used for the Hartmann-Hahn matching.

Since the magnetization transfer from ^1H to ^{13}C in the cross polarization (CP) process relies on the magnetic dipole coupling between these nuclei, any dynamic process, averaging this dipole interaction, will reduce the corresponding signal intensity. Therefore, the CP spectra are intrinsically non-quantitative, all signals from dynamic species (e.g. free ethanol within the pores) is essentially filtered out. Thus, the spectra confirm the formation of immobilized 2-methoxyethanol and acetylacetonate species, presumably connected to Nb. The ^{29}Si MAS NMR spectra for all samples (Figure 5.2b) reveal several resonances in a range between -50 and -70 ppm. These could not completely be resolved due to the strong overlap between the signals. Based on literature data, this is the region of T_2 (C-Si(OSi) $_2$ OH, -56 ppm) and T_3 species (C-Si(OSi) $_3$, -66 ppm). In accordance with the ^{13}C data, this confirms the survival of the ethylene bridge during the hydrolysis/condensation steps. From an analysis of the spectra, the degree of condensation was estimated (0 % for T_0 , 100% for T_3). Since a deconvolution of the spectra was not possible in all cases, we determined the center of gravity (CG) for all spectra, which was found to be in the range of -59 ppm to -60 ppm for all samples (Table 5.1). The resulting condensation degree in % - $67 + (\delta_{\text{CG}} - \delta_{T_2}) \cdot 33 / (\delta_{T_3} - \delta_{T_2})$ is found in the range of 75%, independent on the synthesis method. Fig. 2b shows the ^{29}Si MAS NMR spectrum of sample D, annealed at 200 °C. The spectrum was, within the experimental error of these experiments, found to have similar resonances as the corresponding spectrum of the non-annealed sample. No resonance frequencies in the range of -90 ppm to -120 ppm were observed, which indicated the absence of SiO_4 -species. From this we can conclude that the Si-C-C-Si bridge even survives annealing at 200 °C.

While the ^{13}C and ^{29}Si MAS NMR spectra offer some information about the general hydrolysis and condensation of the network, no information is revealed concerning the degree of mixing between Nb and Si. Information about this mixing may be deduced from an estimation of the magnetic dipole coupling between ^{29}Si and ^{93}Nb from the results of ^{29}Si - ^{93}Nb -REAPDOR NMR experiment. However, a more direct approach involves the measurement of the ^{17}O -MAS NMR spectra at very high spinning speeds. This is possible since the isotropic chemical shift values for the possible ^{17}O signals, Si-O-Si, Si-O-Nb, ONb $_2$ and ONb $_3$ are distinctively different. Whereas oxygen bridging two SiO_4 is found at a chemical shift value around 65 ppm, the ^{17}O signals in sol-gel processed Nb $_2\text{O}_5$ are reported at 360 ppm (ONb $_3$) and 560 ppm (ONb $_2$). In a study on mixed Nb $_2\text{O}_5$ -SiO $_2$ glasses, Drake et al. [29] assigned the signal at 250 ppm to Nb-O-Si linkages.

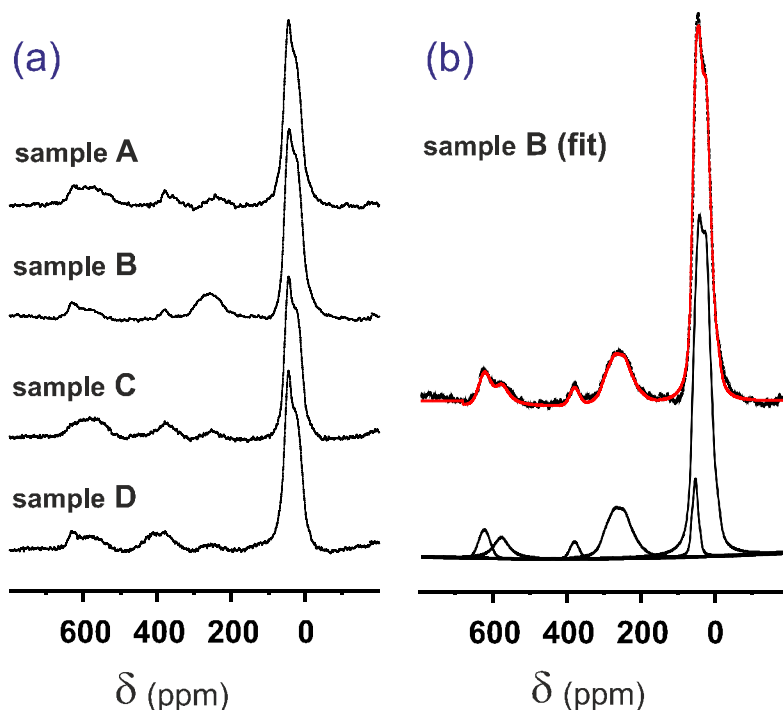


Figure 5.3. a) single pulse ^{17}O -MAS-NMR spectra of ^{17}O -enriched sol-gel derived niobia-hybrid silica powders, samples A-D. The spectra were recorded at 38 kHz, employing $\pi/8$ pulses and a repetition delay of 1s. The signal at 626 ppm represents a spinning sideband of the Si-O-Si signal at 65 ppm. b) ^{17}O MAS NMR spectrum of B together with its deconvolution.

The ^{17}O MAS NMR spectra for the studied samples are shown in Figure 5.3a. The single pulse excitation spectra were recorded using an excitation pulse of width $<\pi/8$ to ensure quantitative excitation. Attempts to detect the spectra employing a spin echo sequence were abandoned since the downfield signals (Nb-O-Si, ONb_2 and ONb_3) exhibited a considerably reduced intensity as compared to the single pulse excitation spectrum, presumably due to short T_2^* values. While the spectra for samples A, C and D exhibit all four signals (Si-O-Si at 65 ppm, Si-O-Nb at 300 ppm, ONb_3 at

350 ppm and ONb₂ at 560 ppm), in the spectrum for sample B only the signals for Si-O-Si, Nb-O-Si and ONb₂ can be identified. For the simulation of the ¹⁷O signal assigned to oxygen in Si-O-Si linkages (65 ppm) we had to use a set of two second order quadrupolar patterns. The dominating contribution exhibits a quadrupolar coupling constant C_Q = 4.8 MHz and an asymmetry parameter η_Q = 0 for all samples, and isotropic chemical shift values of 62 – 64 ppm, in perfect agreement with published data. The minor signal shows quadrupolar parameters of C_Q = 5.3 – 5.8 MHz, η_Q = 0.9 and an isotropic chemical shift of 66 – 72 ppm. This second signal may be assigned to terminal Si-OH groups, the presence of which is suggested by the results of the ²⁹Si MAS NMR spectra (vide supra). For the signal assigned to Nb-O-Si bridges the simulation produces quadrupolar parameters C_Q = 5.3 – 5.7 MHz, η_Q = 0.5 and chemical shift values of 280 – 310 ppm. The remaining signals (ONb₂ and ONb₃) did not have a well-defined shape. Therefore, Gaussian functions were used to simulate the signals of these entities, which can only provide the center of gravity and relative area of these lines. Fig. 3b exemplarily shows the simulation for the ¹⁷O MAS NMR spectrum of sample B. The results of a simulation of the spectra are collected in Table 1.

Before analyzing the results, let us first briefly discuss the expected ¹⁷O spectra for the two limiting cases of a) a complete segregation into a silica-based network and a Nb₂O₅ network and b) a homogeneous distribution of Nb and Si, both for the given Si/Nb ratio of 4:1. For the former, we would expect 71% of the oxygen to be incorporated in Si-O-Si bridges and 29% of the oxygen to be involved in Nb-O-Nb bonding. For a homogeneous distribution on the other hand we can calculate the relative ratios for the various types of A-O-B bridges with A,B = Si, Nb as follows. For a composition 4·(O₃Si-C-C-SiO₃): 1Nb₂O₅, ignoring oxygen triclusters, we have 34 bonds to oxygen, 24 from Si and 10 from Nb. This results in probabilities of (24/34)² = 0.5 for Si-O-Si, 24/34 · 10/34 · 2 = 0.4 for Si-O-Nb and (10/34)² = 0.1 for Nb-O-Nb.

Table 1: results of the simulation of the ^{17}O and ^{29}Si MAS NMR single pulse excitation spectra of the measured samples. The ^{17}O NMR signals for Si-O-Si and Nb-O-Si were simulated assuming a second order quadrupolar line shape. Due to the lack of resolution, the signals for O_3Nb and O_2Nb were simulated using Gaussian functions. For the ^{29}Si MAS NMR spectra, the center of gravity for the signals is given.

		Sample	A	B	C	D
^{17}O	Si-O-Si	C_Q (MHz)	4.9	4.9	4.9	4.8
		η_Q	0.2	0.3	0.3	0.3
		δ_{iso} (ppm)	64	64	64	62
		rel. area (%)	55	66	58	56
		C_Q (MHz)	3.3	3.2	3.5	3.5
		η_Q	0.9	0.9	0.9	n.d.
		δ_{iso} (ppm)	66	66	72	68
		rel. area (%)	13	7	10	14
	Nb-O-Si	C_Q (MHz)	5.3	5.7	5.2	5.3
		η_Q	0.5	0.4	0.6	0.6
		δ_{iso} (ppm)	280	303	291	293
		rel. area (%)	6	16	5	5
O_3Nb	δ (ppm)	372	381	379	394	
	rel. area (%)	6	3	10	12	
O_2Nb	δ (ppm)	583	585	582	586	
	rel. area (%)	20	10	18	10	
^{29}Si		δ_{CG} (ppm)	-60.0	-59.2	-59.2	-59.3

Based on the ^{13}C NMR data a distinct amount of acetylacetonate (sample B) and 2-methoxy-ethanol (sample C) is still present in the samples. This affects the total number of possible Nb-O-Si and Nb-O-Nb in the above calculation. As a consequence, no quantitative evaluation of the network adopted is possible and we can only take the relative fraction of Nb-O-Si as a rough measure for the degree of mixing in the samples studied.

Two main observations may be drawn from the results presented in Figure 5.3 and Table 5.1. Firstly, all samples exhibit – to a given extent – a mixing between Nb and Si on the atomic scale, as evidenced by the existence of the resonance at 300 ppm which originates in oxygen involved in Nb-O-Si linkages. Secondly, the extent of mixing between Nb and Si, proves to be rather limited, with the exception of sample B, which was prepared employing acetylacetonate as the complexing agent. Thus in samples A, C, and D, our results indicated a segregation of the networks in a Nb-rich and a silica rich part. These Nb₂O₅ segregations contain O-Nb₃ and O-Nb₂ which produce the signals around 380 ppm and 585 ppm. These values are rather close to those of the corresponding signals in a sol-gel derived Nb₂O₅ (550 ppm and 360 ppm) [30, 34].

The network in these samples can be described by a silsesquioxane-based network with segregated Nb₂O₅ particles distributed within the matrix. Only some Nb-O-Si bridges link these Nb₂O₅ segregates to the silica network. Contrary to this, in sample B the degree of mixing seems to be much more pronounced. Here, the observed relative areas of the individual ¹⁷O signals are much closer to a homogeneous mixture of Nb and Si. Moreover, in this case, no ONb₃ units are observed. Clearly, addition of acetylacetonate succeeds in slowing down the hydrolysis and polycondensation of Nb(OEt)₅, prevents larger aggregates of Nb₂O₅ being formed and consequently increases the relative amount of Si-O-Nb bridges.

A network model in accordance with all the observed data is presented in Figure 4. Small regions rich in Nb-O-Nb bonding are embedded within a silsesquioxane-based matrix, both connected via Nb-O-Si linkages. For samples A, C and D, these regions are relatively large and are more adequately described by nanoscaled Nb₂O₅ clusters. For sample B, these regions are considerably smaller, in addition, only a rather small amount of ONb₃ units seems to be present. The fraction of Nb-O-Si linkages found in this sample is 40 - 70% of the value expected for a statistical mixing of Nb and Si (depending on the amount of acac complexing Nb in the final material). The ethylene bridge is still present in the final network. Even at an annealing temperature of 200 °C, the bonds between Si and C do not suffer from being cleaved, as illustrated by the ¹³C and ²⁹Si MAS NMR spectra of sample D, annealed at 200 °C (data not shown). This result supports previously reported TGA-MS and FTIR measurements, which suggested that methylene bridged carbon atoms remained present in BTESE-based hybrids up to T=300°C [38]. Yet, more specifically the survival

of the Si-C bond upon annealing was unambiguously proved by these ^{13}C and ^{29}Si MAS NMR results.

5.5. Conclusions

Among the different approaches that were applied to enhance the dispersion of sol-gel derived niobia within the silsesquioxane matrix, the use of acetylacetone as a chelating ligand was found to be the most effective approach. The acac complex partly blocks the hydrolysis of niobium ethoxide. This entails an enhanced degree of hydrolyzed BTESE, as suggested by the enlarged intensity of the Si-OH stretch vibration in the FTIR experiment. The ^{17}O data indicate an increased chance that a hydrolyzed silicon crosslinks with a niobium species.

The distribution of oxygen among Si-O-Si, Nb-O-Si and Nb-O-Nb is found to be rather close to a statistical distribution, indicating an effective mixing of Nb and Si. Addition of 2-methoxyethanol on the other hand does not entail a substantial effect on the hydrolysis/polycondensation kinetics and subsequently on the network being formed. Contrary to the case of the acac ligand, only a fraction of Nb^{5+} will be coordinated by 2-MOE unless all the ethanol is removed by evaporation, as reported earlier. Therefore, its stabilizing effect is limited. As a consequence, the reactivity of NPE is only slightly reduced, in accordance with our observations.

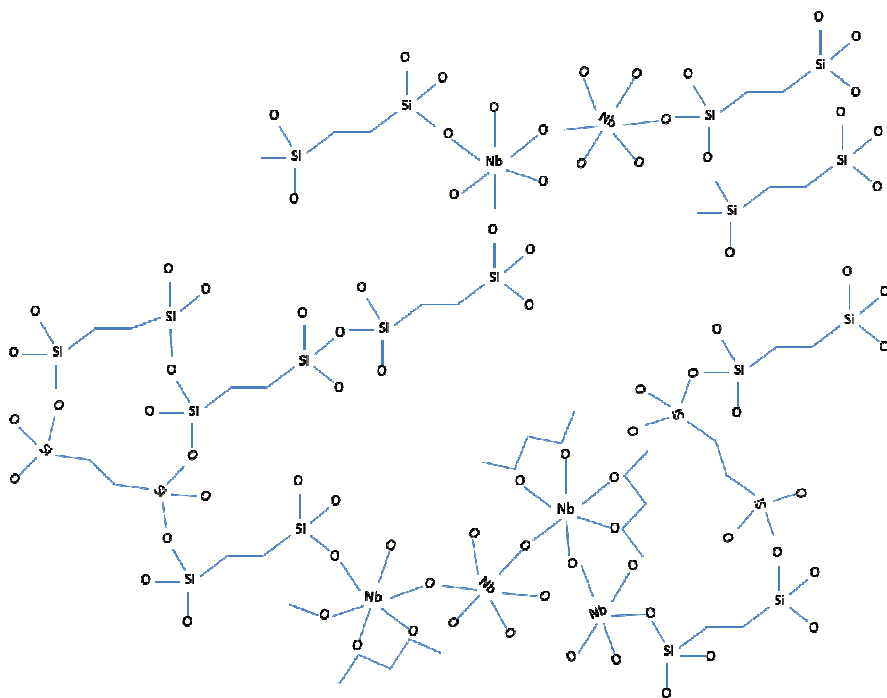


Figure 5.4. Sketch that illustrates the network organization in sample B as deduced from the NMR results.

5.6. References

1. Castricum, H.L., et al., *High-performance hybrid pervaporation membranes with superior hydrothermal and acid stability*. J. Membr. Sci., 2008. **324**(1-2): p. 111-118.
2. Kong, C., et al., *Enhanced performance of inorganic-polyamide nanocomposite membranes prepared by metal-alkoxide-assisted interfacial polymerization*. J. Membr. Sci., 2011. **366**(1-2): p. 382-388.
3. Castricum, H.L., et al., *Hybrid ceramic nanosieves: Stabilizing nanopores with organic links*. Chem. Commun., 2008 (9): p. 1103-1105.
4. Kreiter, R., et al., *Stable hybrid silica nanosieve membranes for the dehydration of lower alcohols*. ChemSusChem, 2009. **2**(2): p. 158-160.

5. Agirre, I., et al., *Hybrid organosilica membranes and processes: Status and outlook*. Sep. Purif. Technol., 2014. **121**: p. 2-12.
6. Kanezashi, M., et al., *Organic–inorganic hybrid silica membranes with controlled silica network size: Preparation and gas permeation characteristics*. J. Membr. Sci., 2010. **34** (1–2): p. 310-318.
7. Kreiter, R., et al., *Evaluation of hybrid silica sols for stable microporous membranes using high-throughput screening*. J. Sol-Gel Sci. Technol., 2011. **57**(3): p. 245-252.
8. Chang, K.-S., et al., *A molecular dynamics simulation of a homogeneous organic-inorganic hybrid silica membrane*. Chem. Commun., 2010. **46**(48): p. 9140-9142.
9. Igi, R., et al., *Characterization of co-doped silica for improved hydrothermal stability and application to hydrogen separation membranes at high temperatures*. J. Am. Ceram. Soc., 2008. **91**(9): p. 2975-2981.
10. Kanezashi, M. and M. Asaeda, *Hydrogen permeation characteristics and stability of Ni-doped silica membranes in steam at high temperature*. J. Membr. Sci., 2006. **271**(1-2): p. 86-93.
11. Qi, H., et al., *Effect of Nb content on hydrothermal stability of a novel ethylene-bridged silsesquioxane molecular sieving membrane for H₂/CO₂ separation*. J. Membr. Sci., 2012. **421–422**: p. 190-200.
12. Qi, H., et al., *Hybrid Organic–Inorganic Microporous Membranes with High Hydrothermal Stability for the Separation of Carbon Dioxide*. ChemSusChem, 2010. **3**(12): p. 1375-1378.
13. Boffa, V., et al., *Microporous niobia-silica membrane with very low CO₂ permeability*. ChemSusChem, 2008. **1**(5): p. 437-443.
14. Boffa, V., et al., *Microporous niobia-silica membranes: Influence of sol composition and structure on gas transport properties*. Micropor. Mesopor. Mat., 2009. **118**(1-3): p. 202-209.
15. Yoshida, K., et al., *Hydrothermal stability and performance of silica-zirconia membranes for hydrogen separation in hydrothermal conditions*. J. Chem. Eng. Jpn., 2001. **34**(4): p. 523-530.
16. Ziolk, M. and I. Nowak, *Synthesis and characterization of niobium-containing MCM-41*. Zeolites, 1997. **18**(5–6): p. 356-360.
17. Nowak, I., *Frontiers in mesoporous molecular sieves containing niobium: From model materials to catalysts*. Catal. Today, 2012. **192**(1): p. 80-88.
18. Sedlar, M. and M. Sayer, *Reactivity of titanium isopropoxide, zirconium propoxide and niobium ethoxide in the system of 2-*

- methoxyethanol, 2,4-pentanedione and water*. Journal of Sol-Gel Science and Technology, 1995. **5**(1): p. 27-40.
19. Spijksma, G.I., et al., *Stabilization and destabilization of zirconium propoxide precursors by acetylacetone*. Chem. Commun., 2004. **10**(16): p. 1874-1875.
 20. Bradley, D.C. and C.E. Holloway, *Nuclear magnetic resonance studies on niobium and tantalum penta-alkoxides*. J. Chem. Soc. A 1968: p. 219-223.
 21. Ibers, J.A., *Crystal and Molecular Structure of Titanium (IV) Ethoxide*. Nature, 1963. **197**(4868): p. 686-687.
 22. Blanchard, J., et al., *Hydrolysis and Condensation Reactions of Transition Metal Alkoxides: Calorimetric Study and Evaluation of the Extent of Reaction*. European J. Inorg. Chem., 1998. **1998**(8): p. 1115-1127.
 23. Leautic, A., F. Babonneau, and J. Livage, *Structural investigation of the hydrolysis-condensation process of titanium alkoxides Ti(OR)₄ (OR = OPr-iso, OEt) modified by acetylacetone. 1. Study of the alkoxide modification*. Chem. Mater., 1989. **1**(2): p. 240-247.
 24. Pickup, D.M., et al., *A structural study of (TiO₂)_x (SiO₂)_{1-x} (x= 0.18, 0.30 and 0.41) xerogels prepared using acetylacetone*. J. Mater. Chem., 1999. **9**(6): p. 1299-1305.
 25. Gervais, C., F. Babonneau, and M.E. Smith, *Detection, Quantification, and Magnetic Field Dependence of Solid-State 17O NMR of X-O-Y (X, Y = Si, Ti) Linkages: Implications for Characterizing Amorphous Titania-Silica-Based Materials*. The Journal of Physical Chemistry B, 2001. **105**(10): p. 1971-1977.
 26. Delattre, L. and F. Babonneau, *17O Solution NMR Characterization of the Preparation of Sol-Gel Derived SiO₂/TiO₂ and SiO₂/ZrO₂ Glasses*. Chemistry of Materials, 1997. **9**(11): p. 2385-2394.
 27. Nowak, I. and M. Ziolk, *Niobium Compounds: Preparation, Characterization, and Application in Heterogeneous Catalysis*. Chemical Reviews, 1999. **99**(12): p. 3603-3624.
 28. Bonhomme, C., et al., *Advanced Solid State NMR Techniques for the Characterization of Sol-Gel-Derived Materials*. Acc. Chem Res., 2007. **40**(9): p. 738-746.
 29. Drake, K.O., et al., *A multinuclear solid state NMR study of the sol-gel formation of amorphous Nb₂O₅-SiO₂ materials*. Solid State Nuc. Mag., 2005. **27**(1-2): p. 28-36.
 30. Julián, B., et al., *Solid-State 17O NMR Characterization of PDMS-MxOy (M = Ge(IV), Ti(IV), Zr(IV), Nb(V), and Ta(V))*
-

-
- Organic–Inorganic Nanocomposites*. Chem. Mater., 2004. **16**(3): p. 521-529.
31. Holland, M.A., et al., *Synthesis, characterisation and performance of (TiO₂) 0.18 (SiO₂) 0.82 xerogel catalysts*. J. Mater. Chem., 2000. **10**(11): p. 2495-2501.
 32. Babonneau, F. and J. Maquet, *Nuclear magnetic resonance techniques for the structural characterization of siloxane–oxide hybrid materials*. Polyhedron, 2000. **19**(3): p. 315-322.
 33. Cedeño, L., et al., *Synthesis of Nb-containing mesoporous silica molecular sieves: Analysis of its potential use in HDS catalysts*. Appl. Catal. A: General, 2003. **241**(1–2): p. 39-50.
 34. Julián, B., et al., *Synthesis and Characterization of Transparent PDMS–Metal-Oxo Based Organic–Inorganic Nanocomposites*. Chem Mater., 2003. **15**(15): p. 3026-3034.
 35. Nakamoto, K., *Infra red and Raman spectra of Inorganic and coordination compounds*. 4 ed, ed. K. Nakamoto 1986, New York: John Wiley & Sons. 259-263.
 36. Jiang, H., Z. Zheng, and X. Wang, *Kinetic study of methyltriethoxysilane (MTES) hydrolysis by FTIR spectroscopy under different temperatures and solvents*. Vib. Spectrosc., 2008. **46**(1): p. 1-7.
 37. Cai, Y., et al., *Electrochemical synthesis, characterization and thermal properties of niobium ethoxide*. J. Cent. South Univ. T., 2011. **18**(1): p. 73-77.
 38. Castricum, H.L., et al., *Hydrothermally stable molecular separation membranes from organically linked silica*. J. Mater. Chem., 2008. **18**(18): p. 2150-2158.

6.

Crystallized $\text{Nb}_8\text{O}_{10}(\text{OEt})_{20}$ from condensation of niobium ethoxide and acetone that exhibits remarkable anisotropy in thermal expansion

6.1. Abstract

Acetone is a useful oxolation source for niobium penta-ethoxide (NPE). Its mild reactivity allows the controlled condensation and crystallization of nanosized $\text{Nb}_8\text{O}_{10}(\text{OEt})_{10}$ at room temperature. The condensation process occurs via two complementary routes: (1) aldol condensation and (2) ether elimination. The structure refinement on the crystallites at $T=150\text{K}$ and $T=296\text{K}$ revealed a remarkable anisotropy in the thermal expansion of $\text{Nb}_8\text{O}_{10}(\text{OEt})_{20}$ with a negative expansion coefficient along the c -axis. At reduced temperatures the $\text{Nb}_8\text{O}_{10}(\text{OEt})_{20}$ clusters were tilted towards the a and c -axis, most likely driven by a reduction of thermal motion and steric hindrance. Moreover, the irregular shape of the clusters allowed a relatively large compression along the a -axis and a relatively large expansion along the c -axis.

6.2. Introduction

Nanosized molecular clusters are extremely useful building blocks for the bottom-up synthesis of advanced materials in a variety of different applications, such as catalysts, optics, electronics, and membranes [1-6]. By coordination of such clusters with organic linkages or coordination polymers, complex 3D hierarchal and polymeric structures can be synthesized that exhibit well-defined pore sizes and tailor-made functionalities [1-6]. Well defined clusters can be formed through controlled hydrolysis and condensation of metal alkoxides. Yet, conventional hydrolysis and condensation routes have extremely high reactivity, which complicates the synthesis of monodisperse metal-oxo clusters [7, 8]. Alternatively, water may be replaced by less nucleophilic oxolation sources, such as alcohols, esters and ketones [9-12], which therefore reduced its activation energy: a pathway that is referred as the non-hydrolytic sol-gel (NHSG) route. Even without the use of surfactants well-defined monodisperse crystalline nanosized metal oxides can be synthesized [13, 14].

The research presented here was particular focused on nanosized niobium oxo-alkoxo clusters. Nanosized niobia crystallites are well known Brönsted/Lewis acidic catalysts [15-18] and niobia is an n -type semiconductor with a band gap of 3.4 eV, suitable for applications including

gas sensing, photocatalysis and dyes for solar cells [18-21]. Despite its potential and contrary to group IV transition metal oxo alkoxide clusters [1, 22], relatively little is known about group V oxo alkoxide clusters and only a few different isolated niobium oxo alkoxide clusters have been reported [23-30]. The results presented here demonstrate the formation of high purity $\text{Nb}_8\text{O}_{10}(\text{OEt})_{20}$ via a straightforward synthesis and crystallization procedure at room temperature.

The crystal structure was refined at two different temperatures, i.e. 150 K and 296 K, and was found to exhibit anisotropic thermal expansion behavior, with a negative thermal expansion coefficient along the *c*-axis. Strongly negative thermal expansion behavior is typically observed in frameworks that exhibit strongly anharmonic interatomic or intermolecular potentials along certain orientations, such as metal cyanides [31, 32], metal tungstates/vanadates [33], zeolites [34] and metal organic frameworks [35]. In organic molecules where steep anharmonic potentials are absent and molecules are held together through rather weak Van der Waals (VdW) forces, anisotropic thermal expansion is rarely observed [36, 37]. A remarkable exception is the anisotropic thermal expansion behavior of several acene crystals which are held together solely through VdW forces [36]. These elongated acene molecules were packed together, not exactly plane parallel, but slightly tilted. As illustrated in Figure 6.1 the tilt angle of the elongated molecules increased with increasing temperature due to increased thermal motion and steric hindrance. Consequently, the unit cell elongated particularly along the *a*-axis and to a much smaller extent along the *b*-axis. Among several acene molecules the thermal deformation showed the highest anisotropic behavior for the most elongated molecule that was being analyzed, i.e. pentacene, which was found to have a negative thermal expansion coefficient along the *b*-axis of $\alpha_b = -35 \pm 6 \cdot 10^{-6} \text{ K}^{-1}$. In analogy with pentacene, elongated $\text{Nb}_8\text{O}_{10}(\text{OEt})_{20}$ clusters consist of a rather rigid core, where they are packed in a similar

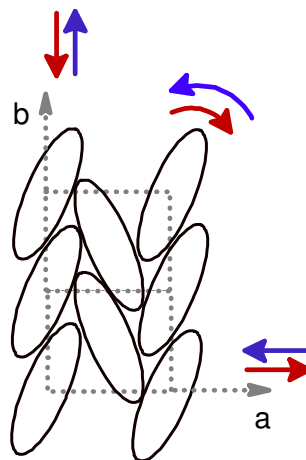


Figure 6.1. Thermal expansion behavior of elongated pentacene molecules as described by Haas et al. [36].

tilted arrangement. Due to the surrounding ethoxide groups intermolecular attractive forces are solely rather weak VdW forces. As will be shown below, the thermal expansion behavior is similar to that of acene.

6.3. Experimental Section

Before use, toluene (99%, Alfa Aesar) and acetone (99,9%) were dried over anhydrous sodium sulphate (99,0%, Sigma-Alrich). All samples were prepared inside a glove box under dry nitrogen atmosphere and the crystallites were grown inside 5 mL polypropylene test tubes with polypropylene screw caps (VWR).

Procedure A: 50 mmol acetone was added to 5 mmol niobium(V) ethoxide (ABCR Chemicals, 99,99%, abbreviated as NPE). After vigorous shaking the mixture was aged for 1 week at room temperature. Crystallites were removed with tweezers and characterized by ^1H and ^{13}C NMR spectroscopy. Procedure B: 5 mmol NPE was dissolved in 30 mmol toluene. While gently stirring the solution with a lab dancer, 20 mmol acetone was added dropwise. After aging the solution for 2 weeks another 10 mmol acetone was added dropwise and then after 2 h the crystallites were removed with tweezers and characterized by ^1H and ^{13}C NMR spectroscopy and by single X-ray diffraction.

At room temperature ($T = 298(3)$ K), the data collection was carried out at room temperature using Bruker SMART Apex-II diffractometer with Mo-K_α radiation ($\lambda = 0.71073$ Å). 9356 symmetrically independent reflections were collected in the interval $2.73 < 2\theta < 29.46$. The structure was solved by direct methods. All metal atom coordinates were located in the initial solution and the oxygen and carbon atoms were found in the subsequent difference Fourier syntheses. All non-hydrogen atoms were refined first isotropically and then anisotropically. Hydrogen atom coordinates were calculated geometrically and the results of their isotropic refinement were included into the final solution. Final discrepancy factors were $R1 = 0.0430$ and $wR2 = 0.1097$ for the 6419 observed with $I > 2$ sigma(I). For the measurements at $T = 150\text{K}$, the crystal was cooled with an Oxford cryosystem liquid nitrogen cooling.

6.4. Results and Discussion

6.4.1. Synthesis and characterisation of crystallites

Procedure A: When acetone was added to NPE a white haze formed, which slowly disappeared under vigorous shaking. After 2 days of aging, the first crystallites of ~ 0.5 mm diameter were observed by the naked eye and after ~ 1 week, the crystallites seemed to have stopped growing. The hexagonal/trigonal prism shaped crystallites (Figure 6.2a) have sizes varying between 1 and 6 mm. The crystallites were characterized by NMR spectroscopy and the characteristic resonances are given in Table 6.1. During aging, the solution changed its colour from colourless to orange/yellow in one week time.

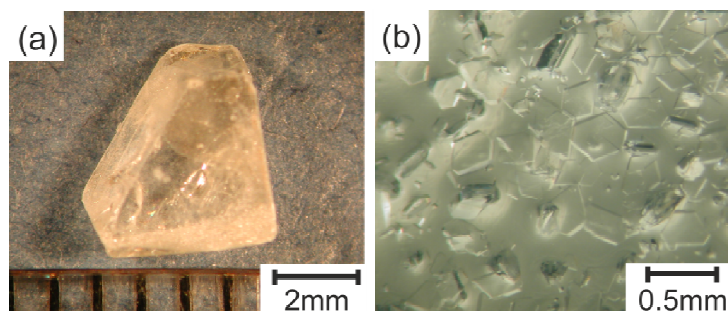
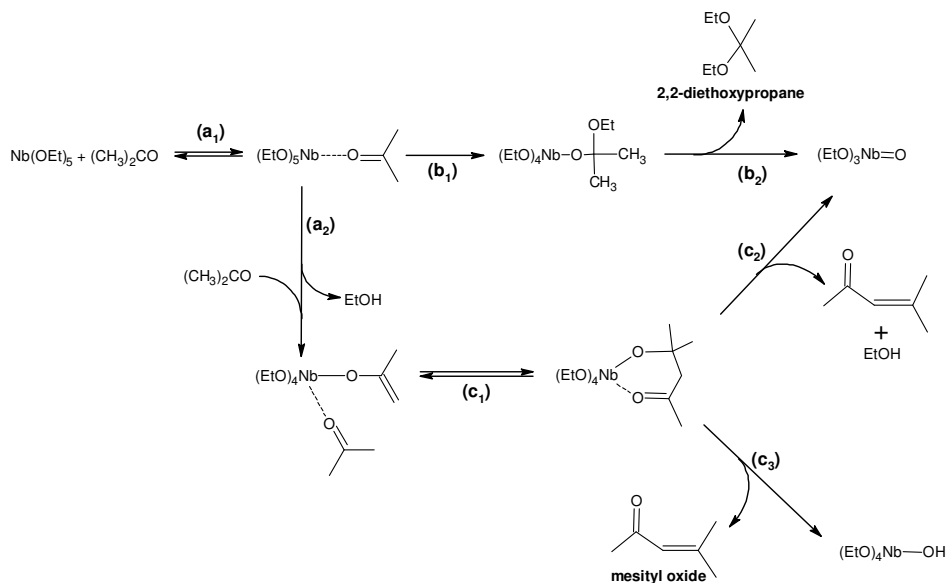


Figure 6.2. Optical images of crystallized $\text{Nb}_8\text{O}_{10}\text{OEt}_{20}$ following (a) procedure A, (b) procedure B.

Table 6.1. ^1H and ^{13}C NMR assignment of $\text{Nb}_8\text{O}_{10}(\text{OEt})_{20}$.

Assignment		$\delta^1\text{H}$	$\delta^{13}\text{C}$
Bridged ethoxide	CH_2	4.67 (dq)	70.64
		4.48 (m)	
	CH_3	1.24 (m)	18.45
Pendant ethoxide	CH_2	4.45 (m)	69.55
		4.36 (m)	
	CH_3	1.19 (m)	18.11

$^1\text{H-NMR}$ and $^{13}\text{C-NMR}$ measurements revealed that residual solvent after filtration contained 0.55 mol 2,2-diethoxypropane and 0.67 mol mesityl oxide per mol NPE that was added to the solution. Both by-products originated from two different complementary processes: (1) 2,2-diethoxypropane, which was most likely being formed through an ether elimination process as reported for $\text{MoO}(\text{OEt})_4$ [38]. After coordination of acetone to the Nb-cation (Scheme 6.1a₁), nucleophilic ethoxy groups were substituted to the enolic carbon atom of acetone (Scheme 6.1b₁, b₂). Then, by the release of the enolic oxygen from acetone $(\text{EtO})_3\text{Nb}=\text{O}$ was formed, which through further ether elimination yielded $\text{Nb}_8\text{O}_{10}(\text{OEt})_{20}$ [24]. (2) Mesityl oxide, a known self-condensation product of acetone, which formed through an aldol addition (Scheme 6.1c₁), followed by crotonization of diacetone alcohol (Scheme 6.1c₂ and c₃) [12, 39]. After two days FTIR experiments revealed a broad OH-stretch vibration at 2480 cm^{-1} which was associated with Nb-OH groups [40] and Nb=O vibrations at 920 and 860 cm^{-1} [24]. Therefore, crotonization may yield both $(\text{EtO})_3\text{Nb}=\text{O}$ (Scheme 6.1c₂) and $(\text{EtO})_4\text{Nb-OH}$ (Scheme 6.1c₃). Subsequently, $\text{Nb}_8\text{O}_{10}(\text{OEt})_{20}$ can be formed through further condensation and ether elimination mechanisms.



Scheme 6.1. Possible non-hydrolytic hydrolysis pathways of NPE with acetone: (a₁) Coordination of acetone onto the Nb⁵⁺ cation, (a₂) Ligand exchange between enolic acetone and an ethoxy ligand, (b₁ and b₂) ether elimination of NPE, (c₁) aldol addition, (c₂ and c₃) crotonization of diacetone alcohol to mesityl oxide.

Procedure B: During aging the solution for 2 weeks the colour of the solution changed from colourless to orange/yellow. No precipitate/crystallite formed after 0-4 weeks of aging the solution. After 2 weeks of aging crystallization was induced by adding another 10 mmol of acetone. Following, this procedure smaller hexagonal prism shaped crystallites were formed with lateral dimensions in the range between 0.1 - 0.5 mm (Figure 6.2b). These crystallites were found to be more suitable for single X-ray diffraction and gave identical resonance peaks than the crystals from procedure A.

6.4.2. Structure refinement

By means of single X-ray diffraction the crystallites that had formed in procedure B were identified as Nb₈O₁₀(OEt)₂₀ clusters arranged in a monoclinic unit cell with a P2₁/n symmetry. The structure was resolved at two different temperatures, i.e. 150 and 296 K, on two different crystallites. The lattice dimensions are listed in Table 6.2. Similar structures have been reported by Kessler [24] and Bradley [23], however these had been synthesized following other procedures. Kessler synthesized Nb₈O₁₀(OEt)₂₀ by ligand exchange of NbOCl₃ with NaOEt, which was followed by ether elimination of NbO(OEt)₃. Already in 1968 Bradley and coworkers isolated Nb₈O₁₀(OEt)₂₀ after partial hydrolysis of Nb(OEt)₅ [23]. Yet, due to some uncertainties, the structure was not completely resolved. The lattice dimensions were reported but not the exact atomic positions. For the sake of comparison the reported unit cell dimensions are also listed in Table 6.2. The bond angles and bond distances of the resolved structures at 150 K, at 296 K and the structure derived from NbOCl₃ [24] are given for all core atoms in Table S6.1 and S6.2 of the supplementary information, respectively. We used the same labels as previously reported [24]. However, distorted atoms were represented by A and B-labels Figure 6.3 for the 150K structure and the C7 label was not being used.

The differences in lattice dimensions between the 296 K sample and the NbOCl₃-derived sample [24] were substantially smaller as compared to structural differences at 150 and 296 K. Among the structures being resolved at different temperatures a remarkable anisotropic deformation was observed. With a decreasing temperature both the *a* and *b* axis reduced in length, i.e. $\alpha_a \sim 2.3 \cdot 10^{-6} \text{ K}^{-1}$ and $\alpha_b \sim 104 \cdot 10^{-6} \text{ K}^{-1}$), while the *c*-axis

increased in length ($\alpha_c \sim -47 \cdot 10^{-6} \text{ K}^{-1}$). On the other hand, bond angles and bond distances between niobium and the bridging oxygen atoms (O1-O8) changed with less than 1% (Table 6.3), Appendix Table A1 and A2). Therefore, the deformation was probably not induced by distortion of the Nb octahedra. Instead, the anisotropy in thermal expansion in this case is probably caused by differences in VdW forces between clusters along different directions. The directions along which the intermolecular interactions between clusters are relatively weak allow a larger expansions as compared to the directions along which these interactions are relatively strong [41].

Table 6.2. Comparison of lattice parameters between several refined structures of $\text{Nb}_8\text{O}_{10}\text{OEt}_{20}$.

Synthesized from		$\text{Nb}(\text{OEt})_5$ + $(\text{CH}_3)_2\text{CO}$	$\text{Nb}(\text{OEt})_5$ + $(\text{CH}_3)_2\text{CO}$	NbOCl_3 + NaOEt	Hydrolysis of $\text{Nb}(\text{OEt})_5$
Temperature diffraction measurements		150 K	296 K	283-303 K	283-303 K
Reference		This work	This work	[24]	[23]
Symmetry space group H-M		P 21/n	P 21/n	P 21/n	P 21/n
Lattice parameters					
cell lengths (Å)	<i>a</i>	14.9279(12)	14.933(3)	14.9169(9)	14.96
	<i>b</i>	14.0269(15)	14.242(3)	14.2541(7)	14.36
	<i>c</i>	16.9730(15)	16.856(3)	16.8726(8)	16.84
cell angles (°)	α, γ	90	90	90	90
	β	91.733(4)	91.577(2)	91.754(4)	91.0
cell volume (Å ³)		3402.3(6)	3583.7(12)	3585.9(3)	3617

Since the niobium-oxo core is well shielded by ethoxide groups cluster-cluster interactions are dominated by VdW forces which strongly decay with increasing atomic distances. The intermolecular carbon-carbon distances in reveal several short range interactions in the range between 3.7 and 4.5 Å along the [100], [010], [111] and $[\bar{1}\bar{1}\bar{1}]$ directions (Table 6.4). In contrast, the shortest and second shortest C-C distances at 296 K along the [001] direction were 5.4 and 7.2 Å, respectively. As is also illustrated in Figure 6.4a and Figure 6.4b, the gap along the [001] is substantially larger than along [100] and [010]. At lower temperatures, Van der Waals

interactions become increasingly important, causing contraction along the [100] and [010] axes due to stronger VdW interactions than in the [001] direction. Since clusters are packed in a body centered cube-like geometry, compression along [100] and [010] cause stress along close-packed [111] and $[\bar{1}\bar{1}\bar{1}]$ diagonals (Figure 6.4a). Consequently, the stress along the diagonals causes expansion of clusters along [001].

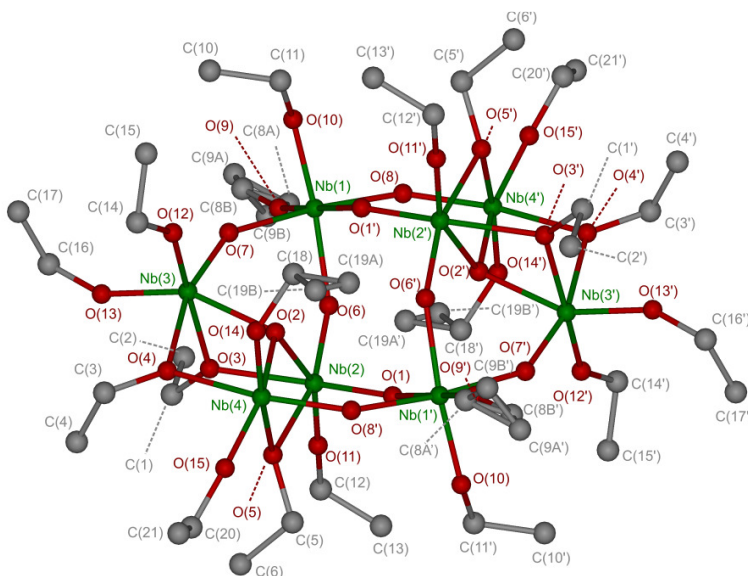


Figure 6.3. Assignment of the resolved $\text{Nb}_8\text{O}_{10}(\text{OEt})_{20}$ structure measured at 150K.

The compression along the $\langle 111 \rangle$ diagonals also caused a screw-like rotation of the clusters. In analogy with acene crystals, the elongated direction of the molecules become more aligned upon reducing the temperature. The direction of elongation of the rigid core could be described by a vector going from the origin of inversion symmetry to the O4 atom (Figure 6.3). Note that pendant oxygen atoms that are more flexible were not considered to be part of the rigid core.

Table 6.3. Selection of relevant bond angles of the Nb₈O₁₀(OEt)₂₀ structures.

	Bond angles			Differences (°)	
	Nb(OEt) ₅	Nb(OEt) ₅	NbOCl ₃	150K vs. 296K	NbOCl ₃ vs. Nb(OEt) ₅
Synthesized from					
Temperature	150 K	296 K	283-303 K		
Reference	This work	This work	[24]		
Nb1-O1-Nb2	144.61(9)	143.75(16)	144.2(2)	0.9	0.4
Nb1-O6-Nb2	147.02(10)	147.28(16)	147.1(2)	-0.3	-0.2
Nb1-O7-Nb3	145.74(10)	146.08(18)	146.3(2)	-0.3	0.2
Nb1-O8-Nb4	144.86(9)	144.70(17)	144.3(3)	0.2	-0.4
Nb2-O5-Nb4	101.54(7)	101.32(12)	101.42(19)	0.2	0.1
Nb2-O2-Nb3	106.95(7)	107.14(13)	106.9(2)	-0.2	-0.2
Nb2-O2-Nb4	108.24(7)	108.19(13)	107.79(17)	0.0	-0.4
Nb2-O3-Nb3	102.23(7)	102.12(12)	102.25(18)	0.1	0.1
Nb3-O2-Nb4	111.49(7)	111.39(13)	111.62(19)	0.1	0.2
Nb3-O4-Nb4	103.40(7)	103.19(12)	103.33(19)	0.2	0.1
O6-Nb1-O9	95.59(8)	92.77(14)	93.2(2)	2.8	0.4
O6-Nb1-O10	164.89(8)	166.00(16)	166.49(19)	-1.1	0.5
O7-Nb1-O9	94.92(8)	93.80(15)	94.54(19)	1.1	0.7
O7-Nb1-O10	86.37(8)	85.59(16)	85.90(17)	0.8	0.3
O1-Nb1-O7	89.68(7)	88.36(12)	88.47(17)	1.3	0.1
O8-Nb1-O9	90.49(8)	92.44(15)	91.61(19)	-2.0	-0.8
O9-Nb1-O10	95.31(9)	95.17(17)	94.6(2)	0.1	-0.6
O1-Nb1-O9	175.34(8)	176.14(13)	175.73(19)	-0.8	-0.4
O1-Nb1-O10	85.72(8)	88.18(16)	88.61(17)	-2.5	0.4
O2-Nb4-O14	94.07(7)	96.13(13)	95.57(18)	-2.1	-0.6
O5-Nb4-O14	168.23(7)	170.69(14)	170.56(19)	-2.5	-0.1
O14-Nb4-O15	100.38(8)	98.77(18)	98.8(2)	1.6	0.0
O8-Nb4-O14	93.44(8)	92.30(15)	92.95(19)	1.1	0.7

Consequently, the screw-like rotation with decreasing temperature from 296 to 150 K can be described by two rotations: Firstly, a clockwise rotation of $\theta_{O4} = 1.605^\circ$ along the unit vector $u_{-O4} = [0.769, -0.025, 0.639]$. The unit vector was chosen perpendicular to both O4 vectors to align the O4 at 296 K to the O4 at 150 K. Secondly, a counter-clockwise rotation of $\phi_{O4} = 0.662^\circ$ along the unit vector $u_{O4} = [0.395, 0.804, -0.445]$ that was chosen in line with the O4 vector to align Nb1 atoms. For the sake of comparison an overlay of packed clusters was made within the (110) plane at 150 and 296 K, with the right bottom cluster being aligned using the above described rotation angles, see Figure 6.5. As compared to the 296 K structure the 150 K structure is tilted, causing clusters to be packed more closely along the

[110] direction. Due to reduction of the tilt angle with respect to the [001] direction the crystal structure was elongated along the [001] direction.

Table 6.4. Intermolecular distances (Å) between specific carbon atoms between Nb₈O₁₀(OEt)₂₀ clusters.

Along the axes			Along the diagonals †		
[100]	T = 150K	T = 296K	[111] †	T = 150K	T = 296K
C9A-C9A	6.00(3)	6.24(3)	C6-C10A	4.033(6)	4.27(3)
C9B-C9B	4.71(3)		C6-C10B		3.98(3)
C9A-C19A	4.425(17)	4.36(3)	C6-C11A	4.827(6)	4.12(3)
C9B-C19B	4.06(6)		C6-C11B		4.38(3)
C9A-C19B	3.689(15)		C10A-C2	3.937(6)	4.79(4)
C9B-C19A	5.04(4)		C10B-C2		3.98(3)
C9A-C21	4.074(18)	4.14(3)	C11A-C2	4.192(5)	4.12(3)
C9B-C21	3.72(7)		C11B-C2		4.38(3)
			C10A-C16	4.494(6)	4.79(4)
[010]	T = 150K	T = 296K	C10B-C16		4.69(3)
C4-C2	5.558(6)	4.278(17)	C11A-C16	3.852(7)	4.16(3)
C4-C12	4.041(6)	4.475(15)	C11B-C16		4.01(3)
C4-C13	4.941(7)	4.983(19)	C10A-C17	5.543(6)	5.39(3)
C6-C1	4.098(4)	4.275(14)	C10B-C17		5.65(3)
C6-C2	4.647(6)	4.431(18)	C11A-C17	4.65(6)	4.59(3)
C6-C16	4.419(5)	4.474(15)	C11B-C17		4.65(3)
[001]	T = 150K	T = 296K	[111] †	T = 150K	T = 296K
C10A-C15	5.475(5)	5.36(3)	C3-C12	4.64(4)	5.508(13)
C10B-C15		5.60(3)	C3-C13	3.92(6)	3.977(16)
C13-C17	6.952(5)	7.210(17)	C3-C19A	4.040(13)	4.21(3)
			C3-C19B	3.77(3)	
			C4-C19A	4.57(3)	4.26(3)
			C4-C19B	4.04(3)	
			C14-C13	4.1(3)	4.266(18)
			C19A-C13	5.141(9)	4.30(3)
			C19B-C13	4.38(4)	

† Distance from (x,y,z) to (½-x,½+y,½-z) positions.

† Due to symmetry [111] = [1̄1̄1] and [111] = [1̄1̄1]

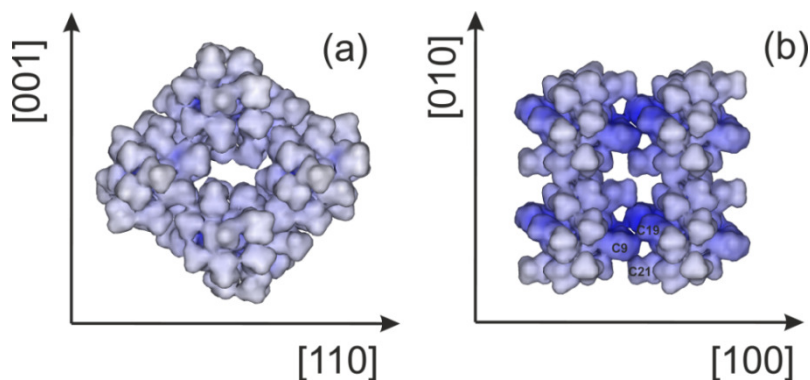


Figure 6.4 Surface exposed representation of packed $\text{Nb}_8\text{O}_{10}(\text{OEt})_{20}$ clusters at 150 K: (a) 4 clusters packed within the $(\underline{11}0)$ plane and (b) 4 clusters packed within the (001) plane.

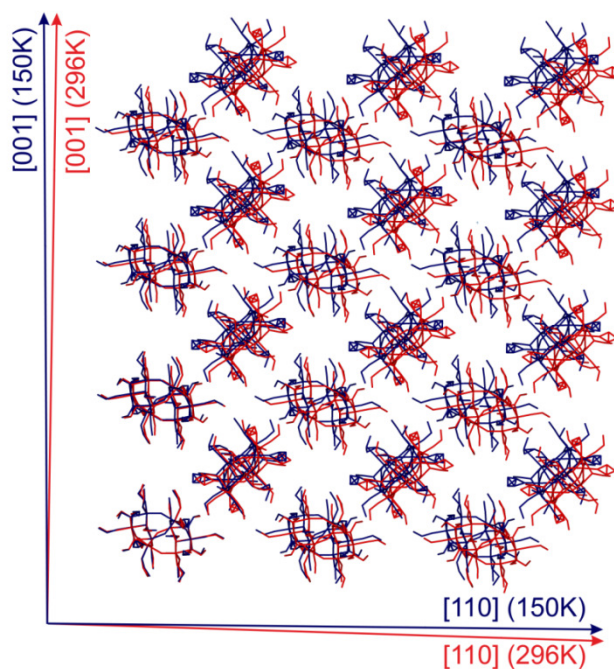


Figure 6.5. Comparison of stacking of $\text{Nb}_8\text{O}_{10}(\text{OEt})_{20}$ clusters at 150 K and 296 K, respectively, within the $(\underline{11}0)$ plane, with the right bottom clusters being aligned with each other by clockwise rotations: $\theta_{O_4} = 1.605^\circ$ along the unit vector $\mathbf{u}_{\perp O_4} = [0.769, -0.025, 0.639]$, $\phi_{O_4} = 0.662^\circ$ along the unit vector $\mathbf{u}_{\parallel O_4} = [0.395, 0.804, -0.445]$, in line with the O_4 vector.

Moreover, the contraction along the *b*-axis is substantially larger than along the *a*-axis. In comparison with the previous reported structure [24] the *a*-axis was even slightly larger while the temperature was lower. To understand the cause of this large difference we may consider the niobium-oxo core as an ellipsoidal cage with O4, Nb1 and Nb2 that span this cage, as illustrated in Figure 6.6. The vector $\mathbf{v}_1 = [1.82, 3.92, -2.04]$ was described as the vector going from the origin of inversion to O(4), $\mathbf{v}_2 = [-2.36, 0.20, -1.72]$ was described as an orthogonal vector to \mathbf{v}_1 such that the ellipse that spans $\{\mathbf{v}_1, \mathbf{v}_2\}$ crosses Nb1, and $\mathbf{v}_3 = [-0.84, 1.05, 1.24]$ was described such that Nb2 lies within the ellipsoidal surface that spans $\{\mathbf{v}_1, \mathbf{v}_2, \mathbf{v}_3\}$. Moreover, \mathbf{v}_4 is the vector within the ellipse that spans $\{\mathbf{v}_2, \mathbf{v}_3\}$ and is perpendicular to the rotation vector \mathbf{u}_{-O4} . The ellipse that spans $\{\mathbf{v}_1, \mathbf{v}_4\}$ is more elongated ($\|\mathbf{v}_1\| / \|\mathbf{v}_4\| = 2.57$) than the ellipse that spans $\{\mathbf{v}_2, \mathbf{v}_3\}$ with $\|\mathbf{v}_2\| / \|\mathbf{v}_3\| = 1.57$. Therefore, the θ_{O4} rotation along \mathbf{u}_{-O4} has a more profound effect on the thermal expansion as compared to the ϕ_{O4} rotation. Upon cooling the θ_{O4} rotation caused the \mathbf{v}_1 vector to engage both the *a* and *c* axis with 0.069 and 0.086 Å, respectively, and it moved 0.076 Å away from the *b*-axis. The θ_{O4} rotation explained the substantial shrinkage along *b*, however it would cause a similar degree of expansion along both *a* and *c* upon cooling. In addition, the ϕ_{O4} rotation caused the vector \mathbf{v}_2 to approach the *a*-axis which would also imply a small increase of the *a*-axis upon cooling.

The limited expansion along the *a*-axis can be explained by the irregular shape of the Nb₈O₁₀(OEt)₂₀ cluster. Upon contraction along the *a*-axis the C9 atom of an ethoxide group being attached to Nb1 penetrated in between C21 and C19 of ethoxide groups being attached to Nb3 of its adjacent cluster along the *a*-axis as illustrated in Figure 6.4b. Hence, it allows Nb1 to approach its neighbouring Nb3 from 10.19 Å at 296K to 9.47 Å at 150K without paying a very high penalty in terms of repulsive forces between the ethoxide groups.

However, this compression caused some disorder in the case of both C9 and C19. Due to the reduced amount of available space the ethoxide groups of these carbon atoms may have difficulties finding their optimal geographical configuration, which allows for the existence of two

configurations. Moreover, O-Nb-O bond angles revealed a substantial deformation of the ethoxide groups being attached to Nb1, i.e. the O9-C8-C9 and the O10-C11-C10 ethoxide groups (Table 6.3) O9 engaged O8 with 2.0° and O10 engaged O1 with 2.4° , while the angle O9-Nb1-O10 remained almost constant. Thus, the interaction between C9 with both C19 and C21 of its adjacent cluster caused a tilt of the O9 atom, which engaged the O10 atom that consequently tilted as well. In addition, the O2-Nb4-O14 decreased with 2.0° and the O15-Nb4-O14 increased with 1.6° . The deformation of the O14-C18-C19 ethoxide was most likely also a consequence of the C19-C9 interference of adjacent clusters along the a -axis at a reduced temperature.

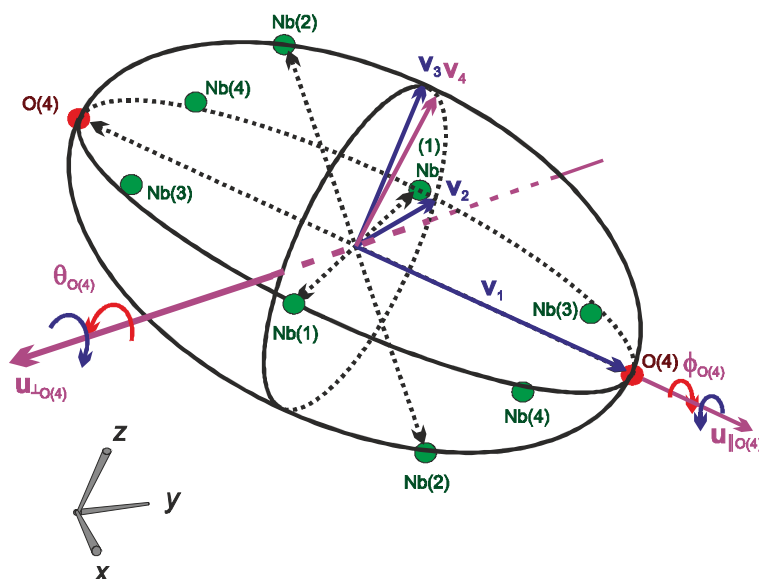


Figure 6.6. Sketch of core atoms that span an ellipsoidal cage which is described by the orthogonal vectors v_1 , v_2 and v_3 .

Nevertheless, the results should be interpreted with caution, since the measurements were done on different crystallites. The clusters were held together solely through relatively weak VdW forces, while strong directional forces such as hydrogen bonds were absent. Therefore, we cannot exclude the coexistence of metastable phases with clusters that were packed under a slightly different angle. Moreover, subtle differences

were observed with a previously reported structure of Nb₈O₁₀(OEt)₂₀ [24] and the structure refined at 296 K. Especially, of ethoxide groups along the α -axis, where differences of 0.8° and 0.7° were observed in the case of the O8-Nb1-O9 and O4-Nb4-O14 bond angles respectively. To ensure that the deformation is predominantly caused by a difference in temperature the structure should be refined on the same crystal at different temperatures.

6.5. Conclusions

Nb₈O₁₀(OEt)₂₀ was synthesized through a slow and controlled condensation of niobium(V)ethoxide with acetone as a oxolation source at room temperature. It confirms the potential of acetone for controlled condensation of metal alkoxides. This condensation occurred to a similar extent via two complementary pathways: (1) ether elimination and (2) aldol condensation.

A comparison between the structures being refined at 150 and 296 K revealed a remarkable anisotropy in the thermal expansion with negative thermal expansion along the c -axis. The anisotropy originates from the following factors: (1) Weak VdW interactions along the c -axis due to the relative large atom-atom distances, which allow large expansions; (2) A screw-like tilt of the rigid and elongated niobium oxo core, which was most likely driven by reducing thermal motion and steric hindrance at reducing temperatures; (3) The irregular shape of the clusters that allow a relatively large compression along the α -axis.

6.6. References

1. Rozes, L. and C. Sanchez, *Titanium oxo-clusters: precursors for a Lego-like construction of nanostructured hybrid materials*. Chem Soc Rev, 2011. **40**(2): p. 1006-1030.
2. Sanchez, C., et al., "*Chimie douce*": A land of opportunities for the designed construction of functional inorganic and hybrid organic-inorganic nanomaterials. C.R. Chim., 2010. **13**(1–2): p. 3-39.
3. Sanchez, C., et al., *Designed Hybrid Organic-Inorganic Nanocomposites from Functional Nanobuilding Blocks*. Chem Mater., 2001. **13**(10): p. 3061-3083.

4. Schubert, U., *Cluster-based inorganic–organic hybrid materials*. Chem. Soc. Rev., 2011. **40**(2): p. 575-582.
5. Schubert, U., *Polymers Reinforced by Covalently Bonded Inorganic Clusters*. Chem. Mater., 2001. **13**(10): p. 3487-3494.
6. Tranchemontagne, D.J., et al., *Secondary building units, nets and bonding in the chemistry of metal-organic frameworks*. Chem. Soc. Rev., 2009. **38**(5): p. 1257-1283.
7. Sanchez, C., et al., *Chemical modification of alkoxide precursors*. J. Non-Cryst. Solids, 1988. **100**(1): p. 65-76.
8. Livage, J., M. Henry, and C. Sanchez, *Sol-gel chemistry of transition metal oxides*. Prog. Solid State Ch., 1988. **18**(4): p. 259-341.
9. Mutin, P.H. and A. Vioux, *Nonhydrolytic Processing of Oxide-Based Materials: Simple Routes to Control Homogeneity, Morphology, and Nanostructure*. Chem. Mater., 2009. **21**(4): p. 582-596.
10. Vioux, A., *Nonhydrolytic sol-gel routes to oxides*. Chem. Mater., 1997. **9**(11): p. 2292-2299.
11. Goel, S.C., et al. *New chemistry for the sol-gel process: Acetone as a new condensation reagent*. in *MRS Proceedings*. 1992. Cambridge Univ Press.
12. Steunou, N., et al., *Ketones as an oxolation source for the synthesis of titanium-oxo-organoclusters*. New J Chem., 1999. **23**(11): p. 1079-1086.
13. Niederberger, M. and G. Garnweitner, *Organic Reaction Pathways in the Nonaqueous Synthesis of Metal Oxide Nanoparticles*. Chem. Eur. J., 2006. **12**(28): p. 7282-7302.
14. Pinna, N. and M. Niederberger, *Surfactant-Free Nonaqueous Synthesis of Metal Oxide Nanostructures*. Angew. Chem. Int. Edit., 2008. **47**(29): p. 5292-5304.
15. Wachs, I.E., et al., *Molecular structure and reactivity of the Group V metal oxides*. Catal. Today, 2003. **78**(1–4): p. 13-24.
16. Nowak, I., et al., *Catalytic properties of niobium and gallium oxide systems supported on MCM-41 type materials*. Appl. Catal. A: General, 2007. **325**(2): p. 328-335.
17. Carniti, P., A. Gervasini, and M. Marzo, *Dispersed NbOx Catalytic Phases in Silica Matrixes: Influence of Niobium Concentration and Preparative Route*. J. Phys. Chem. C, 2008. **112**(36): p. 14064-14074.
18. Tsang, E., et al., *Nanostructured Nb₂O₅ catalysts*. Nano Rev., 2012. **3**.

19. Wang, Y.-D., et al., *Effects of calcining temperature on lattice constants and gas-sensing properties of Nb₅O₂*. Mater. Lett., 2001. **49**(5): p. 277-281.
20. Prado, A.G., et al., *Nb₂O₅ as efficient and recyclable photocatalyst for indigo carmine degradation*. Appl. Catal. B, 2008. **82**(3): p. 219-224.
21. Jose, R., V. Thavasi, and S. Ramakrishna, *Metal Oxides for Dye-Sensitized Solar Cells*. J Am. Ceram. Soc., 2009. **92**(2): p. 289-301.
22. Cotton, S.A., *Titanium, zirconium and hafnium*. Annu. Rep. A, 2006. **102**(0): p. 171-180.
23. Bradley, D., M. Hursthouse, and P. Rodesiler, *The structure of a crystalline niobium oxide ethoxide, Nb₈O₁₀(OEt)₂₀*. Chem. Commun. 1968(18): p. 1112-1113.
24. Kessler, V.G., et al., *The structure of Nb₈O₁₀(OEt)₂₀ and the nature of crystalline metal alkoxides*. Russ. J. Inorg. Chem., 1991. **36**(7): p. 7.
25. Hubert-Pfalzgraf, L.G., et al., *Metal alkoxides with polymerizable ligands: synthesis and molecular structure of [Nb₄(μ-O)₄(μ, η²-O₂CMe-CH₂)₄(OPri)₈]*. Polyhedron, 1997. **16**(4): p. 581-585.
26. Hubert-Pfalzgraf, L., *Hydroxyethylmethacrylate as a source of ethyleneglycolate ligands. Synthesis and characterization of Nb₄(Á, η¹, η²-OC₂H₄O)₂(Á₃, η¹, η²-OC₂H₄O)₂(Á-OC₂H₄O)(OPri)₁₀*. J. Chem. Soc., Dalton Transactions, 1999(15): p. 2407-2408.
27. Boyle, T.J., et al., *Crystallographic characterization of the esterification pathway of Group V alkoxides*. Polyhedron, 2002. **21**(23): p. 2333-2345.
28. Steunou, N., et al., *A tetranuclear niobium oxo acetate complex. Synthesis, X-ray crystal structure, and characterization by solid-state and liquid-state NMR spectroscopy*. Inorg. Chem., 1998. **37**(5): p. 901-910.
29. Boyle, T.J., et al., *Niobium (V) Alkoxides. Synthesis, Structure, and Characterization of [Nb(μ-OCH₂CH₃)(OCH₂C(CH₃)₃)₄]{[H₃CC(CH₂O)(CH₂-μ-O)(C(O)₂)] Nb₂(μ-O)(OCH₂CH₃)₅]₂, and {[H₃CC(CH₂O)₂(CH₂-μ-O)] Nb(OCH₂CH₃)₂]₂ for Production of Mixed Metal Oxide Thin Films*. Chem. Mater., 1997. **9**(12): p. 3187-3198.
30. Herbst, L., et al., *cyclo-Tetra--oxido-tetrakis [(acetylacetonato-2O, O') bis (ethanolato-O) niobium (V)]*. Acta Crystallographica Section E: Structure Reports Online, 2011. **67**(12): p. m1669-m1670.
31. Goodwin, A.L., et al., *Colossal positive and negative thermal expansion in the framework material Ag₃[Co(CN)₆]*. Science, 2008. **319**(5864): p. 794-797.

32. Phillips, A.E., et al., *Nanoporosity and Exceptional Negative Thermal Expansion in Single-Network Cadmium Cyanide*. *Angew. Chem.*, 2008. **120**(8): p. 1418-1421.
33. S. O. Evans, J., *Negative thermal expansion materials [dagger]*. *J. Chem. Soc., Dalton Transactions*, 1999(19): p. 3317-3326.
34. Attfield, M.P. and A.W. Sleight, *Exceptional Negative Thermal Expansion in AlPO₄-17*. *Chem. Mater.*, 1998. **10**(7): p. 2013-2019.
35. Dubbeldam, D., et al., *Exceptional negative thermal expansion in isorecticular metal-organic frameworks*. *Angew. Chem.*, 2007. **119**(24): p. 4580-4583.
36. Haas, S., et al., *Large uniaxial negative thermal expansion in pentacene due to steric hindrance*. *Phys. Rev. B*, 2007. **76**(20): p. 205203.
37. Smeets, S. and M. Lutz, *Hexakis(urea-[kappa]O)zinc(II) dinitrate at 110 and 250 K: uniaxial negative thermal expansion*. *Acta Crystallogr. C*, 2011. **67**(2): p. m50-m55.
38. Kessler, V.G., K.V. Nikitin, and A.I. Belokon, *A new argument in favor of the ether elimination mechanism: formation of acetals on action of molybdenum alkoxides on carbonyl compounds*. *Polyhedron*, 1998. **17**(13): p. 2309-2311.
39. Salvapati, G., K. Ramanamurty, and M. Janardanarao, *Selective catalytic self-condensation of acetone*. *J. Mol. Catal.*, 1989. **54**(1): p. 9-30.
40. Sathyanarayana, D. and C. Patel, *Studies on the Hydroxide and Peroxide of Niobium*. *Z. Anorg. Allg. Chem.*, 1967. **353**(1-2): p. 103-108.
41. Salud, J., et al., *Anisotropy of intermolecular interactions from the study of the thermal-expansion tensor*. *J. Appl. Crystallogr.*, 1998. **31**(5): p. 748-757.

S6.) Supporting information

Crystallized Nb₈O₁₀(OEt)₂₀ from condensation of niobium ethoxide and acetone that exhibits remarkable anisotropy in thermal expansion

S6.1. Extended lists of bond lengths and angles

Table S6.1. Bond lengths of Nb₈O₁₀(OEt)₂₀ structures.

Synthesized from	Bond lengths			Relative difference	
	Nb(OEt) ₅	Nb(OEt) ₅	NbOCl ₃	150K vs. 296K	NbOCl ₃ vs. Nb(OEt) ₅
	+ (CH ₃) ₂ CO	+ (CH ₃) ₂ CO	+ NaOEt		
T	150 K	296 K	283-303 K		
Reference	This work	This work	[1]		
Nb1-O1	2.0439(16)	2.044(3)	2.039(4)	0.0%	-0.2%
Nb1-O6	1.9929(17)	2.000(3)	1.994(4)	-0.4%	-0.3%
Nb1-O7	2.0486(17)	2.045(3)	2.054(4)	0.2%	0.4%
Nb1-O8	1.9742(17)	1.959(3)	1.976(4)	0.8%	0.9%
Nb1-O9	1.867(2)	1.869(3)	1.839(4)	-0.1%	-1.6%
Nb1-O10	1.8994(18)	1.885(4)	1.889(5)	0.8%	0.2%
Nb2-O1	1.8286(17)	1.826(3)	1.831(4)	0.1%	0.3%
Nb2-O2	2.0869(16)	2.083(3)	2.103(4)	0.2%	1.0%
Nb2-O3	2.1772(17)	2.179(3)	2.191(5)	-0.1%	0.6%
Nb2-O5	2.1791(17)	2.194(3)	2.199(4)	-0.7%	0.2%
Nb2-O6	1.8592(17)	1.843(3)	1.854(4)	0.9%	0.6%
Nb2-O11	1.8651(18)	1.862(3)	1.867(4)	0.2%	0.3%
Nb3-O2	2.0655(16)	2.063(3)	2.063(4)	0.1%	0.0%
Nb3-O3	2.1091(17)	2.110(3)	2.106(5)	0.0%	-0.2%
Nb3-O4	2.1784(17)	2.185(3)	2.184(5)	-0.3%	0.0%
Nb3-O7	1.8153(17)	1.818(3)	1.812(4)	-0.1%	-0.3%
Nb3-O12	1.8869(18)	1.870(4)	1.876(5)	0.9%	0.3%
Nb3-O13	1.8755(19)	1.874(5)	1.885(5)	0.1%	0.6%
Nb4-O2	2.0207(16)	2.021(3)	2.022(4)	0.0%	0.0%
Nb4-O4	2.1251(17)	2.120(3)	2.123(5)	0.2%	0.1%
Nb4-O5	2.1175(17)	2.103(3)	2.107(5)	0.7%	0.2%
Nb4-O14	1.8903(19)	1.878(4)	1.868(5)	0.7%	-0.5%
Nb4-O15	1.8667(19)	1.863(4)	1.876(4)	0.2%	0.7%
Nb4-O8	1.8695(17)	1.876(3)	1.869(4)	-0.3%	-0.4%

Table S6.2. Nb-O-Nb and O-Nb-O bond angles of Nb₈O₁₀(OEt)₂₀ structures.

Synthesized from	Bond angles			Differences (°)	
	Nb(OEt) ₅ + (CH ₃) ₂ CO	Nb(OEt) ₅ + (CH ₃) ₂ CO	NbOCl ₃ + NaOEt	150K vs. 296K	NbOCl ₃ vs. Nb(OEt) ₅
Temperature	150 K	296 K	283-303 K		
Reference	This work	This work	[1]		
Nb1-O1-Nb2	144.61(9)	143.75(16)	144.2(2)	0.9	0.4
Nb1-O6-Nb2	147.02(10)	147.28(16)	147.1(2)	-0.3	-0.2
Nb1-O7-Nb3	145.74(10)	146.08(18)	146.3(2)	-0.3	0.2
Nb1-O8-Nb4	144.86(9)	144.70(17)	144.3(3)	0.2	-0.4
Nb2-O5-Nb4	101.54(7)	101.32(12)	101.42(19)	0.2	0.1
Nb2-O2-Nb3	106.95(7)	107.14(13)	106.9(2)	-0.2	-0.2
Nb2-O2-Nb4	108.24(7)	108.19(13)	107.79(17)	0.0	-0.4
Nb2-O3-Nb3	102.23(7)	102.12(12)	102.25(18)	0.1	0.1
Nb3-O2-Nb4	111.49(7)	111.39(13)	111.62(19)	0.1	0.2
Nb3-O4-Nb4	103.40(7)	103.19(12)	103.33(19)	0.2	0.1
O6-Nb1-O7	82.31(7)	82.38(12)	82.52(16)	-0.1	0.1
O6-Nb1-O8	92.02(7)	93.02(12)	92.89(16)	-1.0	-0.1
O6-Nb1-O9	95.59(8)	92.77(14)	93.2(2)	2.8	0.4
O6-Nb1-O10	164.89(8)	166.00(16)	166.49(19)	-1.1	0.5
O1-Nb1-O6	84.26(7)	84.34(12)	84.15(17)	-0.1	-0.2
O7-Nb1-O8	172.50(7)	172.42(13)	172.51(18)	0.1	0.1
O7-Nb1-O9	94.92(8)	93.80(15)	94.54(19)	1.1	0.7
O7-Nb1-O10	86.37(8)	85.59(16)	85.90(17)	0.8	0.3
O1-Nb1-O7	89.68(7)	88.36(12)	88.47(17)	1.3	0.1
O8-Nb1-O9	90.49(8)	92.44(15)	91.61(19)	-2.0	-0.8
O8-Nb1-O10	98.32(8)	98.14(16)	97.86(18)	0.2	-0.3
O1-Nb1-O8	84.86(7)	85.18(12)	85.16(17)	-0.3	0.0
O9-Nb1-O10	95.31(9)	95.17(17)	94.6(2)	0.1	-0.6
O1-Nb1-O9	175.34(8)	176.14(13)	175.73(19)	-0.8	-0.4
O1-Nb1-O10	85.72(8)	88.18(16)	88.61(17)	-2.5	0.4
O1-Nb2-O2	92.54(7)	92.52(12)	92.20(17)	0.0	-0.3
O1-Nb2-O3	161.48(7)	161.76(12)	161.40(18)	-0.3	-0.4
O1-Nb2-O5	87.21(7)	87.07(12)	87.07(18)	0.1	0.0
O1-Nb2-O6	102.06(7)	102.18(13)	101.93(19)	-0.1	-0.3
O1-Nb2-O11	101.89(8)	101.60(13)	101.80(17)	0.3	0.2
O2-Nb2-O3	71.38(6)	71.41(11)	71.21(17)	0.0	-0.2
O2-Nb2-O5	71.69(6)	71.66(11)	71.59(17)	0.0	-0.1
O2-Nb2-O6	91.72(7)	92.43(12)	92.28(17)	-0.7	-0.2
O2-Nb2-O11	157.83(7)	157.48(12)	157.40(18)	0.4	-0.1
O3-Nb2-O5	79.17(6)	79.80(11)	79.87(17)	-0.6	0.1

Table S6.2. Second Part.

Synthesized from	Bond angles			Differences (°)	
	Nb(OEt) ₅ + (CH ₃) ₂ CO	Nb(OEt) ₅ + (CH ₃) ₂ CO	NbOCl ₃ + NaOEt	150K vs. 296K	NbOCl ₃ vs. Nb(OEt) ₅
Temperature	150 K	296 K	283-303 K		
Reference	This work	This work	[1]		
O3-Nb2-O6	87.92(7)	87.47(12)	87.45(17)	0.5	0.0
O3-Nb2-O11	91.18(7)	91.42(13)	91.74(17)	-0.2	0.3
O5-Nb2-O6	161.49(7)	162.09(12)	161.97(18)	-0.6	-0.1
O5-Nb2-O11	92.09(7)	91.44(12)	91.30(19)	0.7	-0.1
O6-Nb2-O11	101.46(8)	101.49(13)	101.91(19)	0.0	0.4
O2-Nb3-O3	73.18(6)	73.21(12)	73.72(17)	0.0	0.5
O2-Nb3-O4	71.03(6)	71.08(11)	71.02(17)	0.0	-0.1
O2-Nb3-O7	92.53(7)	92.88(13)	92.79(17)	-0.3	-0.1
O2-Nb3-O12	99.39(7)	98.79(15)	98.7(2)	0.6	-0.1
O2-Nb3-O13	154.72(7)	155.03(17)	155.19(19)	-0.3	0.2
O3-Nb3-O4	84.41(7)	84.61(12)	84.98(18)	-0.2	0.4
O3-Nb3-O7	90.69(7)	89.68(13)	89.40(17)	1.0	-0.3
O3-Nb3-O12	170.03(7)	169.83(15)	169.9(2)	0.2	0.1
O3-Nb3-O13	87.58(7)	88.25(17)	87.9(2)	-0.7	-0.3
O4-Nb3-O7	163.56(7)	163.92(13)	163.77(18)	-0.4	-0.1
O4-Nb3-O12	86.89(7)	86.85(16)	86.3(2)	0.0	-0.5
O4-Nb3-O13	91.31(8)	91.05(16)	91.3(2)	0.3	0.3
O7-Nb3-O12	96.36(8)	97.09(17)	97.7(2)	-0.7	0.6
O7-Nb3-O13	104.18(8)	103.82(17)	103.8(2)	0.4	0.0
O12-Nb3-O13	97.48(8)	97.43(19)	97.3(2)	0.0	-0.1
O2-Nb4-O4	72.98(6)	73.24(11)	73.06(16)	-0.3	-0.2
O2-Nb4-O5	74.26(6)	74.79(12)	75.11(17)	-0.5	0.3
O2-Nb4-O14	94.07(7)	96.13(13)	95.57(18)	-2.1	-0.6
O2-Nb4-O15	157.84(7)	158.42(16)	158.50(19)	-0.6	0.1
O2-Nb4-O8	93.58(7)	92.79(12)	93.28(18)	0.8	0.5
O4-Nb4-O5	87.45(7)	88.13(12)	88.23(18)	-0.7	0.1
O4-Nb4-O14	90.62(7)	91.18(14)	90.45(19)	-0.6	-0.7
O4-Nb4-O15	90.04(8)	90.88(17)	90.83(19)	-0.8	0.0
O4-Nb4-O8	166.22(7)	165.90(12)	166.20(19)	0.3	0.3
O5-Nb4-O14	168.23(7)	170.69(14)	170.56(19)	-2.5	-0.1
O5-Nb4-O15	91.23(8)	90.52(17)	90.59(19)	0.7	0.1
O5-Nb4-O8	85.89(7)	86.23(13)	86.23(18)	-0.3	0.0
O14-Nb4-O15	100.38(8)	98.77(18)	98.8(2)	1.6	0.0
O8-Nb4-O14	93.44(8)	92.30(15)	92.95(19)	1.1	0.7
O8-Nb4-O15	102.15(8)	102.08(17)	101.9(2)	0.1	-0.2

S6.2. References

1. Kessler, V.G., et al., *The structure of Nb₈O₁₀(OEt)₂₀ and the nature of crystalline metal alkoxides*. Russ. J. Inorg. Chem, 1991. **36**(7): p. 7.

7.

A novel malonamide bridged silsesquioxane precursor for enhanced dispersion of transition and lanthanide metal ions in hybrid silica membranes

7.1. Abstract

Microporous hybrid silica membranes have superior (hydro)thermal and chemical stability. However, the permselectivities for small gases including H₂, CO₂, N₂ and CH₄ is limited due to the limited differences between the kinetic diameters of these gases. By incorporating metal ions, such as Ce⁴⁺ and Ni²⁺, the affinity and therefore the selectivity of these membranes towards particular gases may be altered. To promote the dispersion of metal ions within the hybrid silica matrix, the silica precursor *N,N,N',N'*-tetrakis-(3-(triethoxysilyl)-propyl)-malonamide (TTPMA) was synthesized successfully. The malonamide ligands clearly coordinated the Ce⁴⁺ and Ni²⁺ metal centers and enhanced their dispersion. During calcination these metal centers redistributed into small nanosized grains of CeO₂ (<5 nm) and Ni₂O₃ (<15 nm). These Ce-TTPMA and Ni-TTPMA membranes showed higher H₂/N₂ permselectivities as compared to previously reported hybrid BTESE (1,2-bis-(triethoxysilyl)ethane) membranes [1]. The TTPMA-precursor was found suitable for membrane separation and can be a promising and versatile precursor for the incorporation of metal ions within hybrid silica matrices.

7.2. Introduction

At present over 85% of the global energy is provided by burning fossil fuels [2]. This leads to increasing amounts of CO₂ into the atmosphere. Although the increasing CO₂ emissions are relatively small compared to the CO₂ involved in the natural carbon fluxes, the CO₂ concentration increase leads to a substantial climate change in a relative short time period [2, 3], so that we need to reduce CO₂ emission. This stresses the need for separation membranes, preferentially in a post-combustion scheme in which CO₂ is separated from flue gas N₂ [2]. Post-combustion setups can be implemented most easily in our current power plants. CO₂ separating membranes are also useful for conversion of H₂ and CO₂ into synthetic fuels such as CH₃OH and dimethyl ether, that can be stored more easily than H₂ and CO₂ [4].

Nevertheless, separation of CO₂ and N₂ is difficult, since these gases have a similar kinetic diameter of 3.30 and 3.64 Å, respectively [3]. Most of the membranes that have been developed so far do not reach the required CO₂/N₂ selectivity of 200 to make them economically feasible [5]. The

membranes that meet these requirements are based on affinity with CO₂, such as glycine-sodium glycerol, where performance relies on the presence of moisture [6]. Currently, solution based adsorption on amines is still the most commonly applied technique to sequester CO₂, but regeneration requires a lot of energy, the amine loading capacity is limited due to corrosion problems, and the amines degrade too fast [2, 4].

As alternative to post-combustion schemes, CO₂ can also be separated from H₂ after gasification in a pre-combustion setup [2, 7]. The difference in kinetic diameter between H₂ and CO₂ is slightly larger (2.89 versus 3.30 Å) and these gases can be separated by size exclusion in silica membranes with a permselectivity of 70 [8]. The selectivity of silica membranes towards H₂ was increased with one order of magnitude by doping them with cobalt or nickel oxide [9, 10]. These metal centres increased the surface adsorption and thereby the surface diffusion rate of H₂ on the pore walls. Although inorganic size exclusion membranes will never exceed the permselectivity of palladium membranes, they are less expensive, catalytically inactive and do not suffer from hydrogen embrittlement and surface poisoning [7, 11].

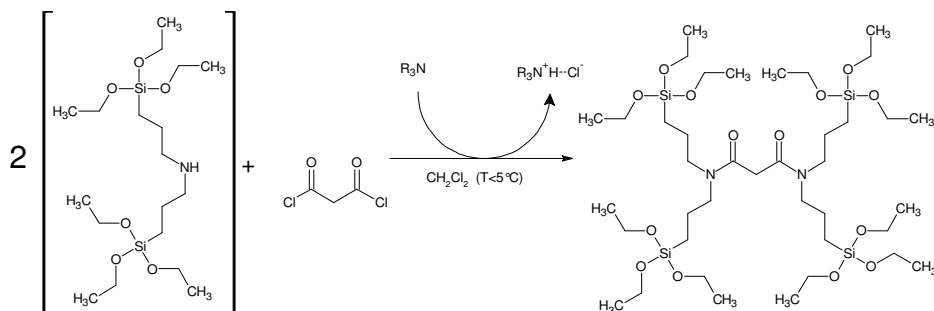
The CO₂/N₂ permselectivity of size exclusion membranes such as sol-gel derived silica membranes can be altered by increasing their affinity towards CO₂ [10, 12-15]. However, CO₂ is known to bind irreversibly with a large variety of metal oxides and the choice of a proper adsorbent is difficult [16, 17]. CO₂ has a particularly strong affinity towards nucleophilic, electron donating species due to its electron-deficient carbonyl atom, and chemisorbs strongly and irreversibly onto basic sites of alkaline earth metal oxides [18, 19]. This explains the poor mobility of CO₂ in mesoporous magnesia doped γ -alumina [20]. By doping γ -alumina with magnesia the amount of CO₂ adsorbed on the surface did not increase. However, the mobility of adsorbed CO₂ species decreased. The authors suggested that this was caused by the replacement of weakly basic sites by strongly basic sites. On the other hand, the amphoteric character of CO₂ allows chemisorption on acidic sites as well [21], which explains the low permeance of CO₂ in microporous niobia doped silica [14]. Ceria may be a good alternative, since it is a weaker nucleophile as compared to earth alkaline oxides [22], while Fourier Transform Infrared (FTIR) experiments revealed substantial affinity of CO₂ on a ceria surface [23, 24].

Dispersion of metal centres on atomic scale into a microporous silica or hybrid silica network is not a straightforward task: the metal oxide that is introduced, either in the form of a metal salt or a metal alkoxide, tends to phase separate while the silica matrix forms. Metal salts, e.g. metal nitrates, have limited solubility within the alcoholic environments in which the silica sol is formed and these salts tend to precipitate while the sol is drying [10]. Metal alkoxides dissolve well in apolar silicates, but they are much more reactive towards hydrolysis and condensation than silica precursors, generally resulting in the formation of dense metal oxide clusters within the silica sol [25-27]. The reactivity of these alkoxides can be tempered by chelating ligands such as acetylacetone and they clearly retard the gelation in the presence of water [28-30]. It has been debated whether the reactivity is reduced by reduction of the nucleophilic character, or that the chelating ligands shield the surface from reactive species, i.e. a steric hindrance effect [26, 30]. In the latter case, the introduction of chelating ligands would not help to increase the degree of dispersion of the metal oxide in a silica matrix, since they would be shielding the metal centre from silicon species as well.

A more elegant solution was proposed by Rupp et al. [31-33], who synthesized a triethoxysilylpropyl adduct to acetylacetone and subsequently coupled this molecule to a titanium, zirconium or aluminium alkoxide. This approach solved two complications simultaneously: (1) it connects the metal alkoxide precursors to the silica precursors before the sol-gel process, thereby increasing the dispersion of the metal alkoxides within the glassy silica matrix; (2) it tempers and shields the reactive metal centre in the metal alkoxide precursor, thereby reducing its tendency to form a condensed metal oxide [31]. The latter possibility was supported by XRD data that revealed a strong reduction of the anatase and rutile grain sizes [31], and SAXS data that revealed a limited metal oxide size cluster size with aluminium alkoxides [33].

In the present work we used a similar approach. However, we chose to form a bridged silsesquioxane precursor with four triethoxysilyl-propyl groups attached to a single malonamide chelating group. As compared to pendant silsesquioxanes, bridged silsesquioxanes exhibit much higher mechanical strength and fracture resistance due to enhanced connectivity and the absence of dangling carbon substituents [34-36]. A bridged silsesquioxane that consists of a malonamide chelating group was formed through the formation of amide bonds between malonyl chloride and two

bis-(3-(triethoxysilyl)-propyl)-amine molecules. The synthesis was performed via a base catalyzed (by using a tertiary amine) N-acylation of malonyl chloride on N-substituted amines in dichloromethane at temperatures below $T=5^{\circ}\text{C}$ as reported before [37, 38] (Scheme 7.1).



Scheme 7.1 Synthesis of *N,N,N',N'*-tetrakis-(3-(triethoxysilyl)-propyl)-malonamide (TTPMA)

Malonamides are strong chelating units. Through the formation of an enolic bidentate ligand they can easily form complex bonds with a large variety of metals cations, including lanthanides and actinides [39-46]. Since a large variety of metal cations can thus be incorporated into a hybrid silica matrix, the approach is very versatile and its affinity towards certain probe molecules can be controlled by the choice of metal(s). In this study, we doped the TTPMA matrix with cerium (IV) isopropoxide isopropanol adduct and nickel nitrate hexahydrate in an attempt to enhance the affinity towards carbon dioxide and H_2 , respectively.

7.3. Experimental section

7.3.1. Synthesis of *N,N,N',N'*-tetrakis-(3-(triethoxysilyl)-propyl)-malonamide (TTPMA)

The synthesis was performed inside a glovebox under nitrogen atmosphere. Before starting the synthesis dichloromethane (BOOM, 99%) triethylamine (Sigma aldrich, 99%), and dimethylsulfoxide (Sigma Aldrich 99%) were dried over anhydrous sodium sulphate (Sigma Aldrich, 99%) and dichloromethane was cooled down to $T= -5^{\circ}\text{C}$ for 24 h in a freezer. Then, 30 mmole of bis-(3-(triethoxysilyl)-propyl)-amine (ABCR chemicals, 97%) was dissolved in 183

mL of dichloromethane inside a 250 mL Erlenmeyer flask. Subsequently, 30 mmole of triethylamine was added to the solution. In a dropping funnel, a 10% excess (16.5 mmole) of malonylchloride (Sigma Aldrich, 97%) was dissolved in 48.4 mL of dichloromethane, which was added dropwise to the solution in the Erlenmeyer flask in 30 min. Please note that malonyl chloride is rather reactive and may decompose with the formation of hydrochloric acid when the temperature increases, thus after use the bottle was immediately returned to the fridge. After addition, the Erlenmeyer flask was stirred for 7 days at room temperature.

While stirring the Erlenmeyer flask inside an oil bath at $T=20^{\circ}\text{C}$, the dichloromethane was distilled using a Vacuumbrand vacuum pump that automatically adapts its pressure to the solvent pressure. Then 150 mL of hexane was used to extract TTPMA from the remnant slurry. The triethylammonium chloride that was formed during the reaction was removed by filtration using a $2.7\ \mu\text{m}$ filter paper (Whatman, grade 50) over a Büchner funnel. The Erlenmeyer flask and Büchner funnel were washed twice with 50 mL hexane. The filtered hexane solution was washed once with dimethylsulfoxide to remove remnant ammonium byproducts. From the hexane solution the hexane was removed by vacuum distillation at room temperature. Afterwards the dimethylsulfoxide was removed by vacuum distillation at $T=80^{\circ}\text{C}$.

7.3.2. NMR-measurements

All measurements were done on a Bruker Ascend-400 spectrometer operating at 400,13MHz for ^1H - and 100,61 MHz for ^{13}C , using a 5 mm gradient-probe. Concerning the 1D NMR-experiments 16, 4096 and 2048 scans were accumulated for ^1H -NMR, inverse gated ^1H -decoupled ^{13}C -NMR and ^{13}C -DEPT-135-NMR (Distortionless Enhancements by Polarization Transfer) experiments, respectively. The 1D experiments were performed following the pulse program sequences: zg30, zgig30 and deptsp135 as described in Bruker's pulse program catalogue [47].

A homonuclear ^1H - ^1H correlation spectrum was obtained with 4 scans by using a magnitude mode gradient enhanced 2D-COSY (CORrelation Spectroscopy) experiment. The direct H-C couplings were measured by an $^1J_{\text{H-C}}$ scalar correlation spectrum, which was acquired with a phase-sensitive gradient selected HSQC pulse sequence (Heteronuclear Single Quantum

Coherence) [48]. The measurement was acquired with 32 scans and a delay $1/(4 \cdot {}^1J_{C-H}) = 1.72$ ms, which corresponds to a mean ${}^1J_{C-H} = 145$ Hz. A heteronuclear 1H - ${}^{13}C$ long range scalar correlation spectrum was obtained using gradient selected HMBC pulse sequence (Heteronuclear Multiple Bond Correlation) [49, 50]. Several one bond H-C correlation peaks in the 2D spectrum appeared as doublets, since the direct ${}^1J_{C-H}$ -bond correlations were not completely suppressed by the low-pass J -filter. The measurement was acquired with 64 scans, a delay $1/(2 \cdot {}^1J_{C-H}) = 3.45$ ms and a delay $\tau = 0.05$ s for long range couplings. The COSY, HSQC and HMBC experiments were performed following the pulse program sequences: cosyppppqf, hsqcetgp and hmbcgpplndqf [47].

7.3.3. Sol preparation and DLS measurements

Before preparing the Ce-TTPMA sol a stock-solution was prepared: At first approximately 3 mmole of $Ce(O^iPr)_4 \cdot iPrOH$ (CeTiP; ABCR Chemicals, 31.5-32.4% Ce weight) was weighed accurately in a 50 mL polypropylene vessel. Then, a stoichiometric amount of TTPMA was added to yield a $[Ce]/[Si]$ ratio of 1:9, which corresponded to $[Ce]/[TTPMA] = 1/2.25$. This mixture was diluted in 15 mL of isopropanol, yielding a solution with a density of 1.28 g/mL, which corresponded to $[TTPMA] = 0.295$ mol/L and $[Ce] = 0.131$ mole/L. After stirring the solution for 24 h at room temperature, it was further diluted to yield a $[OR] = 1.8$ mole/L, where $[OR]$ represents the concentration of reactive alkoxy groups, i.e. the sum of both ethoxy and isopropoxy groups from TTPMA and cerium isopropoxide, respectively. Then, 30 mL of an acidic solution of water and nitric acid in isopropanol ($[H_2O] = 1.8$ mol/L; $[HNO_3] = 0.06$ mol/L) to 30 mL of diluted stock solution to yield a solution with the following characteristics: $[OR] = 0.9$ mole/L, $[H_2O]/[OR] = 1$, $[HNO_3]/[OR] = 1/30$, $[TTPMA] = 65.4$ mmole/L and $[Ce] = 29.1$ mmole/L. Finally, sol particles were formed by heating the solution for 1 h at $T=60^\circ C$ in a closed 100 mL round bottom flask. For membrane preparation the $[OR] = 0.9$ mol/L Ce-TTPMA sol was diluted 6 times by volume before coating it on the mesoporous support.

At first, for the Ni-TTPMA sol, a Ni^{2+} stock solution was prepared: Approximately 10 g of $Ni(NO_3)_2 \cdot 6H_2O$ was weighed accurately in a 50 mL glass bottle and dissolved in approximately 46 mL of ethanol which was weighed afterwards. This yielded a stock solution with $[Ni] = 0.691$ mole/L and $\rho = 0.922$ g/mL. The Ni stock solution and TTPMA were dissolved in

ethanol to yield diluted solutions with $[OR] = 1.8, 2.4, 3.0$ and 3.6 mole/L, where $[OR]$ is defined as the sum of both ethoxy groups of TTPMA and nitrate groups from nickel nitrate, i.e. $[OR] = [NO_3^-] + [-OEt]$. After stirring these solutions for 2 h at room temperature, acidic solutions of nitric acid and water were added dropwise to yield 8 different sols with two different acid ratios $[H^+]/[OR] = 1/30$ and $1/15$, and four different concentrations $[OR] = 0.9, 1.2, 1.5$ and 1.8 , respectively. The water ratio $[H_2O]/[OR] = 1$ (including crystal water from the Ni-stock) and complexing ratio $[Ni]/[TTPMA] = 1$ were held constant for all sols. The sols were heated in closed glass round bottom flasks for 1 h at $T=60^\circ C$ while stirring. Before the particle size was analyzed by dynamic light scattering (DLS), all sols were diluted to yield an overall concentration $[OR] = 0.9$ mol/L ($[TTPMA] = 64.3$ mmole/L). The sol with $[OR] = 1.2$ mol/L (during synthesis) and $[H^+]/[OR] = 1/15$ was diluted to $[OR] = 0.9$ mol/L and used for membrane fabrication.

After 75 vol% dilution in ethanol, the hydrodynamic diameter of freshly prepared Ce-TTPMA and Ta-TTPMA sols were determined by dynamic light scattering (DLS) technique using a Malvern Zetasizer Nano ZS at $25^\circ C$. The hydrodynamic diameter of the sol particles was determined from Brownian motion of particles as defined by the translational diffusion coefficient D in the ethanol solvent.

7.3.4. FTIR measurements

The Fourier Transform Infra Red (FTIR) measurements were performed by using a Bruker Tensor 27 equipped with a KBr beam splitter, a Pike Gladi ATR diamond attenuated total reflectance (ATR) unit and a liquid nitrogen cooled MCT broadband detector. The FTIR spectra were recorded in 5 min, with a resolution of 1 cm^{-1} . The Fourier transform (FT) was performed with 9480 phase interferogram points and a Blackman-Harris 3-term apodization function.

FTIR measurements were used as a tool to measure the extent of complexation after aging TTPMA with $Ce(O^iPr)_4 \cdot iPrOH$ (CeTiP) in different ratios. Therefore, TTPMA and CeTiP, both viscous liquids, were mixed inside a glovebox for 24 h in the absence of any solvent with complexation ratios $r_C = [Ce]/[TTPMA]$ is $\frac{1}{4}, \frac{1}{3}, \frac{1}{2}, 1$ and 2 , respectively. Since the FTIR equipment was located outside the glovebox, a septum was mounted on the ATR

sample unit to minimize the contact with atmospheric water and then the sample was loaded with a syringe.

Complexation of Ni-TTPMA mixtures were also characterized by FTIR. Therefore, the same 0.691 mol/L Ni stock solution in ethanol as described in section 2.3 was used. Then, TTPMA and the nickel stock solution were mixed in different molar ratios, with $r_c = [\text{Ni}]/[\text{TTPMA}]$ is $\frac{1}{4}$, $\frac{1}{2}$, 1 and 2, respectively and diluted with ethanol to yield a concentration $[\text{TTPMA}] = 0.2$ mole/L for all mixtures. These mixtures were aged for 2 h before performing the FTIR measurements. Moreover, FTIR measurements were performed on the Ni-TTPMA sample with $r_c = 1$ at several time intervals of 15 min, with a total duration between 15 min and 24 h. For the sake of comparison the same experiment was repeated using *N,N,N',N'*-tetra-*n*-propyl-malonamide (ABCR-chemicals, TPMA) instead of TTPMA under the same conditions as in the $r_c = 1$ sample of TTPMA.

For further characterization the undiluted Ce-TTPMA sol ($[\text{OR}] = 0.9$ mole/L, $[\text{H}^+]/[\text{OR}] = 1/30$) and Ni-TTPMA ($[\text{OR}] = 0.9$ M, $[\text{H}^+]/[\text{OR}] = 1/15$) were spin-cast on plasma oxidized Si-substrates with a Laurell WS- 400B-6NPP-Lite spincoater at 3000 rpm for 1 min. For both Ni-TTPMA and Ce-TTPMA sol two substrates were coated: one was dried for 24 h at $T=60^\circ\text{C}$ and the other one was dried for 24 h at $T=60^\circ\text{C}$ and subsequently calcined at $T=250^\circ\text{C}$. These spincoated films were used for FTIR and XPS characterization.

7.3.5. TEM, SEM and XPS measurements

For the Transmission electron microscopy (TEM) measurements carbon TEM copper grids (CF200-Cu, Electron Microscopy Sciences) were dipcoated in Ni-TTPMA ($[\text{OR}] = 0.9$ mol/L, $[\text{H}^+]/[\text{OR}] = 1/15$) and undiluted Ce-TTPMA sol ($[\text{OR}] = 0.9$ mol/L, $[\text{H}^+]/[\text{OR}] = 1/30$). Then, the as-prepared films were dried at 60°C for 24 h in a furnace. Subsequently, these samples were analyzed with a Philips CM300STFEG TEM at 300 kV. Samples were investigated at low magnification to find typical areas and features of interest were examined at high magnification (GATAN 2048 Ultrascan1000 CCD camera).

X-ray photoelectron spectra (XPS) were recorded with a Quantera SXM scanning XPS microprobe with a 50 W monochromated Al K_{α} X-ray source of 1486.6 eV and a spot size of 200 μm . These measurements were

performed on the spincoated silicon substrates as described in section 2.4. Scanning electron microscopy (SEM) was performed with a Zeiss Merlin HR-SEM using 1.4 kV acceleration voltage.

7.3.6. Membrane fabrication and gas permeation measurements

Disk-shaped α -alumina supported γ -alumina membranes (pore size 3-5 nm) were prepared by a dip-coating procedure of a boehmite sol on α -alumina supports (support thickness of 2.08 ± 0.01 mm and pore diameter of 100 nm; Pervatech B.V., The Netherlands), followed by drying and calcination, as described elsewhere [51]. A boehmite-polyvinyl alcohol (PVA) sol was prepared for dipcoating the mesoporous intermediate layer. 0.55 mol aluminium-tri-sec-butoxide (Merck) was added to 1150 mL water under vigorous stirring at $T=100^\circ\text{C}$ and refluxing for 1 hour. At a lower temperature ($T = 60^\circ\text{C}$) the pH was adjusted to 2.8 with 1 mol/L HNO_3 and the sol was refluxed for another 21 h at $T = 90^\circ\text{C}$.

In a separate vessel, 3.0 g PVA (Merck, MW = 72000g/mol) was dissolved in 100 g of 0.05 M HNO_3 solution while stirring it for 2 h at $T = 80^\circ\text{C}$. For dipcoating, 30 mL of boehmite sol was filtered (Schleicher&Schuell, FP030/50 pore size 0.8 μm , cellulose acetate, green) and mixed with 20 mL of PVA solution. Then, dipcoating was performed with a Velterop DA 3960/02 dipcoater (turn velocity 10, dip velocity 0.2). A pore size of the γ -alumina intermediate layer of 3-5 nm was determined by permporometry, as described elsewhere [52]. Dip coating of a Ce- and Ni-TTPMA sol (with dip sol concentration $[\text{Si}] = 0.3$ M and dipping speed of 1.4 cm/s) on γ -alumina membranes was done in a flow cupboard class 100, situated in a clean room class 1000 to minimize defect formation due to dust particles. The dipping procedure was performed only once to deposit a selective layer on the mesoporous support. After coating of the sol, the membranes were calcined at 250°C for 3 h under nitrogen flow (99.99% pure), applying heating and cooling rates of $0.5^\circ\text{C}/\text{min}$.

Membrane flux and selectivity were determined on a home built single gas permeation (SGP) set-up in a dead-end mode without back pressure. The membranes were sealed in a stainless steel module using Viton[®] 51414 O-rings with the separation layer exposed to the feed side. The gas permeance was measured at 200°C in a sequence, starting with the gas

with smallest kinetic diameter, i.e. He (0.255 nm), H₂ (0.289 nm), CO₂ (0.33 nm), N₂ (0.364 nm), CH₄ (0.389 nm) to SF₆ (0.55 nm) at 200°C with a pressure difference of 2 bar. Then the hydrogen flux was determined again to ensure that no change had occurred on the membrane microstructure due to permeation of the gases.

The membrane flux via SGP was derived by the following equation:

$$F_i = \frac{N_i}{\Delta P} \quad (7.1)$$

where F_i is the permeance of gas i , defined as the ratio between the molar permeance (N) of the gas going through the membrane and the applied pressure difference between the feed and permeate side of the membrane (ΔP).

7.4. Results and discussion

7.4.1. synthesis and characterization of TTPMA

The *N,N,N',N'*-tetrakis-(3-(triethoxysilyl)propyl)-malonamide (TTPMA) that was formed was analysed by ¹H- and ¹³C-NMR spectroscopy (Figure 7.1). Concerning the assignment of the resonances the CH_x-moieties were divided into three groups: an alkoxy (or ethoxy) group designated by A1 and A2, a bridging propyl group designated by B1, B2 and B3, and a chelating group designated by C1 and C2. The assignments are clarified by the numbers in Figure 7.2. The proton resonances (Figure 7.1a, Table 7.1) of CH₃ (designated by A1) and CH₂ (designated by A2) remained at the same position with respect to the reactant bis-(3-triethoxysilylpropyl)-amine (BTESPA). These atoms are not close to the nitrogen atoms that were involved in the reaction and therefore these resonances were unaffected by the formation of the amide bonds. The difference in the assigned chemical shifts between BTESPA and TTPMA was most pronounced for the CH₂-group next to the amine/amide bond designated by B3, where the resonating proton became more shielded (0.23 ppm) by the formation of an amide.

The assigned proton resonances were also compared with the assignments of *N,N,N',N'*-tetra-*n*-propyl-malonamide (TPMA) [53] and are given in Table 7.1. For TPMA two slightly different chemical shifts were reported for the methylene groups, due to their geographical orientation with respect to the carbonyl group. The protons of the methylene group that are *cis*-oriented with respect to the carbonyl oxygen atom designated by B3a are slightly more shielded by the π -electrons of the carbonyl group in comparison with the *trans*-oriented methylene group (B3b), causing a difference in chemical shift of 0.03 ppm (Table 7.1). The proton NMR spectrum of TTPMA (Figure 7.1a) reveals a multiplet at $\delta = 3.24$ ppm that consists of overlapping resonances of *cis* and *trans* oriented CH₂ groups. It is not possible to deconvolute them solely by H-NMR, although these resonances can be distinguished by the ¹H,¹³C-HSQC-spectrum (Figure 7.1d) as discussed below. This multiplet was found at a slightly lower chemical shift (0.07 ppm) with respect to TPMA due to electron repulsion of the silicon atom. The differences between the proton resonances of the propyl groups of TTPMA and TPMA became more pronounced when going from the methylene group B3 towards the methylene group B1 next to the silicon atom. Finally, the H-NMR spectrum consisted of a sharp singlet at $\delta = 3.38$ ppm that was associated with the CH₂-group of the malonyl segment in between the carbonyl groups that are designated by C2.

The H-NMR assignments were supported by the cross correlation peaks that were found in the ¹H,¹H-COSY spectrum. Correlation between the methyl and methylene moieties of the ethoxide groups were confirmed by the cross correlation peaks between the A1 and A2 resonances as indicated by the purple dotted lines Figure 7.1c. The correlations between B1 and B2, and B2 and B3 as clarified by the blue lines in Figure 7.1c correspond to the vicinal J-couplings between the neighbouring methylene groups of the propylene linkage.

The resonances of the B3a and B3b methylene groups that were *cis*- and *trans*-coordinated with respect to the carbonyl group became more distinct in the ¹H,¹³C-HSQC-spectrum (Figure 7.1d), since the differences between the ¹³C chemical shifts were more substantial (2.32 ppm). The resonances belonging to the methylene groups next to the B3a and B3b methylene groups, designated by B2a and B2b, respectively, were also well separated in the ¹H,¹³C-HSQC spectrum. Contrary to the TPMA spectrum, the ¹H,¹³C-HSQC did not reveal a clear difference between B1a and B1b resonances.

Most likely, these chemical shifts were predominantly determined by electron repulsion of silicon. In comparison, the carbonyl group had only a minor effect which was insufficient to separate the resonances. Due to the absence of silicon in the case of TPMA, the influence of the carbonyl group was more pronounced as compared to TTPMA.

The negative signals in the ^{13}C -DEPT-135° spectrum (Figure 7.1b) confirm that the resonances A2, B1, B2a, B2b, B3a, B3b and C2 can be associated with CH_2 -groups. The positive signal of resonance A1 was consistent with a CH_3 -group. Each assigned propylene bridging resonance, i.e. B1, B2a, B2b, B3a and B3b, seemed to be split into at least two different resonances in the ^{13}C -DEPT-135° spectrum. This may indicate the existence of several conformations of the TTPMA molecule.

Direct ^1J - ^1H - ^{13}C couplings were not completely suppressed by the low-pass J -filter and consequently the resonances were split into doublets on the proton axis in the HMBC-spectrum (Figure 7.1f). In the image we clarify the position of these doublets with dotted boxes that connect them with each other. Cross-correlation peaks were observed for the CH_x -groups of the ethoxide groups, i.e., between A1 and A2, and between the methylene groups of the propylene linkage, i.e., B1-B2-B3, which are in good agreement with the cross-correlation observed in the COSY spectrum as described above. In addition, the HMBC confirms a coupling between the methylene resonance (C2) and a carbon resonance at 166.8 ppm that was associated with the carbonyl-group (assigned as C1) of the malonamide unit (Figure 7.1e,f). Interestingly, a cross-correlation between the carbonyl group carbon atom (C1) and the methylene protons next to the nitrogen atom of the propyl-linkage, i.e., B3a and B3b, was also observed. These long range couplings were also observed for other types of amines and they are a strong evidence that both resonances were connected through the amide bond [54-56].

Nevertheless, the ^1H , ^{13}C -HMBC and the inverse gated ^{13}C -NMR reveal the presence of some other carbonyl moieties that most likely belong to byproducts of the reaction. These impurities were divided in two sets of correlated resonances. Set 1 contains two carbonyl moieties at 196.6 and 166.8 ppm, respectively, that were coupled with a CH_2 -group (^{13}C -DEPT-135° spectrum, Figure 7.1b) with a proton resonance of 3.62 ppm and carbon resonance of 47.08 ppm. The resonance at 166.8 ppm corresponds

with the resonance of the carbonyl-moiety of TTPMA and was most likely also attached to an $-NR_2$ group that originated from BTESPA.

The other resonance at 196.6 ppm could neither be associated with enolic malonamide (due to the low chemical shift of the CH_x -moiety), nor with an aldehydic carbonyl group (due to the absence of a proton shift at 9-10 ppm), and its chemical shift is too high to be associated with an ester, amide or carbonyl chloride [57]. Most likely, it was attached to another carbon atom. Set 2 contained two carbonyl resonances at 165.2 and 196.6 ppm that were coupled with a CH_x -moiety with a proton resonance at 5.13 ppm, and, according to the HSQC-spectrum (Figure 7.1d), a carbon resonance at 62.67 ppm. The chemical shifts of the CH_x -moiety were outside the range that is associated with CH_3 -groups, or with an unsaturated $C=C$ -bond as in the case of enolic β -diketones [57].

Moreover, the positive signal in the ^{13}C -DEPT 135°-spectrum (Figure 7.1b) eliminated the possibility to assign these resonances to a CH_2 -group. Most likely, this moiety consists of an $(-CHX-)$ group in between two carbonyl moieties, where X may be a chlorine atom. Similar shifts (61.45 and 4.82 ppm) as found here were reported for the $(-CHCl-)$ group of ethyl 2-chloro-3-oxobutyrate [58]. The X-atom may also correspond to other substituents ($-NR_2$ or $-OR$). However, the $^1H,^1H$ -COSY spectrum did not reveal an additional set of correlated peaks that belongs to either $-NR_2$ or $-OR$ substituents. If one of them would have been attached to this carbon atom, then their chemical nature would have been substantially different.

The resonance at 196.6 ppm could not be discriminated from a similar resonance in set 1 in the inverse gated ^{13}C -NMR spectrum, see Figure 7.1g. Thus, it is most likely that both resonances are associated with the same carbonyl atom despite the absence of other couplings between both sets of coupled resonances in the HMBC-spectrum (Figure 7.1e,f). This resonance was reasonably close to a similar carbonyl moiety in diethyl-3-oxoglutarate (195.6 ppm) [59], which made the formation of 2-chloro-pentane-1,3,5-trione a plausible scenario. In summary, the best explanation for the additional resonances that were found in the NMR-spectra is that 2-chloro-3-oxo-*N,N,N',N'*-tetrakis-(3-(triethoxysilyl)-propyl)-pentanediamide was formed as a by-product.

A similar phenomenon was observed for *N*-hydroxylsuccinimidyl activated malonic acid half esters that self-condense via a base catalyzed Claisen

condensation [60], also resulting in the formation of a pentane-1,3,5-trione. The additional resonances that were assigned to this by-product are listed in Table 7.2. Most of the proton and carbon resonances corresponding to the propylene linkages strongly overlap with similar resonances of TTPMA. Only the CH₂-group of the propylene linkages closest to the (-CHCl-) linkage that were assigned as R6a and R6b deviated slightly from the B3a and B3b resonances that were assigned to TTPMA.

Table 7.1. List of ¹H- and ¹³C-NMR resonances assigned to the TTPMA-spectra.

Assignment	A1	A2	B1a	B1b	B2a	B2b	B3a	B3b	C1	C2	
Group	CH ₃	CH ₂	CH ₂	CH ₂	CH ₂	CH ₂	CH ₂	CH ₂	CO	CH ₂	
Coordination propyl-linkage with respect to C=O-group	-	-	<i>cis</i>	<i>trans</i>	<i>cis</i>	<i>trans</i>	<i>cis</i>	<i>trans</i>	-	-	
¹ H – resonances	TPMA ^{1,2}	-	-	0.89	0.92	1.57	1.61	3.29	3.32	-	3.46
	TTPMA ^{1,3}	1.14	3.74	0.51 ^{4,5}		1.57 ⁴	1.59 ⁴	3.22 ⁴	3.25 ⁴	-	3.38
	BTESPA ^{1,3}	1.17	3.77	0.58 ⁶		1.55 ⁶		2.55 ⁶		-	-
	Malonyl chloride ³	-	-	-	-	-	-	-	-	-	4.29
¹³ C resonances	TPMA ^{1,2}	-	-	11.23	11.36	20.81	22.16	47.7	50.1	167	40.8
	TTPMA ^{1,3}	18.3	58.4	7.57		20.8	22.3	48.6	50.9	167	41.0
	BTESPA ^{1,3}	18.3	58.3	7.96		23.4		52.7		-	-
	Malonyl chloride ³	-	-	-	-	-	-	-	-	164	61.3

¹BTESPA refers to bis-(3-(triethoxysilyl)-propyl)-amine, TTPMA refers to *N,N,N',N'*-tetrakis-(3-(triethoxysilyl)-propyl)-malonamide and TPMA refers to *N,N,N',N'*-tetra-*n*-propyl-malonamide. ²Data from Spectral Data Base System (SDBS) of organic compounds. ³Experimental data from this work. ⁴Data assigned by using HSQC-spectrum. ⁵No difference was observed between B1a and B1b resonances in the case of TTPMA. Most likely the CO group had a negligible influence on the electron repelling silicon atom next to this CH₂-group, which is absent in the TPMA-molecule. ⁶In the case of BTESPA both CH₂-groups are chemically identical, since due to the absence of a double bond the bonds can freely rotate and no distinction between *cis*- and *trans*-coordinated atoms can be detected.

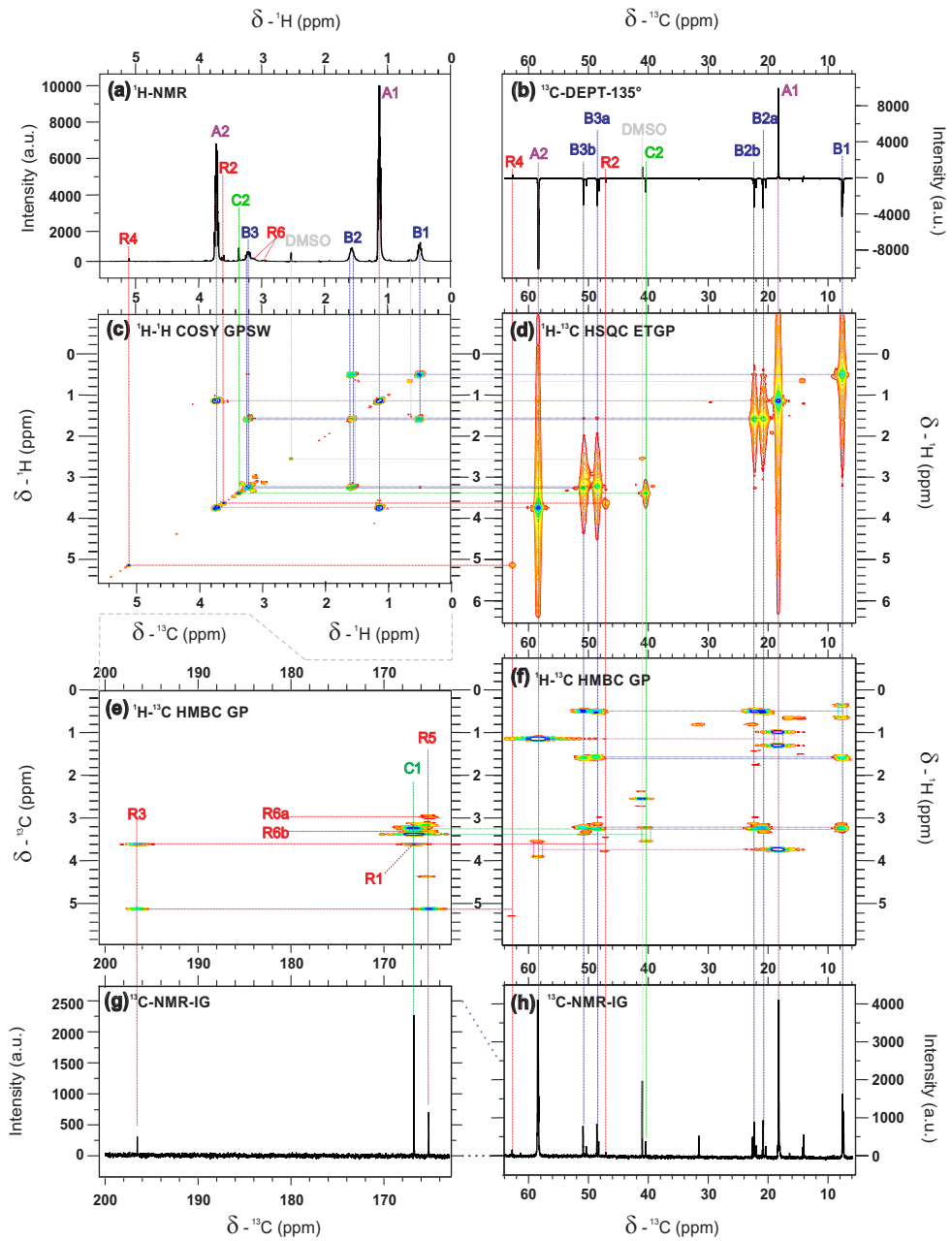


Figure 7.1 (left page) ^1H - and ^{13}C -NMR spectra of synthesized TTPMA dissolved in deuterated chloroform. (a) ^1H -NMR spectrum, (b) ^{13}C -DEPT-135 spectrum, (c) ^1H - ^1H COSY spectrum, (d) ^1H - ^{13}C HSQC spectrum, (e-f) ^1H - ^{13}C HMBC spectrum, with (e) a region of carbonylic carbon atoms ($\text{C}=\text{O}$) and (f) a region of methyl, methylene and methine carbon atoms (CHX), and (g-h) inverse gated ^{13}C -NMR spectrum, with (g) a region of carbonylic carbon atoms ($\text{C}=\text{O}$) and (h) a region of methyl, methylene and methine carbon atoms (CHX). Correlations between the resonances are clarified with dotted lines that connect them. The resonances of TTPMA were divided into three categories: (A) CHX -resonances of the ethoxide groups that were designated as A1 and A2, and connected by purple dotted lines; (B) CHX -resonances of the bridging propylene linkages that were designated as B1-B3(a,b) and connected by blue dotted lines; and (C) $\text{C}=\text{O}$ and CH_2 -resonances of the chelating malonamide segment designated as C1 and C2 and connected by green dotted lines. In addition, the resonances designated as R1-R6 belong to a byproduct that was formed during the reaction and connected by the red dotted lines. The chemical groups that belong to the given designations are shown in Figure 7.2.

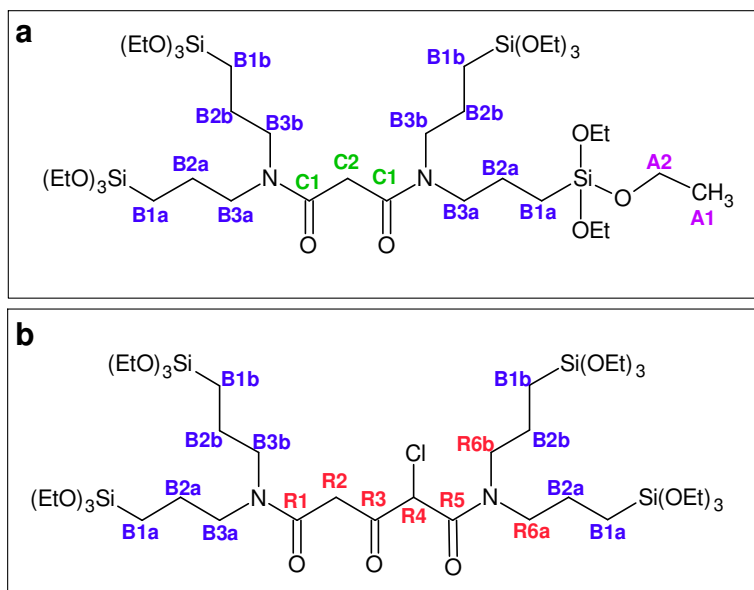


Figure 7.2. Clarification of proton and ^{13}C -NMR assignments with respect to their positions within the chemical structure. (a) TTPMA (N,N,N',N'-tetrakis-(3-(triethoxysilyl)-propyl)-malonamide); (b) a byproduct, most likely (2-chloro-3-oxo-N,N,N',N'-tetrakis-(3-(triethoxysilyl)-propyl)-pentanediamide).

Table 7.2. List of remnant ^1H - and ^{13}C -NMR resonances assigned to the byproduct 2-chloro-3-oxo-*N,N,N',N'*-tetrakis-(3-(triethoxysilyl)-propyl)-pentanediamide.

Assignment	R1	R2	R3	R4	R5	R6a	R6b
Group	C=O	CH ₂	C=O	CHCl	C=O	CH ₂	CH ₂
δ ^1H (ppm)	-	3.62	-	5.13	-	3.32	2.97
δ ^{13}C (ppm)	167	47.1	197	62.7	165	48.4	50.5

7.4.2. Ce-TTPMA complexation

The FTIR-spectrum of TTPMA (Figure 7.3a) in the absence of cerium tetra-isopropoxide isopropanol adduct (CeTiP) revealed a vibration at $\tilde{\nu} = 1638$ cm^{-1} that was associated with the C=O vibration of a malonamide [39, 53, 57]. As CeTiP was added (Figure 7.3c-f), new vibrations arose at $\tilde{\nu} = 1589$ and 1513 cm^{-1} . The shoulder at 1589 cm^{-1} was caused by a reduced force constant when the free C=O moiety was engaged by a metal cation, and the vibration at $\tilde{\nu} = 1513$ cm^{-1} implies the presence of enolic entities [39, 57, 61, 62]. Upon further addition of CeTiP additional vibrations were found at $\tilde{\nu} = 1595$ and 1554 cm^{-1} , respectively, which should be associated with a different type of enolic $\nu\text{C}=\text{O}$ vibration.

Probably, in analogy with the complexation of β -diketones with zirconium and hafnium isopropoxide, the latter vibrations may be associated with the formation of a mixed malonamide/isopropoxide dimer, while the former could be designated to monomeric species [62]. At the highest ratio (Figure 7.3f) the free amide C=O peak ($\tilde{\nu} = 1638$ cm^{-1}) was not completely diminished, indicating the presence of some unbound malonamide ligand. Meanwhile, vibrations arose at $\tilde{\nu} = 1327$, 834 and 816 cm^{-1} that were associated with unbound CeTiP [63]. Besides the interaction between cerium and the malonamide group, additional vibrations also arose at $\tilde{\nu} = 1039$, 903 and 883 cm^{-1} . This indicated the presence of additional electrostatic μ -bridged bonds of oxygen atoms between the ethoxide groups of TTPMA with the cerium cation and/or the isopropoxide groups of CeTiP and a silicon cation. Hence, this gave rise to new vibrations with reduced force constants as compared to the free, unbound molecules.

The exact structure of this complex seems to be rather complex. However, all electrostatic interactions strongly enhance the dispersion of cerium,

making TTPMA a suitable candidate to disperse cerium within a hybrid silica matrix.

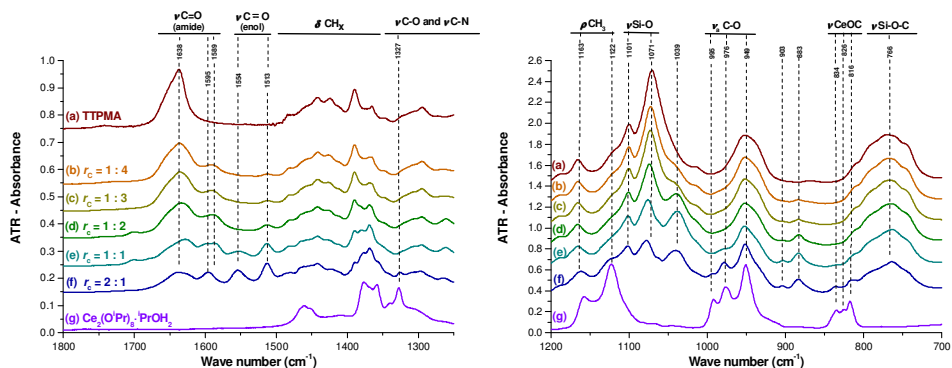


Figure 7.3. FTIR-ATR absorbance spectra of Ce/TTPMA mixtures in the absence of a solvent. Left: 1800-1250 cm^{-1} and right 1200 - 700 cm^{-1} . The intensity of the vibrations are weaker in the 1800-1250 cm^{-1} region and its scale is therefore enhanced relative to the 1200 - 700 cm^{-1} region. The lower intensity in the 1800 - 1250 cm^{-1} region was partly due to substantial absorption by the diamond ATR and the strong contributions from the siloxane bonds in the 1200 - 700 cm^{-1} region. ATR-FTIR spectra of (a) as-synthesized TTPMA; (b-f) mixture of TTPMA and cerium(IV) isopropoxide isopropanol adduct in different molar ratios: $r_c = [\text{Ce}]/[\text{TTPMA}]$, where r_c is $\frac{1}{4}$, $\frac{1}{3}$, $\frac{1}{2}$, 1 and 2 for b-f, respectively, and (g) cerium (IV) isopropoxide isopropanol adduct as received from the supplier.

7.4.3. Ce-TTPMA sol preparation

In the case of the undoped hybrid silica sol from 1,2-bis(triethoxysilyl)ethane, an intensity weighted average particle size distribution of 7 nm was found to be optimal for deposition on these γ -alumina membrane supports [1, 64]. Consequently, several additional Ce-TTPMA sols were made with molar ratios $[\text{H}^+]/[\text{OR}] = 1/30$ and $1/200$, varying temperature (20, 40 and 60°C) and reflux time (30 min and 60 min). Yet, all sols were found to have the same bimodal particle size distribution as shown in Figure 7.4. Among these sols the Ce-TTPMA sol with $[\text{H}^+]/[\text{OR}] = 1/30$, $T = 60^\circ\text{C}$, and $t=60$ min, with intensity weighed hydrodynamic diameters of 2.8 and 34 nm and an overall average particle size of 13 nm (Figure 7.4) was considered to match the optimal particle size distribution of ~ 7 nm most closely.

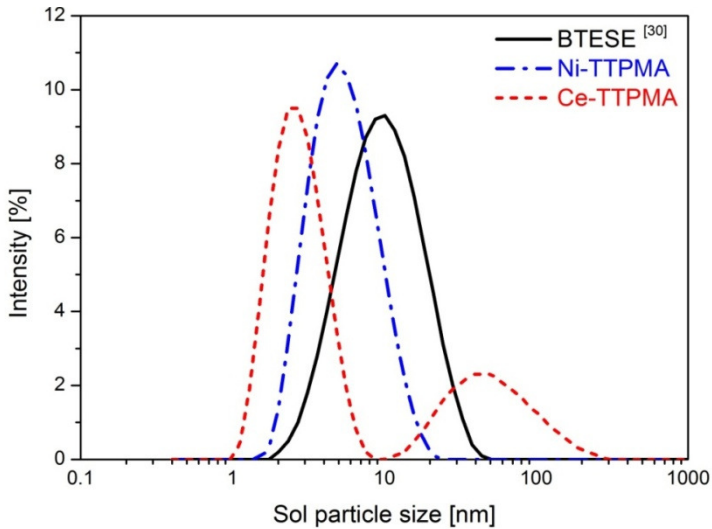


Figure 7.4. Sol particle size distributions of Ce-TTPMA and Ni-TTPMA sols obtained by dynamic light scattering. Results are compared with a previously described recipe of undoped hybrid 1,2-bis-(triethoxysilyl)ethane (BTESE) [1].

7.4.4. Dispersion of cerium within the condensed TTPMA matrix

The FTIR-spectrum of the as-prepared sol of Ce-TTPMA with $r_c = \frac{1}{2}$ revealed a broad peak in the range between $1680\text{--}1580\text{ cm}^{-1}$ (Figure 7.5a). It is a convoluted signal that consists of water deformations ($\delta\text{H}_2\text{O}$) and carbonyl vibrations ($\nu\text{C=O}$). Due to the overlap with $\delta\text{H}_2\text{O}$ and the fact that the diluted sol has a weak $\nu\text{C=O}$ contribution, it is difficult to discriminate between the different entities. When the sol was coated on a silicon wafer and dried at $T=60^\circ\text{C}$, the water contribution was diminished and a more pronounced $\nu\text{C=O}$ was observed with a maximum at $\tilde{\nu} = 1604\text{ cm}^{-1}$ (Figure 7.5b). This vibration clearly shifted with respect to the free malonamide $\nu\text{C=O}$ vibration at $\tilde{\nu} = 1628\text{ cm}^{-1}$ (Figure 7.5d), although no additional peak arose near $\tilde{\nu} = 1628\text{ cm}^{-1}$ as was observed for the mixture of TTPMA and CeTiP before hydrolysis and condensation (Figure 7.3d(left)). After calcining the sample at $T=250^\circ\text{C}$ for 3 h a new vibration appeared at $\tilde{\nu} = 1637\text{ cm}^{-1}$, which is very close to the maximum of $\nu\text{C=O}$ of liquid TTPMA (Figure 7.3a). Meanwhile, the absorbance vibration near $\tilde{\nu} = 1604\text{ cm}^{-1}$ clearly decreased,

which seems to correspond with a reduction of the number of malonamide ligands that are coordinated to Ce^{4+} .

In conclusion, these FTIR measurements clearly reveal malonamide ligands being coordinated to Ce^{4+} . The nature of this complex (monomeric, dimeric, etc.) depends on the complexation ratio. However, the exact structure could not be resolved solely by FTIR. Cerium remains coordinated to the TTPMA ligand during sol-gel processing and drying. However, during calcination at $T=250^\circ\text{C}$ a substantial amount of malonamide ligands became detached from cerium, which may subsequently have phase separated in the form of ceria.

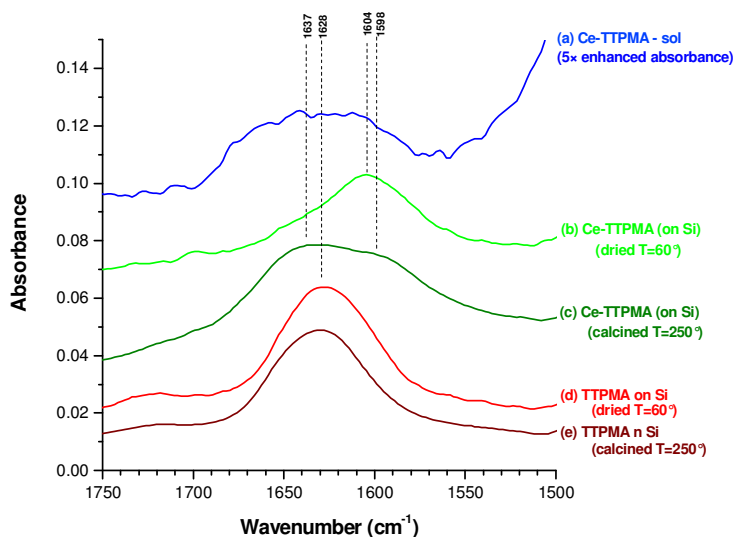


Figure 7.5 FTIR-ATR absorbance spectra (carbonyl-region). (a) as prepared Ce-TTPMA sol; (b-c) spin-coated Ce-TTPMA sol on a plasma oxidized silicon wafer, where (b) was dried at $T=60^\circ\text{C}$ and (c) calcined at $T=250^\circ\text{C}$; (d-e) spincoated TTPMA-sol without ceria, where (d) was dried at $T=60^\circ\text{C}$ and (e) calcined at $T=250^\circ\text{C}$.

TEM measurements were performed on calcined samples of dipcoated holey TEM grids to gain insight into the dispersion of ceria within the hybrid silica matrix. These data revealed the phase separation of small nanosized (2-5 nm) crystallites within an amorphous matrix (Figure 7.6a). The crystallites were found to have lattice spacings of $d\sim 3.1 \text{ \AA}$, as indicated by

the encircled particle (Figure 7.6a) and its fast fourier transform image (Figure 7.6b). This value is consistent with CeO_2 (111) planes [65].

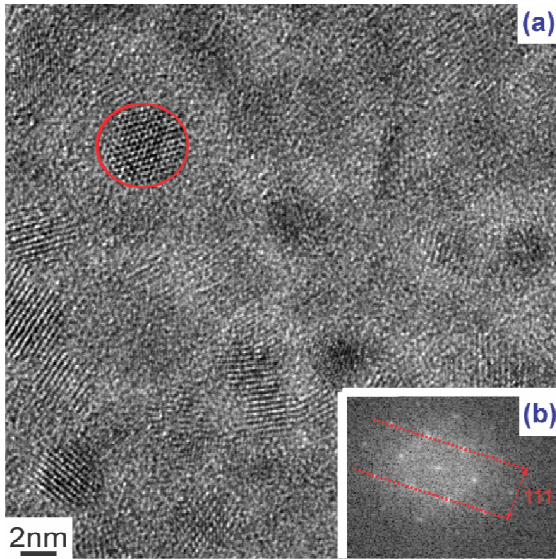


Figure 7.6 (a) HR-TEM images of a holey copper grid (with a carbon film) dipcoated with Ce-TTPMA sol and calcined at $T=250\text{ }^{\circ}\text{C}$. (b) fourier transform of the encircled region in section (b) of this figure.

7.4.5. Membrane characteristics of the Ce-TTPMA coated layer

After dipcoating the diluted Ce-TTPMA sol and calcination at $T=250\text{ }^{\circ}\text{C}$ a thin selective layer of approx. 35 nm was formed on top of the mesoporous $\gamma\text{-Al}_2\text{O}_3$ layer, as shown by the secondary electron HR-SEM-image (Figure 7.7a). The smooth Ce-TTPMA coating seems to penetrate partly into the mesoporous $\gamma\text{-Al}_2\text{O}_3$ layer. This observation is supported by an image that was made by using the energy selective backscatter (ESB) detector (Figure 7.7b), which is particularly sensitive to electron rich elements such as cerium. The data revealed that the cerium containing layer was approx. 58 nm thick, 23 nm thicker than determined by the secondary electron detector (SE2) that is more sensitive to surface morphology. Probably, the Ce-TTPMA sol particles were smaller than the pore size of the $\gamma\text{-Al}_2\text{O}_3$ layer, resulting in partial penetration into the mesoporous $\gamma\text{-Al}_2\text{O}_3$ layer.

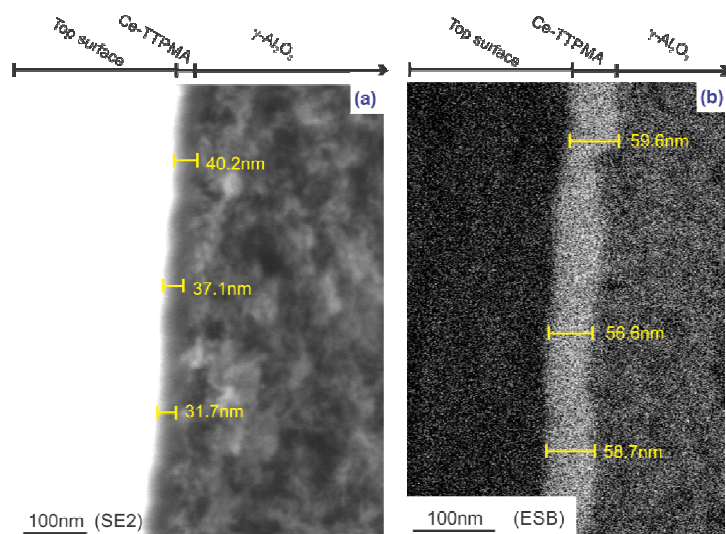


Figure 7.7 HR-SEM images of a Ce-TTPMA top layer on a meso/macroporous γ $\text{Al}_2\text{O}_3/\alpha\text{-Al}_2\text{O}_3$ support. (a) secondary electron detector (SE2) image; (b) energy selective backscatter detector (ESB).

Ce-doped TTPMA membrane with an H_2/N_2 permselectivity of 20 showed a slightly better performance than a BTESE (1,2-bis-(triethoxysilyl)-ethane) based membrane with $\text{H}_2/\text{N}_2 = 14$ as reported elsewhere [1], even though the layer thickness was much smaller (50–60 nm) than that of the BTESE membrane (~ 260 nm). Despite the reduced film thickness and bimodal sol size distribution, no permeation of SF_6 was observed. This indicates a pore size of less than 0.55 nm and the absence of large defects. Moreover, only a minimal variation of less than 5% was observed in the hydrogen permeance between start and at end of the gas permeation analyses. This indicates that Ce-TTPMA derived membranes have a sustainable pore microstructure for gas separation.

The H_2/CO_2 permselectivity of 6 was slightly larger than its corresponding Knudsen diffusion value of 4.7. Since the resistance towards N_2 increased to the same extent as CO_2 , the increased performance was not associated with affinity, but mainly with narrowing of the pore size distribution. Similar helium and hydrogen fluxes were obtained with a substantially thinner selective layer. Thus, the selective layer was much more resistive than the BTESE membrane. This may have several causes: (1) narrower pores, (2) CeO_2 particles that effectively block pores, and/or (3) lower porosity.

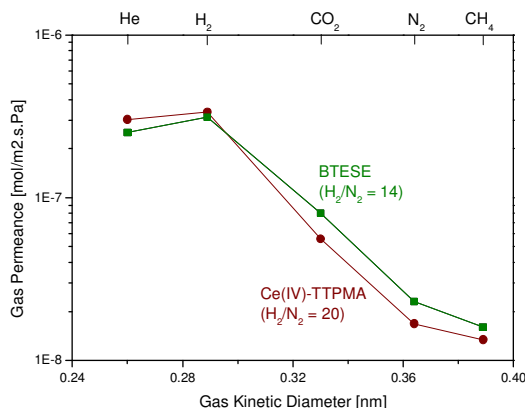


Figure 7.8. Single gas permeance of a Ce-TTPMA membrane and a hybrid BTESE membrane [1] on a macroporous α -Al₂O₃ supported mesoporous γ -Al₂O₃ layer.

7.4.6. Nickel(II)-TTPMA-complexation

In the region between $\tilde{\nu} = 1730$ and 1620 cm^{-1} a broad peak was observed for a $0.4\text{ M Ni}(\text{NO}_3)_2 \cdot 6\text{ H}_2\text{O}$ solution in ethanol (Figure 7.9a (left)) which was caused by H₂O deformations. The maximum was shifted to higher frequencies compared to free water due to electrostatic interactions with nickel [66]. These deformations overlap with C=O vibrations when studying the complexation of nickel with TTPMA. However, they were substantially broader than the C=O vibrations and seemed to be distinguishable.

When $\text{Ni}(\text{NO}_3)_2 \cdot 6\text{ H}_2\text{O}$ was mixed with TTPMA new vibrations arose at $\tilde{\nu} = 1612$ and 1590 cm^{-1} , which led to reduced force constants when (C=O) vibrations were electrostatically coordinated to Ni^{2+} (Figure 7.9b-e (left)), similar to the CeTiP precursor described above. Upon increasing the nickel content the vibration at $\tilde{\nu} = 1590\text{ cm}^{-1}$ increased, while the vibration at $\tilde{\nu} = 1612\text{ cm}^{-1}$ diminished. Both vibrations can be associated with different Ni-malonamide entities, for instance with different coordination number of malonamide ligands on Ni^{2+} . For the sake of comparison $\text{Ni}(\text{NO}_3)_2 \cdot 6\text{ H}_2\text{O}$ was also mixed with tetrapropylmalonamide (Figure 7.9f-g (left)). Similar to the Ni-TTPMA complex, the vibration $\tilde{\nu} = 1612\text{ cm}^{-1}$ was predominant at a low complexation ratio ($r_c = \frac{1}{4}$), while the vibration $\tilde{\nu} = 1590\text{ cm}^{-1}$ was predominant at higher complexation ratio ($r_c = 1$). Moreover, for the Ni-TTPMA samples with $r_c = 1$ or 2 a vibration was clearly observed at 1527 cm^{-1} which is associated with chelated bidentate nitrate ions [42, 67],

indicating that some nitrate ions remain coordinated to nickel upon complexation.

During complexation the water molecules coordinated to nickel were replaced by malonamide ligands. The released water partly hydrolyzed the ethoxide groups of TTPMA, as suggested by the decreasing intensity of ν SiOC ($\tilde{\nu} = 958 \text{ cm}^{-1}$) with increasing r_c (Figure 7.9b-f (right)) [68, 69]. This was accompanied by the increasing intensity of ν SiOH ($\tilde{\nu} = 920 \text{ cm}^{-1}$). Also, the H₂O deformations ($\tilde{\nu} = 1730$ and 1620 cm^{-1}) almost diminished upon aging, and significant H₂O deformation was only observed at the highest complexation ratio (Figure 7.9f (left)). Furthermore, a small increase of ν SiOSi ($\tilde{\nu} = 1010 \text{ cm}^{-1}$) indicated that some SiOH entities condensed to form Si-O-Si bridges [70, 71] within 2 h of aging.

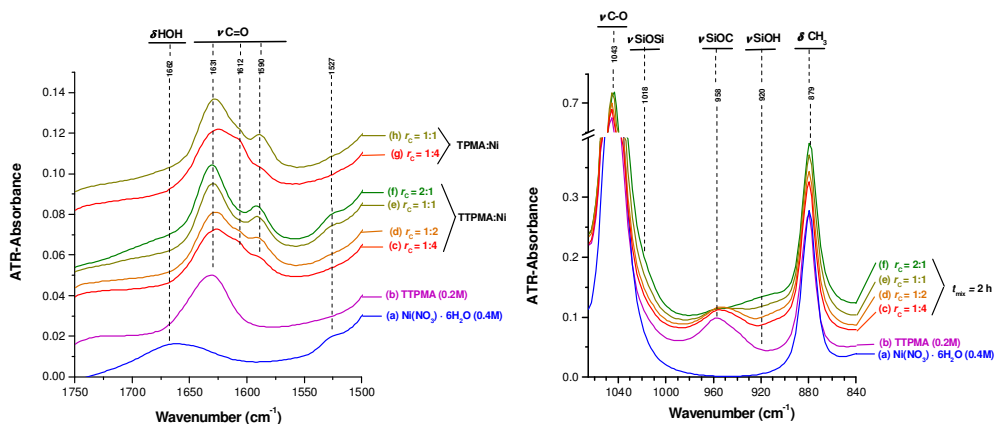


Figure 7.9. FTIR-ATR absorbance spectra of $\text{Ni}(\text{NO}_3)_2/\text{TTPMA}$ solutions in ethanol. Left: $1750\text{-}1500 \text{ cm}^{-1}$ and right: $1065 - 840 \text{ cm}^{-1}$. The intensity of the vibrations are weaker in the former region and its scale is therefore enhanced relative to the right figure. The lower intensity in the $1750\text{-}1500 \text{ cm}^{-1}$ region was partly due to substantial absorption by the diamond ATR and the strong contributions from the siloxane bonds in the $1065 - 840 \text{ cm}^{-1}$ region. ATR-FTIR spectra of (a) $0.4 \text{ mol/L Ni}(\text{NO}_3)_2 \cdot 6\text{H}_2\text{O}$ solution in ethanol; (b) 0.2 mol/L TTPMA solution in ethanol; (c-f) $0.2 \text{ mol/L TTPMA-Ni}(\text{NO}_3)_2 \cdot 6\text{H}_2\text{O}$ solutions in ethanol with $r_c = [\text{Ni}]/[\text{TTPMA}] = \frac{1}{4}, \frac{1}{2}, 1$ and 2 for c-f, respectively, after 2 h aging at room temperature; (g,h) $0.2 \text{ mol/L TTPMA-Ni}(\text{NO}_3)_2 \cdot 6\text{H}_2\text{O}$ solutions in ethanol with $r_c = [\text{Ni}]/[\text{TPMA}] = \frac{1}{4}$ and 1 for f and g, respectively, after 2 h aging at room temperature.

The extent of complexation was also found to be time-dependent, as indicated by FTIR experiments for different aging times at fixed ratio $r_C = 1$, see Figure 7.10 (left). Immediately after aging, two carbonyl vibrations were observed: one at $\tilde{\nu} = 1631 \text{ cm}^{-1}$ that is associated with the free malonamide ligand and another vibration at $\tilde{\nu} = 1590 \text{ cm}^{-1}$. With increasing aging time at room temperature a vibration arose at $\tilde{\nu} = 1612 \text{ cm}^{-1}$, which became the predominant carbonyl vibration after 8 h of ageing. Apparently, this complex was slowly changing into a different conformation. Then, for the sake of comparison the same time-dependent experiment was performed with TPMA. Initially, at $t=0$ the Ni-TPMA spectrum had the same C=O vibrations with similar intensities as Ni-TTPMA. However, unlike C=O vibrations of Ni-TTPMA, the C=O vibrations of Ni-TPMA remained unchanged for 24 h. Thus, in the initial stage Ni-TTPMA and Ni-TPMA have similar conformations. However, the additional triethoxysilane groups cause the Ni-TTPMA to gradually rearrange its conformation upon ageing the Ni-TTPMA-mixture, while for Ni-TPMA the original conformation remained intact.

In uranium complexes of tetra-substituted malonamides an additional C=O vibration (1604 cm^{-1}) in between the C=O vibration of free malonamide (1623 cm^{-1}) and single bonded malonamide (1592 cm^{-1}) was associated with a double bonded malonamide [42]. The authors supported their claim by the fact that upon reducing r_C from 1 to $\frac{1}{2}$, the vibration at 1604 cm^{-1} became predominant while the bidentate chelating nitrate vibration at 1524 cm^{-1} diminished, similar to our case. This suggestion is plausible since when a nitrate ligand is replaced by a more nucleophilic malonamide, the acidity of nickel is reduced. Consequently, nickel will have a smaller effect on the force constant of the C=O vibration and this vibration will shift towards the frequency of a free ligand. A similar shift was observed for $\text{Ni}(\text{acac})_2\text{L}$ complexes when increasing the nucleophilic character of the bidentate ligand L [72]. Thus, the gradual change Ni-TTPMA spectrum could be associated to a redistribution of a single malonamide bond to Ni^{2+} towards a complex of multiple malonamide ligands coordinated to Ni^{2+} . This also means that due to rearrangement of this complex at $r_C = 1$, at least half of the Ni^{2+} ions were not coordinated to malonamide. Remarkably, this rearrangement did not occur for Ni-TPMA and the presence of the triethoxysilyl groups may be responsible for this rearrangements process.

As the aging time increased, the extent of hydrolysis and condensation also increased. After 24 h the SiOC vibration diminished almost completely and

almost all alkoxide groups were hydrolyzed. The optimal microporosity in acid catalyzed polymeric sols is typically achieved when the extent of hydrolysis and condensation is limited during the mixing stage [27, 73].

As evidenced by FTIR, the malonamide ligands were coordinating nickel and enhancing its dispersion within the silsesquioxane matrix. Water that was initially coordinated to nickel was released and caused some hydrolysis and condensation of Si-OEt groups. Moreover, the conformation of the Ni-TTPMA complex changed upon aging mixture. This shift was associated with an increasing number of TTPMA ligands being coordinated to Ni. Due to disproportionation of the Ni-TTPMA complex several Ni-ions would not be coordinated to a malonamide ligand. Both aspects, i.e. hydrolysis/condensation before the addition of acidic catalyst and the release of Ni being coordinated to TTPMA, do not present an optimal microstructure for the selective membrane layer. Therefore, the aging time should be kept limited. An aging time $t_{\text{mix}}=2$ h was chosen to ensure for some complexation of nickel before preparing the sol.

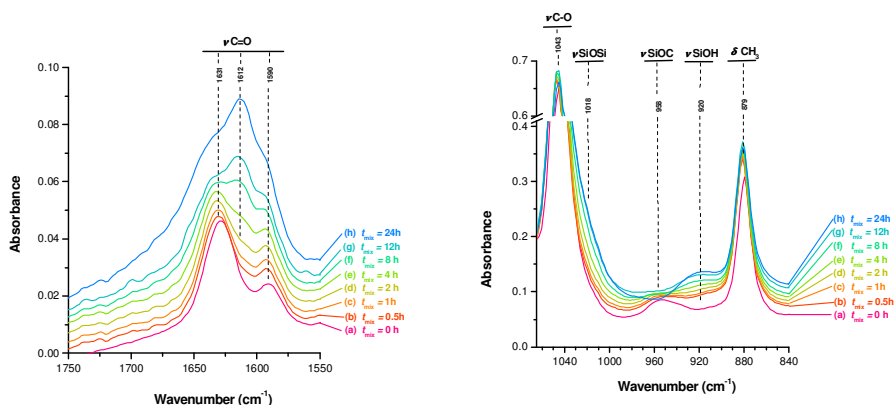


Figure 7.10. FTIR-ATR absorbance spectra of Ni(NO₃)₂/TTPMA solutions in ethanol, with ageing times after aging of 0, 0.5, 1, 2, 4, 8, 12 and 24 h for graphs a-h, respectively. Left: 1750-1550 cm⁻¹ and right: 1065 - 840 cm⁻¹. The intensity of the vibrations are weaker in the 1750-1550 cm⁻¹ region and its scale is therefore enhanced relative to the figure to the right. The lower intensity in the 1750-1550 cm⁻¹ region was partly due to substantial absorption by the diamond ATR, as well as the strong contributions from the siloxane bonds in the 1065 - 840 cm⁻¹ region.

7.4.7. Ni-TTPMA-sol preparation

The sol particle size was easily tuned by the overall concentration [OR], defined here as $[OR] = [-OEt] + [NO_3^-]$. Two different acid ratios were employed: $[H^+]/[OR] = 1/30$ and $1/15$ (Figure 7.11). The sol particle size clearly increased with [OR] for both acid ratios. The higher acid ratio yielded larger sol particles due to an increased condensation rate. Since TTPMA may contain traces of amines and since the Ce-TTPMA layer was found to be quite resistive to gas permeation, the higher ratio $[H^+]/[OR] = 1/15$ was preferred over the smaller one. This ensured an acid catalyzed hydrolysis and condensation mechanism that typically leads to polymeric sol particles in the case of silicates [27, 74]. The optimal particle size (~ 7 nm) with a monomodal particle size distribution (Figure 7.4) for membrane coating onto an $\gamma\text{-Al}_2\text{O}_3/\alpha\text{-Al}_2\text{O}_3$ support [1, 64] was found for sols with $[H^+]/[OR] = 1/15$ and $[OR] = 1.2$ mol/L.

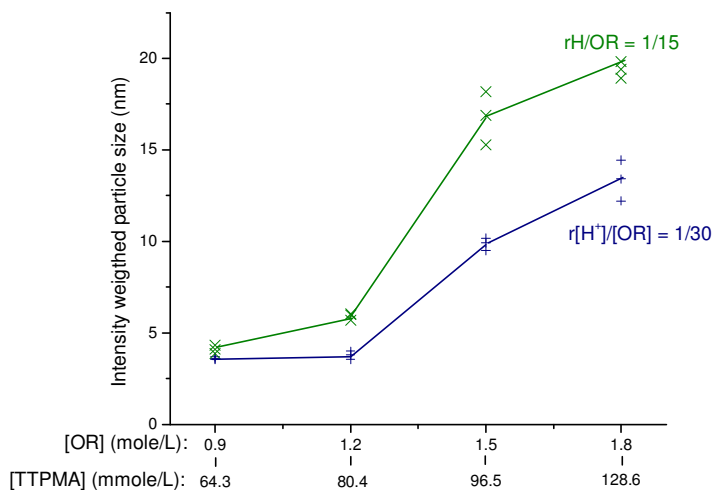


Figure 7.11. Particle size analysis by dynamic light scattering with concentrations $[-OR]$ of 0.9, 1.2, 1.5 and 1.8 and $[H^+]/[OR] = 1/30$ and $1/15$.

7.4.8. Dispersion of Ni²⁺ within the condensed TTPMA matrix.

After sol formation for 1 h at $T=60^{\circ}\text{C}$ the vibration at $\tilde{\nu} = 1612\text{ cm}^{-1}$ was clearly enlarged with respect to the vibration at $\tilde{\nu} = 1590\text{ cm}^{-1}$ (Figure 7.12a). Thus, the system may have reorganized into a mixture of nickel with multiple malonamide ligands and free nickel (nitrate) ions. After coating the sol on a Si-wafer and drying at $T=60^{\circ}\text{C}$, the maximum of the carbonyl vibration was slightly shifted to $\tilde{\nu} = 1604\text{ cm}^{-1}$ (Figure 7.12b). Since this vibration was rather broad, it was not clear whether it should be considered as a different species or as a convolution of the vibrations at $\tilde{\nu} = 1612$ and 1590 cm^{-1} .

However, this vibration was clearly shifted with respect to the coated TTPMA-sol in the absence of nickel (Figure 7.12d), indicating that a substantial amount of nickel remained coordinated to the malonamide ligand. Upon calcination the carbonyl vibration nearly changed (Figure 7.12c) and only a marginal increase of a shoulder at $\tilde{\nu} = 1628\text{ cm}^{-1}$ was observed. In the calcined Ni-TTPMA sample the decomposition of nitrates clearly occurred as shown by reduction of absorbances in the range between $\tilde{\nu} = 1420, 1300\text{ cm}^{-1}$ and 1040 cm^{-1} due to reduction of N=O and N-O vibrations [67, 75, 76]. The reduction of the N-O vibration (1040 cm^{-1}) was less pronounced due to the strong overlap with the increasing asymmetric Si-O-Si vibration ($\tilde{\nu} = 1007\text{ cm}^{-1}$) [70]. The absence of a sharp vibration at $\tilde{\nu} = 3640\text{ cm}^{-1}$ indicates the absence of a hydroxyl group attached to nickel that could have formed during decomposition. However, a broad νOH ($\tilde{\nu} = 3600\text{-}2900\text{ cm}^{-1}$) remained, most likely due to remnant water that is known to remain present in hydrated nickel oxide up to $T=400^{\circ}\text{C}$ [76].

In summary, FTIR measurements reveal that a substantial amount of Ni remains coordinated upon calcination at $T= 250^{\circ}\text{C}$. However, not all Ni ions may be coordinated to malonamide due to the disproportionation of the Ni-TTPMA complex as discussed in section 3.6. Meanwhile, nitrate ions were clearly decomposed, however a substantial amount of water remained present in the microstructure as indicated by the νOH . This could possibly affect the permeability of gases going through the selective membrane layer.

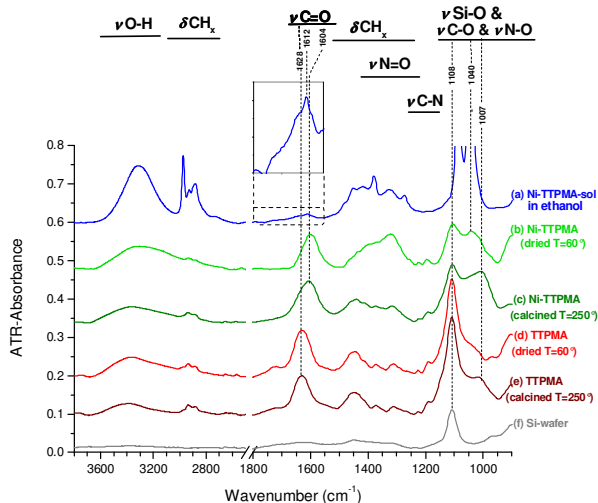


Figure 7.12. FTIR-ATR absorbance spectra. (a) as-prepared Ni-TTPMA sol, with an elongated section of the region with C=O vibrations and H₂O deformations (1800–1550 cm⁻¹); (b-c) spincoated Ni-TTPMA sol on a plasma oxidized silicon wafer, where (b) was dried at T=60°C and (c) was calcined at T=250°C; (d-e) spincoated TTPMA-sol without cerium ions, where (d) was dried at T=60°C and (e) was calcined at T=250°C; (f) clean (O₂-plasma oxidized) Si-wafer.

The Ni-2p region in the XPS spectrum of the dried and calcined sample were identical within experimental error and therefore only the spectrum of the calcined sample is shown Figure 7.13. The Ni 2p^{3/2} binding energies at 856.0 eV and a satellite peak at 861.2 eV clearly revealed the absence of NiO, since NiO has two main peaks at 854.1 and 856.2 eV and two satellite peaks at 861.2 and 863.8 eV [77].

On the other hand, the energies were consistent with a nickel (II) acetylacetonate complex (856.3 eV and a satellite at 861.3 eV), which will have similar binding energies as nickel coordinated to malonamide ligands, as they both have a β-diketonate structure [78]. Also an energy difference of 5.2 eV between the main peak and its satellite peak in the current sample implies that the Ni species has a more ionic character than is found in nickel(II)oxide (7.2 eV) [78]. However, the decomposition of pure Ni(NO₃)₂·6H₂O in nitrogen atmosphere at T=250°C has been reported to lead to formation of Ni₂O₃ due to partial oxidation caused by the presence of nitrate ions [75]. Different energies have been reported for the main Ni 2p_{3/2} peak of Ni₂O₃, ranging from 855.6 to 856.9 eV [79–83]. Thus, the

presence of Ni_2O_3 nanoparticles within the TTPMA-coating cannot be excluded.

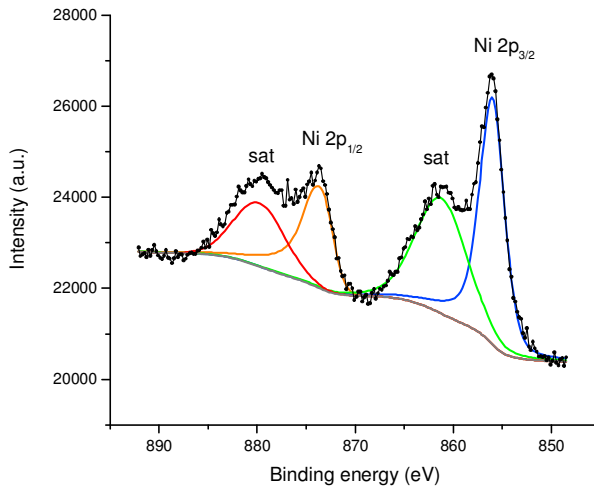


Figure 7.13. XPS-spectrum of Ni-TTPMA-sol after spin-casting on a plasma-oxidized silicon substrate, followed by drying at $T=60^\circ\text{C}$ and calcination at $T=250^\circ\text{C}$ in N_2 .

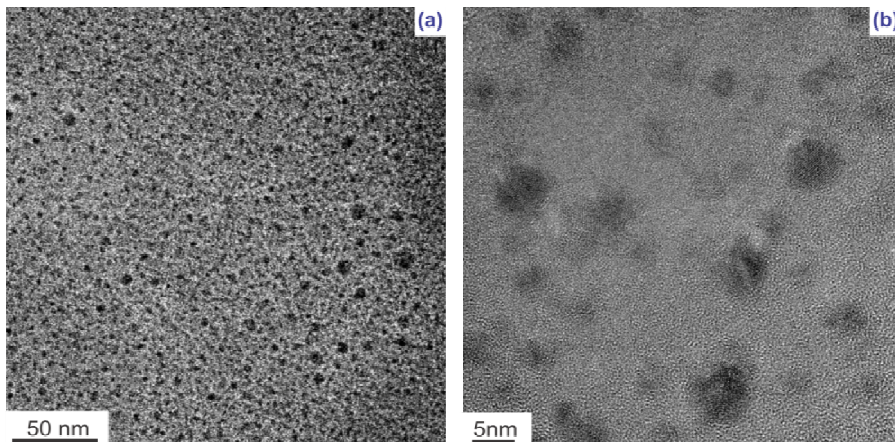


Figure 7.14 HR-TEM images of a holey copper grid dipcoated with Ni-TTPMA after calcination at $T=250^\circ\text{C}$ at 2 different length scales. (a) overview image; (b) magnified image showing phase separated particles with sizes between 1 and 15 nm.

TEM experiments revealed a substantial amount of phase separated electron rich particles. These particles with sizes ranging from 1 to 15 nm (Figure 7.14) most likely consist of hydrated Ni_2O_3 , which seems consistent with the XPS binding energies and the broad OH-stretch vibrations that remained present. Moreover, the polydispersity of these particles is much larger than in the Ce-TTPMA system. Contrary to the Ce-TTPMA system, where phase separation seemed to occur during the calcination process, phase separation in the Ni-TTPMA system was probably initiated by the redistribution of malonamide ligands.

7.4.9. Membrane characteristics of the Ni-TTPMA coated layer

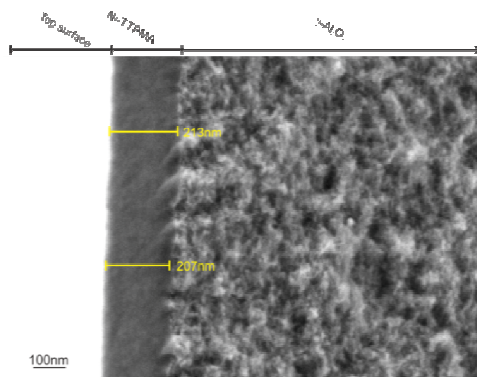


Figure 7.15. HR-SEM image of a selective Ni-TTPMA coated layer on a meso/macroporous $\gamma\text{-Al}_2\text{O}_3/\alpha\text{-Al}_2\text{O}_3$ support.

A thin selective layer of approx. 210 nm thickness was formed on top of the mesoporous $\gamma\text{-Al}_2\text{O}_3$ layer after dipcoating the Ni-TTPMA sol, drying and calcination at $T=250^\circ\text{C}$ (Figure 7.15). The thickness of the defect-free permselective membrane layer was similar to a previously described BTESE (1,2-bis-(triethoxysilyl)ethane) membrane [1]. Helium and hydrogen fluxes were one order of magnitude smaller than through hybrid silica (BTESE)

membranes. Thus, the selective layer was much more resistive than the BTESE membrane. This may have several causes: (1) narrower pores, (2) Ni_2O_3 particles that effectively block pores, (3) lower porosity and/or (4) by the presence of water that remained present in the structure. It has been demonstrated that remnant water in amino-functionalized silsesquioxane membranes reduced their gas permeability [84].

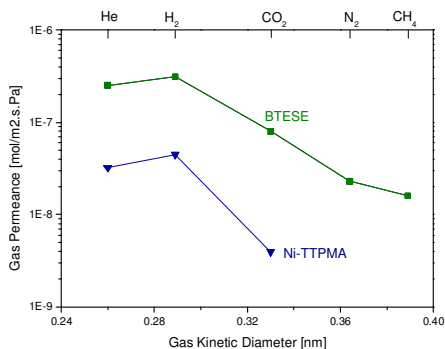


Figure 7.16 Single gas permeances of a Ni-TTPMA membrane layer on a meso/macroporous $\gamma\text{-Al}_2\text{O}_3/\alpha\text{-Al}_2\text{O}_3$ support, and a hybrid BTESE-membrane as reported elsewhere [1].

Remarkably, the membrane was not permeable to N_2 so that it exhibited an infinitely high H_2/N_2 permselectivity. To our knowledge, Ni doping in any silica or any bridged silsesquioxane precursor has not yielded any nitrogen impermeable membrane to date. The high permselectivity can be attributed to a small pore size and a narrow pore size distribution. No indication was found for affinity between Ni species and H_2 . Most likely, the size of the Ni_2O_3 particles needs to be reduced further to measure a significant effect of affinity towards H_2 .

7.5. Conclusions

N,N,N',N'-tetrakis-(3-(triethoxysilyl)-propyl)-malonamide (TTPMA) was synthesized successfully through a base catalyzed nucleophilic substitution of bis-(3-(triethoxysilyl)-propyl)-amine onto malonyl chloride. The malonamide ligand of TTPMA was found to coordinate both Ce^{4+} and Ni^{2+} of cerium isopropoxide and nickel nitrate hexahydrate, respectively.

In the case of Ce-TTPMA CeO_2 phase separated while calcining the mixed hybrid film at $T = 250^\circ\text{C}$. Consequently, nanosized clusters (2-3 nm) of CeO_2 were formed. The single gas permeances revealed a slightly larger H_2/N_2 permselectivity as compared to a previously reported BTESE hybrid membrane, which was substantially thicker (260nm) than the Ce-TTPMA layer.

The conformation of the Ni-TTPMA complex slowly evolves while aging the complex in ethanol. Consequently, some nickel nitrate could phase separate while drying the sol. After calcination nanosized (1-15 nm) nickel oxide particles (most likely Ni_2O_3) were observed by TEM. The 210 nm

selective layer of Ni-TTPMA was approx. 1 order of magnitude more resistive towards gas permeation of H₂, He and CO₂ as compared to a hybrid BTESE layer of similar thickness [1]. No N₂ permeance was observed within the experimental error, which makes this material a promising gas-selective material for CO₂/N₂ separation.

7.6. References

1. Qureshi, H.F., A. Nijmeijer, and L. Winnubst, *Influence of sol-gel process parameters on the micro-structure and performance of hybrid silica membranes*. J. Membr. Sci., 2013. **446**: p. 19-25.
2. Li, J.-R., et al., *Carbon dioxide capture-related gas adsorption and separation in metal-organic frameworks*. Coordin. Chem. Rev., 2011. **255**(15-16): p. 1791-1823.
3. Shekhawat, D., D.R. Luebke, and H.W. Pennline, *A review of carbon dioxide selective membranes*. US Department of Energy, 2003.
4. Olah, G.A., A. Goepfert, and G.K.S. Prakash, *Chemical Recycling of Carbon Dioxide to Methanol and Dimethyl Ether: From Greenhouse Gas to Renewable, Environmentally Carbon Neutral Fuels and Synthetic Hydrocarbons*. J. Org. Chem., 2008. **74**(2): p. 487-498.
5. Ho, M.T., et al., *Economics of CO₂ and Mixed Gas Geosequestration of Flue Gas Using Gas Separation Membranes*. Ind. Eng. Chem. Res., 2005. **45**(8): p. 2546-2552.
6. Chen, H., A.S. Kovvali, and K.K. Sirkar, *Selective CO₂ Separation from CO₂-N₂ Mixtures by Immobilized Glycine-Na-Glycerol Membranes*. Ind. Eng. Chem. Res. 2000. **39**(7): p. 2447-2458.
7. Granite, E.J. and T. O'Brien, *Review of novel methods for carbon dioxide separation from flue and fuel gases*. Fuel Processing Technology, 2005. **86**(14-15): p. 1423-1434.
8. de Vos, R.M. and H. Verweij, *Improved performance of silica membranes for gas separation*. Journal of Membrane Science, 1998. **143**(1-2): p. 37-51.
9. Kanezashi, M. and M. Asaeda, *Hydrogen permeation characteristics and stability of Ni-doped silica membranes in steam at high temperature*. J. Membr. Sci., 2006. **271**(1-2): p. 86-93.
10. Igi, R., et al., *Characterization of co-doped silica for improved hydrothermal stability and application to hydrogen separation*

- membranes at high temperatures.* J. Am. Ceram. Soc., 2008. **91**(9): p. 2975-2981.
11. Buxbaum, R.E. and A.B. Kinney, *Hydrogen transport through tubular membranes of palladium-coated tantalum and niobium.* Ind. Eng. Chem. Res., 1996. **35**(2): p. 530-537.
 12. Qi, H., et al., *Effect of Nb content on hydrothermal stability of a novel ethylene-bridged silsesquioxane molecular sieving membrane for H₂/CO₂ separation.* J. Membr. Sci., 2012. **421–422**(0): p. 190-200.
 13. Qi, H., et al., *Hybrid Organic–Inorganic Microporous Membranes with High Hydrothermal Stability for the Separation of Carbon Dioxide.* ChemSusChem, 2010. **3**(12): p. 1375-1378.
 14. Boffa, V., et al., *Microporous niobia-silica membrane with very low CO₂ permeability.* ChemSusChem, 2008. **1**(5): p. 437-443.
 15. Kanezashi, M. and M. Asaeda, *Stability of H₂-permselective Ni-doped silica membranes in steam at high temperature.* J. Chem Eng. Jpn., 2005. **38**(11): p. 908-912.
 16. Takaba, H., et al., *The effect of gas molecule affinities on CO₂ separation from the CO₂/N₂ gas mixture using inorganic membranes as investigated by molecular dynamics simulation.* J. Membr. Sci., 1996. **121**(2): p. 251-259.
 17. Busca, G. and V. Lorenzelli, *Infrared spectroscopic identification of species arising from reactive adsorption of carbon oxides on metal oxide surfaces.* Mater. Chem., 1982. **7**(1): p. 89-126.
 18. Sakakura, T., J.-C. Choi, and H. Yasuda, *Transformation of carbon dioxide.* Chem. Rev., 2007. **107**(6): p. 2365-2387.
 19. Lan, J., et al., *Doping of alkali, alkaline-earth, and transition metals in covalent-organic frameworks for enhancing CO₂ capture by first-principles calculations and molecular simulations.* ACS nano, 2010. **4**(7): p. 4225-4237.
 20. Uhlhorn, R.J.R., K. Keizer, and A.J. Burggraaf, *Gas and surface diffusion in modified γ -alumina systems.* J. Membr. Sci., 1989. **46**(2–3): p. 225-241.
 21. Busca, G., *The surface Acidity and Basidity of Solid Oxides and Zeolites*, in *Metal Oxides, Chemistry and Applications*, F.J.L. G., Editor 2006, CRC Press Taylor & Francis Group: Boca Raton. p. 247-318.
 22. Bordes-Richard, E.C., P., *Optical basicity: A scale of Acidity/Basidity of Solids and its Application to Oxidation Catalysis*, in *Metal Oxides Chemistry and applications*, J.L.G. Fierro, Editor 2006, CRC press Taylor & Francis Group: New York. p. 319-352.

23. Appel, L.G., J.G. Eon, and M. Schmal, *The CO₂–CeO₂ interaction and its role in the CeO₂ reactivity*. Catal. Lett., 1998. **56**(4): p. 199-202.
24. Du, X., et al., *Diffuse reflectance infrared Fourier transform and Raman spectroscopic studies of MoO₃ dispersed on CeO₂ support*. Langmuir, 1999. **15**(5): p. 1693-1697.
25. Gaudon, A., et al., *Phase separation in sol-gel derived ZrO₂-SiO₂ nanostructured materials*. J. Eur. Ceram. Soc., 2005. **25**(2-3 SPEC. ISS.): p. 283-286.
26. Kessler, V.G., et al., *New insight in the role of modifying ligands in the sol-gel processing of metal alkoxide precursors: A possibility to approach new classes of materials*. J. Sol-Gel Sci. Technol., 2006. **40**(2-3): p. 163-179.
27. Brinker, C.J.S., G. W. , *Sol Gel Science, The Physics and Chemistry of Sol-Gel Processing*. Vol. 1. 1990, San Diego: Academic Press. 1-881.
28. Sanchez, C., et al., *Chemical modification of alkoxide precursors*. J. Non-Cryst. Solids, 1988. **100**(1-3): p. 65-76.
29. Sedlar, M. and M. Sayer, *Reactivity of titanium isopropoxide, zirconium propoxide and niobium ethoxide in the system of 2-methoxyethanol, 2,4-pentanedione and water*. J. Sol-Gel Sci. Technol., 1995. **5**(1): p. 27-40.
30. Percy, M., et al., *The influence of β -diketones on the induction times for hydrolysis of zirconium (IV) alkoxides*. J. Mater. Chem., 1999. **9**(2): p. 499-505.
31. Rupp, W., N. Hüsing, and U. Schubert, *Preparation of silica–titania xerogels and aerogels by sol–gel processing of new single-source precursors*. J. Mater. Chem., 2002. **12**(9): p. 2594-2596.
32. Puchberger, M., et al., *Reaction of metal alkoxides with 3-alkyl-substituted acetylacetonone derivatives—coordination vs. hydrodeacylation*. New J. Chem., 2004. **28**(11): p. 1289-1294.
33. Peterlik, H., et al., *Structural investigation of alumina silica mixed oxide gels prepared from organically modified precursors*. Journal of Non-Crystalline Solids, 2007. **353**(16-17): p. 1635-1644.
34. Dubois, G., et al., *Molecular Network Reinforcement of Sol–Gel Glasses*. Adv. Mater., 2007. **19**(22): p. 3989-3994.
35. Dubois, G., et al., *Superior mechanical properties of dense and porous organic/inorganic hybrid thin films*. J. Sol-Gel Sci. Technol., 2008. **48**(1-2): p. 187-193.
36. Oliver, M.S., et al., *Molecular Origins of the Mechanical Behavior of Hybrid Glasses*. Adv. Funct. Mater., 2010. **20**(17): p. 2884-2892.

37. Tian, Q. and M.A. Hughes, *Synthesis and characterisation of diamide extractants for the extraction of neodymium*. Hydrometallurgy, 1994. **36**(1): p. 79-94.
38. Kudo, H., F. Sanda, and T. Endo, *Efficient synthesis of macrocycles by oxidation of cysteine-based dithiols*. Tetrahedron Lett., 2001. **42**(44): p. 7847-7850.
39. Ellis, R.J. and M.R. Antonio, *Coordination Structures and Supramolecular Architectures in a Cerium(III)–Malonamide Solvent Extraction System*. Langmuir, 2012. **28**(14): p. 5987-5998.
40. Ellis, R.J., et al., *Solvent extraction of cerium (III) using an aliphatic malonamide: The role of acid in organic phase behaviors*. Separation Science and Technology, 2012. **47**(14-15): p. 2007-2014.
41. Parks, B.W., et al., *Solution and Structural Investigations of Ligand Preorganization in Trivalent Lanthanide Complexes of Bicyclic Malonamides*. Inorganic chemistry, 2006. **45**(4): p. 1498-1507.
42. Lumetta, G.J., et al., *Synthesis and characterization of mono- and bis-(tetraalkylmalonamide)uranium(VI) complexes*. Inorganica Chimica Acta, 2000. **309**(1–2): p. 103-108.
43. Chan, G.Y., et al., *Solvent extraction of metal ions from nitric acid solution using N, N'-substituted malonamides. Experimental and crystallographic evidence for two mechanisms of extraction, metal complexation and ion-pair formation*. Journal of the Chemical Society, Dalton Transactions, 1997(4): p. 649-660.
44. Drew, M.G., et al., *Crystal structure of [Yb (L (NO₃)₂ (H₂O)₂)](NO₃), L= bromo-N, N, N', N'-tetraethylmalonamide*. Journal of Chemical Crystallography, 2000. **30**(7): p. 455-458.
45. Fedosseev, A.M., et al., *Synthesis, crystal structure and some properties of new perrhenate and pertechnetate complexes of Nd³⁺ and Am³⁺ with 2,6-bis(tetramethylfuran)-1,2,4-triazin-3-yl-pyridine, tris(2-pyridylmethyl)amine and N,N'-tetraethylmalonamide*. Polyhedron, 2008. **27**(8): p. 2007-2014.
46. Iveson, P.B., et al., *Structural studies of lanthanide complexes with new hydrophobic malonamide solvent extraction agents†*. Journal of the Chemical Society, Dalton Transactions, 1999(20): p. 3605-3610.
47. Parella, T., *Pulse Program Catalogue*. NMR Guide, 2004. **4**.
48. Poppe, L. and H. van Halbeek, *¹³C-selective, ¹H-detected 2D {¹H, ¹³C} correlation spectra of oligosaccharides*. Magnetic Resonance in Chemistry, 1991. **29**(8): p. 848-851.

49. Bax, A. and M.F. Summers, *Proton and carbon-13 assignments from sensitivity-enhanced detection of heteronuclear multiple-bond connectivity by 2D multiple quantum NMR*. Journal of the American Chemical Society, 1986. **108**(8): p. 2093-2094.
50. Hurd, R.E. and B.K. John, *Gradient-enhanced proton-detected heteronuclear multiple-quantum coherence spectroscopy*. J. Mag. Reson. (1969), 1991. **91**(3): p. 648-653.
51. De Vos, R.M. and H. Verweij, *High-selectivity, high-flux silica membranes for gas separation*. Science, 1998. **279**(5357): p. 1710-1711.
52. Cao, G.Z., et al., *Permporometry study on the size distribution of active pores in porous ceramic membranes*. J. Membr. Sci., 1993. **83**(2): p. 221-235.
53. *N,N,N',N'-tetrapropylmalonamide (SDBS-no= 51018)*, Available from SDBSWeb: <http://sdb.srioddb.aist.go.jp>, (National Institute of Advanced Industrial Science and Technology (AIST)), accessed on 14-05-2013.
54. Bradley, E.K., et al., *NMR structural characterization of oligo-N-substituted glycine lead compounds from a combinatorial library*. Mol. Divers., 1997. **3**(1): p. 1-15.
55. Bradley, E.K., *A Method for Sequential NMR Assignment of ^1H and ^{13}C Resonances of N-Substituted Glycine Peptoids*. J. Mag. Reson. B, 1996. **110**(2): p. 195-197.
56. Bax, A., S.W. Sparks, and D.A. Torchia, *Long range heteronuclear correlation. A powerful tool for the NMR analysis of medium-size proteins*. J. Am. Chem. Soc., 1988. **110**(23): p. 7926-7927.
57. X.Webster, R.M.S.F., *Spectrometric identification of organic compounds. 6th ed.* 1998, New York: John Wiley & Sons, Inc.
58. *ethyl 2-chloro-3-oxobutyrate (SDBS-no= 12496)*. Available from SDBSWeb: <http://sdb.srioddb.aist.go.jp> (National Institute of Advanced Industrial Science and Technology (AIST)) accessed on 14-05-2013.
59. *diethyl 3-oxoglutarate (SDBS-No= 6503)*. Available from SDBSWeb: <http://sdb.srioddb.aist.go.jp>, (National Institute of Advanced Industrial Science and Technology (AIST)), accessed on 14-05-2013.
60. Ryu, Y. and A.I. Scott, *Self-condensation of activated malonic acid half esters: a model for the decarboxylative Claisen condensation in polyketide biosynthesis*. Tetrahedron Lett., 2003. **44**(40): p. 7499-7502.

61. Den Auwer, C., et al., *Crystallographic, X-ray Absorption, and IR Studies of Solid- and Solution-State Structures of Tris(nitrato) N,N,N',N'-Tetraethylmalonamide Complexes of Lanthanides. Comparison with the Americium Complex*. Inorg. Chem., 2000. **39**(7): p. 1487-1495.
62. Fleeting, K.A., et al., *Studies on Mixed β -Diketonate/Isopropoxide Compounds of Zirconium and Hafnium, the X-ray Single-Crystal Structures of $[M_2(OPri)_6(tmhd)_2]$ ($M = Zr, Hf$): Some Chemistry Important in the MOCVD of Oxides*. Inorg. Chem., 1999. **38**(7): p. 1432-1437.
63. Vaartstra, B.A., et al., *Alcohol adducts of alkoxides: intramolecular hydrogen bonding as a general structural feature*. Inorg. Chem., 1990. **29**(17): p. 3126-3131.
64. Castricum, H.L., et al., *Hydrothermally stable molecular separation membranes from organically linked silica*. J. Mater. Chem., 2008. **18**(18): p. 2150-2158.
65. Bo, L., et al., *High-pressure Raman study on Ce O₂ nanospheres self-assembled by 5 nm Ce O₂ nanoparticles*. Phys Status Solidi B: 2011. **248**: p. 1154-1157.
66. Bickley, R.I., et al., *Vibrational spectroscopic study of nickel(II) hypophosphite, Ni(H₂PO₂)₂*. J. Mol. Struct., 1992. **273**: p. 61-72.
67. Nakamoto, K., *Infra red and Raman spectra of Inorganic and coordination compounds*. 4 ed, ed. K. Nakamoto 1986, New York: John Wiley & Sons. 259-263.
68. Matos, M., L. Ilharco, and R. Almeida, *The evolution of TEOS to silica gel and glass by vibrational spectroscopy*. J. Non-Cryst. Solids, 1992. **147**: p. 232-237.
69. Niznansky, D. and J. Rehspringer, *Infrared study of SiO₂ sol to gel evolution and gel aging*. J. Non-Cryst. Solids, 1995. **180**(2): p. 191-196.
70. Chen, S.G., Y.S. Yin, and D.P. Wang, *Formation of Ring-Like Si-O-Zr Bonds at Intergranular Interfaces in Silica-Doped Zirconia*. J. Am. Ceram. Soc., 2005. **88**(4): p. 1041-1045.
71. Tejedor-Tejedor, M.I., L. Paredes, and M.A. Anderson, *Evaluation of ATR-FTIR Spectroscopy as an "in Situ" Tool for Following the Hydrolysis and Condensation of Alkoxysilanes under Rich H₂O Conditions*. Chem. Mater., 1998. **10**(11): p. 3410-3421.
72. Niven, M.L. and G.C. Percy, *The infrared spectra (3500-140 cm⁻¹) of the 2, 2'-bipyridine, 2-aminomethylpyridine and ethylenediamine adducts and the sodium tris-compounds of cobalt (II), nickel (II) and*

- zinc (II) acetylacetonates*. *Transit. Metal Chem.*, 1978. **3**(1): p. 267-271.
73. Castricum, H.L., et al., *Microporous structure and enhanced hydrophobicity in methylated SiO₂ for molecular separation*. *J. Mater. Chem.*, 2007. **17**(15): p. 1509-1517.
74. de Vos, R.M., W.F. Maier, and H. Verweij, *Hydrophobic silica membranes for gas separation*. *J. Membr. Sci.*, 1999. **158**(1-2): p. 277-288.
75. Brockner, W., C. Ehrhardt, and M. Gjikaj, *Thermal decomposition of nickel nitrate hexahydrate, Ni(NO₃)₂·6H₂O, in comparison to Co(NO₃)₂·6H₂O and Ca(NO₃)₂·4H₂O*. *Thermochim. Acta*, 2007. **456**(1): p. 64-68.
76. Mansour, S.A.A., *Spectroscopic and microscopic investigations of the thermal decomposition of nickel oxysalts: Part 2. Nickel nitrate hexahydrate*. *Thermochim. Acta*, 1993. **228**(0): p. 173-189.
77. Mansour, A., *Characterization of NiO by XPS*. *Surf. Sci. Spectra*, 1994. **3**: p. 231.
78. de Souza, M.O., et al., *XPS characterization of nickel-acetylacetonate impregnated in NaX and NaY zeolites*. *Micropor. Mesopor. Mat.*, 2004. **69**(3): p. 217-221.
79. Ho, S.-C. and T.-C. Chou, *The Role of Anion in the Preparation of Nickel Catalyst Detected by TPR and FTIR Spectra*. *Ind. Eng. Chem. Res.*, 1995. **34**(7): p. 2279-2284.
80. Lian, K., D. Kirk, and S. Thorpe, *Investigation of a "Two-State" Tafel Phenomenon for the Oxygen Evolution Reaction on an Amorphous Ni-Co Alloy*. *J. Electrochem. Soc.*, 1995. **142**(11): p. 3704-3712.
81. Zhao, G., et al., *Ni₂O₃-Au⁺ hybrid active sites on NiO_x@Au ensembles for low-temperature gas-phase oxidation of alcohols*. *Catal. Sci. Technol.*, 2013. **3**(2): p. 404-408.
82. Salvati, L., et al., *Surface spectroscopic study of tungsten-alumina catalysts using x-ray photoelectron, ion scattering, and Raman spectroscopies*. *J. Phys. Chem.*, 1981. **85**(24): p. 3700-3707.
83. Dufresne, P., et al., *Study of nickel-molybdenum-gamma-aluminum oxide catalysts by x-ray photoelectron and Raman spectroscopy. Comparison with cobalt-molybdenum-gamma-aluminum oxide catalysts*. *J. Phys. Chem.*, 1981. **85**(16): p. 2344-2351.
84. Paradis, G.G., et al., *Amino-functionalized microporous hybrid silica membranes*. *J. Mater. Chem.*, 2012. **22**(15): p. 7258-7264.

8.

Conclusions and Outlook

8.1. General Conclusions

The hydrolysis and condensation of silsesquioxanes cannot compete with the fast kinetics of metal alkoxides such as niobium penta ethoxide (NPE). Consequently, the speed of nucleation of NPE was scarcely affected by the presence of a silsesquioxane: 1,2-bis-(triethoxysilyl)-ethane (BTESE) (**Chapter 3**). Nevertheless, subsequent growth was affected by the presence of BTESE as indicated by a reduced growth exponent and reduced mass-fractal dimension. Growth of BTESE/NPE sols most likely occurred through reversible Lifshitz-Slyozov type agglomeration kernels unlike growth in the absence of BTESE that most likely occurred through irreversible Smoluchowski type agglomeration kernels.

During the initial stages of the drying process of BTESE/NPE sols the size of primary building blocks increased in size while the overall agglomerate size remained almost constant (**Chapter 4**). This could be associated with a coarsening effect of branched particles [1, 2]. This agrees with Lifshitz-Slyozov type agglomeration, since irreversible agglomeration kernels would not allow structural rearrangements. During the next stage of the drying process electron rich domains became apparent that were associated with phase separated niobia. The size of phase separated niobia was reduced when BTESE was hydrolysed first before adding NPE.

Nevertheless, following the ^{17}O -NMR spectroscopy (**Chapter 5**) the prehydrolysis of BTESE before adding NPE did not lead to a substantial increase in the number of Si-O-Nb linkages. On the other hand the use of acetylacetonate that effectively blocked coordination sites of NPE led to a substantial increase in the number of Si-O-Nb linkages. Moreover ^{29}Si -NMR proved the survival of the Si-C linkage up to $T=200^\circ\text{C}$ in air.

$\text{Nb}_8\text{O}_{10}(\text{OEt})_{20}$ could be synthesized through a slow and controlled condensation of niobium(V)ethoxide with acetone as a oxolation source at room temperature (**Chapter 6**). These recovered $\text{Nb}_8\text{O}_{10}(\text{OEt})_{20}$ crystallites were found to exhibit a remarkable anisotropic thermal expansion coefficient.

N,N,N',N'-tetrakis-(3-(triethoxysilyl)-propyl)-malonamide (TTPMA) was synthesized successfully through a base catalyzed nucleophilic substitution of bis-(3-(triethoxysilyl)-propyl)-amine onto malonyl chloride (**Chapter 7**). The malonamide ligand of TTPMA was found to coordinate both Ce^{4+} and Ni^{2+} of cerium isopropoxide and nickel nitrate hexahydrate, respectively. However, phase separation of both CeO_2 and NiO was not completely avoided. Despite the phase separated metal oxide clusters single gas permeation measurements gave reasonable results: Although, the Ce-TTPMA and Ni-TTPMA the layers were more resistant to gas permeation as compared to previously measured BTESE membranes [3], they also became more selective.

8.2. Additional observations and remarks

This paragraph described additional results that were not incorporated in one of the previous chapters.

Nonhydrolytic Sol-Gel Synthesis: These synthesis were expected to yield Nb-O-SI more selectively. However, several different non-hydrolytic ester elimination and ethyl halide elimination reactions were verified at $T=110^\circ C$ which includes: (1) Ester elimination between niobium penta ethoxide and di-*t*-butoxy-di-acetoxysilane in dichloromethane, (2) Ethyl halide elimination niobium penta ethoxide and 1,2-bis-(trichlorosilyl)-ethane in dichloromethane and (3) Ethyl halide elimination niobium penta chloride and 1,2-bis-(triethoxysilyl)-ethane in tetrahydrofuran. H-NMR results indicated that ligand exchange easily occurred, which enabled a faster condensation of metal alkoxide as compared to the silicon alkoxide. In conclusion, although the condensation rates of niobium ethoxide may be reduced through a nonhydrolytic pathways, it did not resolve the mismatch in condensation rates between silicon and metal alkoxides.

Noesy-correlations TTPMA-NPE complex: By means of the nuclear Overhauser effect cross-correlations can be measured between protons that are in a close surrounding to each other ($\sim 5 \text{ \AA}$ in distance)[4]. Hence, it can confirm cross-correlation between protons of a metal alkoxide that engaged protons of the *N,N,N',N'*-tetrakis-(3-(triethoxysilyl)-propyl)-malonamide (TTPMA) molecule upon complexation. After mixing a mixture of niobium penta ethoxide (NPE) with TTPMA in a 1:1 ratio for one day a noesygpphpp [5] was performed in CDCl_3 (Figure 8.1a). Clear cross-correlations were observed between particular CH_2 entities of NPE and CH_2 entities of the propylene bridge of TTPMA as being assigned by the symbols (I) and (II). These assignments were schematically illustrated in Figure 8.1b. The exact nature of this complex was difficult to resolve and several entities coexisted in a range between $4.0 < \delta < 4.5$.

To confirm Ce-TTPMA complexation as being discussed in **Chapter 7** noesy experiments on such mixtures may be useful as well. However, NMR-spectroscopy measurements of Cerium(IV)isopropoxide did not give reliable results, since no cross-correlations were found in a $^1\text{H}, ^1\text{H}$ -Cosy experiments. This may be a consequence of paramagnetic impurities.

8.3. Future perspective and outlook

In the last decennia, the chemistry of metal alkoxide / silicon alkoxide mixtures have been exploited to a large extent. The extent of phase separation can be reduced to certain extent but it rarely completely avoided. Therefore, this direction does not offer much possibilities anymore. On the other hand the hybrid chemistry of silsesquioxanes still offer many opportunities, since the many combinations of organic chemistry approaches with silicon alkoxide chemistry are far from being exploited:

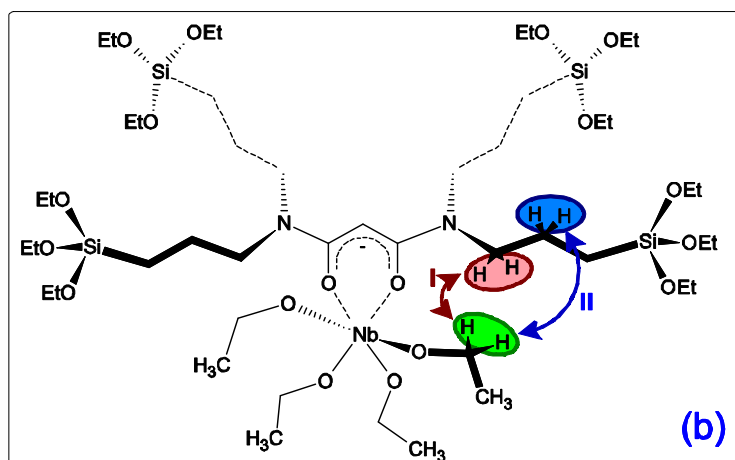
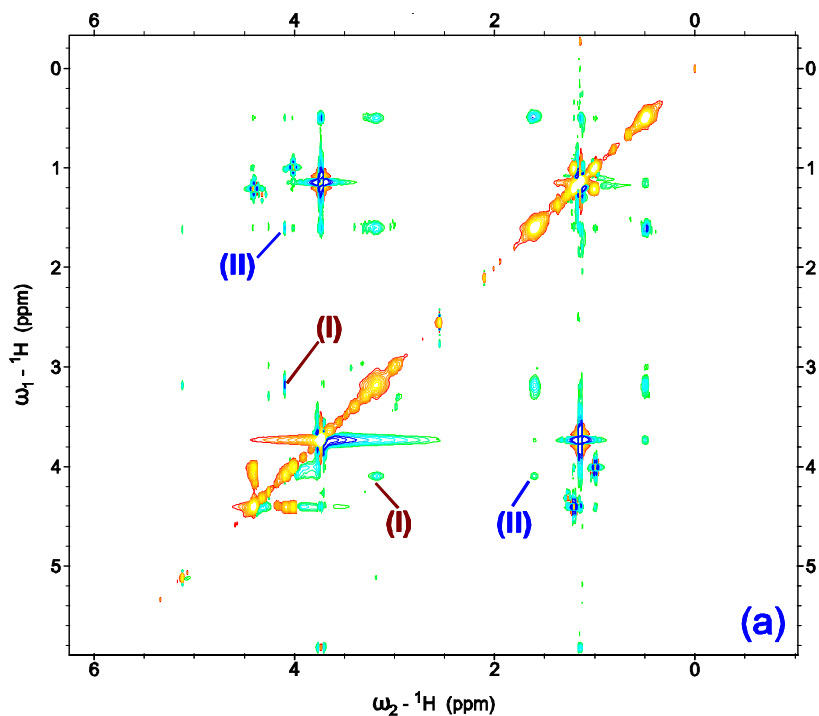


Figure 8.1. (a) $^1\text{H}, ^1\text{H}$ -noesy experiment of an 1:1 NPE:TTPMA mixture in CDCl_3 . (b) Molecular illustration of cross-correlation between protons of NPE and TTPMA in the $^1\text{H}, ^1\text{H}$ -noesy experiment (a).

Hydrothermal and chemical stability: A higher hydrothermal and chemical stability may be achieved by further engaging the boundary between ceramics and polymers. Thus, replacing the bridged silsesquioxane precursor that contained $2x$ $-\text{Si}(\text{OR})_3$ entities for small oligomers that contained $3 - 20x$ $-\text{Si}(\text{OR})_3$ entities. The highest network stability is probably achieved by a smart combination of different chemical bonds that build-up the network. For instance by combining amide-bonds that are more resistant to bases with siloxane-bonds that are more resistant to acids. Consequently, attack of either one of them would have a lower impact.

Alter the membrane's affinity for particular gases or molecules: Silsesquioxanes can be attached to organometallic entities such as (1) porphyrins, or (2) metaloscenes. One very famous porphyrin: heme is responsible for the transport of oxygen and carbon dioxide through the human body.

8.3. References

1. Conti, M., A. Lipshtat, and B. Meerson, *Scaling anomalies in the coarsening dynamics of fractal viscous fingering patterns*. Physical Review E, 2004. **69**(3): p. 031406.
2. Sharon, E., et al., *Coarsening of Fractal Viscous Fingering Patterns*. Physical review letters, 2003. **91**(20): p. 205504.
3. Qureshi, H.F., A. Nijmeijer, and L. Winnubst, *Influence of sol-gel process parameters on the micro-structure and performance of hybrid silica membranes*. Journal of Membrane Science, 2013. **446**(0): p. 19-25.
4. Anet, F.A.L. and A.J.R. Bourn, *Nuclear Magnetic Resonance Spectral Assignments from Nuclear Overhauser Effects1*. Journal of the American Chemical Society, 1965. **87**(22): p. 5250-5251.
5. Parella, T., *Pulse Program Catalogue*. NMR Guide, 2004. **4**.

Summary.

Chapter 1 Introduces the Sol-Gel Chemistry of silicon and metal alkoxides and the fundamental differences between them. In addition strategies to manipulate their chemistry were being discussed. Then, it continues with by describing the processes being involved to make microporous membranes. This is being followed by a description of microporous membranes and their transport mechanisms. Then, this chapter was finalized by describing the scope of the thesis with a brief outline.

Chapter 2 evaluated theoretical aspects of Small Angle X-ray Scattering (SAXS), which are useful for the understanding of **Chapter 3** and **Chapter 4** where this technique was evaluated extensively. It evaluated the basic concepts of form and structure functions for mass-fractal and correlated systems with the main focus on isotropically dispersed spherical like agglomerates.

Chapter 3 involved rapid in-situ SAXS measurements were performed to measure early-stage agglomeration processes under niobium ethoxide mixtures in the presence and absence of 1,2-bis-(triethoxysilyl)-ethane (BTESE). A newly derived mass-fractal model was used that allowed the characterisation of the radii of gyration (R_G), mass-fractal dimension (D_f) and Z-parameter that was associated with the polydispersity. The trends of the experiments in the presence and absence of BTESE were consistent diffusion limited cluster aggregation. Moreover the growth processes led to self-preserving polydispersities. Nevertheless, growth in the absence of BTESE was consistent with irreversible Smoluchowski type agglomeration kernels, while growth in the presence of BTESE was more consistent with reversible Lifshitz-Slyozov type agglomeration kernels.

Chapter 4 evaluated in-situ SAXS measurements while drying mixed niobium ethoxide bridged silsesquioxane sol at $T=40-80^\circ\text{C}$. During this drying process the system changed from a system that contains branched polymer-like particles into a system with correlated domains. The correlated domains were associated with nanosized electron rich niobia clusters that were embedded inside an condensed silsesquioxane matrix. Therefore, these SAXS-measurements could be used to minimize the size of the phase-separated niobia domains. When the silsesquioxane precursor (1,2-bis-triethoxysilyl)-ethane) was hydrolysed first before addition of niobium penta ethoxide slightly smaller niobia particles had phase

separated as compared to the case when both precursors were hydrolyzed simultaneously.

In **Chapter 5** different synthesis routes were evaluated with the aim of optimizing the incorporation of niobium within a hybrid silica matrix on an atomic scale. Due to mismatch in hydrolysis/condensation rates between 1,2-bis-triethoxy-ethane (BTESE) and niobium penta-ethoxide (NPE), phase separated domains of Nb₂O₅ inside the silsesquioxane matrix were expected. To overcome this effect we a) performed a prehydrolysis of BTESE prior to adding NPE, or b) attempted to reduce the availability of Nb via a complexation of Nb by either acetyl acetone or 2-methoxy-ethanol. The network organization was evaluated from results of FTIR as well as ¹³C, ²⁹Si and ¹⁷O MAS NMR spectroscopy. Whereas the prehydrolysis of BTESE and the addition of 2-methoxy-ethanol induced a but only moderate mixing of Nb and Si, leading to a network in which islands of Nb₂O₅ are linked to the hosting silica based matrix via Nb-O-Si bonds, the use of acetylacetonate lead to a mixing of Nb and Si on the atomic scale, producing a mixed Nb-O-Si network without any extended clusters of segregated Nb₂O₅.

In **Chapter 6** Acetone was evaluated as an oxolation source of niobium penta ethoxide to synthesize nanosized Nb₈O₁₀(OEt)₁₀ clusters. Its mild reactivity allows a controlled condensation and crystallization of this molecule. A process occurs via two complementary routes: (1) aldol condensation and (2) ether elimination. The structure refinement on the crystallites at $T=150\text{K}$ and $T=296\text{K}$ revealed a remarkable anisotropy in the thermal expansion of Nb₈O₁₀(OEt)₁₀ with a negative expansion coefficient along the *c*-axis. At reduced temperatures the Nb₈O₁₀(OEt)₁₀ clusters were tilted towards the *a* and *c*-axis, most likely driven by a reduction of thermal motion and steric hindrance. Moreover, the irregular shape of the clusters allowed a relatively large compression along the *a*-axis and a relatively large expansion along the *c*-axis.

In **Chapter 7** we applied a different approach to the dispersion of metal ions within the silsesquioxane matrix: With the aim to synthesize single source precursors a malonamide bridged silsesquioxane was synthesized. These malonamide ligands were able to coordinate Ce⁴⁺ and Ni²⁺ metal centers and enhanced their dispersion. However, during calcination these metal centers redistributed into small nanosized grains of CeO₂ (<5 nm) and Ni₂O₃

(<15 nm). Nevertheless, these Ce-TTPMA and Ni-TTPMA membranes showed higher H₂/N₂ permselectivities as compared to previously reported hybrid BTESE (1,2-bis-(triethoxysilyl)ethane) membranes [1]. The TTPMA-precursor was found suitable for membrane separation and can be a promising and versatile precursor for the incorporation of metal ions within hybrid silica matrices.

Samenvatting.

Dit proefschrift beschrijft een aantal methoden om metaalionen / metaaloxiden in microporeuze hybride silicaat glazen te verwerken om daarmee zijn eigenschappen aan te manipuleren. Een microporeus glas kan worden gezien als een wanordelijk web van atomen, waar minuscule poriën tussen gevormd zijn. Deze poriën zijn net groot genoeg om de kleinste moleculen zoals, koolzuurgas (CO₂), stikstof (N₂), waterstof (H₂), water (H₂O), helium (He), methanol (CH₃OH) en methaan (CH₄) door te laten. Zodoende is het bruikbaar als een moleculaire filter waarbij kleine moleculen als waterstof (d = 2.9Å) makkelijker door het membraan gaan als een molecuul dat net wat groter is zoals stikstof (d = 3.6Å). Met het incorporeren van bepaalde metaalionen zouden we ten eerste de chemische stabiliteit kunnen verhogen om daarmee het materiaal meer corrosiebestendig te maken, en ten tweede de affiniteit voor bepaalde gassen kunnen manipuleren zodat bepaalde gassen gemakkelijker door het membraan migreren als anderen. Echter, het inbrengen van metaalionen is niet eenvoudig, daar zij zich meestal niet goed inmengen in de silica / hybride silica structuur en zich afscheiden als dichte metaaloxide clusters. Om die reden werd er ten eerste verscheidene stadia van deze syntheses bestudeerd waarin dit soort afscheidingen plaatsvinden, en werden er ten tweede alternatieve methoden toegepast om dit soort verschijnselen te onderdrukken.

Dit proefschrift start met een inleiding in chemie en processen die plaatsvinden voor de fabricage van dergelijke type membranen gevolgd door een beschrijving van de eigenschappen en transportprocessen in deze membranen (**hoofdstuk 1**). Vervolgens wordt er in **hoofdstuk 2** een theoretische beschrijving gegeven voor de interpretatie van kleine hoek röntgen verstrooiing (SAXS) dat ons in staat stelt deeltjesgroei, agglomeratie en fase-separatie in situ te volgen gedurende mix, reflux en droogprocessen. Deze theorie is vervolgens toegepast in de experimentele hoofdstukken 3 en 4. Daarin beschrijft **hoofdstuk 3** de eerste groeistadia van de niobium(V)ethoxide (NPE) met en zonder de aanwezigheid van een hybride silica precursor 1,2-bis-(triethoxysilyl)-ethane (BTESE). Hoewel BTESE nagenoeg een invloed lijkt te hebben op het snelle nucleatieproces van NPE, wordt daarentegen het groeiproces duidelijk veranderd. In tegenstelling tot de situatie zonder BTESE gaat deeltjesgroei over naar een reversibel agglomeratieproces. Dit leidt op zijn beurt tot een lagere massa-fractale dimensie wat overeenkomt met een meer open structuur.

Vervolgens richt **hoofdstuk 4** zich op een later stadium van het fabricageproces: het droogproces. Dit proces was gekenmerkt door in drie stadia: (I) een stadium van verruwing of Oswald ripening waarbij de kleinste entiteiten uit het systeem blijken te verdwijnen, (II) een overgangsproces naar een gel/vaste stof, en (III) een verdichtingproces. Met name gedurende het overgangsproces (II) vind er een radicale verandering plaats in het verstrooiingspatroon, waarbij een correlatiepiek verschijnt. Een correlatie piek dat geassocieerd kan worden met fasegesepareerde metaal oxide clusters. Een zorgvuldige analyse van deze patronen geeft informatie betreffende de grote van dergelijke type clusters. Daarbij blijkt een voortijdige hydrolyse van de BTESE-precursor een kleine reductie van fasegesepareerde clusters op te leveren.

In het opvolgende **hoofdstuk 5** werden de gedroogde glasachtige NPE-BTESE poeders geanalyseerd met vaste stof kernspinresonantie spectroscopie. Dit stelde ons in staat iets meer te zeggen over de moleculaire verbindingen die in het systeem gevormd waren. In het bijzonder de kernspinresonantiemetingen op het ^{17}O met ^{17}O verrijkte samples gaven een goed inzicht in de dispersie van niobium ionen in de glas-achtige matrix. Daaruit bleek met name dat het gebruik van het afschermdende legand acetylaceton een toenemende mate dispersie van de niobium ionen in de hybride silica matrix tot gevolg had.

In **hoofdstuk 6** zijn de nonhydrolytische hydrolyse en condensatie van NPE onderzocht met acetone als een initiator in plaats van water. Een mildere initiator voor het condensatieproces leidt tot een tragere beter controleerbare condensatie van NPE dat in de afwezigheid van BTESE uitkristalliseerde tot vrij zuivere $\text{Nb}_8\text{O}_{10}(\text{OEt})_{20}$ kristallen. Hoewel deze kristallen al eens eerder waren gesynthetiseerd, werd er dit keer een opmerkelijke thermische anisotropie waargenomen wat uitvoerig in het hoofdstuk beschreven is. In de aanwezigheid van BTESE bleken dit type condensatie mechanismen echter niet te werken.

Om een verschillende ionen beter in de hybride silica matrix te dispergeren werd in **hoofdstuk 7** een alternative hybride silica precursor gesynthetiseerd met een gebrugde malonamide groep, namelijk: *N,N,N',N'*-tetrakis(triethoxysilylpropyl)malonamide, wat we voor het gemak afgekort was als TTPMA. Deze entiteit zou ons in staat stellen metal ionen te dispergeren in de hybride silica precursor alvorens de condensatie reactie met behulp van een in ethanol verdunde water/salpeterzuur mengsel in

werking werd gezet. Hierbij werd gekozen voor de incorporatie van cerium en nikkel ionen die in potentie affiniteit zullen vertonen met respectievelijk CO₂ en H₂ gas. Ondanks het feit fase-separatie niet helmaal vermeden kon worden en gaspermeatiemetingen geen aanwijzingen vertoonden voor een veranderde affiniteit voor CO₂ en/of H₂ was er zowel in het geval van nikkel als cerium gemixte TTPMA een verbeterde selectiviteit waargenomen ten opzichte van eerder gerapporteerde BTESE-membranen. Een verbetering dat waarschijnlijk geassocieerd moet worden met een betere poriegrootteverdeling.

Acknowledgement.

A promotion is a little difficult without the help of others and consequently I should thank some that made it possible. First of all I should thank my promoter André ten Elshof for his guidance. André is a nice supervisor who gave me always much confidence and most of the time he sees the bright perspectives of particular results. I had always appreciated his optimism. Beside that I could always walk into his office whenever I needed advise.

Moreover, I would like to thank Tomek as a supervisor (during my masters), colleague and good friend. We shared much thoughts, particularly, concerning small angle X-ray scattering (SAXS). Together we dove into the theory of this phenomena and we became a bit the SAXS-experts of the group. I also like to thank you and Kasia for nice trips to Gogol Bordello, Leeds and a memorable birthday party of your daughter Maja in Poland.

Besides that, I like to thank all the other members of the SAXS-clan (Sjoerd, Hessel, Suresh, Sajid, Pablo en Huiyu) for the nice trips to the European Synchrotron Radiation Facility (ESRF) in Grenoble, the explorative measurements and interesting discussions. Of course non-stop measurements at the beamline for 3-4 days and a planning that was susceptible to modifications, sometimes gave some tensions and insomnia. Nevertheless, during these trips we really get to know each other and I these experiences were very useful to me. Also, I must thank the technicians of the Dutch Belgium beamline (DUBBLE, Bm26). Particularly I would like to thank Guiseppe, however also Daniel, Fabian and Wim for their preparative work, assistance and their willingness to solve issues after office hours.

Furthermore, I will tank a few people for measurements that were performed outside the inorganic materials science (IMS) group: Therefore, I firstly like to thank Leo and Sabarinathan from the University of Ausburg for the solid state Magic angle spinning nuclear magnetic resonance spectroscopy (solid-state MAS NMR) measurements on mixed niobia hybrid silica systems. Particularly, his expertise of the exotic ^{17}O but also on ^{29}Si and ^{13}C provided a useful insight in the structural connection being formed within these glassy materials (chapter 5).

Secondly, I would like to thank Martin Lutz and Vadim Kessler for single crystalline X-ray diffraction measurements on the $\text{Nb}_8\text{O}_{10}(\text{OEt})_{20}$ crystallites. Thirdly, I would like to thank Hessel for a constructive cooperation within the STW-project (National Institute of Technical Sciences). Particularly

concerning the chemical stability measurements, however we also cooperated in the field of SAXS. Although sometimes, he overloaded me with lots of ideas, it mostly contained some useful information. Additionally I should also thank Hammad, Arjan and Louis for a good cooperation with the inorganic membranes group (IM). Particularly, with Hammad I worked together in applying mixed metal oxide hybrid silica for membrane applications. Moreover, I thank Mariëlle, Jaap en Wim for their help and cooperation in coating tubular membranes as well as I appreciated their critical input which kept me thinking further. Also, I would like to thank all the other members of the STW: Rob (ECN), Frans (Pervatech), Monique (STW), Arjan (Shell), Gerald (Akzo Nobel) and Gadi (University of Amsterdam) for their constructive interferences and financial support.

Next, I would like to thank the technicians Henk en Dominic which are crucial to our group and I could reach them for all sorts of technical issues. Dominic helped me substantially with the design and fabrication of a SAXS-mixing setup, which eventually led to a nice chapter (chapter 3). With Henk I shared much thoughts concerning several issues as a flowbox, peltier reactor cooling systems and a mixing setup. It was handy to gain some good advice from an experienced technician.

Furthermore I would like to thank the lab course students David and Kristianne that I had under my supervision for their orienting work. I let them suffer with complex spectroscopic data, which they manage quite well. I also like to thank Robin a bachelor student who performed some research on the TTPMA precursor. With you it was always a surprise what happens in the lab.

Moreover, I like to thank everyone from IMS, including my roommates Michiel, Janneke, Victor, Huiyu, Robert, Mohammed and of course Wouter. Wouter managed to survive 4 years with me in one office and we shared a lot of thoughts. Also, I liked working in the lab with the chemical brothers including: Maarten, Antony, Pablo, Huiyu, Michiel, Gerard, Tomek, Ronald, Ole, Suresh, Nicolas, Petra, Liz, Joren, Sajid, Sjoerd and Wouter (3x). It was a nice place where we gained lots of new ideas and we always made time for some Friday afternoon experiments. Yet, is also like to thank all the other members of IMS for a great memorable time and nice trips to Smalenberg and Oxford, including: Dave, Mark, Bernard, Guus, Gertjan, José, Josée, Marion, Peter (2x), Alim, Nirupam, Bouwe, Ruud, Kurt, Brian, Hajo, Michelle, Rik, Tom, Werner, Anirban, Kenan, Deba, Minh, Anuj, Evert, Ben,

Tjeerd, Zhaoliang, Xin, Hans, Oktay, Gerwin, Tülin, Petra, Vera, Bahruz, Maarten en Roy.

Close to the end of the acknowledgement, I would like to thank a few good friends for a great period. Including, a former house-mate and a true chemist, Michiel Beij. I like the way that we can fantasize and speculate about new possibilities. Also, I would like to thank formal IMS-er Sandra Stadman and I share her passion for nice food and spices. In addition, I would the whole marksman guild St. Jan Keijenburg, where I Played the trumpet, since the age of 11 for the nice trips and events.

Last, but not least, I would like to thank my family for their support: My brother Maurits with Ritagna, my sister Bernadette with Bas and my farther Wim. Of course, I would like to thank my mother Alice, who I lost almost 10 years ago. Dear Alice, you were a great mother and I believe you may be a bit proud on me.

Dankwoord.

Promoveren gaat natuurlijk niet zonder de hulp van anderen en ik wil dan ook een paar mensen bedanken. Allereerst wil ik mijn begeleider/promotor André bedanken. André is een fijne begeleider, heeft mij altijd veel vertrouwen gegeven en bekijkt resultaten vrijwel altijd met een positieve insteek. Zelfs bij moeilijk verklaarbare metingen waar ik niet zoveel heil in zag. Daarnaast kon ik eigenlijk altijd bij zijn kantoor binnen komen waaien als ik advies nodig had. Ik heb veel nuttig advies van hem gekregen met name in het schrijven van artikelen waar ik volgens mij wel aardig in gegroeid ben.

Eveneens wil ik Tomek bedanken als begeleider (gedurende mijn master), collega en goede kameraad. We hebben veel van gedachte gewisseld, met name op het gebied van kleine hoek röntgen verstrooiing (SAXS). Samen zijn we in de theorie van dit verschijnsel gedoken en werden we toch een beetje de SAXS goeroes van onze vakgroep. Ook wil ik jou en Kasia bedanken voor de leuke uitjes naar Gogol Bordello, Leeds en de aparte vakantie met de eerste verjaardag van je dochter Maja in Polen.

Daarnaast wil ik alle andere leden van de SAXS clan (Sjoerd, Hessel, Suresh, Sajid, Pablo en Huiyu) bedanken voor de interessante exploratieve metingen, nuttige discussies en de gezelligheid tijdens de tripjes naar de Europese Synchrotron Straling Faciliteit (ESRF) in Grenoble. Natuurlijk, non-stop meten op de röntgenbundel voor 3-4 dagen en een planning die continue aangepast werd, gaf soms wat strubbelingen, slapeloosheid en stress. Toch was het een erg nuttige ervaring en leer je elkaar zo wel beter kennen. Tevens wil ik de technici van de Nederlands/Belgische röntgenbundel (DUBBLE Bm26) bedanken. Met name Guiseppe, maar ook Daniel, Fabian en Wim voor het voorbereidende en assisterende werk hun probleem oplossend denkvermogen, en de bereidheid om nog even door te werken om problemen opgelost te krijgen.

Ook heb ik een aantal metingen buiten IMS laten doen: Daarvoor wil ik allereerst Leo en Sabarinathan van de universiteit in Ausburg bedanken voor de vaste stof magische spinninghoek kernspinresonantie spectroscopie metingen (solid state MAS-NMR) op gemixte niobia hybride silica systemen.

Met name zijn expertise op het gebied van de exotische ^{17}O kern alswel op de ^{29}Si en ^{13}C kernen gaven een goed inzicht in de structurele verbindingen die in het glasachtig materiaal gevormd werden (hoofdstuk 5).

Ten tweede zou ik graag Martin Lutz en Vadim Kessler willen bedanken voor de éénkristal röntgendiffractiemetingen op de $\text{Nb}_8\text{O}_{10}(\text{OEt})_{20}$ kristallieten (hoofdstuk 6). Ten derde wil ik Hessel bedanken voor de fijne samenwerking binnen het project van STW (Stichting Technische Wetenschappen). Met name met betrekking op de chemische stabiliteit metingen, maar we hebben eveneens samengewerkt op het gebied van SAXS. Ik waardeer zijn eigenzinnige karakter en hoewel hij mij soms overviel met een spaakwaterval aan woorden rollen er meestal wel een aantal nuttige tips uit. Natuurlijk gaat mijn dank ook uit naar Hammad, Louis en Arjan binnen de anorganische membranen group (IM). Met Hammad heb ik samengewerkt om mijn ideeën met betrekking tot metaal oxide gedoopte hybride silicaten toe te passen in membranen. Met de tetrakis-(triethoxysilylpropyl)-malonamide (TTPMA) systemen heeft het uiteindelijk wel tot aardige resultaten geleid (Hoofdstuk 7). Daarnaast wil ik Mariëlle, Jaap en Wim van het Nederlandse energie onderzoekscentrum (ECN) bedanken voor de samenwerking met het coaten van cilindrische membranen. Tevens waardeer ik hun kritische input, dat me weer verder aan het denken heeft gezet. Ook wil ik alle andere leden van STW: Rob (ECN), Frans (Pervatech), Monique (STW), Arjan (Shell) Gerald (Akzo Nobel) en Gadi (Universiteit van Amsterdam) voor het constructief meedenken en de financiële ondersteuning van mijn project.

Daarnaast zou ik de technici van onze vakgroep Henk en Dominic bedanken. Goede technici zijn cruciaal, en ik kon vrijwel altijd bij ze terecht voor allerlei technische probleempjes. Dominic heeft me ontzettend veel geholpen met het ontwerp en de bouw van een mix-setup voor SAXS wat me uiteindelijk toch weer een mooi hoofdstuk heeft opgeleverd (hoofdstuk 3). Samen met Henk heb ik onder andere gebrainstormd voor een extra stikstofdoorstroombox (flowbox) voor reacties die gevoelig zijn voor water, aangezien er in de huidige handschoenenbox (glovebox) weinig ruimte over was voor chemische reacties. Het is een heel degelijke box geworden. Het

kwam voor mij helaas een beetje als mosterd na de maaltijd, maar het is sowieso nuttig voor nieuwe promovendi zoals Petra. Ik wens haar er dan ook veel plezier mee.

Tevens wil ik de practica-studenten David en Kristianne bedanken. In heb hen veelal opgezadeld met lastig interpreteerbare infrarood en kernspinresonantie spectroscopie data waar zij zich, met enige begeleiding, toch karig doorheen geworsteld hebben. Ook wil ik Robin voor zijn oriënterend onderzoek naar de TTPMA precursor. Het was altijd feest met jouw in het lab en je hebt dan ook een onvergetelijke indruk gemaakt.

Eveneens wil ik de IMS-ers bedanken voor een fijne PhD-periode. Waaronder mijn kantoorgenoten: Michiel, Janneke, Victor, Huiyu, Victor, Robbert, Mohammed en in het bijzonder Wouter. Wouter, met wie ik 4 jaar op het kantoor heb gezeten, was meestal mijn eerste aanspraakpunt met allerlei gedachtecronkels en lichte frustraties. Ook buiten IMS zijn we veel opgetrokken, zo nu en dan schaatsen waar ik toch al wel een stuk beter in geworden ben. Daarnaast wil ik alle chemische broeders bedanken: Maarten, Antony, Pablo, Gerard, Michiel, Tomek, Sjoerd, Ole, Suresh Ronald, Huiyu, Sajid, Nicolas, Ronald, Wouter (3x), Joren, Liz en Petra. Het chemisch lab was een relaxte werkplek waar tussen de experimenten veel idiote ideeën gespuid werden en vaak wel tijd gemaakt werd voor een vrijdagmiddag experimentje.

Natuurlijk wil ik ook alle andere IMS-ers bedanken die ik nog niet genoemd heb: Dave, Mark, Bernard, Guus, Gertjan, José, Josée, Marion, Peter (2x), Alim, Nirupam, Bouwe, Ruud, Kurt, Brian, Hajo, Michelle, Rik, Tom, Werner, Anirban, Kenan, Deba, Minh, Anuj, Evert, Ben, Tjeerd, Zhaoliang, Xin, Hans, Oktay, Gerwin, Tülin, Petra, Vera, Bahruz, Maarten en Roy. Ik wil hen bedanken voor een onvergetelijke tijd en gezellige uitjes naar Smallenberg en Oxford.

Tegen het einde van deze ietwat lange dankwoord wil ik nog een paar goede vrienden bedanken voor een mooie periode. Waaronder Michiel Beij een oud huisgenoot uit Deventer en een chemicus pur sang. Ik vind het mooi over hoe wij over van alles kunnen speculeren en fantaseren.

Daarnaast wil ik ex-IMS-ster Sandra Stadman ook nog even noemen. Ik deel haar liefde voor lekker eten, maar ze kan veel beter taarten bakken als ik. Ook wil ik het hele schuttergilde St. Jan Keijenborg, waar ik al sinds mijn 11e trompet bespeel, voor de nodige ontspanning, de gezellige uitjes met concoursen, oktoberfest en dergelijke.

Tenslotte, wil ik mijn familie bedanken voor alle steun: Mijn broer Maurits met Ritagna, mijn zus Bernadette met Bas en mijn pa Wim. Natuurlijk wil ik ook mijn moeder bedanken wie helaas al bijna 10 jaar heb moeten missen. Beste, Alice je was een geweldige moeder en ik denk ook wel dat nu wel een beetje trots op mij zult zijn.